1-1-2019

Electro- and photocatalytic carbon dioxide reduction and thermal isomerization of highly strained tricyclocompounds

Weiwei Yang

ELECTRO- AND PHOTOCATALYTIC CARBON DIOXIDE REDUCTION AND THERMAL

ISOMERIZATION OF HIGHLY STRAINED TRICYCLOCOMPOUNDS

A Dissertation
presented in partial fulfillment of requirements
for the degree of Doctor of Philosophy
in the Department of Chemistry and Biochemistry
The University of Mississippi

by

WEIWEI YANG

August 2019

ABSTRACT

Anthracene-bridged dinuclear rhenium complexes are reported for electrocatalytic and photocatalytic carbon dioxide (CO_2) reduction to carbon monoxide (CO). Related by hindered rotation of each rhenium active site to either side of the anthracene bridge, *cis* and *trans* conformers have been isolated and characterized. Electrochemical studies reveal distinct mechanisms, whereby the *cis* conformer operates via cooperative bimetallic CO_2 activation and conversion and the *trans* conformer reduces CO_2 through well-established single-site and bimolecular pathways analogous to $Re(bpy)(CO)_3Cl$. Higher turnover frequencies are observed for the *cis* conformer (35.3 s^{-1}) relative to the *trans* conformer (22.9 s^{-1}), with both outperforming $Re(bpy)(CO)_3Cl$ (11.1 s^{-1}). Photocatalytic reactivity shows the plausible pathway for dinuclear system is one site acting as an efficient, covalently-linked photosensitizer to the second site performing CO_2 reduction. The excited-state kinetics and emission spectra reveal that the anthracene backbone plays a more significant role beyond a simple structural unit.

The isomerizations of 3,4-diazatricyclo[4.1.0.0^{2,7}]hept-3-ene and 3,4 diazatricyclo[4.1.0.0^{2,7}]heptane to their corresponding products were studied by *ab initio* calculations at multiconfiguration self-consistent field level to study the stabilization effects from π bond electrons and lone pair electrons. The isomerization of 3,4-diazatricyclo[4.1.0.0^{2,7}]hept-3-ene occurs through four unique pathways. The 12.2 kcal mol^{-1} disparity in the disrotatory barriers is explained through π electron delocalization in the transition state. The 3,4-

diazatricyclo[4.1.0.0^{2,7}]heptane structure has eight separate reaction channels for isomerization. Resonance stabilization from lone pair electron for two of the forbidden pathways results in a relative energy lowering. The isomerization of benzvalene to benzene has barriers of 20.6 kcal mol^{-1} for the disrotatory channel and 26.8 kcal mol^{-1} for the conrotatory channel. The isomerization of benzvalene back to benzvalene occurs by the transition state disTS$_{back}$ with barrier of 29.8 kcal mol^{-1}. For the isomerization of benzvalyne, the barriers are 22.9 kcal mol^{-1} for disrotatory channel and 21.7 kcal mol^{-1} for conrotatory channel. Intrinsic reaction coordinate shows the 122.2 kcal mol^{-1} relative energy could be released only by 1.4 kcal mol^{-1} due to the absence of normally intermediate with *trans* double bond.

LIST OF ABBREVIATIONS AND SYMBOLS

CO_2 carbon dioxide

CO   carbon monoxide

NHE   normal hydrogen electrode

PTCE   proton couple electron transfer

MOST   molecular solar thermal system

DATCE   3,4-diazatricyclo[4.1.0.0^{2,7}]hept-3-ene

DAP   3*H*-1,2-diazepine

DATCA   3,4-diazatricyclo[4.1.0.0^{2,7}]heptane

DHDAP   2,3-dihydro-1*H*-1,2-diazepine

TATCE   3,4,5-triazatricyclo[4.1.0.0^{2,7}]hept-3-ene

TAP   1*H*-1,2,3-triazepine

DMF   *N,N*-dimethylformamide

DMSO   dimethyl sulfoxide

NMR   nuclear magnetic resonance

ESI-MS   electrospray ionization mass spectra

FTIR   Fourier transformer infrared spectroscopy

CV   cyclic voltammetry

CPE   controlled potential electrolysis

GC	gas chromatograph
FID	flame ionization detector
TCD	thermal conductivity detector
SEC	spectroelectrochemical
DFT	density functional theory
TS	transition state
COSMO	conductor-like screening model
Re_2Cl_2	1,8-di(2,2'-bipyridine)anthracene$(Re(CO)_3Cl)_2$
anthryl-Re	[1-(2,2'-bipyridine)anthracene][$Re(CO)_3Cl$]
$Fc^{+/0}$	ferrocenium/ferrocene
$E_{p,c}$	cathodic peak potential
$i_{p,c}$	cathodic peak current
ν	scan rate
Bu_4NPF_6	tetrabutylammonium hexafluorophosphate
K_C	comproportionation constant
i_{cat}	limiting catalytic current in the presence of CO_2
n_{cat}	the number of electrons transferred in the catalytic process
F	Faraday's constant
A	area of the electrode

[cat]	molar concentration of the catalyst
D	diffusion coefficient
k_{cat}	rate constant of the catalytic reaction
[S]	molar concentration of dissolved CO_2
n_p	the number of electrons transferred in the noncatalytic process
R	ideal gas constant
T	temperature
i_p	peak current observed for the catalyst in the absence of substrate
TOF	turnover frequency
TON	turnover number
FOWA	foot-of-the-wave analysis
TFE	2,2,2-trifluoroethanol
MeOH	methanol
PhOH	phenol
E_{appl}	applied potential
PS	photosensitizer
BIH	1,3-dimethyl-2-phenyl-2,3-dihydro-1H-benzoimidazole
TEA	triethylamine
ϕ	quantum yield

MLCT   metal-to-ligand charge transfer

MCSCF   multiple configuration self-consistent field

MRMP   multireference Moller-Plesset

CCSD   couple cluster single and double excitations

ZPE   zero-point energy

NOON   natural orbital occupation number

IRC   intrinsic reaction coordinates

ACKNOWLEDGEMENTS

There are so many people that I would like to express my sincere gratitude for their help during my way to doctoral degree. First, I am very grateful to my advisors, Prof. Jonah W. Jurss and Prof. Steven Davis, for their support for my academic and research progress. I have learned a lot from Prof. Jurss about fundamentals of scientific research during the first part of my graduate school's time. He always deeply inspired me by his hardworking and passion for scientific research. Especially I want to thank for his support and consideration when I decided to be more involved in another research field. The first time I really knew Prof. Davis was in 2018 he taught me physical chemistry class. He is the most intelligent person I have ever met. On the academic level, Prof. Davis have built me up by advanced physical chemistry and quantum chemistry. His patience and motivation also lead me to the world of computational chemistry where I learned to solve chemistry problems from calculation perspectives. I could not imagine to successfully complete my Ph.D. study without those two respectful advisors, Prof. Jurss and Prof. Davis.

Besides my advisors, I would like to thank the rest of my dissertation committee members: Prof. Walter Cleland, Prof. Jared Delcamp and Prof. Adam E. Smith for their insightful advice and great encouragement.

I would like to thank all my labmates and collaborators for their continue support. I could never finish my dissertation without their cooperation and contribution in various projects. Moreover, I thank them for bring all the fun and joys into my graduate school.

Last but not least, I would like to deeply thank all my family and friends for their encouragement and support, whenever and wherever I feel discouraged while I pursue my academic dream. Especially I want to thank my husband Jiaxiang Zhang for his spiritually supporting and endless love through my Ph. D. study and whole life. I want to formally say thank you to my son Geoffrey Zhang for the joys and happiness he brought to me. He is also the person make me feel more strong, more capable and more confident.

TABLE OF CONTENTS

LIST OF TABLES

LIST OF FIGURES

xvi

INTRODUCTION

Finding a sustainable energy conversion strategy is an urgent scientific and technological challenge given our reliance on non-renewable fossil fuels as a primary energy source coupled with increasing global energy demand.[1] Carbon dioxide is the chief component of this waste stream which has been linked to climate change and other environmental concerns.[2,3] Renewable energy sources such as wind and solar are attractive, but they are intermittent, site specific, and geographically diffuse. Additionally, they require energy storage before they can be relied on to power society.[4] To address this challenge while reducing CO_2 emissions, solar energy or renewable electricity can be used to drive the conversion of carbon dioxide and water into fuels whereby energy is stored indefinitely in the form of chemical bonds for on-demand use. The efficient catalytic conversion of CO_2 into energy-rich compounds could close the carbon cycle and allow an underutilized resource to be tapped into.[5-11]

Carbon dioxide is a non-polar, linear, and inert molecule. The single-electron reduction of carbon dioxide to radical ion $CO_2^{\cdot-}$ can be achieved by a significant amount of energy input, witnessed by a reduction potential of -1.90 V vs. NHE in Table 1.[12] The presence of proton make carbon dioxide reduction feasible at lower energy cost by the use of proton couple electron transfer (PCET). Additional concern existing in this process is the proton is utilized selectively for carbon dioxide reduction rather than hydrogen generation, since the proton reduction required comparatively less negative potential of -0.42 V vs. NHE in Table 1.

Table 1. Electrochemical reduction of CO_2 in the presence of a proton source (aqueous solution, pH 7, vs. NHE).

$$CO_2 + e^- \longrightarrow CO_2{}^{\cdot -} \qquad -1.90$$
$$2H^+ + 2e^- \longrightarrow H_2 \qquad -0.42$$
$$CO_2 + 2H^+ + 2e^- \longrightarrow HCO_2H \qquad -0.61$$
$$CO_2 + 2H^+ + 2e^- \longrightarrow CO + H_2O \qquad -0.53$$
$$CO_2 + 4H^+ + 4e^- \longrightarrow HCHO + H_2O \qquad -0.48$$
$$CO_2 + 6H^+ + 6e^- \longrightarrow CH_3OH + H_2O \qquad -0.38$$
$$CO_2 + 8H^+ + 8e^- \longrightarrow CH_4 + 2H_2O \qquad -0.24$$
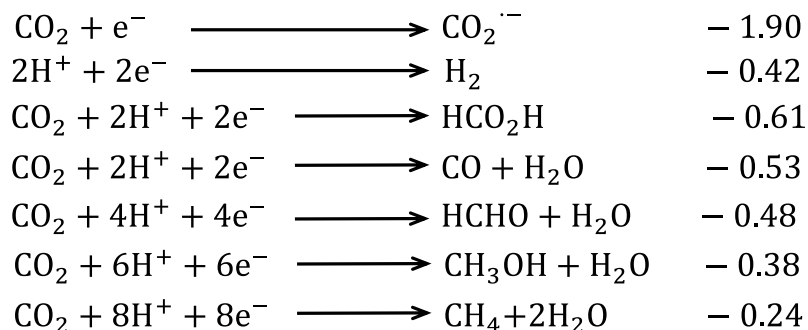
Molecular metal-based catalysts for CO_2 reduction have been widely pursued as transition metals generally have multiple redox states accessible to facilitate multi-electron chemistry. The bulk of these catalysts employ a single metal center.[5-11] Re(bpy)(CO)₃Cl (where bpy is 2,2'-bipyridine) and related derivatives continue to attract attention as competent electrocatalysts for CO_2 reduction, in addition to being single component photocatalysts.[13-27] Recently, these systems have been functionalized with phosphonate anchoring groups for surface attachment to photocathodes where they exhibit long-term stability for CO_2 reduction.[28-33] Successful translation of these catalysts into working devices emboldens their continued development where lower overpotentials and faster rates are remaining challenges.

Current investigations focusing on the direct conversion of solar energy to stored chemical energy could be divided into two categories.[34] One is open cycle solar system, using solar energy for the splitting of water into hydrogen and/or the reduction of carbon dioxide into methanol. The stored chemical energy in hydrogen and/or methanol would be released by subsequent combustion process. An alternative is closed cycle solar system, also called molecular solar thermal systems. The low-energy precursor would convert to high-energy isomer

by photoisomerization. This metastable isomer with high energy density would thermally isomerize back to precursor along with releasing the stored energy.[34] Inspired by the existing MOST including stilbenes, azobenzenes, anthracenes, ruthenium fulvalene and norbornadiene-quadricyclane systems,[35] the thermal isomerization of analogous polycyclic compounds is worthy of exploration for possible energy storage and release due to their highly strained energy.

Strained polycyclic hydrocarbons are often more stable than anticipated considering their possession of large amounts of strain energy. This fact provoked exploration of such molecules as potential fuel sources due to the exothermicity manifest during activation. The bicyclobutane moiety plays an important structural role in high energy density fuels on the basis of its high strain energy. The thermal isomerization of bicyclobutane has gained considerable interest on account of the various possible pathways of strain release.[36-40] The mechanism of the opening of the two fused three-member rings is important to understand the release of thermal energy related to liquid fuel vaporization ahead of the flame front.[41] Nguyen and Gordon examined the isomerization channels of bicyclobutane to butadiene at the multiconfiguration self-consistent field level and reported the allowed conrotatory pathway and forbidden disrotatory pathway.[40] They also showed that a multideterminant wavefunction was necessary to describe the forbidden pathway due to the strong singlet biradical character. Connecting the two methylene carbons of bicyclobutane with a carbon chain results in a tricyclo structure which imparts additional steric constraints. The isomerization still proceeds through cleavage of two nonadjacent C–C bonds in the bicyclobutane moiety but the bridge-connected methylenes are no longer free to rotate during the isomerization. In the conrotatory pathway, the orbitals comprising the cleaved bonds rotate in

3

the same direction, i.e. both clockwise or both counterclockwise. In the disrotatory pathway, the orbitals comprising the cleaved bonds rotate in opposite directions. The conrotatory transition state for bicyclobutane is about 15 kcal mol^{-1} lower in energy than the disrotatory transition state so the conrotatory is labeled ''allowed'' and the disrotatory ''forbidden''. When the two methylene groups of bicyclobutane are bridged as shown in Figure 1, the conrotatory rotation of the cleaving orbitals causes a *trans* double bond to form, while for the disrotatory rotation, both double bonds are in the cis geometry. The presence of a *trans* double bond in a six or seven membered conjugated cyclic diene produces considerable bond strain. This strain can also be relieved by simple rotation of the *trans* double bond with a very small activation barrier.[42] It is the highly strained nature of the *trans* double bond that is worthy of exploration for possible energy storage motifs inspired by the strained ring quadricyclane to norbonadiene couple.[43]
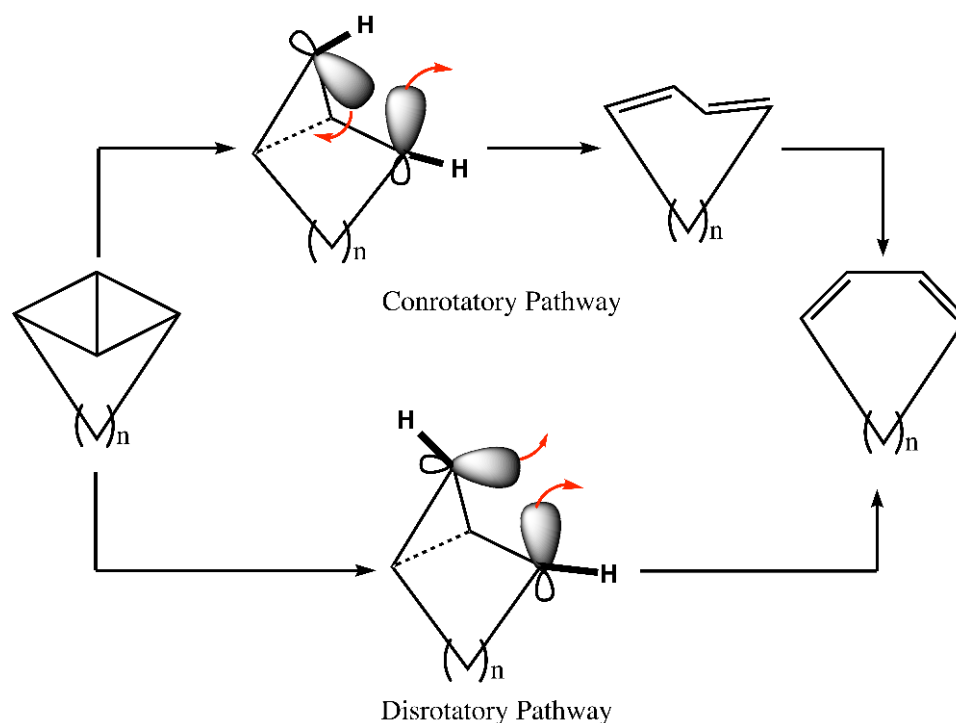
Figure 1. Schematic representation of conrotatory and disrotatory pathways.

In this dissertation, the electro- and photocatalytic reduction of carbon dioxide for open solar cycle system from experimental chemistry perspective were discussed. Also the thermal isomerization of tricylco-compounds for possible energy storage and release from computational chemistry perspective were studied. In chapter one, electrocatalytic CO_2 reduction with a dinuclear rhenium complex and comparison of the monometallic and cooperative bimetallic pathways were discussed. After electrocatalytically evaluation of aforementioned dinuclear rhenium complex, photochemical CO_2 reduction with mononuclear and dinuclear rhenium catalysts bearing a pendant anthracene chromophore were studied in chapter two. Chapter three included the *ab initio* calculation of thermal isomerization of 3,4-diazatricyclo[4.1.0.0^{2,7}]hept-3-ene (DATCE), 3,4-diazatricyclo[4.1.0.0^{2,7}]heptane (DATCA), and 3,4,5-

triazatricyclo[4.1.0.0^{2,7}]hept-3-ene (TATCE). The *ab initio* study of thermal isomerization of benzvalene to benzene and benzvalyne to benzyne were discussed in chapter four.

This dissertation used materials from three articles in journals.[44-46] Chapter one used content from the article in Inorganic Chemistry journal,[44] reprinted (adapted) with permission from (I*norg. Chem.* 201857159564-9575). Copyright (2018) American Chemical Society. Weiwei Yang, Rebekah L. Nelson and Jonah W. Jurss synthesized and characterized the catalyst; Weiwei Yang, Sayontani Sinha Roy and Jonah W. Jurss performed and analyzed the electrochemical measurements; Winston C. Pitts carried out the DFT calculations. Chapter two was based on the article in Chemical Communication journal,[45] (*Chem. Commun.*, 2019, **55**, 993)- reproduced by permission of The Royal Society of Chemistry. Weiwei Yang and Jonah W. Jurss synthesized and characterized the catalyst; Nalaka P. Liyanage and Jared H. Delcamp collected and analyzed the photocatalysis data; Sayontani Sinha Roy obtained Stern-Volmer quenching data; Stephen Guertin, Rebecca E. Adams and Russel H. Schmehl obtained photophysical properties. Chapter three was based on the article in Physical Chemistry Chemical Physics,[46] (Phys.Chem.Chem.Phys., 2018, 20, 26608) - reproduced by permission of the PCCP Owner Societies. It is coauthored by Weiwei Yang, Kimberley N. Poland and Steven R. Davis. Finally, some materials from those articles were incorporated in chapter introduction and chapter conclusion.[44-46]

CHAPTER I

ELECTROCATALYTIC CO$_2$ REDUCTION WITH *CIS* AND *TRANS* CONFORMERS OF A RIGID DINUCLEAR RHENIUM COMPLEX

1.1 Introduction

Mechanistic studies of Re(bpy)(CO)$_3$X-type catalysts have provided evidence for the concentration-dependent formation of dinuclear intermediates during catalysis.[16,17,47-55] Indeed, bimetallic and monometallic pathways exist as dimer formation is in competition with CO$_2$ reduction at a single metal.[49] Disentangling the contributions of competing pathways, in addition to the transient nature of their respective intermediates, has made it difficult to assess the possible advantages of two metal centers in activating and reducing CO$_2$ in a cooperative fashion. A beneficial interaction between two active sites is further clouded as a Re-Re bonded dimer has been indicted as a deactivated intermediate.[52,53]

Several bimetallic catalyst designs have been pursued based on flexible alkyl tethers[56,57] or hydrogen bonding interactions,[58,59] which suffer from a lack of rigidity and variable solution compositions. Other examples feature dinucleating scaffolds that preclude intramolecular bimetallic CO$_2$ activation and conversion.[60-63] Thus, the desirable design parameters surrounding this approach are poorly understood.

In this context, we sought to develop catalysts with a rigid dinucleating ligand that positions two rhenium active sites in close proximity with a predictable intermetallic distance and orientation (Scheme 1). The ability to isolate and even select from competing mechanisms (i.e. bimetallic *vs* monometallic pathways) would allow us to compare and understand differences in efficiency, activity, and stability. Herein the synthesis, characterization, and electrocatalytic activity of homogeneous *cis* and *trans* conformers of a Re₂ catalyst supported by an anthracene-based polypyridyl ligand are described.

Scheme 1 Synthesis of 1,8-di([2,2'-bipyridin]-6-yl)anthracene 1 and its bimetallic Re(I) conformers, *cis*-Re₂Cl₂ and *trans*-Re₂Cl₂.
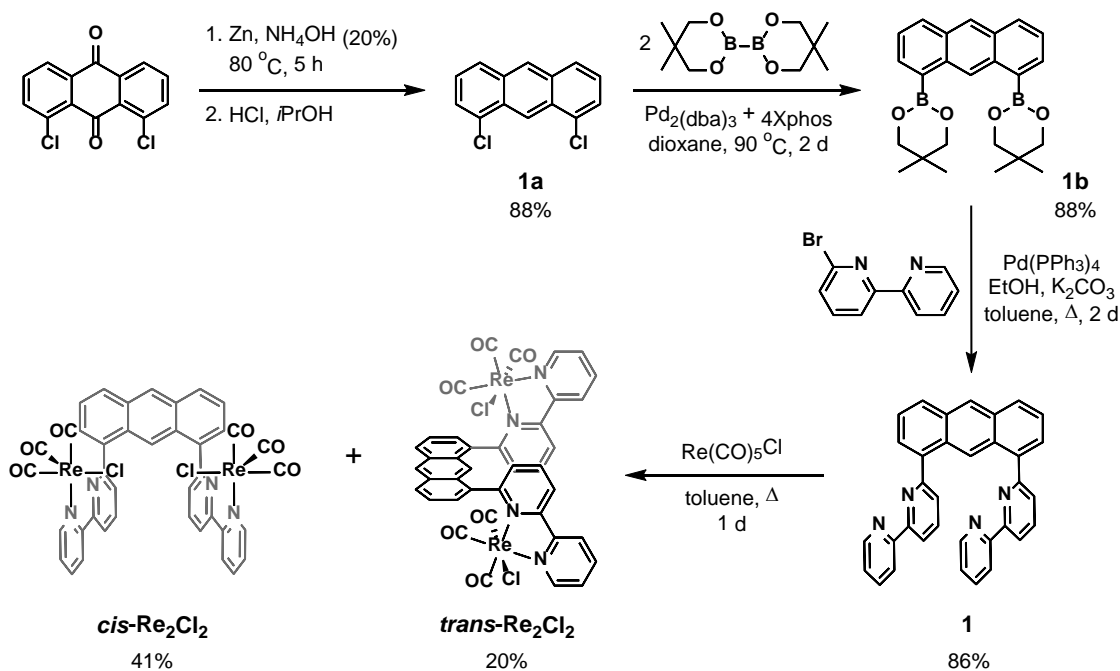
1.2 Experimental section

1.2.1 Materials and methods

Unless otherwise noted, all synthetic manipulations were performed under N_2 atmosphere using standard Schlenk techniques or in an MBraun glovebox. Toluene was dried with a Pure Process Technology solvent purification system. Anhydrous *N,N*-dimethylformamide (DMF) was purchased from Alfa Aesar, packaged under argon in ChemSeal bottles. The rhenium precursor $Re(CO)_5Cl$ was purchased from Strem and stored in the glovebox. All other chemicals were reagent or ACS grade, purchased from commercial vendors, and used without further purification. ^1H and ^{13}C NMR spectra were obtained using a Bruker Advance DRX-500 spectrometer operating at 500 MHz (^1H) or 126 MHz (^{13}C). Spectra were calibrated to residual protiated solvent peaks; chemical shifts are reported in ppm. Electrospray ionization mass spectra (ESI-MS) were obtained with a Waters SYNAPT HDMS Q-TOF mass spectrometer. UV-Vis spectra were recorded on an Agilent / Hewlett-Packard 8453 UV-Visible Spectrophotometer with diode-array detector. Infrared spectra were obtained on an Agilent Technologies Cary 600 series FTIR spectrometer equipped with a PIKE GladiATR accessory.

1.2.2 Electrochemical measurement

Electrochemistry was performed with a Bioanalytical Systems, Inc. (BASi) Epsilon potentiostat. Cyclic voltammetry studies employed a three-electrode cell equipped with a glassy carbon disc (3 mm dia.) working electrode, a platinum wire counter electrode, and a silver wire quasi-reference electrode that was referenced using ferrocene as an internal standard at the end of

9

experiments. Electrochemistry was conducted in anhydrous DMF containing 0.1 M Bu_4NPF_6

supporting electrolyte. Solutions for cyclic voltammetry were thoroughly degassed with Ar or

CO_2 before collecting data. All voltammograms were cycled from the most positive potential to

the most negative potential and back.

Controlled potential electrolysis were carried out in a 3-neck glass cell with a glassy

carbon rod (2 mm diameter, type 2, Alfa Aesar) working electrode, a silver wire quasi-reference

electrode, and a platinum mesh (2.5 cm^2 area, 150 mesh) counter electrode that was separated

from the other electrodes in an isolation chamber comprised of a fine glass frit. Solutions were

degassed with CO_2 for 30 min before collecting data. The applied potential values were

determined by cyclic voltammetry before controlled potential electrolysis were performed.

Evolved gases during electrolysis measurements was quantified by gas chromatographic analysis

of headspace samples using an Agilent 7890B Gas Chromatograph and an Agilent PorapakQ (6'

long, 1/8" O.D.) column. CO was measured using an FID detector, while H_2 was quantified at

the TCD detector. Constant stirring was maintained during electrolysis. Integrated gas peaks

were quantified with calibration curves obtained from known standards purchased from

BuyCalGas.com. From the experimental amount of product formed during electrolysis, Faradaic

efficiencies were calculated against the theoretical amount of product possible based on the

accumulated charge passed and the stoichiometry of the reaction.

UV-visible spectroelectrochemical (SEC) measurements were conducted with a

commercial "honeycomb" thin-layer SEC cell from Pine Research Instrumentation employing a

gold working electrode, a silver wire quasi-reference electrode, and a platinum wire counter electrode.

1.2.3 X-ray crystallography

Single crystals were coated with Paratone-N hydrocarbon oil and mounted on the tip of a MiTeGen micromount. Temperature was maintained at 100 K with an Oxford Cryostream 700 during data collection at the University of Mississippi, Department of Chemistry and Biochemistry, X-ray Crystallography Facility. Samples were irradiated with Mo-Kα radiation with $\lambda = 0.71073$ Å using a Bruker Smart APEX II diffractometer equipped with a Microfocus Sealed Source (Incoatec IμS) and APEX-II detector. The Bruker APEX2 v. 2009.1 software package was used to integrate raw data which were corrected for Lorentz and polarization effects.[64] A semi-empirical absorption correction (SADABS) was applied.[65] The structure was solved using direct methods and refined by least-squares refinement on F^2 and standard difference Fourier techniques using SHELXL.[66-68] Thermal parameters for all non-hydrogen atoms were refined anisotropically, and hydrogen atoms were included at ideal positions. Poorly resolved outersphere DMF molecules could not be modeled successfully in the difference map. The data was treated with the SQUEEZE procedure in PLATON;[69,70] details are provided in the CIF file.

1.2.4 Computational methods

All calculations were performed in Gaussian 09.[71] All energies discussed in this work contain zero point energy corrections. Global minimums of the *cis* and *trans* conformers were

located using density functional theory (DFT) and the ωB97X-D[72] functional.[73] The 6-311+G*

basis set was used for all coordinating atoms which includes the carbon monoxide. The 6-311G*

basis was used for all hydrogen and carbon atoms of the ligand manifold. LanL2TZ (f) was used

for the two rhenium atoms. The minimums were confirmed by calculating the harmonic

vibrational frequencies and finding all real values. To obtain a structure close to the transition

state (TS) of conformational isomerization (*via* rotation), an initial relaxed scan was performed

using semi-empirical PM6 and was parametrized by the dihedral angle C(14)-C(15)-C(23)-N(39)

or C(6)-C(5)-C(29)-N(40) for TS1 and TS2, respectively, as labeled in Figure A1. From these

scans, the maximum was used as a starting point for a transition state optimization using the

Berny algorithm at the level of theory and basis sets mentioned previously.

Structural optimization and infrared spectra calculations were performed using the BP86-

D3/def2-TZVP functional-basis set combination with Beck's and Johnston's dispersion

corrections. The rhenium atoms were described with the LanL2TZ (f) effective core potential

with the added polarization function. These calculations also included DMF solvent-induced

corrections using the COSMO solvation model. Frequency analysis confirmed global minimums.

Global minimums for the Re-Re dimers were found using the ωB97X-D functional with

basis sets LanL2TZ (f) for rhenium atoms and 6-31++G* for all light atoms. An ultrafine

numerical integration grid was employed for both species. Cartesian coordinates and energies are

given in Table A1-Table A10.

1.2.5 Synthetic procedures.

Re(bpy)(CO)$_3$Cl was prepared as previously described.[74] Ligand precursors 6-bromo-2,2'-bipyridine[75] and 1,8-bis(neopentyl-glycolatoboryl)anthracene[76] were prepared according to literature procedures.

1,8-di(2,2'-bipyridine)anthracene, **1**. In an oven-dried 2-neck round bottom flask were added 1,8-bis(neopentylglycolatoboryl)anthracene (1.0 g, 2.49 mmol), 6-bromo-2,2'-bipyridine (1.4 g, 5.97 mmol), and Pd(PPh$_3$)$_4$ (0.172 g, 6 mol %) under inert atmosphere. Degassed toluene (50 mL), ethanol (5 mL), and 2 M aqueous K$_2$CO$_3$ (5 mL) were added to the reaction vessel under N$_2$ and refluxed for 2 days. After cooling to room temperature, 25 mL saturated aqueous NH$_4$Cl and 25 mL H$_2$O were added to the mixture. The crude product was extracted with dichloromethane and purified by silica gel chromatography (1:1 hexanes:ethyl acetate) to yield pure product (1.04 g, 86%). ^{1}H NMR (500 MHz, DMSO-d_6): δ 9.80 (s, 1H), 8.83 (s, 1H), 8.62 (ddd, J = 4.7, 1.8, 0.9 Hz, 2H), 8.27 (d, J = 8.4 Hz, 2H), 7.98 (dt, J = 7.8, 1.0 Hz, 2H), 7.83 (dq, J = 7.9, 1.0 Hz, 2H), 7.78 – 7.73 (m, 4H), 7.71 – 7.65 (m, 4H), 7.57 (td, J = 7.7, 1.8 Hz, 2H), 7.33 (ddt, J = 6.9, 4.8, 1.1 Hz, 2H). ^{13}C NMR (126 MHz, DMSO-d_6): δ 157.60, 154.89, 154.52, 149.01, 137.99, 137.85, 137.01, 131.55, 129.14, 129.06, 127.38, 126.91, 125.50, 124.92, 123.84, 123.61, 119.96, 118.61. ESI-MS (M$^+$) m/z calc. for [**1** + H$^+$], 487.2, found, 487.2.

1,8-di(2,2'-bipyridine)anthracene(Re(CO)$_3$Cl)$_2$, Re$_2$Cl$_2$. To an oven-dried 2-neck round bottom flask were added 1,8-di(2,2'-bipyridine)anthracene (100 mg, 0.205 mmol) and Re(CO)$_5$Cl (148 mg, 0.41 mmol) under inert atmosphere. Anhydrous toluene (5 mL) was added and the reaction mixture was refluxed overnight. The mixture was cooled to room temperature,

13

the precipitate was collected by filtration with a glass frit, and washed with toluene and diethyl ether several times. The crude product was purified by silica gel chromatography with gradient elution from dichloromethane to 2:3 acetone:dichloromethane using a Biotage automated flash purification system to give pure compounds, *cis*-Re$_2$Cl$_2$ (41% yield) and *trans*-Re$_2$Cl$_2$ (20%).

cis-Re$_2$Cl$_2$: ^{1}H NMR (500 MHz, DMSO-*d$_6$*): δ 9.04 (d, J = 5.4 Hz, 2H), 8.87 (s, 1H), 8.77 (d, J = 8.3 Hz, 2H), 8.68 (d, J = 8.1 Hz, 2H), 8.39 (d, J = 8.5 Hz, 2H), 8.35 (t, J = 7.9 Hz, 2H), 7.90 (t, J = 7.9 Hz, 2H), 7.83 (s, 1H), 7.74 (m, 4H), 7.61 (d, J = 7.6 Hz, 2H), 7.54 (d, J = 6.6 Hz, 2H). ^{13}C NMR (126 MHz, DMF-*d$_7$*): δ 199.47, 195.09, 195.07, 161.87, 158.22, 157.57, 154.10, 141.11, 140.77, 133.41, 131.90, 131.57, 131.42, 131.02, 128.77, 128.71, 128.48, 128.32, 126.82, 126.10, 125.93, 124.94, 124.04. ATR-FTIR: ν(CO) at 2015, 1915 (with shoulder at 1924), and 1871 cm^{-1}. ESI-MS (M$^+$) m/z calc. for [*cis*-Re$_2$Cl$_2$ + Cs$^+$], 1230.9, found, 1230.9.

trans-Re$_2$Cl$_2$: ^{1}H NMR (500 MHz, DMSO-*d$_6$*): δ 9.01 (d, J = 5.4 Hz, 1H), 8.98 (d, J = 5.4 Hz, 1H), 8.87 (s, 1H), 8.77 (d, J = 8.3 Hz, 1H), 8.73 (d, J = 8.2 Hz, 1H), 8.61 (d, J = 8.1 Hz, 1H), 8.57 (d, J = 8.1 Hz, 1H), 8.42 (t, J = 8.0 Hz, 1H), 8.39 - 8.32 (m, 3H), 8.02 (t, J = 7.9 Hz, 1H), 7.83 (t, J = 6.6 Hz, 1H), 7.77 – 7.68 (m, 3H), 7.65 (d, J = 7.1 Hz, 2H), 7.53 (t, J = 7.8 Hz, 1H), 7.49 (d, J = 6.8 Hz, 1H), 7.44 (d, J = 7.7 Hz, 1H), 7.33 (s, 1H). ^{13}C NMR (126 MHz, DMF-*d$_7$*): δ 199.36, 198.83, 195.14, 194.84, 191.95, 190.96, 162.48, 162.45, 157.90, 157.83, 157.60, 157.06, 154.20, 154.09, 141.80, 141.36, 141.12, 140.91, 140.59, 139.59, 133.31, 133.22, 131.91, 131.60, 131.50, 130.92, 130.57, 130.37, 129.28, 128.81, 128.61, 128.51, 126.67, 126.12, 126.01, 125.90, 124.42, 124.39, 123.92. ATR-FTIR: ν(CO) at 2015 and 1891 cm^{-1}. ESI-MS (M$^+$) m/z calc. for [*trans*-Re$_2$Cl$_2$ + Cs$^+$], 1230.9, found, 1230.9.

1-(2,2'-bipyridine)anthracene, **2**. In an oven-dried 2-neck round bottom flask were added 1-(neopentylglycolatoboryl)anthracene (1.0 g, 3.46 mmol), 6-bromo-2,2'-bipyridine (1.0 g, 4.15 mmol), and $Pd(PPh_3)_4$ (0.2 g, 5 mol %) under inert atmosphere. Degassed toluene (50 mL), ethanol (5 mL), and 2 M aqueous solution of K_2CO_3 (5 mL) were added to the reaction vessel under N_2 and refluxed for 2 days. After cooling to room temperature, 25 mL saturated NH_4Cl and 25 mL H_2O were added into mixture. The crude product was extracted with dichloromethane and purified by silica gel chromatography (5:1 hexanes:ethyl acetate) to yield pure product (0.6 g, 52%). ^1H NMR (500 MHz, DMSO-d_6): δ 8.84 (s, 1H), 8.76 (dd, J = 88.9, 4.7 Hz, 1H), 8.72 (s, 1H), 8.52 (d, J = 7.8 Hz, 1H), 8.41 (d, J = 8.0 Hz, 1H), 8.24 (d, J = 8.4 Hz, 1H), 8.18 (t, J = 7.8 Hz, 1H), 8.13 (d, J = 8.5 Hz, 1H), 8.00 (d, J = 8.4 Hz, 1H), 7.93 (td, J = 7.8, 1.6 Hz, 1H), 7.85 (d, J = 7.6 Hz, 1H), 7.73 (d, J = 6.5 Hz, 1H), 7.66 (dd, 1H), 7.58 – 7.52 (m, 1H), 7.51 – 7.44 (m, 2H). ^{13}C NMR (126 MHz, DMSO-d_6): δ 158.47, 155.82, 155.49, 149.84, 138.87, 138.32, 137.89, 132.16, 131.98, 131.49, 129.73, 129.41, 129.06, 128.26, 127.78, 127.13, 126.43, 126.26, 125.69, 125.50, 124.86, 124.79, 121.07, 119.57. ESI-MS (M^+) m/z calc. for [**2** + H^+], 333.1, found, 333.1.

[1-(2,2'-bipyridine)anthracene][Re(CO)$_3$Cl], anthryl-Re. To an oven-dried 2-neck round bottom flask were added 1-(2,2'-bipyridine)anthracene (100 mg, 0.300 mmol) and Re(CO)$_5$Cl (108.5 mg, 0.300 mmol) under inert atmosphere. Anhydrous toluene (5 mL) was added and the reaction mixture was refluxed overnight. The mixture was cooled to room temperature, the precipitate was collected by filtration with a glass frit, and washed with toluene and diethyl ether several times. Pure product was obtained by crystallization from dichloromethane/hexanes (161

mg, 84%). Two conformers are present by ^{1}H NMR with slow rotation observed at room temperature. ESI-MS (M$^+$) m/z calc. for [anthryl-Re + Cs$^+$], 770.9453, found, 770.9452. Elemental analysis for $C_{28}H_{16}N_2O_4Re \cdot 1.5H_2O$ calcd: C 48.76, H 2.88, N 4.21; found: C 49.09, H 2.88, N 4.22.

1.3 Synthesis and characterization

The synthesis of 1,8-di([2,2'-bipyridin]-6-yl)anthracene (**1**) and its metalation to generate conformers *cis*-Re$_2$Cl$_2$ and *trans*-Re$_2$Cl$_2$ is shown in Scheme 1. As previously described,[77] 1,8-dichloroanthraquinone is reduced with Zn to give 1,8-dichloroanthracene (**1a**). Next, the 1,8-diboronate ester (**1b**) is furnished by a Pd-catalyzed borylation with bis(neopentyl glycolato)diboron.[76] The boronate ester is reacted directly by Suzuki cross coupling with 6-bromo-2,2'-bipyridine to give dinucleating ligand **1** in 86% yield. Metalation was achieved by refluxing the ligand with two equivalents of Re(CO)$_5$Cl in anhydrous toluene overnight to give a mixture of two dinuclear Re(I) conformers *cis*-Re$_2$Cl$_2$ and *trans*-Re$_2$Cl$_2$. Despite the possible formation of up to seven isomers (Figure A2), only two species are observed in the reaction mixture under these conditions as shown in the crude ^{1}H NMR spectrum (Figure A3). Two narrow, closely-spaced bands were separated by silica gel chromatography to give an overall isolated yield of 61%. We note that solvent-dependent isomer formation has been reported previously for di- and trinuclear Re(CO)$_3$-based compounds.[78] ^{1}H NMR spectra of the purified *cis* and *trans* conformers are shown in Figure 2. From the NMRs, there is a symmetric species (*cis*-Re$_2$Cl$_2$) with 12 chemically distinct protons and an asymmetric species (*trans*-Re$_2$Cl$_2$) displaying 22 different proton signals. Infrared spectroscopy in DMF established the presence of

16

fac-Re(CO)$_3$ fragments with carbonyl stretching frequencies ν(CO) for *cis*-Re$_2$Cl$_2$ at 2019, 1915, and 1890 cm^{-1} and for *trans*-Re$_2$Cl$_2$ at 2014, 1910, and 1888 cm^{-1} (Figure A4). For comparison, the CO stretching frequencies of the parent complex, *fac*-Re(bpy)(CO)$_3$Cl, are at 2019, 1914, and 1893 cm^{-1} in DMF.[16]
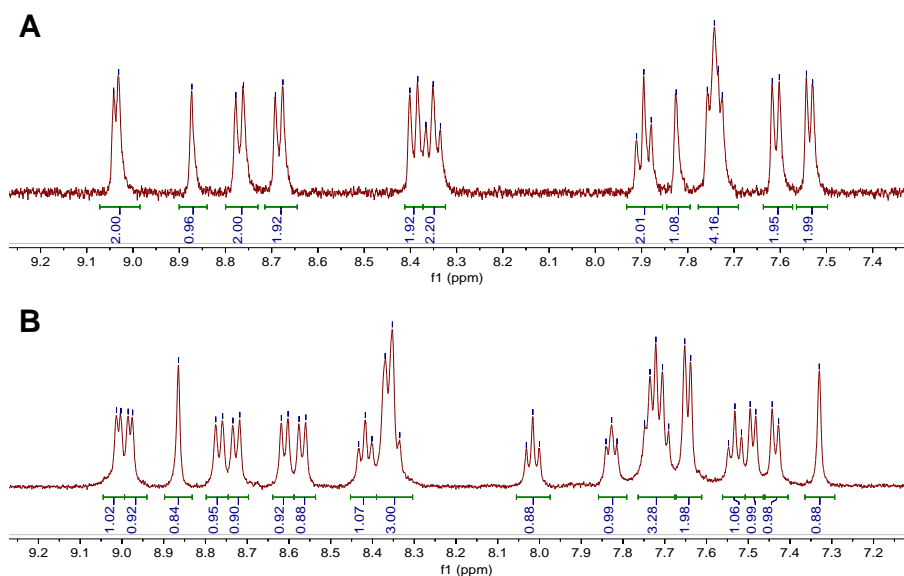
Figure 2. ^{1}H NMR spectra (500 MHz, DMSO-*d$_6$*) showing the aromatic region of A) *cis*-Re$_2$Cl$_2$ and B) *trans*-Re$_2$Cl$_2$.

X-ray quality crystals of the asymmetric *trans* conformer were obtained by slow isopropyl ether diffusion into a concentrated DMF solution. The crystal structure of *trans*-Re$_2$Cl$_2$ is shown in Figure 3, concurrently lending support for a symmetric configuration of the *cis* conformer, which is accessible by rotation (*cis* ↔ *trans*) as observed at elevated temperatures by ^{1}H NMR. However, no interconversion is observed at room temperature over the course of 2 days.
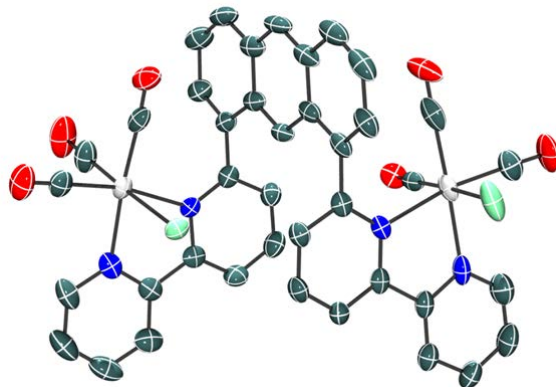
Figure 3. Crystal structure of *trans*-Re$_2$Cl$_2$. Hydrogen atoms are omitted for clarity. Thermal ellipsoids are shown at the 70% probability level.

Our catalyst design aims to channel reactivity through a single mechanism by allowing both active sites to be in close proximity for cooperative catalysis or by isolating each metal center for single-site activity. Importantly, as active sites are generated following chloride dissociation from the metal, two symmetric *cis* conformers are possible, one in which the chloro ligands face each other (*cis*-Re$_2$Cl$_2$), and the other which has its chloro ligands oriented outward (*cis* 2 as labeled in Figure A2). Density Functional Theory (DFT) calculations were used to investigate the barrier to rotation of Re(bpy) moieties to either side of the anthracene bridge by which the *trans* conformer may interconvert to either of the symmetric *cis* conformers in solution. Since the structure of *trans*-Re$_2$Cl$_2$ is known, the energy barrier associated with rotational isomerization from *trans*-Re$_2$Cl$_2$ was calculated (Figure A1). By DFT, the barrier to rotation from the *trans* conformer to *cis*-Re$_2$Cl$_2$ (27.2 kcal/mol) is 4.6 kcal/mol lower in energy than rotation to *cis* 2 (31.8 kcal/mol). These calculations provide indirect evidence that the isolated *cis* conformer has its chloro ligands facing "in" (denoted *cis*-Re$_2$Cl$_2$ as depicted in Scheme 1). Toward more direct

18

evidence, the infrared spectra of *cis*-Re$_2$Cl$_2$ and *cis* 2 were calculated by DFT. Notably, *cis*-Re$_2$Cl$_2$ is predicted to have 3 ν(CO) absorption bands while *cis* 2 is expected to have 4 ν(CO) vibrational modes (Figure A5). The experimental FTIR spectrum of the *cis* conformer (Figure A4) confirms its stereochemistry.

1.4 Results and discussion

1.4.1 Electrochemistry

Following characterization, the redox behavior of *cis*-Re$_2$Cl$_2$ and *trans*-Re$_2$Cl$_2$ was analyzed in the absence of CO$_2$ by cyclic voltammetry in anhydrous DMF containing 0.1 M Bu$_4$NPF$_6$ supporting electrolyte. Re(bpy)(CO)$_3$Cl and a mononuclear derivative (anthryl-Re) bearing a pendant anthracene (shown in Figure 4) were studied in parallel to provide insight into catalytic activity and ligand-based redox chemistry. Cyclic voltammograms (CVs) were referenced internally at the end of experiments to the ferrocenium/ferrocene (Fc$^{+/0}$) couple. The electrochemical properties of Re(bpy)(CO)$_3$Cl have been studied extensively, most often in acetonitrile solutions. Its CV in DMF, overlaid with that of anthryl-Re (Figure 4), exhibits a quasireversible redox process with $E_{p,c}$ at -1.80 V vs Fc$^{+/0}$ and an irreversible reduction at -2.25 V. Notably, the CV of anthryl-Re has a third reduction at -2.54 V that is absent in the parent complex. Similar behavior is observed for the dinuclear catalysts (Figure 4). CVs of *cis*-Re$_2$Cl$_2$ and *trans*-Re$_2$Cl$_2$ reveal two closely-spaced, quasireversible, one-electron reductions at $E_{p,c}$ = -1.77 and -1.87 V and $E_{p,c}$ = -1.78 and -1.88 V, respectively, followed by reductions at $E_{p,c}$ = -2.34 and -2.65 V and $E_{p,c}$ = -2.40 and -2.67 V, respectively, at a scan rate of 100 mV/s. The number of

19

electrons transferred in each redox process based on integrated cathodic peak areas corresponds

to a 1:1:2:1 stoichiometry. From scan rate dependent CVs of the dinuclear conformers and both

mononuclear complexes, linear fits were obtained in plots of the reductive peak current ($i_{p,c}$)

versus the square root of the scan rate ($v^{1/2}$) consistent with freely diffusing systems (Figure A6-

Figure A9).[79,80]
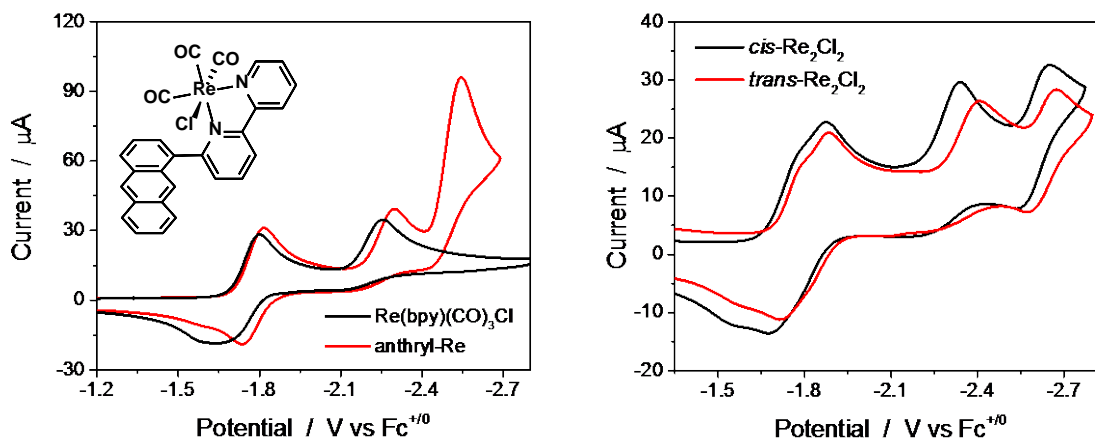
Figure 4. CVs of A) 2 mM Re(bpy)(CO)$_3$Cl and anthryl-Re, and B) 1 mM *cis*-Re$_2$Cl$_2$ and *trans*-Re$_2$Cl$_2$ in DMF/0.1 M Bu$_4$NPF$_6$ under Ar, glassy carbon disc, $v = 100$ mV/s.

Comproportionation constants (K_C) for the dinuclear catalysts were estimated from the

overlapping one-electron reductions as a measure of electronic coupling between Re(bpy)

units.[81] Based on the difference in potentials, ΔE, between $E_{p1,c}$ and $E_{p2,c}$, a K_C value of 50 was

calculated for both Re$_2$ conformers, indicative of weak electronic coupling through the

anthracene bridge.[81] Weak electronic coupling is not surprising given the number of bonds

between redox sites. These results are summarized in Table 2.

Table 2. Reduction potentials, diffusion coefficients, and comproportionation constants (K_C) from cyclic voltammetry in anhydrous DMF/0.1 M Bu$_4$NPF$_6$ solutions.

Catalyst	$E_{p1,c}$	$E_{p2,c}$	$E_{p3,c}$	$E_{p4,c}$
cis-Re$_2$Cl$_2$	-1.77	-1.87	-2.34	-2.65
	$K_C = 50$			
trans-Re$_2$Cl$_2$	-1.78	-1.88	-2.40	-2.67
	$K_C = 50$			
Re(bpy)(CO)$_3$Cl	-1.80	-2.25	-	-
	$D = 5.40 \times 10^{-6}$ cm^2 s^{-1}			
anthryl-Re	-1.82	-2.29	-2.54	-
	$D = 5.48 \times 10^{-6}$ cm^2 s^{-1}			

On the basis of these results and previous work,[58,59,62,63,82] we assign the most positive overlapping one-electron redox events to ligand-centered bipyridine reductions to form [Re^I(bpy•)(CO)$_3$Cl]$^-$ moieties followed by a third (overall) reductive process involving each of the Re(bpy) units, totaling two electrons. The most negative redox event is ascribed to a one-electron, anthracene-based reduction. A CV of free ligand **1** is shown in Figure A10.

Electrocatalytic CO$_2$ reduction by the dinuclear conformers and monomers Re(bpy)(CO)$_3$Cl and anthryl-Re was then investigated by cyclic voltammetry. CVs of cis-Re$_2$Cl$_2$ and trans-Re$_2$Cl$_2$ at 1 mM concentrations and of monomers at concentrations of 2 mM are shown in Figure 5 in DMF solutions under Ar and CO$_2$ atmospheres. The monomer catalyst concentrations were doubled to maintain a consistent concentration with respect to rhenium.
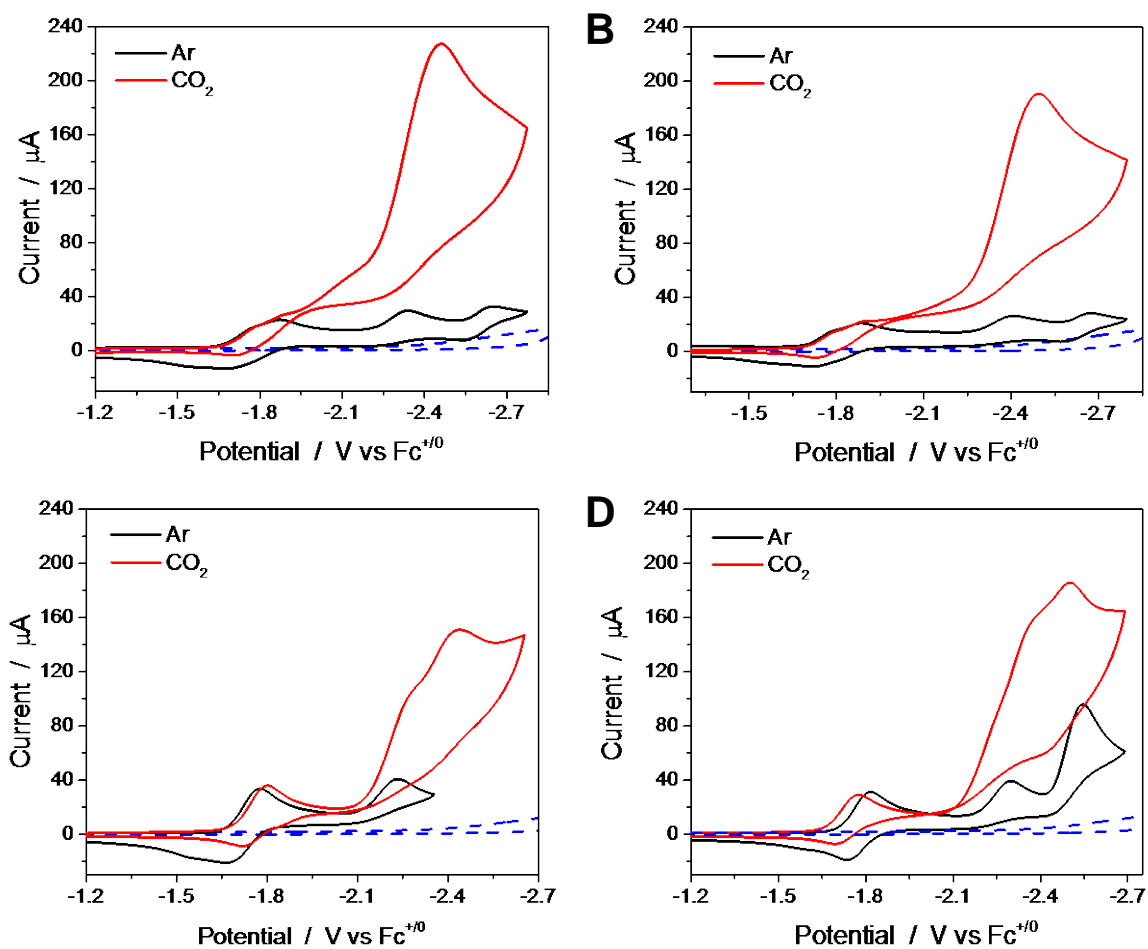
Figure 5. Cyclic voltammetry in Ar- and CO_2-saturated DMF/0.1 M Bu_4NPF_6 solutions with A) 1 mM *cis*-Re_2Cl_2, B) 1 mM *trans*-Re_2Cl_2, C) 2 mM Re(bpy)(CO)$_3$Cl, and D) 2 mM anthryl-Re, glassy carbon disc, ν = 100 mV/s. The background under CO_2 is shown with a dashed blue line.

For an electrocatalytic reaction involving heterogeneous electron transfers at the electrode surface, the peak catalytic current is described by equation 1:[83-85]

$$i_{cat} = n_{cat}FA[cat](Dk_{cat}[S]^y)^{1/2} \tag{1}$$

where i_{cat} is the limiting catalytic current in the presence of CO_2, n_{cat} corresponds to the number of electrons transferred in the catalytic process (here n_{cat} = 2 as CO_2 is reduced to CO), F is Faraday's constant, A is the area of the electrode, [cat] is the molar concentration of the catalyst, D is the diffusion coefficient, k_{cat} is the rate constant of the catalytic reaction, and [S] is the molar concentration of dissolved CO_2. Applying eq 1, the catalytic mechanisms of *cis*-Re_2Cl_2 and *trans*-Re_2Cl_2 were probed using cyclic voltammetry to determine reaction orders with respect to [CO_2] and [cat] (Figure A11 and Figure A12, respectively). First, gas mixtures of Ar and CO_2 were used to vary the partial pressure of CO_2 from 0 to 1 atm to reveal a linear increase in catalytic current for CO_2 reduction as a function of the square root of dissolved CO_2 concentration for both *cis*-Re_2Cl_2 and *trans*-Re_2Cl_2 catalysts (Figure 6). The concentration of dissolved CO_2 in DMF under saturation conditions at 1 atm is 0.20 M.[86]
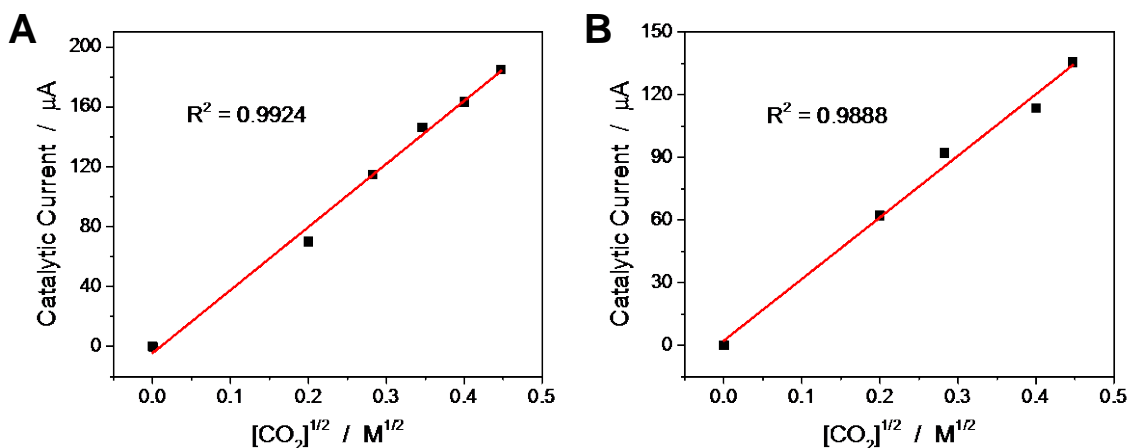
Figure 6. CO_2 concentration dependence for A) 1 mM *cis*-Re_2Cl_2 and B) 1 mM *trans*-Re_2Cl_2 in DMF/0.1 M Bu_4NPF_6, glassy carbon disc, ν = 100 mV/s. Catalytic current (μA) is plotted versus the square root of [CO_2].

Likewise, the dependence of catalytic current (i_{cat}) on the concentration of each dinuclear rhenium catalyst ([cat]) in CO_2-saturated solutions was determined (Figure 7).
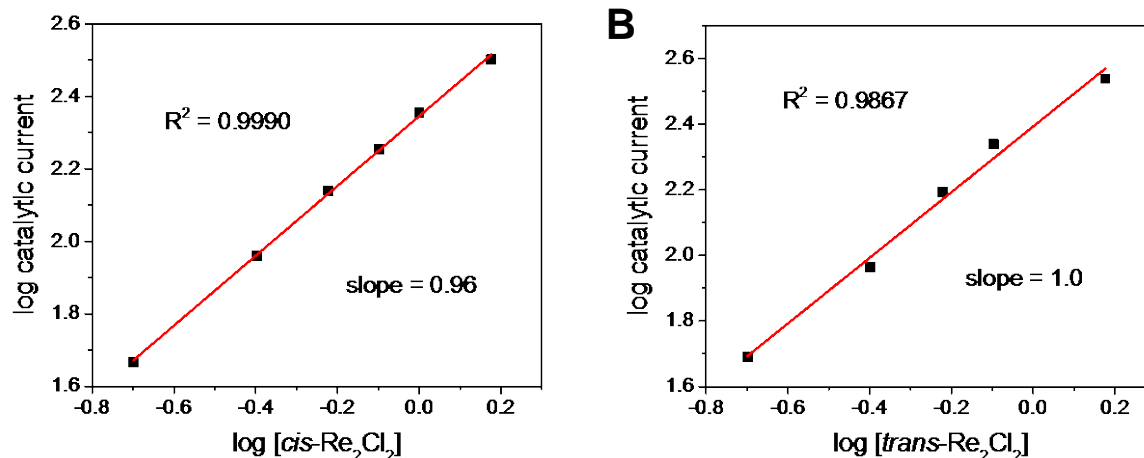
Figure 7. Catalyst concentration dependence for A) *cis*-Re_2Cl_2 and B) *trans*-Re_2Cl_2 in CO_2-saturated DMF/0.1 M Bu_4NPF_6 solutions, glassy carbon disc, $v = 100$ mV/s. Linear fits with slopes of 1 were obtained in log-log plots of catalytic current (μA) versus catalyst concentration (mM).

For both conformers, the data indicates a first order dependence on [Re_2Cl_2] and a first order dependence on [CO_2] in the rate determining step, as expressed by the following rate law:

$$\text{Rate} = -\frac{[CO_2]}{dt} = k_{cat}[Re_2Cl_2][CO_2]$$

It was not possible on the basis of reaction orders alone to distinguish between the reaction mechanisms of *cis* and *trans* conformers. Log-log plots were critical for the correct kinetic analysis of these catalysts, since plots of catalytic current vs [*trans*-Re_2Cl_2] as well as catalytic current vs [*trans*-Re_2Cl_2]$^{1/2}$ both gave reasonable linear fits (Figure A13). The log-log plots confirm the reactions are first order in catalyst with slopes of 1 (Figure 7).

24

Our initial inquiry regarding a half-order dependence on catalyst concentration, specifically for *trans*-Re_2Cl_2, emerged from a previous mechanistic study involving a dinuclear palladium complex, in which its polydentate phosphine ligand was designed to prevent cooperative, intramolecular CO_2 binding between active sites.[87,88] A half-order dependence on catalyst concentration was reported and explained by assuming the metal active sites operate independently of one another, such that only half of the complex is intimately involved in the rate determining step.[88] As rationalized, however, a first order dependence would be expected. A square root dependence on catalyst concentration is typically observed following rate-limiting dissociation of a dinuclear pre-catalyst that is in reversible equilibrium with the active form.[89,90]

Several plausible modes of reactivity with a dinuclear catalyst for CO_2 reduction are expected to yield a first order dependence on catalyst concentration: (1) both metal centers participate in the intramolecular activation, or binding, of CO_2 and its conversion, (2) only one metal center reacts with CO_2 while the other acts as a spectator, (3) only one metal center reacts with CO_2 while the other serves as an electron reservoir capable of intramolecular electron transfer, or (4) both metal centers operate independently and react with one CO_2 molecule each. In cases (2) and (3), the metal fragment that does not bind CO_2 can be thought of more simply as (2) an elaborate ligand substituent of variable electronics depending on its redox state, or (3) a pendant redox mediator that supplies electron(s) to the active site; neither of which would give a half-order dependence on catalyst concentration.

1.4.2 Catalytic rates and faradaic efficiencies

With these results in hand, we sought to compare the catalytic rates of the *cis* and *trans* conformers along with Re(bpy)(CO)$_3$Cl and its anthracene-functionalized derivative, anthryl-Re. The quantity $(i_{cat}/i_p)^2$ can serve as a useful benchmark of catalytic activity that is proportional to turnover frequency (TOF) as shown in equation 2, where v is the scan rate, n_p is the number of electrons transferred in the noncatalytic Faradaic process, R is the ideal gas constant, T is the temperature (in K), and i_p is the peak current observed for the catalyst in the absence of substrate.[58,59]

$$TOF = k_{cat}[CO_2] = \frac{Fvn_p^3}{RT}\left(\frac{0.4463}{n_{cat}}\right)^2\left(\frac{i_{cat}}{i_p}\right)^2 \tag{2}$$

Application of eq 2 requires steady state behavior, which can often be established at sufficiently fast scan rates that avoid substrate depletion and give rise to a limiting catalytic current plateau. Linear sweep voltammograms of *cis*-Re$_2$Cl$_2$ (1 mM), *trans*-Re$_2$Cl$_2$ (1 mM), and the mononuclear catalysts (2 mM) were conducted in DMF/0.1 M Bu$_4$NPF$_6$ solutions under argon and CO$_2$ as a function of scan rate (Figure A14). While scan rate independence was not completely reached, estimated TOFs using eq 2 are plotted versus scan rate in Figure A15 where TOFs of 35.3, 22.9, 11.1, and 19.2 s^{-1} were identified for *cis*-Re$_2$Cl$_2$, *trans*-Re$_2$Cl$_2$, Re(bpy)(CO)$_3$Cl, and anthryl-Re, respectively. Alternatively, Costentin and Savéant's foot-of-the-wave analysis (FOWA)[85,919293] can be applied to find intrinsic catalytic rates *via* equation 3:

$$\frac{i}{i_p} = \frac{2.24\sqrt{\frac{RT}{Fvn_p^3}2k_{cat}[CO_2]}}{1+exp\left[\frac{F}{RT}(E-E_{cat/2})\right]} \tag{3}$$

This electroanalytical method provides access to a TOF maximum, in which the observed catalytic rate constant k_{cat} can be determined at the foot of the catalytic wave where competing factors (i.e. substrate depletion, catalyst inhibition or decomposition) are minimal. Indeed, scan rate independent TOFs were obtained by FOWA (Figure A16). In eq 3, $E_{cat/2}$ is the half-wave potential of the catalytic wave. From the slope of the linear portion of a plot of i/i_p versus $1/\{1+exp[(F/RT)(E-E_{cat/2})]\}$, k_{cat} can be calculated. The maximum TOF under saturation conditions is then found from TOF = k_{cat}[CO_2].

Maximum TOFs determined *via* FOWA for the dinuclear catalysts (11.0 s^{-1}, *cis*-Re$_2$Cl$_2$; 4.4 s^{-1}, *trans*-Re$_2$Cl$_2$) are higher than that of the mononuclear parent catalyst (1.5 s^{-1}) at the same effective concentrations. Likewise, the *cis* conformer is considerably more active than its *trans* counterpart, consistent with the estimated TOFs from eq 2. With regards to anthryl-Re (4.1 s^{-1}), the pendant anthracene results in a higher TOF relative to unsubstituted Re(bpy)(CO)$_3$Cl whereas very similar rates (*via* both electroanalytical equations) are observed relative to *trans*-Re$_2$Cl$_2$. Comparable TOFs of anthryl-Re and *trans*-Re$_2$Cl$_2$ are consistent with the isolated active sites of the dinuclear complex on opposite sides of the anthracene bridge. Notably, slow catalysis begins after the first overlapping one-electron reductions at around -1.9 V with dinuclear catalysts, while no activity is observed until the second reduction at -2.1 V for the monomers.

Brønsted acids are frequently added to polar aprotic solvents to promote the proton-coupled reduction of CO_2. Indeed, significant enhancements in the electrocatalytic CO_2 reduction activity of mononuclear Re catalysts have been observed with various proton source additives.[23,94,95] The influence of four different acids (water, methanol, phenol, and 2,2,2-

trifluoroethanol (TFE)) on the CO_2 reduction activity of *cis*-Re_2Cl_2 in DMF was investigated

(Figure A17). This selection of proton sources affords a good range of acidity with the following

pK_as reported in DMSO:[96] 31.4 (H_2O),[97] 29.0 (MeOH),[97] 23.5 (TFE),[98] 18.0 (PhOH).[99] Catalyst

cis-Re_2Cl_2 shows a decrease in current upon addition of these acids. However, the onset of fast

catalysis is significantly more positive after the addition of a proton source relative to anhydrous

DMF. From cyclic voltammetry, added water produces the most promising catalytic activity for

CO_2 reduction with *cis*-Re_2Cl_2 of the four Brønsted acids investigated, taking into account its

nominal activity under argon. Accordingly, the amount of added H_2O was optimized for *cis*-

Re_2Cl_2 by plotting i_{cat} vs H_2O concentration where catalysis reached a maximum with 3 M H_2O

(Figure A18). The catalytic activity of each catalyst in the presence of 3 M H_2O is shown in

Figure 8 for comparison.
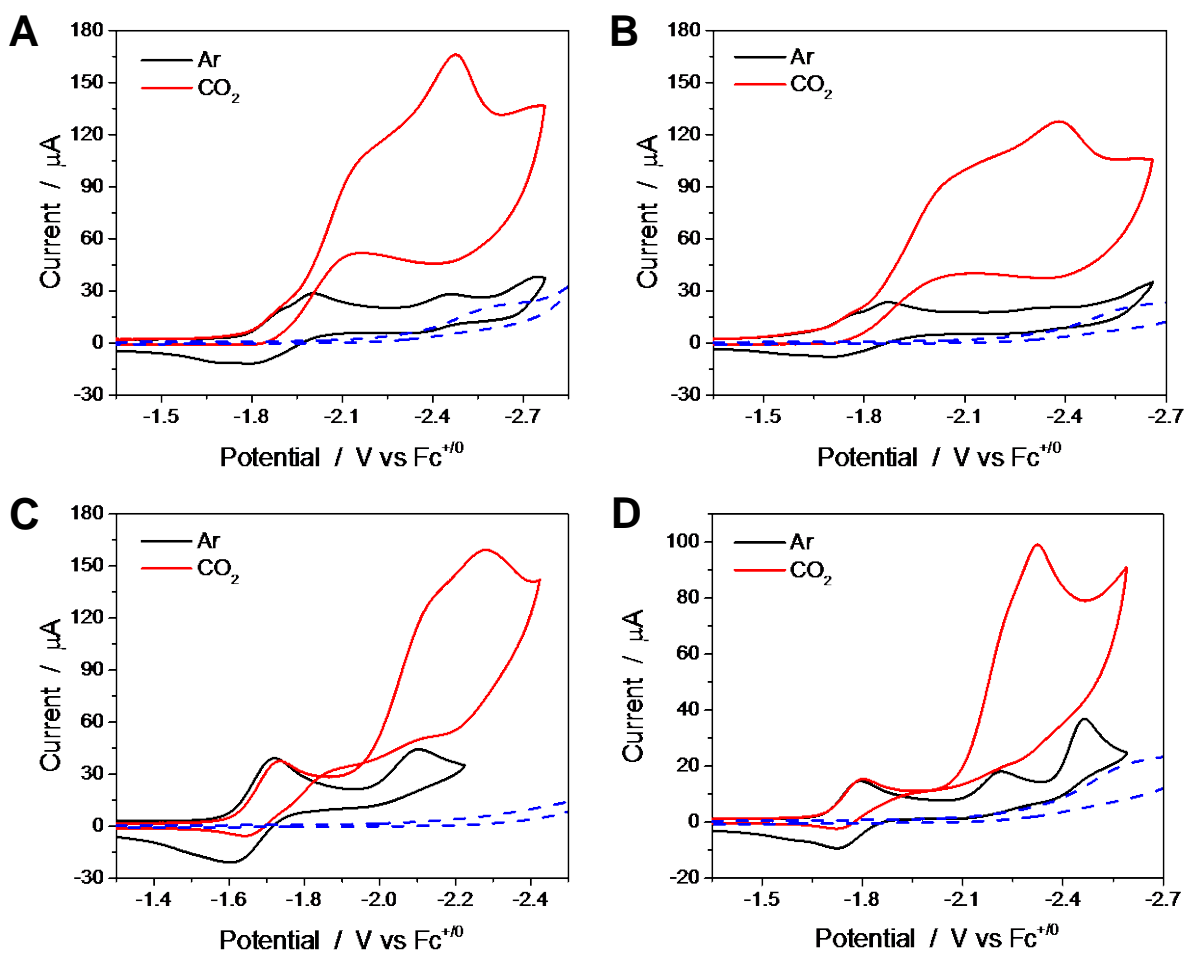
Figure 8. Cyclic voltammograms of A) 1 mM *cis*-Re$_2$Cl$_2$, B) 1 mM *trans*-Re$_2$Cl$_2$, C) 2 mM Re(bpy)(CO)$_3$Cl, and D) 2 mM anthryl-Re with 3 M H$_2$O in DMF/0.1 M Bu$_4$NPF$_6$ under Ar (black) and CO$_2$ (red), glassy carbon disc, $v = 100$ mV/s.

A thermodynamic potential of -0.73 V vs Fc$^{+/0}$ for the 2e$^-$/2H$^+$ CO$_2$/CO couple in pure DMF has been determined *via* a thermochemical approach.[100] In the presence of a Brønsted acid, this standard potential shifts according to equation 4, in which the pK_a of the acid must be taken into account.[100]

$$E = E^0_{CO_2/CO(DMF)} - 0.0592 \cdot pK_a \tag{4}$$

As previously described, carbonic acid (H_2CO_3, pK_a = 7.37) is more acidic than water in

DMF, so its pK_a was used in eq 4 to give an estimated reduction potential of -1.17 V for the

CO_2/CO couple in DMF/H_2O solutions.[62,63] Using these standard potentials, a summary of TOFs

from anhydrous DMF and observed overpotentials from Figure 5 and Figure 8, based on $E_{cat/2}$, is

presented in Table 3. $E_{cat/2}$ is a reliable metric that corresponds to the steepest point, or nearly so,

in the catalytic wave of the current-potential profile.[101]

Table 3. Summary of electrocatalysis obtained from cyclic voltammetry.

Catalyst	TOF (s^{-1}) eq 2	TOF (s^{-1}) eq 3	$E_{cat/2}$ $(\eta)^a$	$E_{cat/2}$ $(\eta)^b$
cis-Re$_2$Cl$_2$	35.3	11.0	-2.29 (1.56)	-2.09 (0.92)
trans-Re$_2$Cl$_2$	22.9	4.4	-2.34 (1.61)	-1.95 (0.78)
Re(bpy)(CO)$_3$Cl	11.1	1.5	-2.22 (1.49)	-2.04 (0.87)
anthryl-Re	19.2	4.1	-2.26 (1.53)	-2.18 (1.01)

a. Anhydrous DMF, b. DMF with 3 M H_2O. $E_{cat/2}$ is the potential at which the current is equal to $i_{cat/2}$. Overpotentials reported here were calculated from expression: $\eta = \left| E_{cat/2} - E^0_{CO_2/CO} \right|$.

Controlled potential electrolyses were carried out to identify products and Faradaic

efficiencies in an air-tight electrochemical cell using a glassy carbon rod working electrode and

CO_2-saturated solutions. The applied potential (E_{appl}) corresponds to the potential at which

maximum current was observed in cyclic voltammograms taken in the same set-up prior to

electrolysis. Headspace gases and electrolytic solutions were analyzed by gas chromatography,

^{1}H NMR, and FTIR spectroscopies.[102-104] CO was found to be the only detectable product under

these conditions where E_{appl} is -2.4 or -2.5 V (Table 4). No other products were observed. In addition to infrared spectroscopy, a titration with barium triflate was also conducted to investigate carbonate as a potential product. Formation of $BaCO_3$ was not apparent.[20,102,103] The absence of carbonate indicates that the dinuclear catalysts do not mediate the reductive disproportionation of CO_2, i.e. $2CO_2 + 2e^- \longrightarrow CO + CO_3^{2-}$ at these potentials, consistent with earlier results with Re(bpy)(CO)₃Cl in DMF solutions.[47] It is well-established that under anhydrous conditions protons can be generated by Hofmann degradation of the quaternary alkylammonium cation of the supporting electrolyte.[47,98,105] This degradation is thought to arise from a highly basic metal carboxylate intermediate that is capable of deprotonating the tetrabutylammonium ion,[98,105] consistent with infrared stopped-flow measurements in the absence of an added proton source.[106]

Table 4. Summary of controlled potential electrolyses and Faradaic efficiencies for CO_2 reduction under various conditions.

Catalyst	Time (min)	E_{appl} (V)	Charge Passed (C)	CO (%)
cis-Re₂Cl₂	60	2.5	1.52 ± 0.32	81 ± 1
trans-Re₂Cl₂	60	2.5	0.60 ± 0.08	89 ± 6
Re(bpy)(CO)₃Cl	60	2.5	1.17 ± 0.15	78 ± 10
cis-Re₂Cl₂ (3 M H₂O)	60	2.4	0.96 ± 0.22	59 ± 5
trans-Re₂Cl₂ (3 M H₂O)	60	2.4	1.01 ± 0.09	74 ± 1
Re(bpy)(CO)₃Cl (3 M H₂O)	60	2.4	0.92 ± 0.29	65 ± 6
cis-Re₂Cl₂	180	2.0	2.24 ± 0.37	52 ± 5
cis-Re₂Cl₂	600	2.0	5.94 ± 0.82	
trans-Re₂Cl₂	180	2.0	1.01 ± 0.12	49 ± 5
cis-Re₂Cl₂ (3 M H₂O)	600	2.0	6.27 ± 0.03	47 ± 3

trans-Re_2Cl_2 (3 M H_2O)	600	2.0	4.46 ± 0.11	49 ± 6

At lower applied potentials, $Re(bpy)(CO)_3Cl$ is known to catalyze the reductive disproportionation of CO_2 through the so-called "one-electron pathway". [47] Following its one-electron reduction, the parent catalyst reduces CO_2 in a bimolecular process to give CO and CO_3^{2-}. In this mechanism, two singly-reduced catalysts are proposed to bind CO_2 to generate a Re_2 carboxylate-bridged intermediate that undergoes insertion with a second equivalent of CO_2 before reductive disproportionation. Here, CO_2 acts as an oxide acceptor to facilitate a proton-independent conversion of CO_2 to CO. By inference, less basic intermediates are generated at these less reducing potentials and oxide transfer to CO_2 is favored over Hofmann degradation. We note that the hydrogen-bonded Re(bpy) dimers developed by Kubiak and coworkers also promote this bimolecular pathway with enhanced rates.[58,59]

In this context, we investigated the *cis* and *trans* conformers at applied potentials immediately following the first overlapping one-electron reductions. Controlled potential electrolyses were conducted in anhydrous DMF/0.1 M Bu_4NPF_6 as well as solutions containing 3 M H_2O. Unsurprisingly, *trans*-Re_2Cl_2 was found to catalyze the reductive disproportionation of CO_2 at an applied potential of -2.0 V in anhydrous DMF. Given its solid-state structure, catalytic activity analogous to $Re(bpy)(CO)_3Cl$ was expected for the *trans* conformer and carbonate was identified as a co-product by infrared spectroscopy with strong C-O stretching frequencies observed at ~1450 and 1600 cm^{-1} (Figure 9) and subsequent precipitation of $BaCO_3$ from DMF solutions. [103,107] Conversely, carbonate was not observed with *cis*-Re_2Cl_2. In order to bolster this

result and ensure that carbonate is not simply sequestered in a stable species (i.e. bound between Re centers), long-term electrolysis were performed in which the evolved CO amounts to greater than 2 turnovers with respect to moles of catalyst in solution. On this basis, *cis*-Re_2Cl_2 does not catalyze the reductive disproportionation of CO_2, consistent with the infrared spectra in Figure 9. Presumably, restricted rotation of the Re(bpy) fragments in *cis*-Re_2Cl_2 impedes the CO_2 insertion step and favors protonation of the CO_2 adduct by slow Hofmann degradation.
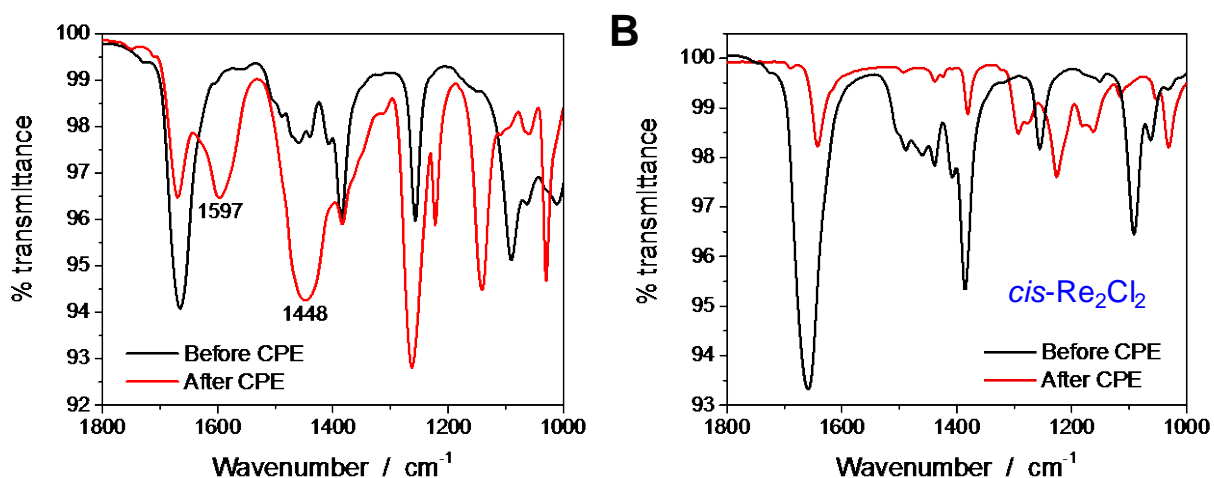
Figure 9. FTIR spectra of A) *trans*-Re_2Cl_2 and B) *cis*-Re_2Cl_2 samples before and after electrolysis. Electrolyzed solutions are evaporated to dryness and washed with the dichloromethane to remove the Bu_4NPF_6 electrolyte. The resulting solid is analyzed.

With 3 M H_2O, at the lower applied potential (-2.0 V vs $Fc^{+/0}$), carbonate or bicarbonate is not produced by *cis*-Re_2Cl_2 or *trans*-Re_2Cl_2. Authentic samples of tetrabutylammonium carbonate and tetrabutylammonium bicarbonate were synthesized[107,108] and detected by FTIR using the established protocol and barium triflate titration to validate these results. The presence of water as a proton source enables the proton-coupled reduction of CO_2, i.e. $CO_2 + 2H^+ +$

$2e^- \rightarrow CO + H_2O$, at lower overpotentials. Representative charge-time profiles from electrolyses in DMF solutions are overlaid in Figure A19. Experiments were performed in duplicate and results are summarized in Table 4.

1.4.3 UV-Vis spectroelectrochemistry

Additional insight into the electrocatalytic CO2 reduction mechanisms of the *cis* and *trans* conformers was gained from UV-Vis spectroelectrochemical measurements. Data was collected stepwise at increasingly negative applied potentials under argon atmosphere using a thin-layer cell with a "honeycomb" working electrode. Representative absorption spectra vs time (Figure 10) are shown for *cis*-Re$_2$Cl$_2$ and *trans*-Re$_2$Cl$_2$.
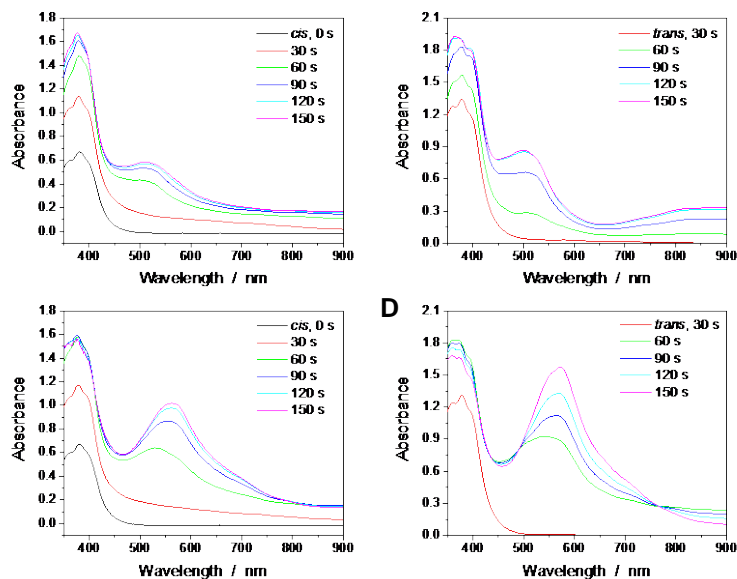
Figure 10. UV-Vis spectroelectrochemistry with A) 0.5 mM *cis*-Re$_2$Cl$_2$ at -1.7 V vs Ag/AgCl, B) 0.5 mM *trans*-Re$_2$Cl$_2$ at -1.7 V vs Ag/AgCl, C) 0.5 mM *cis*-Re$_2$Cl$_2$ at -2.0 V vs Ag/AgCl, D) 0.5 mM *trans*-Re$_2$Cl$_2$ at -2.0 V vs Ag/AgCl in Ar-saturated DMF/0.1 M Bu$_4$NPF$_6$ solutions.

trans-Re$_2$Cl$_2$ catalysts display a new absorption peak at 517 nm, consistent with the one-electron reduced species.[109] The terminology used here refers to reduction at a single rhenium site to facilitate comparison with earlier studies on mononuclear catalysts. The catalysts have been reduced by two electrons in total. At a more negative applied potential of -2.0 V vs Ag$^+$, absorption bands at 562 nm (*cis*-Re$_2$Cl$_2$) and 570 nm (*trans*-Re$_2$Cl$_2$) appear, indicative of the two-electron reduced species.[17] Upon closer inspection of the absorption spectra obtained with E_{appl} = -1.7 V vs Ag$^+$, a broad band centered around 850 nm also emerges for the *trans* conformer. This feature is characteristic of a Re-Re bonded dimer,[17] presumably a Re$_4$ species in this case formed from two equivalents of *trans*-Re$_2$Cl$_2$. Characteristic absorption features of a Re-Re dimer, however, were not observed in experiments with *cis*-Re$_2$Cl$_2$. We reasoned that an added benefit of the rigid anthracene backbone is constraining the metal centers from Re-Re bond formation, a known deactivation pathway.

DFT calculations were conducted to probe the likelihood of forming the neutral Re-Re dimer or its one-electron reduced product with *cis*-Re$_2$Cl$_2$. Optimized geometries are shown in Figure 11. Calculated distances between rhenium centers are 3.38 Å for the neutral species and 3.52 Å for the radical anion. Solid-state structures of the corresponding dimers prepared from Re(bpy)(CO)$_3$Cl reduction have been characterized by X-ray crystallography.[52] A Re-Re bond distance of 3.0791(13) Å was found in the neutral dimer and a longer distance of 3.1574(6) Å was determined in the reduced dimer.[52] Given the calculated intermetallic distances for the anthracene-based catalyst in conjunction with the spectroelectrochemical data, the Re-Re bonded dimer is likely inaccessible following reduction of *cis*-Re$_2$Cl$_2$, or limited to a transient

35

interaction. These results are consistent with the improved stability observed in controlled

potential electrolyses with *cis*-Re$_2$Cl$_2$.

Re-Re distance: **3.38** Å   Re-Re distance: **3.52** Å
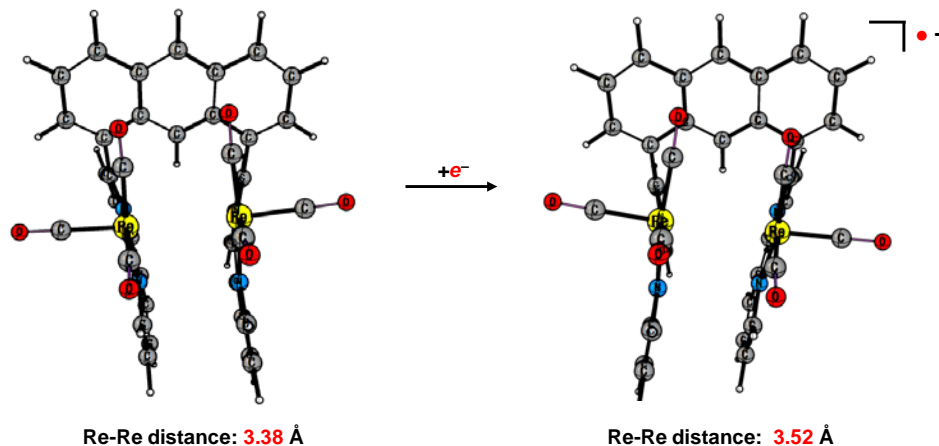
Figure 11. Possible intermediates following reduction and chloride dissociation from *cis*-Re$_2$Cl$_2$. DFT optimized structures of a neutral dinuclear rhenium species and its one-electron reduced radical anion.

It is clear from the structure of *trans*-Re$_2$Cl$_2$ and the observed reactivity that catalysis

occurs by well-established pathways known for Re(bpy)(CO)$_3$Cl (catalytic cycles are shown in

Figure A20), including the "one-electron" bimolecular reductive disproportionation mechanism

at applied potentials just after the initial overlapping one-electron reductions of the Re$_2$ complex

under anhydrous conditions. Carbonate is a co-product of this pathway for *trans*-Re$_2$Cl$_2$. In the

presence of 3 M H$_2$O or more negative potentials, CO$_2$-to-CO conversion occurs, but with water

as the co-product. Different behavior is observed for *cis*-Re$_2$Cl$_2$. Proposed catalytic cycles for the

two applied potential regimes -2.0 V and $\leq$ -2.4 V are given in Figure 12 and Figure A21,

respectively. In contrast to the mononuclear catalyst and *trans*-Re$_2$Cl$_2$, the *cis* conformer does

not generate carbonate at applied potentials immediately following the initial overlapping one-

electron reductions. This difference in reactivity is presumably a consequence of the proximal active sites being confined by hindered rotation about the anthracene bridge. With this catalyst, CO_2 is unable to act as an oxide acceptor by CO_2 insertion into the Re-O bond of the bridging carboxylate; instead, CO_2 reduction is governed by protonation *via* Hofmann degradation of the supporting electrolyte. Along these lines, Kubiak's dynamic hydrogen-bonded dinuclear system mediates reductive disproportionation at low applied potentials, analogous to the "one electron" pathway of Re(bpy)(CO)$_3$Cl and consistent with its flexibility to accommodate a CO_2 insertion step.[58,59] The proposed mechanism of *cis*-Re$_2$Cl$_2$ at more negative potentials (Figure A21) is similar to Figure 12, but with fast catalysis coinciding with further reduction of the catalyst.
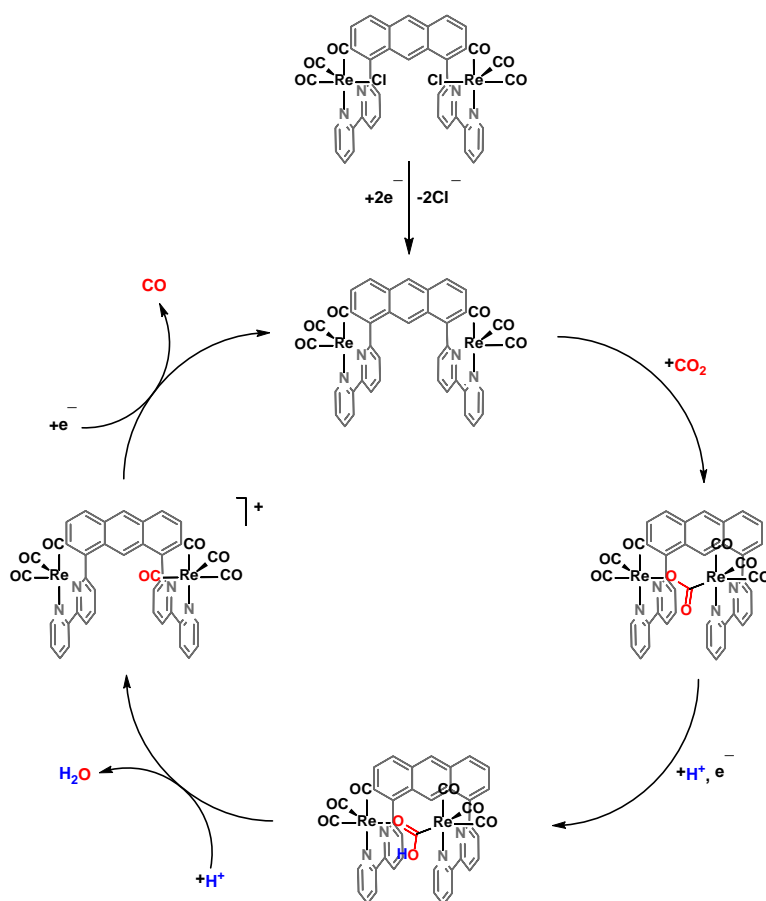
Figure 12. Proposed mechanism for *cis*-Re$_2$Cl$_2$ at E_{appl} = -2.0 V vs Fc$^{+/0}$ in DMF/0.1 M Bu$_4$NPF$_6$.

1.5 Conclusion

We have described a novel ligand platform that gives access to isolable *cis* and *trans* conformers comprised of two rhenium active sites. Indeed, the conformers were purified by silica gel chromatography and characterized. Consistent with its NMR spectra, a crystal structure of *trans*-Re$_2$Cl$_2$ confirmed the asymmetric orientation of Re sites on opposite sides of the anthracene bridge. In contrast, the combined data (^{1}H NMR, FTIR, reactivity studies) indicate that the *cis* conformer is a symmetric species in which the Re sites are on the same side of the

anthracene backbone with their chloro ligands directed toward one another. Both Re_2 compounds are active electrocatalysts for reducing CO_2 to CO. From mechanistic studies, a pathway involving bimetallic CO_2 activation and conversion was identified for *cis*-Re_2Cl_2 whereas well-established single-site and bimolecular pathways, analogous to that of $Re(bpy)(CO)_3Cl$, were observed for *trans*-Re_2Cl_2.

Catalytic rates were measured by cyclic voltammetry for *cis*-Re_2Cl_2, *trans*-Re_2Cl_2, $Re(bpy)(CO)_3Cl$, and anthryl-Re with estimated TOFs of 35.3, 22.9, 11.1, and 19.2 s^{-1}, respectively. The maximum TOFs of *trans*-Re_2Cl_2 and anthryl-Re (at twice the concentration) are approximately equal showing the effect of the pendant anthracene on catalytic activity in comparison to $Re(bpy)(CO)_3Cl$ and with each having single-site reactivity. On the other hand, the *cis* conformer clearly outperforms the *trans* conformer in terms of catalytic rate and stability, indicating the structure of *cis*-Re_2Cl_2 enables improved performance. Indeed, a change in mechanism is observed at low applied potentials in anhydrous conditions where carbonate is not formed as a co-product. Synergistic catalysis by cooperative active sites in *cis*-Re_2Cl_2 are hypothesized. Spectroelectrochemical measurements indicate that *cis*-Re_2Cl_2 does not form a deactivated Re-Re bonded species. The catalyst structure delivers a unique form of protection for catalyst longevity as *intermolecular* deactivation pathways are limited by the cofacial arrangement of active sites, while the rigid anthracene backbone prevents *intramolecular* Re-Re bond formation.

CHAPTER II

PHOTOCHEMICAL CO_2 REDUCTION WITH MONONUCLEAR AND DINUCLEAR RHENIUM CATALYSTS BEARING A PENDANT ANTHRACENE CHROMOPHORE

2.1 Introduction

For photocatalytic applications, the presence of two metal centers may enable more efficient accumulation of reducing equivalents for improved CO_2 conversion.[1] Dinuclear rhenium catalysts, tethered together by flexible alkyl chains linking two bipyridines, have been reported for photocatalytic CO_2 reduction.[57,110] These catalysts were shown to outperform their mononuclear parent catalyst with greater durability and higher TOFs observed as the alkyl chain was shortened. However, this approach lacks structural integrity and samples indiscrete conformations in solution. Other Re_2 catalysts have not been studied photocatalytically or feature ligand scaffolds that preclude intramolecular bimetallic CO_2 activation and conversion.[58,59,60,62] Thus guidelines for designing more effective dinuclear catalysts for CO_2 reduction can be improved.

In general, plausible pathways for accelerated catalysis with a dinuclear complex relative to a mononuclear analogue include: (1) cooperative catalysis in which both metal centers are involved in substrate activation and conversion, or (2) one site acting as an efficient, covalently-linked photosensitizer (PS) to the second site performing CO_2 reduction. The key steps from

these hypothesized pathways are shown in Figure 13. Concerning the dual active site

mechanism (1), an intramolecular pathway may exist involving cooperative binding of the

substrate where CO_2 is bridged between rhenium centers, potentially increasing the basicity of

CO_2 and the rate of catalysis by facilitating C-O bond cleavage and the elimination of water in

subsequent steps. Intramolecular CO_2 binding between metal centers is only expected for *cis*-

Re_2Cl_2 since CO_2 is geometrically inhibited from interacting with both rhenium centers in *trans*-

Re_2Cl_2.
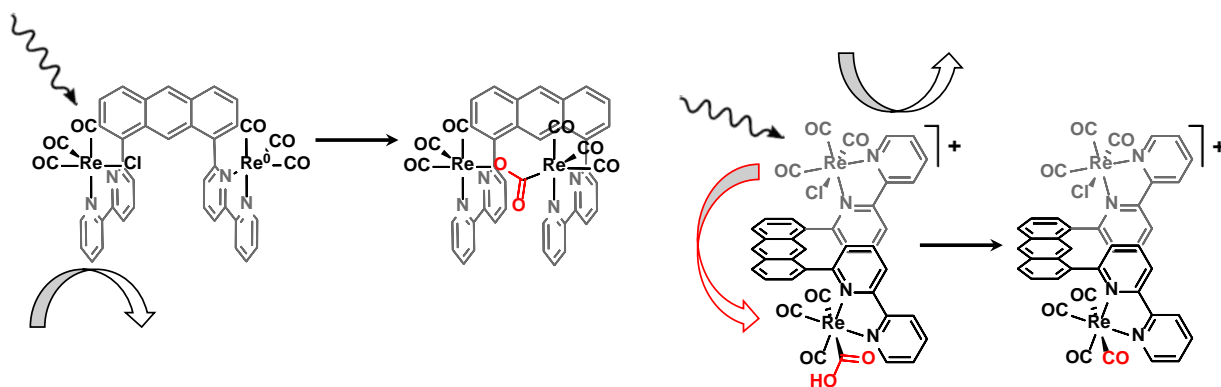
Figure 13. Key steps in potential pathways (1) and (2) with dinuclear rhenium catalysts. Analogous intramolecular electron transfer is expected with *cis*-Re_2Cl_2 in the PS pathway (2).

For the photosensitizer pathway (2), it is generally accepted that $Re(bpy)(CO)_3Cl$

functions through a bimolecular pathway where one complex operates as a photosensitizer (PS)

and a second complex operates initially as a photocatalyst for the first reduction, then as an

electrocatalyst which receives the second electron needed for the $2e^-$ reduction of CO_2 to CO

from a reduced PS in solution.[1] In this pathway, *cis*-Re_2Cl_2 and *trans*-Re_2Cl_2 are predicted to

have superior reactivity to mononuclear derivatives since both dinuclear systems could utilize

one Re site as a PS and the second as the catalyst, thereby increasing the relative concentration of PS near the active site. This effect would be most dramatic at low concentrations where the intermolecular reaction necessary for the monomers would be slow. Higher durability at low concentrations is known for photocatalyst systems; however, most rely on a high PS loading to keep the effective concentration of PS high in the dilute solution.[111,112] The approach pursued here may enable a high rate of reactivity to be retained at low concentrations while promoting increased durability.

Sufficiently long-lived excited states are required for efficient solar-to-chemical energy conversion, where longer lifetimes result in more efficient excited-state quenching to generate catalytic species. One avenue to more persistent excited states in metal polypyridine complexes is to link them with organic chromophores possessing long-lived triplet excited states where decay pathways are strongly forbidden.[113-117] Anthryl substituents have served effectively as the organic component in a variety of systems.[115-117] Important light absorption and excited-state decay pathways of such systems are depicted in Scheme 2 where excited states are ultimately funnelled downhill by internal conversion and/or intersystem crossing to the anthracene-based triplet excited state. Scheme 2 also shows that the anthracene triplet state has enough energy to produce the $1e^-$ reduced Re complex in the presence of easily oxidized sacrificial electron donors such as BIH.
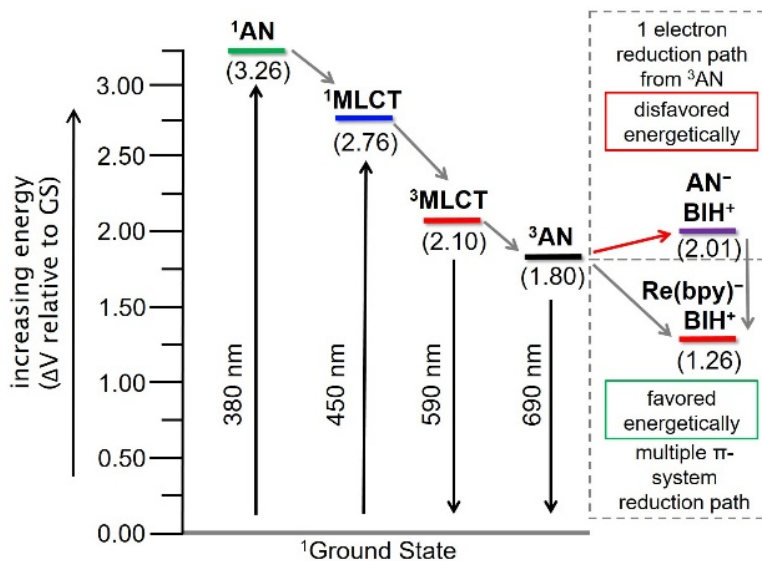
Scheme 2 Light absorption and excited-state electron transfer pathways in Re compounds with pendant anthracene.

Beyond anthracene's potential to act as a triplet excited-state acceptor, a rigid scaffold for promoting cooperative bimetallic reactivity, and its impact on reduced species as a large π-system with extended delocalization, the anthracene moiety also functions as a sterically bulky group that may inhibit deleterious intermolecular catalyst deactivation pathways. Indeed, an iridium-based single-component photocatalyst bearing an anthracene substituent was recently reported for CO_2 reduction with improved stability.[118] The steric bulk of the anthracene was thought to deter bimolecular deactivation of the one-electron reduced catalyst, and a partially deactivated, low-lying anthracene triplet state may also play a role in photoprotection.[118]

In this context, we report the photocatalytic activity and photophysical properties of the dinuclear Re complexes shown in Figure 14. For comparison, experiments employing the same set of conditions were also performed in parallel with mononuclear chromophore/catalysts

43

Re(bpy)(CO)$_3$Cl and anthryl-Re to disentangle the effect of more than one metal active site as well as the possible involvement of the pendant organic chromophore in photocatalytic activity.
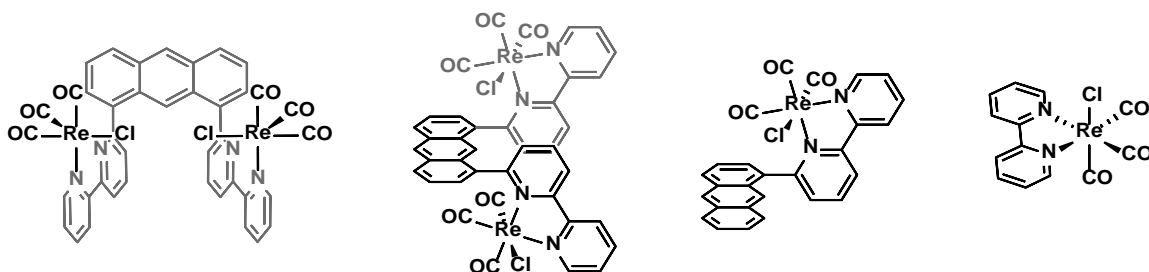
Figure 14. Structures of Re photocatalysts studied for CO$_2$ reduction.

2.2 Experimental section

2.2.1 Materials and characterization

Unless otherwise noted, all synthetic manipulations were performed under N$_2$ atmosphere using standard Schlenk techniques or in an MBraun glovebox. Toluene was dried with a Pure ProcessTechnology solvent purification system. Acetonitrile was distilled over CaH$_2$ and stored over molecular sieves before use. The rhenium precursor Re(CO)$_5$Cl was purchased from Strem and stored in the glovebox. 1,3-dimethyl-2-phenyl-2,3-dihydro-1H-benzoimidazole (BIH) was prepared according to a published procedure.[119] The parent catalyst, Re(bpy)(CO)$_3$Cl,[74] and anthracene-functionalized rhenium catalysts *cis*-Re$_2$Cl$_2$, *trans*-Re$_2$Cl$_2$, and anthryl-Re were prepared as previously described.[44] DMF was distilled with 20% of the solvent volume forecut, and 20% of the solvent volume left in the distillation flask to ensure high purity. DMF was freshly distilled and stored in a flame-dried round bottom flask under argon before being

44

discarded biweekly. Triethylamine (TEA) was freshly distilled prior to use. All other chemicals

were reagent or ACS grade, purchased from commercial vendors, and used without further

purification. ^{1}H and ^{13}C NMR spectra were obtained using a Bruker Advance DRX-500

spectrometer operating at 500 MHz (^{1}H) or 126 MHz (^{13}C). Spectra were calibrated to residual

protonated solvent peaks; chemical shifts are reported in ppm.

2.2.2 Photocatalysis equipment and methods

A 150 W Sciencetech SF-150C Small Collimated Beam Solar Simulator equipped with

an AM 1.5 filter was used as the light source for photocatalytic experiments. Samples were

placed ~10 cm from the source; the distance at which 1 sun intensity (100 mW/cm^2) was verified

with a power meter before each measurement. Headspace analysis was performed using a gas

tight syringe with a stopcock and an Agilent 7890B Gas Chromatograph (GC) equipped with an

Agilent Porapak Q 80-100 mesh (6 ft x 1/8 in x 2.0 mm) Ultimetal column. Quantification of CO

and CH$_4$ was determined using a methanizer coupled to an FID detector, while H$_2$ was quantified

using a TCD detector. All calibrations were done using standards purchased from BuyCalGas.

com. Formate analysis was done according to a previously reported procedure.[120]

2.2.3 Photophysical measurement equipment and methods

Luminescence spectra were obtained with a PTI Quanta Master spectrofluorimeter

equipped with single grating monochromators and a PMT detector. Spectra were not corrected

for PMT wavelength response. Transient absorption spectra and excited state lifetimes were

obtained using an Applied Photophysics LKS 60 optical system with an OPOTek OPO (< 4 ns

pulses) pumped by a Quantel Brilliant Laser equipped with doubling and tripling crystals. Excitation of the chromophores was typically at 420 nm using samples having an optical density of about 0.5. Samples (4 mL volume) containing the Re complex were degassed by nitrogen bubbling for 20 min immediately prior to data acquisition.

2.2.4 Photocatalysis procedure

To a 17 mL vial was added BIH (0.05 g, 0.24 mmol), DMF (1.8 mL), catalyst (as a 0.2 mL DMF stock solution). The solution was bubbled vigorously with CO_2 for at least 15 minutes until the solution volume reached 1.9 mL. Then, 0.1 mL of CO_2 degassed TEA was added, the tube was sealed with a rubber septum, and irradiated with a solar simulator for the indicated time. During the photolysis, headspace analysis was performed at 20, 40, 60, 120, and 240 minute time points. A 300 μL headspace sample was taken with a VICI valve syringe. The gas

in the syringe was compressed to 250 μL and the tip of the syringe was submerged in a solution of diethyl ether before the valve was opened to equalize the internal pressure to atmospheric pressure prior to injecting the contents of the syringe into the GC. The entire 250 μL sample was then injected onto the GC. All experiments are average values over at least 2 reactions. Turnover number (TON) values were calculated by dividing moles of product (carbon monoxide) by moles of catalyst in solution. Reported turnover frequency (TOF) values were determined from the fastest 20 minute time period of photocatalysis within the first 40 minutes as an estimate of the initial rate prior to significant catalyst deactivation and to account for induction periods (i.e. The TON for an initial 20 minute segment was divided by 0.33 h to obtain the reported TOF (h^{-1})).

2.2.5 Quantum yield measurements

Measurements were conducted similarly to a method previously described.[121] The number of moles of CO produced was monitored over time in 20 minute increments for the first hour and then hourly after this time period. The segment of time producing the most CO per hour was used in the calculations for quantum yield to give the maximum quantum yield observed (1 hour time point in these cases). The photon flux in the reaction was calculated by measuring the incident power density with a power meter (Coherent Field Mate with a Coheren PowerMax PM10 detector). The solar simulator spectrum was cut off with a 700 nm cutoff filter since the catalysts do not absorb light beyond 700 nm. Through this method the power density was estimated to be 57.3 mW/cm^2. The illuminated reaction area was measured to be 1.69 cm^2 which gives 96.9 mW or 9.69 x 10^{-2} J/s to the sample. The photon wavelength was taken as centered at 400 nm since each of the catalysts show a low energy transition shoulder in the UV-Vis absorption spectrum at 400 nm for an energy of 4.97 x 10^{-19} J. This gives 1.95 x 10^{17} photon per second in the reaction, which was used to calculate the quantum yield over the most productive CO generating time frame via the equation:

ϕ_{CO} = [(number of CO molecules x 2)/(number of incident photons)] x 100%

Anthracene + e$^-$ ⇌ (Anthracene)$^-$ $E_{(AN/AN^-)}$ = -2.25 V vs Fc$^{+/0}$ (1a)

^{3}(Anthracene) → Anthracene E_g^{opt} ~ 1.8 eV   (1b)

BIH ⇌ BIH$^+$ + + e$^-$ $E_{(BIH^+/BIH)}$ = -0.24 V vs Fc$_{+/0}$ (1c)[122]

2.3 Results and discussion

2.3.1 Photophysical measurement

For photosensitizer-free catalysis, the rhenium catalysts are initially photoexcited directly into their long wavelength metal-to-ligand charge transfer (MLCT) absorption. This is followed by reductive quenching in the presence of a sacrificial donor to form a ligand-centered radical anion. With $Re(bpy)(CO)_3Cl$, the ligand-centered anion is delocalized on the bpy ligand prior to Cl^- dissociation.[55,109] In the Re_2Cl_2 complexes, the Re(bpy) units are in weak electronic communication *via* the anthracene backbone (comproportionation constants (K_C) of 50 were determined electrochemically for each conformer),[44] which could facilitate intramolecular electron transfer between active sites.

As will be shown below, direct irradiation of the Re complexes in the presence of a sacrificial electron donor leads to CO_2 reduction to CO. While photocatalysis was expected, the nature of the lowest energy excited state is different for the catalysts bearing anthracene *versus* $Re(bpy)(CO)_3Cl$. In deaerated solutions (N_2) all three anthracene containing complexes exhibit luminescence in the yellow/red spectral region as well as structured emission at longer wavelengths (Figure B1). The lifetime of the yellow/red emission is approximately 400 ns for the monometallic anthryl-Re complex, and 200 ns for both bimetallic Re complexes. The long wavelength emission (with vibronic components having maxima at 688-700 nm and 764-772 nm) has a double exponential decay with one component being 6-15 μs and the other 23-90 μs (Table B1). This luminescence is completely quenched in the presence of O_2 and, given the energy, lifetime and O_2 quenching behavior, this emission almost certainly arises from an

48

anthracene-localized triplet state obtained following energy transfer from the [3]MLCT excited state.[123] This behavior is similar to reported metal polypyridine photo-sensitizers with pendant anthracene (or pyrene) functionality.[116,117,124]

It is not clear for these systems how the anthracene-localized triplet reacts with the BIH electron donor to generate the reduced Re complex (quenching data shown in Figure B2). Reduction of the anthracene-localized triplet ($E_0 \sim 1.8$ eV) by BIH to generate the anthracene anion / BIH cation pair is thermodynamically uphill by at least 0.21 V (Scheme 2).[122] For the reduced Re/oxidized BIH pair, the energy is 1.36 V above the ground state (Scheme 2) and is therefore accessible from the anthracene triplet (at 1.8 eV), but involves electron transfer between the Re complex and the BIH while using the energy of the anthracene triplet. Note that an intramolecular photoredox reaction between the anthracene triplet and the Re center ($E_{(AN^+/AN)} \sim 0.8$ V; $E_{(Re(bpy)/Re(bpy)^-)} \sim$ -1.5 V) is also endergonic. Regardless of mechanism, these data clearly indicate that photoexcitation of the three anthryl Re complexes results in an excited state that is largely localized on the anthracene as a triplet. Excited-state electron transfer between this triplet and BIH occurs ($k_q \sim$ 1-5 x 10^7 $M^{-1}s^{-1}$ for the three complexes) to produce the reduced complex/oxidized BIH pair that, following decomposition of the BIH cation radical, leaves the reduced Re complex to react with CO_2. Transient absorption spectroscopy shows that the $1e^-$ reduced Re complexes formed by BIH photoreduction under Ar or CO_2 atmosphere exhibit no reaction over the first ~1 ms (Figure 15). This clearly indicates that disproportionation and reaction with CO_2 do not occur on this time scale.
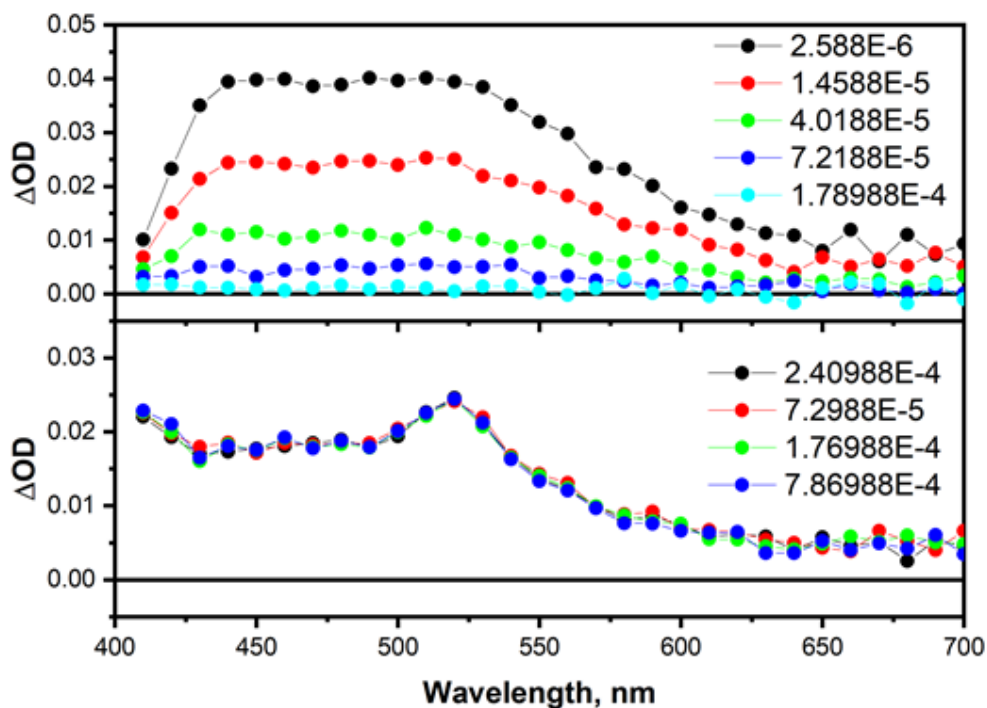
Figure 15. Transient absorption spectra at specified times after pulsed laser excitation (λ_{ex} = 355 nm) of *trans*-Re$_2$Cl$_2$ in DMF under Ar purge (top) and *trans*-Re$_2$Cl$_2$ with BIH (0.01 M) under CO$_2$ purge (bottom). No reaction of the one-electron reduced *trans*-Re$_2$Cl$_2$ complex with CO$_2$ is evident in the first 800 μs following excitation.

2.3.2 Photocatalysis

Having found that anthracene plays a significant role in the photochemistry of *cis*-Re$_2$Cl$_2$, *trans*-Re$_2$Cl$_2$, and anthryl-Re, we turned to photocatalytic CO$_2$ reduction in the presence of BIH to understand how a dinuclear approach affects catalysis in a rigidified framework. Photocatalysis was conducted with a solar simulated spectrum and CO was the only product observed by headspace GC analysis (Figure B3 and Figure B4).

Concentration effects were studied for all catalysts given the mechanistic implications expected of these experiments (Figure 16, Table B2). Reported TOFs are for the fastest 20 min

50

time period within the first 40 min as an estimate of the initial rate prior to significant catalyst deactivation. Broadly comparing dinuclear complexes to mononuclear complexes, significantly higher reactivity is observed at low concentrations (0.05 mM) for the dinuclear complexes (158-128 TOF h^{-1}, 105-95 TON) when compared to the mononuclear complexes (43-17 TOF h^{-1}, 34-16 TON). If the total concentration of metal centers is held constant, the mononuclear catalyst concentration at 0.1 mM can be directly compared to the 0.05 mM dinuclear catalyst concentration. This comparison shows a similar difference in the initial rates of mononuclear versus dinuclear catalysts with the mononuclear catalysts showing TOF values of 43-23 h^{-1}. These results suggest a PS-based pathway is present as this explains how *cis*-Re$_2$Cl$_2$ and *trans*-Re$_2$Cl$_2$ have comparable reactivity despite their structure, while substantially outperforming the mononuclear complexes at low concentrations where intermolecular collisions are fewer. As the concentration increases, TOF and TON values converge to similar rates and durabilities for all catalysts, presumably due to intermolecular deactivation pathways that are prevalent at high concentrations. Interestingly, all of the anthracene-based catalysts effectively stop evolving CO after the first hour, while Lehn's benchmark catalyst continues CO production up to 2 hours. In contrast to reported systems bearing sterically bulky substituents that showed improved stability by limiting bimolecular deactivation pathways, anthryl-Re is found to be less durable (*vide infra*).
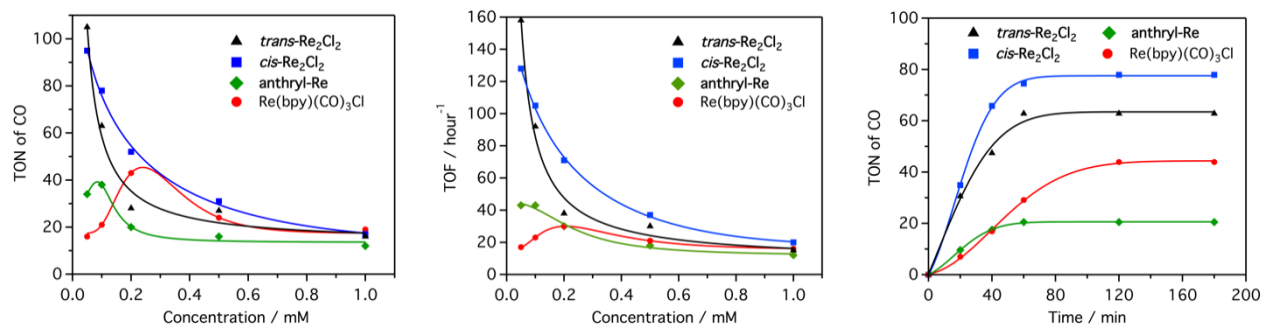
Figure 16. Left) TON *vs* catalyst concentration. Middle) TOF *vs* catalyst concentration. TOF is fastest value measured within first two timepoints. Right) TON for CO production *vs* time for 0.1 mM *cis*-Re$_2$Cl$_2$, 0.1 mM *trans*-Re$_2$Cl$_2$, 0.2 mM anthryl-Re, and 0.2 mM Re(bpy)(CO)$_3$Cl. *Conditions*: DMF containing 5% triethylamine, 10 mM BIH; irradiated with a solar simulator (AM 1.5 filter, 100 mW/cm^2).

Comparing the two dinuclear catalysts, *trans*-Re$_2$Cl$_2$ has higher TOF and TON values at the lowest concentration analyzed in Figure 16 (0.05 mM). As the concentration increases, TOF and TON values diminish faster for the *trans* conformer relative to its *cis* counterpart; qualitatively, their values follow similar trajectories. The faster decrease in TOF and TON for the *trans* conformer suggests that it is more susceptible to intermolecular catalyst-catalyst deactivation pathways. The performance trends for the Re$_2$ complexes strongly suggests one rhenium site is acting as a PS while the other performs catalysis. Moreover, these results indicate intramolecular electron transfer between sites is similar for both dinuclear catalysts, consistent with their equivalent K_C values.[44] To ensure the Re$_2$ complexes are not photoisomerizing to the same species in solution, the catalysts were independently irradiated in d_6-DMSO under N$_2$ for up to 8 h. No appreciable interconversion of either isomer was observed by ^{1}H NMR, which suggests both species retain their conformation over the reaction period. At very low concentrations (1 nM) where some photocatalytic systems show higher TON values,[111] the highest performing catalyst *trans*-Re$_2$Cl$_2$ gives a remarkable 40,000 TON for CO. Notably,

52

carbon monoxide from Re(bpy)(CO)$_3$Cl at 1 nM concentration was undetectable by the GC system used in these studies.

The two mononuclear complexes show TON values at dilute concentrations that are lower than that observed at intermediate concentrations before again decreasing to lower TONs at high concentrations. The TON values for the mononuclear catalysts peak at approximately 0.1-0.2 mM with anthryl-Re peaking at a lower concentration than Re(bpy)(CO)$_3$Cl. This behaviour can be rationalized if the reaction is bimolecular as prior reports strongly suggest for these types of systems.[109] At low concentrations, a PS complex and a catalyst complex interact less frequently and potential decomposition of either species is more competitive. At intermediate concentrations, more productive reactions can occur between PS and catalyst complexes. In the high concentration regime, catalyst-catalyst deactivation pathways become competitive with CO production pathways. This highlights a key difference between the mononuclear catalysts and the dinuclear systems which retain a high effective concentration of PS as it is covalently linked to a reactive site at low overall concentration. This circumvents to some degree the non-catalyst-catalyst deactivation mechanisms by maintaining a fast CO production pathway. Comparing TOFs for the monomers, anthryl-Re has a ~2-fold faster rate of catalysis at low concentrations. A significantly higher molar absorptivity was measured at 370 nm for anthryl-Re (11,100 M^{-1}cm^{-1}) relative to Re(bpy)(CO)$_3$Cl (3,800 M^{-1}cm^{-1}) and the excited state lifetime of anthryl-Re is significantly longer than for Re(bpy)(CO)$_3$Cl (> 1 μs *vs* < 100 ns)[125] enabling a greater degree of BIH quenching. These factors may explain the difference in rates at these concentrations (Figure B5,Table B1).

53

2.3.3 Quantum yield

Quantum yield estimations also show a significant difference in the catalytic behaviour of the mononuclear versus dinuclear catalysts (Figure B6,Table B2). Between 0.05 mM and 0.5 mM the dinuclear complexes have estimated quantum yields of 1.6-4.3% with higher concentrations showing higher quantum yields. In the low concentration regimes, the dinuclear catalysts have roughly double the quantum yield of the mononuclear catalysts. This offers additional evidence that pathway 2 is operable in that both dinuclear complexes have relatively high quantum yields at low concentrations. At the highest concentration evaluated (1.0 mM) where the mononuclear catalyst can operate through an intermolecular PS pathway most efficiently, $Re(bpy)(CO)_3Cl$ and the dinuclear catalysts have similar quantum yields (4.4-4.6%). Based on previous work[55,109] and the results described here, a proposed mechanism for the Re_2 photocatalysts is shown in Figure 17, which illustrates a division of duties for the two active sites and allows access to an exceptional TON value for carbon monoxide of 40 000.
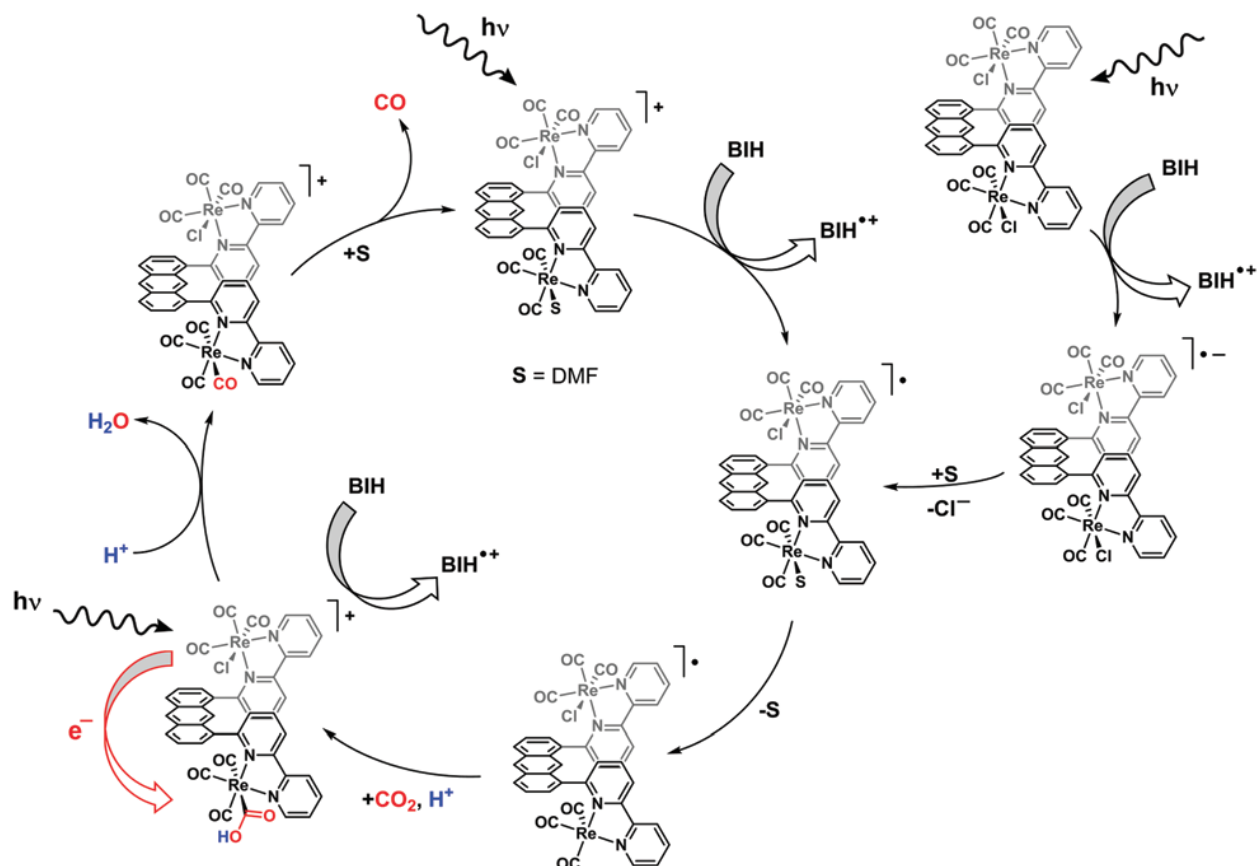
Figure 17. Proposed catalytic cycle for photochemical CO_2 reduction to CO with the dinuclear Re catalysts, *cis*-Re₂Cl₂ or *trans*-Re₂Cl₂. The *trans* conformer is shown in the specific example above.

2.4 Conclusion

Two dinuclear Re catalysts with well-defined, shape persistent structures and a mononuclear analogue have been studied for light-driven CO_2 reduction. Their photocatalytic properties have been explored in parallel with benchmark catalyst, Re(bpy)(CO)₃Cl. Incorporation of a pendant anthracene group on the bipyridyl ligand (anthryl-Re) had a modest effect on the catalytic performance. In contrast, the Re₂ catalysts perform significantly better (~4X higher TON) than the benchmark system when the relative concentration in rhenium is

55

held constant (0.1 mM dinuclear *vs* 0.2 mM mononuclear). Despite the structural differences of

cis-Re$_2$Cl$_2$ and *trans*-Re$_2$Cl$_2$, their initial rates are comparable with both being dramatically faster

(~6X higher) than the mononuclear complexes, which have comparable rates to each other. This

suggests that the mechanism for CO$_2$ reduction may be similar for the two dinuclear complexes

and does not require a specific spatial orientation of the Re active sites. The excited-state kinetics

and emission spectra reveal that the anthracene backbone plays a more significant role beyond a

simple structural unit. Evidence of an anthracene triplet state is observed, and given the unlikely

event of direct reduction of the anthracene triplet state by sacrificial reductant BIH, a more

complex mechanism is likely taking place beyond the Re(bpy) excitation/BIH reduction kinetics.

CHAPTER III

ISOMERIZATION BARRIERS AND RESONANCE STABILIZATION FOR THE CONROTATORY AND DISROTATORY ISOMERIZATIONS OF NITROGEN CONTAINING TRYCYCLO MOIETIES

3.1 Introduction

The effect of electron delocalization on the stabilization of transition states in some similar pericyclic isomerizations has been reported recently.[126-129] In the isomerization of 1, the lowest barrier was calculated to be 39.5 kcal mol^{-1}, while the presence of a double bond in the three carbon bridge in structure 2 provides for electron delocalization in the transition states (see Figure 18), and the lowest allowed barrier (through TS2a) was 31.3 kcal mol^{-1} for the isomerization: electron delocalization from the double bond provided 8 kcal mol^{-1} of stabilization energy.
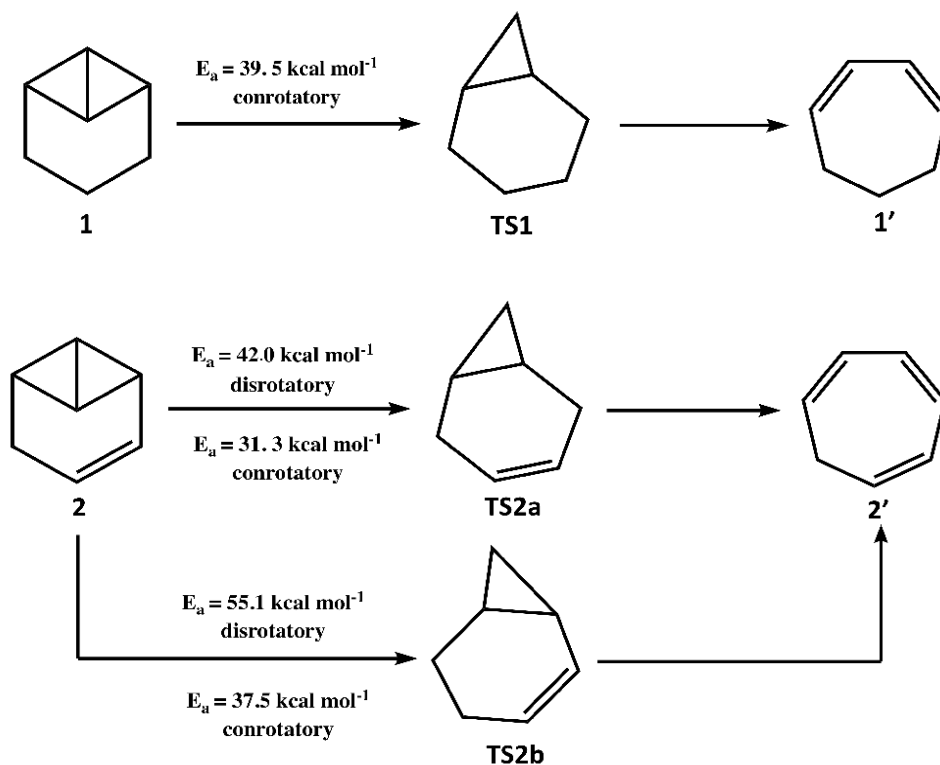
Figure 18. Isomerization of tricyclo[4.1.0.0^{2,7}]heptane to cyclohepta-1,3-diene and tricyclo[4.1.0.0^{2,7}]heptene to cyclohepta-1,3,5-triene.

Even for unsaturated 2 itself, the asymmetric position of C=C double bond leads to various degrees of resonance effect.[126] For the conrotatory channels, if the first bond cleaves adjacent to the double bond in the bridge leading to TS2a, the barrier is 6.2 kcal mol^{-1} lower than for the first bond breaking nonadjacent (through TS2b). For the disrotatory channels, the difference is even greater with a barrier of 13.1 kcal mol^{-1} less when the first bond cleaves adjacent to the double bond following the pathway to TS2a.

Including a heteroatom in the bridge provides an electron lone pair which can also affect the isomerization barriers. The isomerization of 3-aza-dihydrobenzvalene to 1,2-dihydropyridine

provides an example of the stabilizing effect by delocalization from lone pair electrons.[127] Based on whether the first breaking bond is adjacent or not to the N atom, four different isomerization pathways are possible. For the two conrotatory pathways, the barrier for the nitrogen adjacent to the first breaking bond was 3.7 kcal mol^{-1} lower than that of nitrogen nonadjacent. A more substantial stabilization effect is seen for the two disrotatory pathways with a 9.1 kcal mol^{-1} energy difference. This is illustrated in Figure 19.
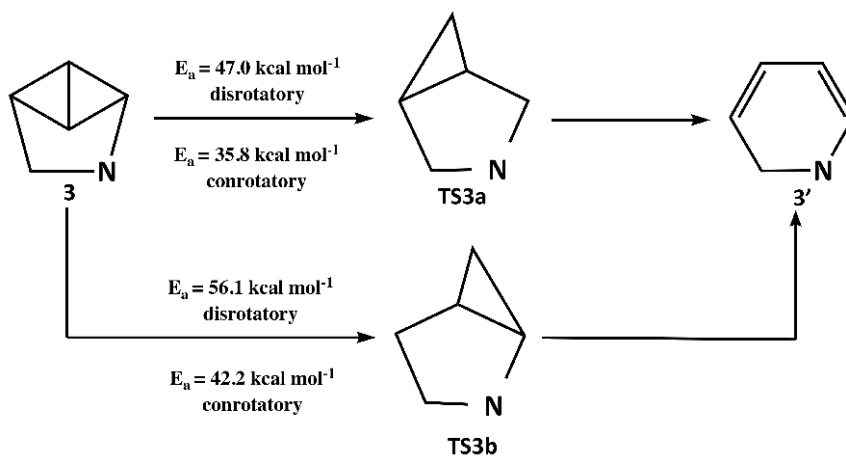
Figure 19. Isomerization of 3-aza-dihydrobenzvalene to 1,2-dihydropyridine.

In a recent paper, the isomerization barriers for 3-aza-benzvalene to pyridine have been calculated[128] (see Figure 20). For this structure, both the lone pair on nitrogen and the π electrons from the double bond in the bridge could provide resonance stabilization. Both possible pathways break bonds adjacent to the double bond, but only one adjacent to the N atom. The two different allowed disrotatory pathways exhibited only 2.8 kcal mol^{-1} stabilization energy with the lower barrier actually being for the bond breaking adjacent to the N atom. It is due to the symmetric position of C=N double bond in the two-member bridge leading to the almost equal effect of electron delocalization. The N atom lone pair is orthogonal to the π bonding electrons

59

and is not in a favorable geometry to delocalize. For the forbidden conrotatory pathways, the stabilization is 7.9 kcal mol^{-1} with the lowest barrier being for the first bond breaking nonadjacent to the N atom, which is the result of steric effect.
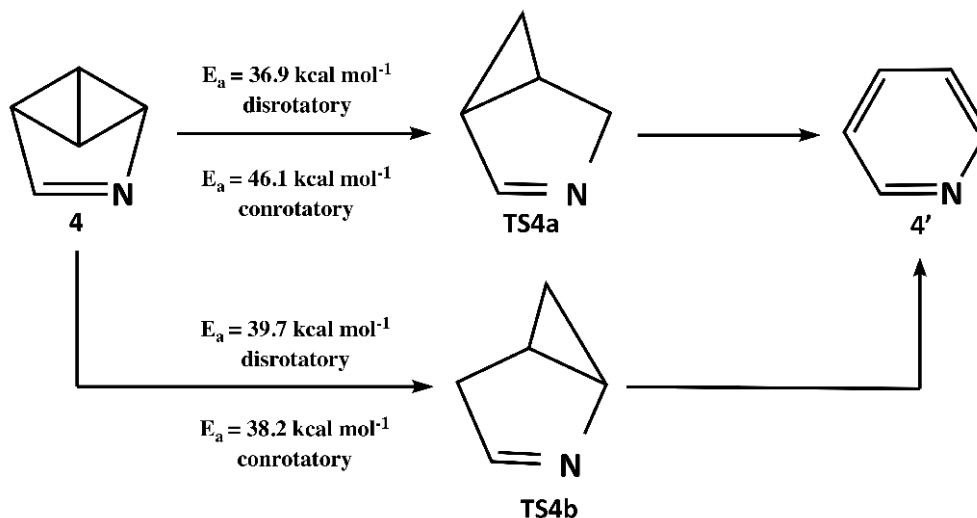
Figure 20. Isomerization of 3-aza-benzvalene to Pyridine.

To gain insight into the stabilizing effect by both π bonding electrons and lone pair electrons simultaneously, we have studied the thermal isomerization barriers for the disrotatory and conrotatory isomerizations of 3,4-diazatricyclo[4.1.0.0^{2,7}]hept- 3-ene (DATCE) to 3H-1,2-diazepine (DAP$_1$ and DAP$_2$ enantiomers) and 3,4,5-triazatricyclo[4.1.0.0^{2,7}]hept-3-ene (TATCE) to 1H-1,2,3-triazepine (TAP$_1$ and TAP$_2$ enantiomers). The seven-member ring makes the position of double bond asymmetric for the bicyclobutane moiety so there can be adjacent and nonadjacent first bond cleavages. The possible delocalization effect of lone pair electrons was studied by the substitution of carbon for nitrogen. For DATCE the first bond cleavage can be adjacent or nonadjacent to the N lone pair, and for TATCE a N lone pair is always adjacent but

the double bond can be either. For assessing just the influence of a N lone pair, we also included

the isomerization pathways for 3,4-diazatricyclo[4.1.0.0^{2,7}]heptane (DATCA) for which only the

N lone pair is present and can be adjacent or nonadjacent to the first breaking bond. The

isomerization barriers of DATCE and DATCA will be compared with tricyclo[4.1.0.0^{2,7}]heptene

to confirm which factors would show greater contribution for molecular stabilization: π bonding

electrons or lone pair electrons. The isomerization of TATCE with an asymmetric position of the

N=N bond and symmetric position of nitrogen atom lone pairs offers a direct comparison of

electron delocalization effect from π bonding electrons and lone pair electrons in same molecular

structure.

This paper reports the thermal isomerization of 3,4-diazatricyclo-[4.1.0.0^{2,7}]hept-3-ene

(DATCE), 3,4-diazatricyclo[4.1.0.0^{2,7}]heptane (DATCA), and 3,4,5-

triazatricyclo[4.1.0.0^{2,7}]hept-3-ene (TATCE) using ab initio methods at the multireference level.

These structures are shown in Figure 21. Transition state structures for each isomerization

pathway were located, and both the conrotatory and disrotatory pathways have been confirmed

by intrinsic reaction coordinate computations.
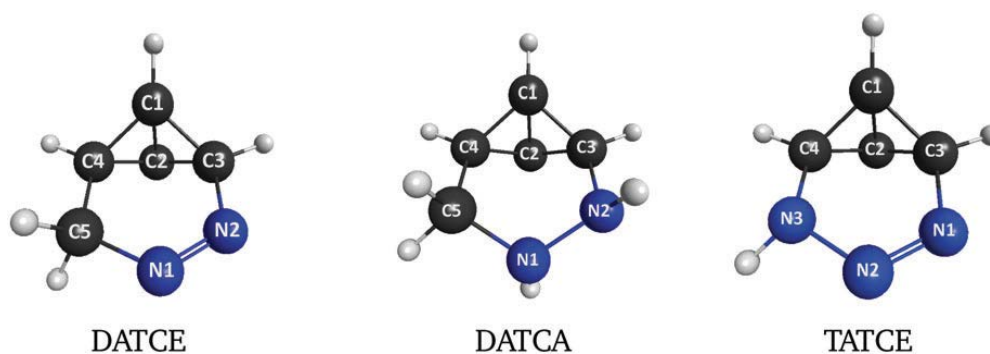
Figure 21. Structures of the Reactants, DATCE, DATCA, and TATCE.

3.2 Computational methods

To examine both the conrotatory and disrotatory pathways at thesame computational level, multiconfigurational self-consistent field calculations were performed. All the multireference calculations were performed using GAMESS[130]. The active space consisted of the C1-C2, C1-C3, C1-C4, C2-C3, and C2-C4 σ and σ∗ orbitals in the reactants (see Figure 21) making 10 electrons in 10 orbitals, MCSCF(10,10). Two C-C bonds break in the bicyclobutane moiety, and two C=C double bonds form during isomerization, so the active space in the products consisted of three C-C σ and σ∗ orbitals plus two π and π∗ orbitals. The orbitals in the active space were chosen after localization by Foster-Boys localization methods[131]. Geometry optimizations were performed at the MCSCF(10,10) level using the cc-pVDZ basis set[132]. Analytical gradients were employed for both geometry optimizations (first derivatives) and harmonic frequency calculations (second derivatives). All transition structures had only one imaginary frequency. Intrinsic reaction coordinates[133] were calculated to verify the connection of the located transition state to the correct reactant and product. Dynamic electron correlation was included by performing single point energy calculations at the single state second order MRMP[134,135] level at the MCSCF optimized geometries using the cc-pVDZ basis set. The resulting energies were used to compare the differences in isomerization barriers and strain energy release. Some structures were also optimized and harmonic frequencies calculated at the CCSD/cc-pVDZ level. Energies for these structures were determined using single point calculations at the CCSD(T)/aug-cc-pVTZ level. To compare the MCSCF results with DFT, the PBEPBE-D3 functional was used to determine the optimized geometries, energies, and harmonic

frequencies for the reactants, transition states, and products using the cc-pVDZ basis set. For

MCSCF wavefunctions that show significant multireference character, an unrestricted, broken

spin symmetry wavefunction was used for the DFT calculations. The coupled cluster and DFT

calculations were performed using Gaussian 16.[136]

3.3 Results and discussion

3.3.1 3,4-Diazatricyclo[4.1.0.0^{2,7}]hept-3-ene

The isomerization of 3,4-diazatricyclo[4.1.0.0^{2,7}]hept-3-ene (DATCE) to the product 3H-

1,2-diazapine (enantiomers DAP$_1$ and DAP$_2$) is discussed in this section. DATCE belongs to

point group C$_s$ with a symmetry plane containing atoms C3, N2, N1, C5, and C4. The molecular

structure of DATCE and its product DAP$_1$ and DAP$_2$ are illustrated in Figure 22.

DATCE   DAP$_1$ DAP$_2$
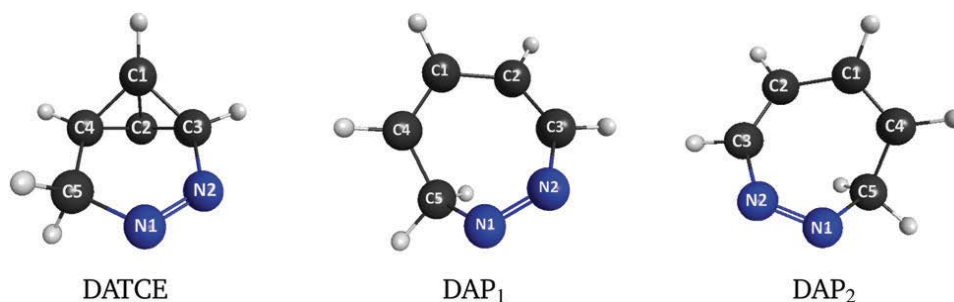
Figure 22. Structures of 3,4-diazatricyclo[4.1.0.0^{2,7}]hept-3-ene (DATCE) and isomerization
products 3H-1,2-diazepine (DAP$_1$ and DAP$_2$).

The two structures DAP$_1$ and DAP$_2$ are enantiomers so have the same electronic energies.

The isomerization occurs by cleavage of two bonds in the bicyclobutane moiety. For one

channel, bond C1-C3 ruptures first and then C2-C4 second. Conversely, C2-C3 can break first

and then C1-C4 second. Both of these possibilities lead to the same transition state due to the Cs

symmetry of the DATCE reactant. Here, the first breaking bond is adjacent to a nitrogen atom

(N2). A second channel exists in which the first breaking bond is adjacent to a carbon atom (C5) leading to a different transition state. C1-C4 can break first and then C2-C3 second, or the symmetrically equivalent C2-C4 bond breaking first and C1-C3 second. Considering the Woodward-Hoffman symmetry rules, the isomerization can go through either conrotatory or disrotatory pathways. For this structure, conrotatory is allowed while disrotatory is forbidden which should have a significantly higher activation barrier. In detail, the isomerization of DATCE can occur via four different pathways: two leading to product DAP$_1$ and the other two leading to product DAP$_2$. For clarity, if the first breaking bond is adjacent to the nitrogen atom (N2), the label "N" is used; if the first breaking bond is adjacent to the carbon atom (C5) the label "C" is used. For the two controtatory pathways, if the first breaking bond is adjacent to N2 the transition state is labeled NconTS1 and if adjacent to the C5 atom is labeled CconTS1. Conversely, for the disrotatory pathways, if the first breaking bond is adjacent to N2 the transition state is labeled NdisTS and CdisTS if adjacent to C5.The two disrotatory pathways lead directly to the product DAP$_1$ while the two conrotatory pathways lead to an intermediate, either NconInt or CconInt, which then can isomerize to the product DAP$_2$. A schematic diagram for the conrotatory and disrotatory reaction channels is shown in Figure 23, while the activation barriers are given in Table 5.
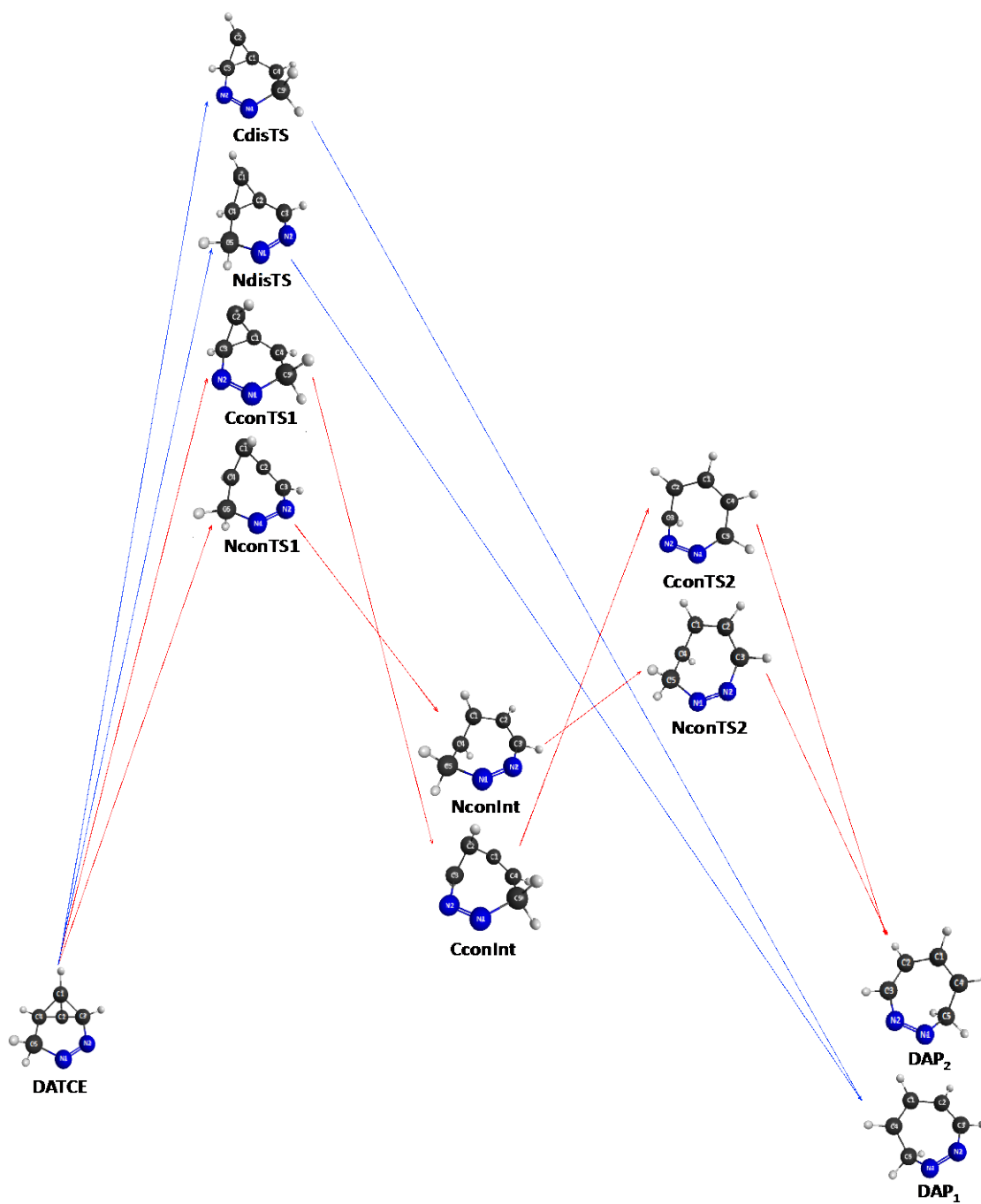
Figure 23. Schematic diagram for the isomerization of DATCE to DAP$_1$ and DAP$_2$.

Table 5. Activation barriers, E_a, for each pathway (kcal mol^{-1}) Including ZPE correction.

Reaction[a]	TS[a]	MCSCF[b]	MRMP2[c]	PBEPBE-D3[d]
DATCE → DAP$_1$	NdisTS	51.1	44.3	44.4[e]
DATCE → DAP$_1$	NdisTS	56.1	56.5	52.9[e]
DATCE → NconInt	NconTS1	41.1	36.1	36.8
DATCE → CconInt	NconTS1	41.3	37.9	39.3
NconInt → DAP$_2$	NconTS2	17.4	14.1	16.8
CconInt→ DAP$_2$	NconTS2	17.8	15.5	30.7

[a] All geometries are optimized at the MCSCF(10,10)/cc-pVDZ level. [b] The energies are calculated at the MCSCF/cc-pVDZ level. [c] The energies are calculated at the MRMP2/cc-pVDZ/MCSCF//cc-pVDZ level. [d] The energies are calculated at the DFT/cc-pVDZ//MCSCF/cc-pVDZ level. [e] Broken spin symmetric wave function. [e] Broken spin symmetry wavefunction.

3.3.1.1 Conrotatory pathways

The transition states NconTS1 and CconTS1 which connect the reactant DATCE and intermediates NconInt and CconInt are presented in Figure 24 while the intermediates are shown in Figure 25.
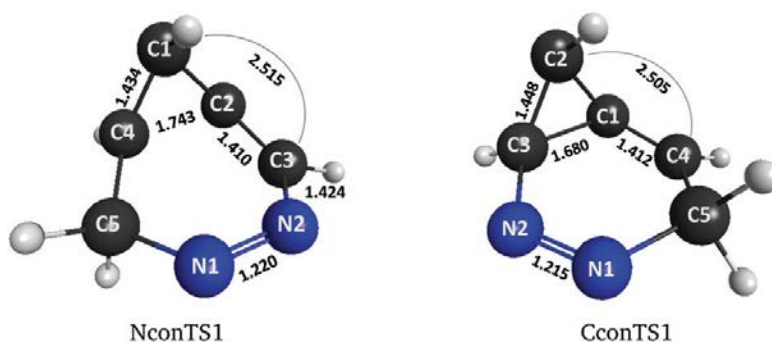
Figure 24. Transition state structures NconTS1 and CconTS1 for the two conrotatory pathways.
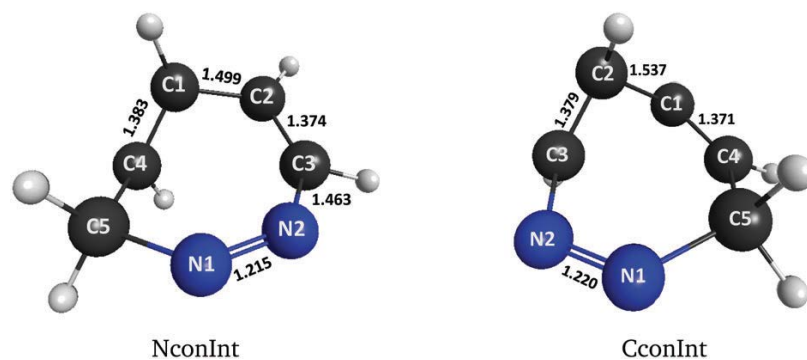
Figure 25. Structures for the *trans* double bond intermediates NconInt and CconInt for the two conrotatory pathways.

The two conrotatory pathways lead to isomerization intermediates via cyclic dienes with a *trans* double bond. For NconTS1, the C1-C3 bond breaks first which is adjacent to N2; for CconTS1, the C2-C4 bond breaks initially which is adjacent to C5. It can also be clearly seen that the hydrogen on C1 for NconTS1 and C2 for CconTS1 rotates back toward the ring which produces the *trans* double bond in the intermediates. The *trans* double bond will be between C1=C4 for NconTS1 and between C2=C3 for CconTS1 as shown in the intermediate structures (see Figure 25). The barrier heights for the two conrotatory pathways show a slight difference of 1.8 kcal mol^{-1} at the MRMP2 level. The activation energy for NconTS1, with the first breaking bond adjacent to the N2 atom, is slightly lower than for CconTS2. One explanation for the energy difference could be electron delocalization between the bonding electrons of the N1=N2 π bond and/or the lone pair electrons on the adjacent N2 atom through resulting orbital on C3 from the cleaved C1-C3 bond. The lone pair orbital on N2 is orthogonal to the N=N π bond so the only orbital with significant overlap with the p-type orbital on C3 is the π orbital. The N1=N2 double bond is slightly longer in NconTS1, being lengthened to 1.220 Å, from 1.213 Å

in the DATCE reactant, consistent with a slight amount of delocalization from the double bond since C3 is adjacent. The N1=N2 bond is 1.215 Å in CconTS1 consistent with virtually no delocalization since C4 is nonadjacent. The two conrotatory barriers for tricyclo[4.1.0.0^{2,7}]heptene (structure 2) were separated by 6.2 kcal mol^{-1}. Comparing the natural orbital occupation numbers (NOON's) for the orbitals comprising the first breaking bond in the active space gives 1.74 for structure 2 and 1.82 for DATCE. The slightly higher NOON value for DATCE would mean less chance for accepting electron density through delocalization of the N2 lone pair or the π electrons consistent with a lower magnitude stabilization. Structural features of NconTS1 and CconTS1 suggest that CconTS1 is an earlier transition state than NconTS1. The second breaking bond is 1.743 Å in NconTS1 while is only 1.680 Å in CconTS1. The forming *trans* double bond is also longer in CconTS1, 1.448 Å compared to 1.434 Å in NconTS1 suggesting an earlier TS for CconTS1. An earlier transition state usually means a competitively lower activation barrier which would be consistent with a smaller separation of the activation barriers between NconTS1 and CconTS1 (1.8 kcal mol^{-1}): the barrier for NconTS1 is lowered through delocalization while CconTS1 is lowered through steric effects manifesting as an earlier transition state.

In the transition states, the H-C1-C4-H dihedral is 169.4° for NconTS1 and the H-C2-C3-H dihedral is 160.5° in CconTS1. This illustrates the formation of the *trans* configuration of the double bond is mostly complete by the transition states. In the intermediate structures for the conrotatory pathway, Figure 25, the values are H-C1-C4-H = 179.2° in NconInt and H-C2-C3-H = 178.9° in CconInt, very close to the 180.0° value of a true *trans* structure. The dihedrals

across the *trans* double bonds for the carbon atoms cannot be close to 180° as it would make is impossible to complete the ring. They are C2-C1-C4-C5 = 104.3° for NconInt and C1-C2-C3-C4 = 105.1° for CconInt. These small angles add a significant amount of strain to the seven-membered rings. The relative energies of NconInt and CconInt are both above the reactant DATCE and the product DAP$_2$ as listed in Table 6. DAP$_1$ and DAP$_2$ are enantiomers so both have the same electronic energies and both are given the relative energy of zero in the reaction energetics.

Table 6. Relative energies including ZPE correction.

Structure[a]	MCSCF[b]	MRMP2[c]
DATCE	38.8	31.2
NconInt	50.7	45.6
CconInt	48.1	44.4
DAP$_1$	0	0
DAP$_2$	0	0

[a] All geometries where optimized at the MCSCF(10,10)/cc-pVDZ level. [b] The geometries and energies are calculated at the MCSCF/cc-pVDZ level. [c] The energies are calculated at the MRMP2/ cc-pVDZ/MCSCF/cc-pVDZ level.

The intermediates NconInt and CconInt are cyclic conjugated trienes with one *trans* double bond and one *cis* double bond along the carbon ring moiety. They are very similar in energy and are 45.6 and 44.4 kcal mol^{-1} above their isomerization product DAP$_2$. They are also higher in energy than the DATCE reactant which is 31.2 kcal mol^{-1} above DAP$_2$. The *trans* double bond imparts a significant amount of strain energy to the intermediates, more so than the bicyclobutane moiety of the DATCE reactant.

The intermediates NconInt and CconInt both isomerize to the product DAP$_2$ through *trans* double bond rotation through the transition states labeled NconTS2 and CconTS2, respectively, which structures are shown in Figure 26.
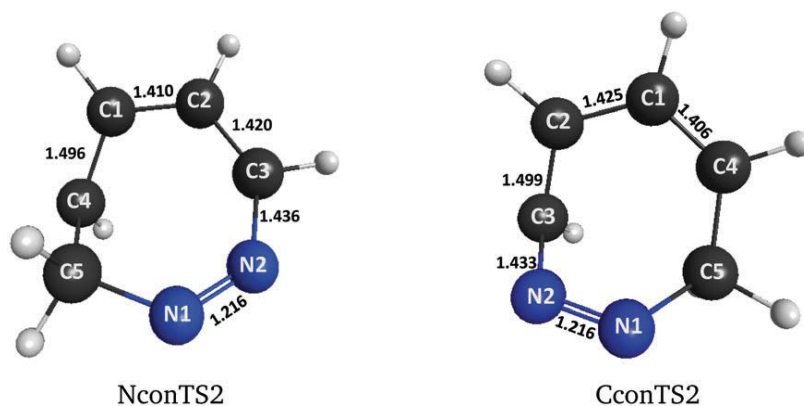
Figure 26. Structures for the transition states for *trans* double bond rotation of NconInt and CconInt to produce DAP$_2$.

As listed in Table 5, the activation barriers are 14.1 kcal mol^{-1} for NconTS2 and 15.5 kcal mol^{-1} for CconTS2. As stated above, the H-C1-C4-H dihedral is 179.2° in NconInt; as the *trans* double bond rotates toward the *cis* configuration, the transition state (NconTS2) has a value of 116.1° for the H-C1-C4-H dihedral. The NconTS2 structure has significant singlet biradical character with NOON values of 1.259 and 0.741 for orbitals 25 and 26 comprising the C1=C2 π bonding and antibonding orbitals, respectively, in the active space. The C1-C4 bond length is 1.383 Å in NconInt while it lengthens to 1.496 Å in the transition state NconTS2, showing that the double bond has broken during the rotation. However, the C1-C2 bond length reduces substantially from 1.499 Å to 1.410 Å in NconTS2 while the *cis* double bond between C2-C3 has lengthened from 1.374 to 1.420 Å. This can be explained by delocalization of the three π

70

electrons from C1, C2, and C3 across the C1-C2-C3 bonded atoms. This same behavior is found in CconInt and CconTS2 with the rotating *trans* bond lengthening the distance between C2-C3 from 1.379 to 1.499 Å, the C1-C2 single bond in CconInt shortening from 1.537 to 1.425 Å in CconTS2, and the length between C1-C4 double bonded atoms increasing from 1.371 to 1.406 Å. Delocalization of the three π electrons on C2, C1, and C4 delocalizes across the C2-C1-C4 bonded atoms.

3.3.1.2 Disrotatory pathways

As mentioned above, there are four pathways for the controtatory channel: two symmetry related pairs which lead to two distinct transition states. The same holds true for the disrotatory pathways: there are two symmetry distinct channels leading to two distinct transition states labled NdisTS and CdisTS. For NdisTS, the first breaking bond is adjacent to N2, while for CdisTS, the first breaking bond is adjacent to C5. These structures are shown in Figure 27.
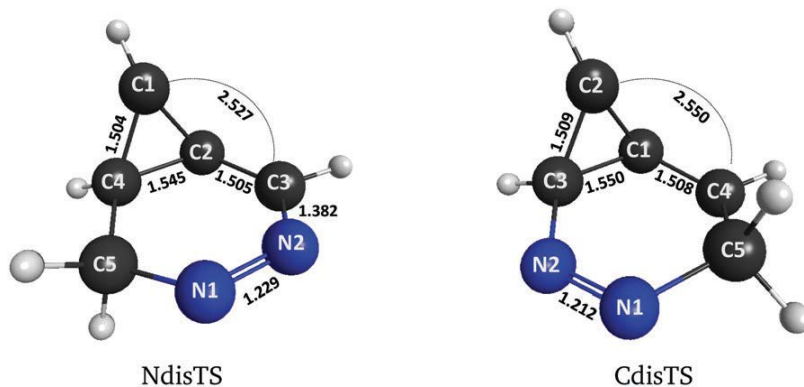
Figure 27. Transition state structures NdisTS and CdisTS for the two disrotatory pathways.

The disrotatory pathways are forbidden so they should have substantially higher barriers than the allowed conrotatory barriers: this is the case with the barrier for NdisTS being 44.3 kcal

mol^{-1} and that for CdisTS being 56.5 kcal mol^{-1} (Table 5). The difference between the allowed

and forbidden barriers for the first breaking bond being adjacent to N2 is NdisTS - NconTS1 =

8.2 kcal mol^{-1}. That for the first breaking bond adjacent to C5 is CdisTS - CconTS1 = 18.6 kcal

mol^{-1}. The disparity of the differences between the allowed and forbidden barriers is reconciled

through resonance delocalization of the π electrons of the N1=N2 double bond. The

wavefunctions for the disrotatory transition states, NdisTS and CdisTS, are highly

multiconfigurational in character as witnessed by their NOON values in the active space. For

NdisTS, orbitals 25 and 26 have NOON values of 1.122 and 0.879, respectively, comprising the

two orbitals that result from the bonding and antibonding s orbitals after cleavage between C1-

C3. These values show that NdisTS is close to being a singlet biradical with a single electron on

C1 and C3 in the transition state. This means that there is available electron density in that orbital

on C3 which can accept density from the π electrons from the N1=N2 double bond. This

resonance delocalization lowers the energy of the transition state reducing the barrier. For

CdisTS, the NOON values are also near unity with   the bonding and antibonding orbitals

between C2-C4 being 1.089 and 0.912, respectively. However, since the orbital on C4 is not

adjacent to the π electrons, delocalization is not possible: there is not a corresponding energy

stabilization of CdisTS. A similar stabilization was observed with tricyclo[4.1.0.0^{2,7}]heptene[126] in

that the bond breaking adjacent to the double bond had a difference in disrotatory (forbidden)

barriers of 13.1 kcal mol^{-1} very similar to the 12.2 kcal mol^{-1} for CdisTS - NdisTS.

The main structural differences in the disrotatory transition states compared to the

conrotatory ones described above are H-C1-C4-H = 11.1° dihedral in NdisTS and the H-C2-C3-

H = 13° dihedral in CdisTS. This illustrates that the resulting double bonds will be in the *cis* configuration leading directly to the DAP₁ product. The second breaking bond is also much shorter in NdisTS and CdisTS compared to NconTS1 and CconTS1 making the reaction much more asynchronous for the bond cleavages.

Another interesting structural difference is the length of the N1=N2 bond in NdisTS versus CdisTS: they are 1.229 Å in NdisTS and 1.212 Å in CdisTS. The longer N1=N2 bond in NdisTS is consistent with electron delocalization from the π bonding orbital into the half empty orbital on C3 slightly weakening the π bond. The shorter N1=N2 bond in CdisTS is consistent with no electron density coming from the π bonding orbital and is virtually the same length as in the DATCE reactant (1.213 Å).

3.3.1.3 Intrinsic reaction coordinates

The intrinsic reaction coordinate profiles for the conrotatory and disrotatory pathways are presented in Figure 28. The IRCs going from NconTS1 and CconTS1 back to the DATCE reactant illustrate the nature of the bond cleavages and strain release of the bicyclobutane moiety. Going from DATCE toward the transition state, the energy rises quickly as the first bond starts to cleave. Then, the slope decreases substantially as the second breaking bond starts to lengthen which allows for ring relaxation and strain energy release. The slightly more pronounced shoulder for NconTS1 is consistent with the longer bond lengths of the breaking bond pair: 2.515 Å and 1.743 Å in NconTS1 compared to 2.505 Å and 1.680 Å in CconTS1. The absence of an analogous shoulder for the disrotatory pathways is consistent with the asynchronous nature of the reaction with the second breaking bond still largely intact minimizing strain release at the

transition state. This would make the disrotatory transition states higher in energy consistent with their forbidden classification.
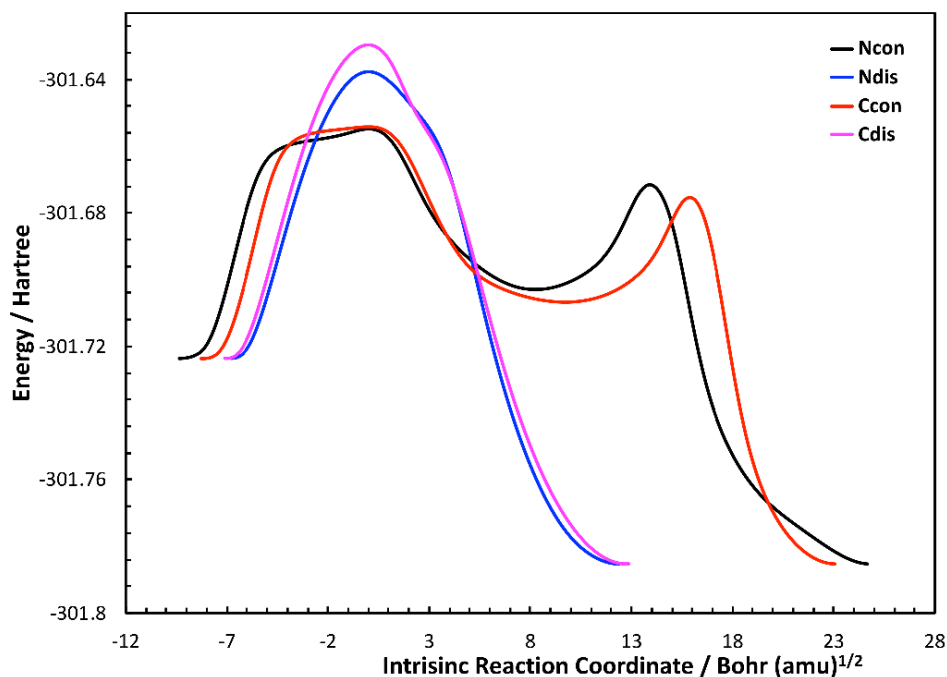
Figure 28. Intrinsic reaction coordinate plots for the DATCE to DAP_1 and DAP_2 isomerization.

3.3.2 3,4-Diazatricyclo[4.1.0.0^{2,7}]heptane

The structure of 3,4-diazatricyclo[4.1.0.0^{2,7}]heptane (DATCA) and its isomerization products 2,3-dihydro-1H-1,2-diazepine (DHDAP$_1$ and DHDAP$_2$) are presented in Figure 29. In this reactant structure, there is a single bond between the two nitrogen atoms so there are no π electrons available to stabilize the transition states - only the lone pair electrons on nitrogen. DATCA belongs to point group C1 so there are eight total reaction channels: four conrotatory and four disrotatory. A similar naming scheme for the DATCE reaction described above is used for the first breaking bond being either adjacent to the N2 atom or the C5 atom. In this case, due

74

to the lack of a symmetry plane, breaking bonds C1-C3 then C2-C4 leads to one transition state (NconTS1′ or NdisTS′) and breaking bonds C2-C3 then C1-C4 leads to a different one (NconTS1″ or NdisTS″). Conversely, bonds C1-C4 then C2-C3 leads to CconTS1′ or CdisTS′, and breaking bonds C2-C4 then C1-C3 leads to CconTS1″ or CdisTS″. The four allowed conrotatory channels lead to cyclic intermediates with a *trans* double bond which can form the DHDAP$_1$ or DHDAP$_2$ product through *trans* double bond rotation. The structural isomers DHDAP$_1$ and DHDAP$_2$ differ only by a few kcal mol-1 in electronic energy. At the MRMP2 level, DHDAP$_1$ is the lowest energy structure by 1.1 kcal mol^{-1}. However, at the CCSD(T)/aug-cc-pVTZ//CCSD/cc-pVDZ level, DHDAP$_1$ is the lowest energy structure by 0.2 kcal mol^{-1}. These values are listed in Table 8. A schematic diagram for the conrotatory and disrotatory reaction channels is shown in Figure 30, while the activation barriers are given in Table 7.
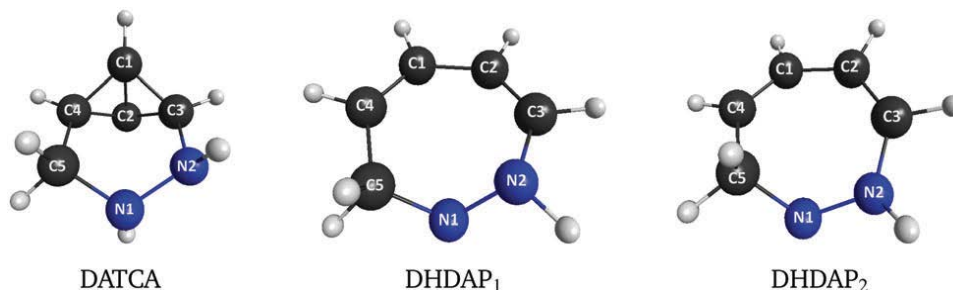

Figure 29. Structures of 3,4-diazatricyclo[4.1.0.0^{2,7}]heptane (DATCA) and isomerization products 2,3-dihydro-1H-1,2-diazepine (DHDAP$_1$ and DHDAP$_2$).
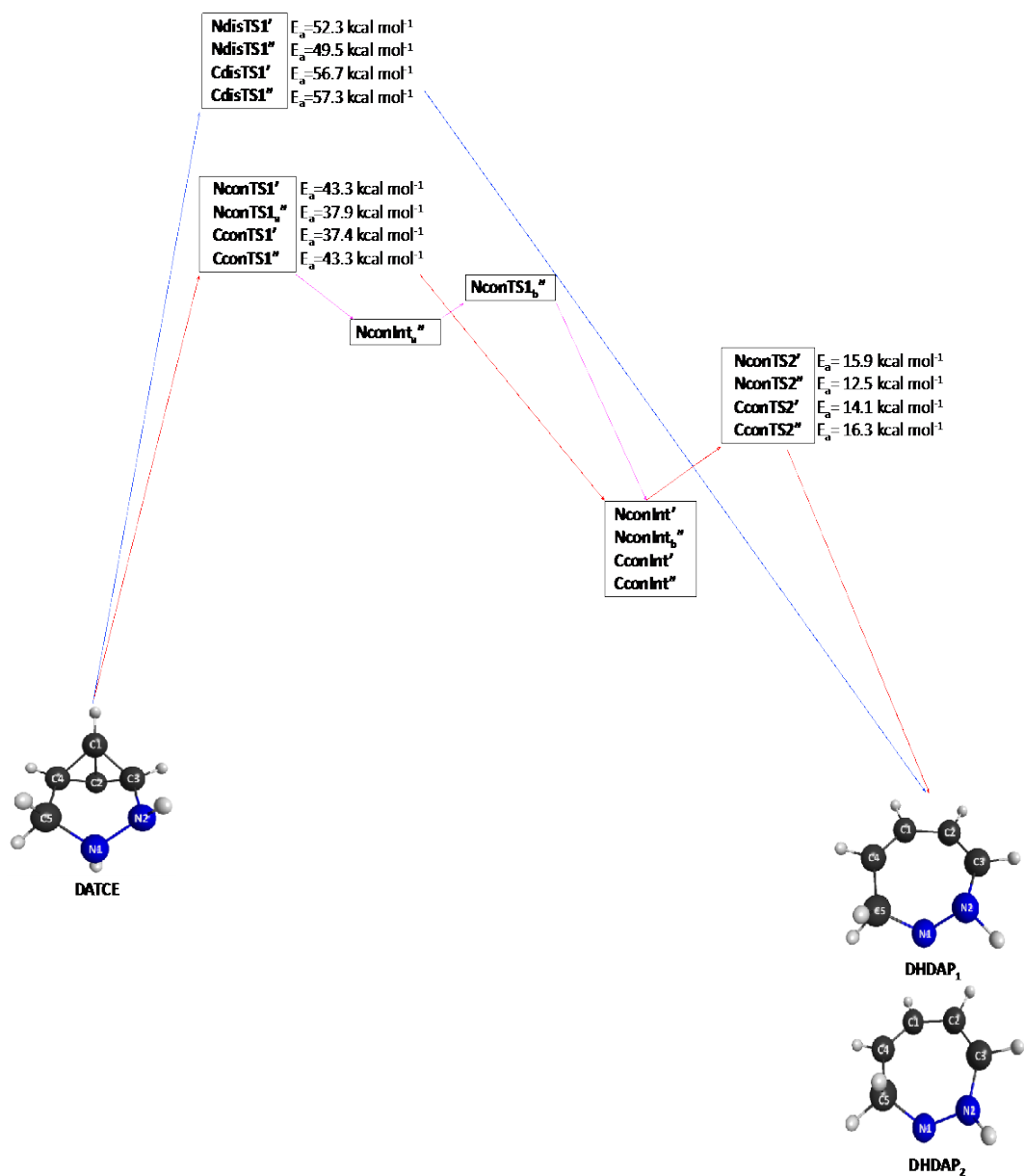
Figure 30. Schematic diagram for the isomerization of DATCA to DHDAP$_1$ and DHDAP$_2$.

Table 7. Activation barriers, E_a, for each pathway (kcal mol^{-1}) including ZPE correction.

Reaction[a]	TS[a]	MCSCF[b]	MRMP2[c]	PBEPBE-D3[d]
DATCA $\rightarrow$ DHDAP$_2$	NdisTS$'$	54.1	52.3	58.6[e]
DATCA $\rightarrow$ DHDAP$_2$	NdisTS$''$	51.8	49.5	54.3[e]

DATCA $\to$ DHDAP$_1$	CdisTS$'$	55.4	56.7	75.2[e]
DATCA $\to$ DHDAP$_1$	CdisTS$''$	55.2	57.3	71.5[e]
DATCA $\to$ NconInt$'$	NconTS1$'$	44.7	43.3	46.9
DATCA $\to$ NconInt$_a''$	NconTS1$_a''$	41.4	37.9	40.7
DATCA $\to$ CconInt$'$	CconTS1$'$	39.9	37.4	41.2
DATCA $\to$ CconInt$''$	CconTS1$''$	44.6	43.3	48.9
NconInt$_a'' \to$ NconInt$_b''$	NconTS1$_b''$	0.2	1.7	1.9
NconInt$' \to$ DHDAP$_1$	NconTS2$'$	20.8	15.9	24.7
NconInt$_b'' \to$ DHDAP$_1$	NconTS2$''$	16.5	12.5	24.9
CconInt$' \to$ DHDAP$_2$	CconTS2$'$	18.4	14.1	25.1
CconInt$'' \to$ DHDAP$_2$	CconTS2$''$	20.0	16.3	27.3

[a] All geometries are optimized at the MCSCF(10,10)/cc-pVDZ level. [b] The energies are calculated at the MCSCF/cc-pVDZ level. [c] The energies are calculated at the MRMP2/cc-pVDZ//MCSCF//cc-pVDZ level. [d] The energies are calculated at the DFT/cc-pVDZ//MCSCF/cc-pVDZ level. [e] Broken spin symmetric wave function.

Table 8. Relative energies including ZPE correction.

Structure[a]	MCSCF[b]	MRMP2[c]	CCSD(T) [d]
DATCA	43.3	31.0	30.8
DHDAP$_1$	0	0	0
DHDAP$_2$	1.6	1.1	0.2
NconInt$'$	46.6	40.8	
NconInt$_a''$	80.6	64.9	62.6
CconInt$'$	44.7	39.1	
CconInt$''$	50.1	44.6	

[a] All geometries where optimized at the MCSCF(10,10)/cc-pVDZ level. [b] The geometries and energies are calculated at the MCSCF/cc-pVDZ level. [c] The energies are calculated at the MRMP2/ cc-pVDZ/MCSCF/cc-pVDZ level. [d] The energies are calculated at the CCSD(T)/aug-cc-pVDZ/CCSD/cc-pVDZ level.

3.3.2.1 Conrotatory pathways

There are four conrotatory channels for the ring opening leading to the DHDAP$_1$ or

DHDAP$_2$ products and can be classified as whether the first breaking bond is adjacent to N2 or

C5. If the first bond breaks adjacent to N2, it is useful to note the position of the H atom bonded

to N2 relative to the first breaking bond. If the C1-C3 bond breaks first, the H-N2-C3-C1 dihedral is positive so that the H on N2 is on the same side of the dihedral looking down N2-C3; if the C2-C3 bond breaks first, the H-N2-C3-C2 dihedral is negative so that the H on N2 is on the opposite side of the dihedral looking down N2-C3. If the first bond breaks adjacent to C5, it is useful to note the position of the H atom bonded to N1. If the first breaking bond is C2-C4, then the H of N1 is on the same side of the dihedral about C5-C4, and if the first breaking bond is C1-C4, the H of N1 is on the opposite side of the dihedral about C5-C4. For notation, a single prime is used for the positive dihedral angle while a double prime is used to denote the negative dihedral angle.

The two transition states for the first breaking bond adjacent to C5 are shown in Figure 31. CconTS1′ is an earlier transition state per the shorter breaking bonds (C2-C4 and C1-C3) and the longer C2-C3 bond (compared to C1-C4, C2-C3, and C1-C3 in the other TS, respectively) which are the two breaking bonds and the forming *trans* double bond. The barrier for NconTS1′ is also lower, 37.4 vs 43.3 kcal mol^{-1} also consistent with an earlier transition state.
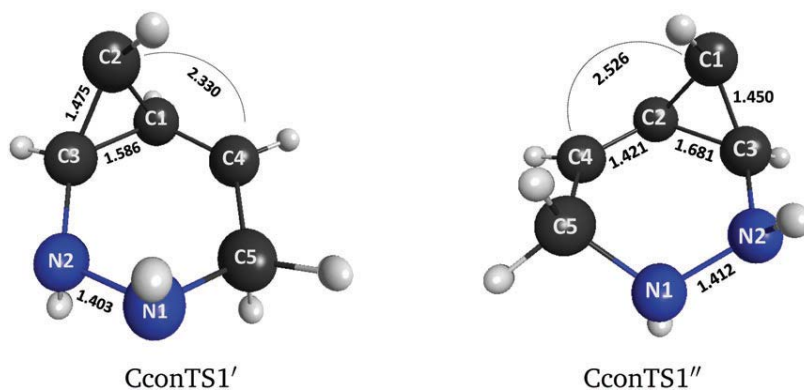
CconTS1′　　　　　　　　CconTS1″

Figure 31. Structures of transition states CconTS1′and CconTS1″.

The transition states for the initial bond cleaving adjacent to the N2 atom are shown in Figure 32 and Figure 33. The transition state barrier leading to NconTS1′ is actually higher than the analogous CconTS1′ showing that the lone pair electrons did not lower the barrier through delocalization with the orbitals resulting from cleavage of the C1-C3 bond: steric effects are the most important here. The NOON values are similar for both transition states being 1.766 and 0.237 for CconTS1′ and 1.774 and 0.234 for NconTS1′. Having NOON values this close to 2 and 0 means there is little opportunity for delocalization of the N2 lone pair into a partially filled orbital on C3. For the other conrotatory channel, there was an unexpected intermediate found on the potential energy surface. The structure of the transition state NconTS1″a appeared to be consistent with the other conrotatory channels described above and lead to the cyclic *trans* double bond intermediate. However, following the IRC led to the reactant but in the forward direction led to a minimum with a geometry very similar to the transition state, NconInt$_a$″ (Figure 33). The NOON values of the transition state NconTS1$_a$″ are 1.786 and 0.216 for the orbitals comprising the first breaking bond, so single reference coupled cluster calculations should be able to adequately describe the wavefunction. In order to get the most accurate energies, and the best description of the PES, the geometry of NconTS1$_a$″ was optimized at the CCSD/cc-pVDZ level. The harmonic frequencies were also determined at this level (numerical second derivatives) and one imaginary frequency was present confirming this as a transition state. Single point energies were calculated at the CCSD(T)/aug-cc-pVTZ//CCSD/cc-pVDZ level for the minima and transition states for this channel. The barrier from DATCA to NconTS1$_a$″ is 37.9 kcal mol^{-1} at the MRMP2 level and 40.5 kcal mol^{-1} at the CCSD(T) level. Comparison of this TS

(NconTS1$_a''$) to the other conrotatory one (NconTS1$'$) shows that NconTS1$_a''$ is a much earlier transition state. The first breaking bond, C2-C3, is 2.216 Å in NconTS1$_a''$ while that for C1-C3 in NconTS1$'$ is 2.518 Å. The second breaking bond, C1-C4, in NconTS1$_a''$ is 1.554 Å while the C2-C4 bond in NconTS1$'$ is much longer at 1.715 Å. The C2-C4 bond of NconTS1$_a''$ will become a *trans* double bond in the cyclic intermediate, and it is 1.505 Å. The C1-C3 bond of NconTS1$_a''$ will become a *trans* double bond in the cyclic intermediate and it is shortened to 1.455 Å. The shorter breaking bonds and longer forming double bonds confirm the TS on an much earlier portion of the PES.
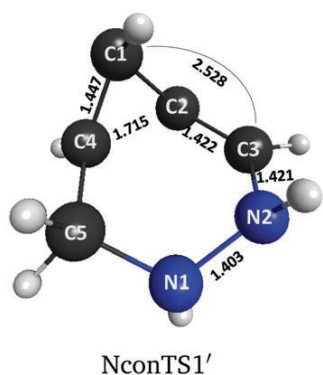
Figure 32. Structure of transition state NconTS1$'$.
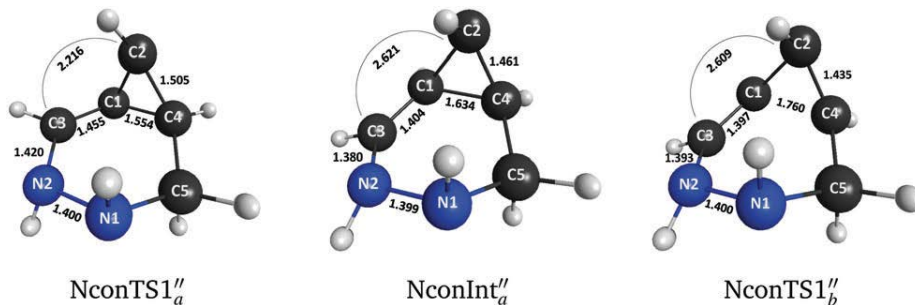
Figure 33. Structures of NconTS1$_a''$, NconInt$_a''$ and NconTS1$_b''$.

80

The structure of the intermediate NconInt$_a''$ is very similar to the conrotatory transition states, and to get a second confirmation that it was actually a minimum, the geometry from the end of the IRC calculation was optimized and the harmonic frequencies computed at the MSCSF level: they were all real values. The calculation was repeated at the CCSD/cc-pVDZ level and the geometries optimized and harmonic frequencies determined: allreal frequencies were present at this level, also. NconInt$_a''$ is just 4.8 kcal mol^{-1} lower than NconTS1$_a''$ at the MRMP2 level and 8.7 kcal mol^{-1} lower at the CCSD(T) level consistent with the very similar structures of the NconTS1$_a''$ and NconInt$_a''$. An explanation for the NconInt$_a''$ intermediate is the availability of the N2 lone pair to delocalize into orbital 27 resulting from the cleavage of the C2-C3 bond in NconTS1$_a''$. These two orbitals are shown in Figure 34. Orbital 27 is localized to C3 and is eclipsed with orbital 20 comprising the N2 lone pair. Orbital 27 of the active space has a NOON of 0.216 so it can readily accept electron density. The same overlap between orbitals 20 and 27 is available in NconInt$_a''$. The shortening of the N2-C3 bond in 1.380 in NconInt$_a''$ is consistent with additional bonding overlap between N2 and C3. In addition, the C1-C3 bond is also shortened having a value of 1.404 Å.
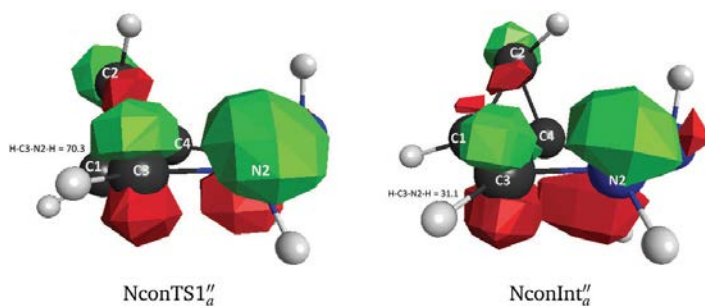
Figure 34. Densities for orbital 20 (p-type on C2 and C3) and orbital 27 (lone pair on N2) of NconTS1$''$ and NconInt$_a''$.

The dihedral angle between the overlap of orbitals 20 and 27 can be approximated by the H-C3-N2-H dihedral angle: the N2 atom is tetrahedral and the C3 is trigonal planar in NconTS1$_a$″ and NconInt$_a$″. Therefore, a H-C3-N2-H=30° would be a totally eclipsed geometry for the p orbital on C3 (#27) and the sp^3 lone pair orbital on N2. It is 70.3° in the transition state NconTS1$_a$″ signifying partial overlap between the two being offset by approximately 40°. In the intermediate NconInt$_a$″ the H-C3-N2-H dihedral is only 31.1° signifying a totally eclipsed geometry giving substantial overlap between orbitals 20 and 27.

The C1-C4 bond in NconInt$_a$″ is also lengthened to 1.634 Å allowing the C2-C4 *trans* π bond to initiate formation. This stabilization allows for the structure to be a minimum of the PES. The N2 lone pair orbital is not eclipsed with orbital 27 in the other conrotatory transition state, NconTS1′, so stabilization is not possible so there is no analogous intermediate formed.

The transition state from NconInt$_a$″ to the cyclic *trans* double bond intermediate is labeled NconTS$_b$″ and shown in Figure 33. The barrier from NconTS1$_a$″ to NconTS1$_b$″ is just 1.7 kcal mol^{-1} at the MRMP2 level and 3.7 kcal mol^{-1} at the CCSD(T) level. The minimum occupied by NconTS1$_a$″ is very shallow with the further release of strain energy going to NconInt$_b$″ the main character of this portion of the PES. Basically, the transition state encompasses the cleavage of the second bond to break: the C1-C4 bond lengthens to 1.760 Å. The C2-C4 length shortens in NconTS1$_b$″ as the double bond continues forming. The barrier for the transition state NconTS1$_b$″ was determined at the MRMP2 and CCSD(T) levels since the barrier is so small and the wavefunction is mostly single configurational having NOON's of 1.866 and 0.122 for the orbitals comprising the C1-C4 breaking bond.

3.3.2.2 Disrotatory pathways

There are four disrotatory transition states possible for DATCA: bond C1-C3 (NdisTS′) or bond C2-C3 (NdisTS″) breaking first, or bond C1-C4 (CdisTS′) or C2-C4 (CdisTS″) breaking first. The transition state structures are shown in Figure 35. Both CdisTS′ and CdisTS″ have almost identical barriers with no possibility of overlap of the N2 lone pair onto C3 consistent with the barriers being the highest. NdisTS′ and NdisTS″ have lower barriers by 4.4 and 7.2 kcal compared to CdisTS′. For these two transition states, the lone pair on N2 can delocalize into orbitals 26 and 27 on C3 consistent with the lower barrier heights. The NOON's are 1.170 and 0.833 for orbitals #26 and # 27 of NdisTS′ and 1.231 and 0.770 for NdisTS″. The lone pair is in phase for overlap relative to both orbitals 26 and 27 on C3, and these two orbitals are basically half filled (singlet biradical). The N2-C3 bond length is 1.441 Å in the DATCA reactant and shortens to 1.406 and 1.409 Å in the two transition states also consistent with delocalization of the N2 lone pair across the N2-C3 bond. The disrotatory transition states are more asynchronous than the conrotatory ones with the second breaking bond much shorter here. The H atom on C1 or C2 also points away from the ring in the configuration to form a *cis* double bond in the DHDAP products.
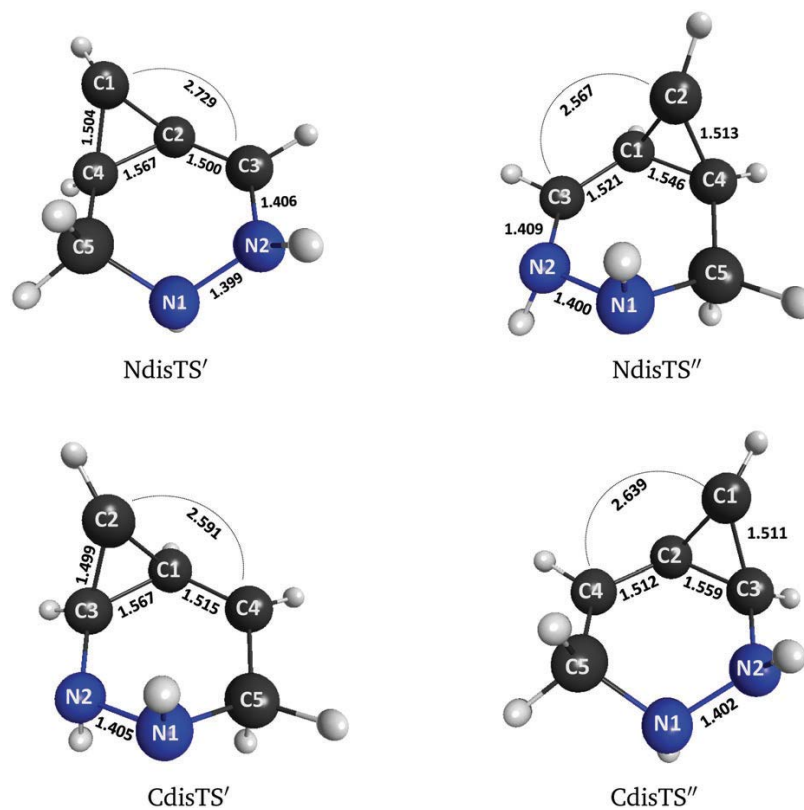
Figure 35. Structures of transition states for the disrotatory channel of DATCA.

3.3.2.3 Intrinsic reaction coordinates

The IRC curves for the four conrotatory channels are shown in Figure 36. The intermediate NconInt$_a$″ is labeled, and the very shallow minimum between it and intermediate NconInt$_b$″ is apparent. The IRC plots connect the DATCA reactant to the *trans* bond intermediates and subsequently to the DHDAP$_1$ and DHDAP$_2$ products. The disrotatory IRC curves are shown in the Figure C1. They contain the single transition state and directly connect the DATCA reactant to the DHDAP$_1$ and DHDAP$_2$ products.
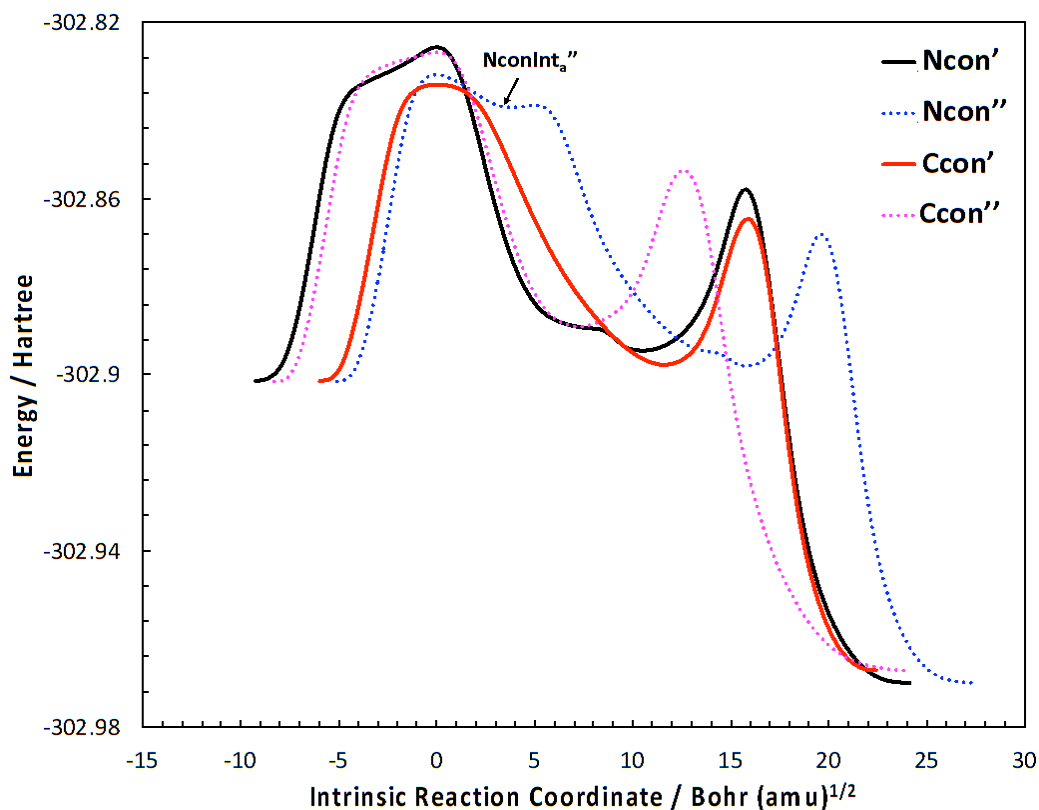
Figure 36. Intrinsic reaction coordinates for the four conrotatory channels for DATCA isomerization.

3.3.3 Orbital stabilization

The disparity between the activation energies among the conrotatory and disrotatory channels is due to steric and resonance effects. This section will discuss the stabilization of some transition states due to delocalization of the π electrons of the N=N double bond and delocalization of the lone pair on the N atom.

For the DATCE reactant, transition states, and DAP_1 and DAP_2 products, the active space consists of orbitals 21-30. Looking at the MCSCF natural orbitals, 18 and 20 consist of a combination of the two lone pairs of the N atoms, and orbital 19 consists of the N=N π bonding

orbital in each structure. The two disrotatory pathways show one barrier significantly lower:

NdisTS is 8.2 kcal mol^{-1} lower than CdisTS. Cleavage of the C1-C3 bond can lead to transition

state NdisTS as shown in Figure 37. The C1-C3 bonding and antibonding orbitals of the reactant

DATCE are now represented by orbitals 25 and 26 in the active space which are π type orbitals

on C1 and C3. The NOON's for orbitals 25 and 26 are close to 1 so can accept significant

electron density. The NOON values for orbitals 25 and 26 for NdisTS are 1.112 and 0.879,

respectively. In comparison, the NOON values for orbitals 25 and 26 for the CdisTS transition

state are 1.089 and 0.912: in this transition state, the breaking bond is not adjacent to the N=N π

bond. As shown in Figure 37, the half empty orbitals 25 and 26, on C3, are both in phase with

the π orbital on N1=N2. The higher NOON value for orbital 25 in NdisTS than for CdisTS

(1.122 vs 1.089) suggest that orbital 25 of NdisTS accepts electron density from the N=N π

bond. The increased occupation number for orbital 25 would lower its energy compared to

orbital 26 which would result in a reduction of the NOON value for orbital 26. This is reflected

in the NOON value of 0.879 compared to 0.912 in the unstabilized CdisTS. The delocalization of

the π electrons into orbital 25 would lower the electronic energy of the transition state, lowering

the activation barrier.

NdisTS (Orbitals 19,25)   NdisTS (Orbitals 19,26)
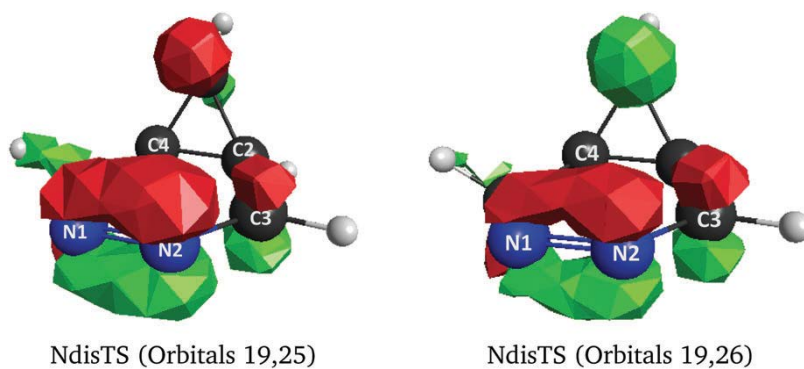
Figure 37. Densities for orbital 19 (p-bonding on N1=N2), orbital 25 (p-type on C1 and C3), and orbital 26 (p-type on C1 and C3) from the MCSCF natural orbitals for NdisTS1.

Cleavage of the C1-C3 bond can also result in transition state NconTS1 shown in Figure 38. Orbitals 25 and 26 of the active space are the p-type orbitals resulting from the cleaved C1-C3 bonding and antibonding orbitals. The phases of 25 and 26 are opposite on C3 but the same on C1. The density from orbital 19 on N2 and orbital 25 on C3 are opposite in phase so there is an antibonding overlap between N2 and C3 for these two orbitals: the N=N π bonding orbital (19) and the p-type orbital on C3 (25). Orbital 25 has a NOON value of 1.815, close to being doubly occupied. However, orbital 26 has a NOON value of 0.195 and is in phase with the N=N p bond. Orbital 26 being mostly empty, and in phase with the N=N p orbitals, can accept electron density from the N=N π bond; however, since orbital 26 is mostly unoccupied, its energy will be significantly higher than the N=N π bonding orbital (19), and the overlap will be decreased on that energetic standpoint. This smaller stabilization energy follows the smaller 1.8 kcal mol^{-1} barrier lowering for NconTS1 compared to CconTS1.

NconTS1 (Orbitals 19,25)   NconTS1 (Orbitals 19,26)
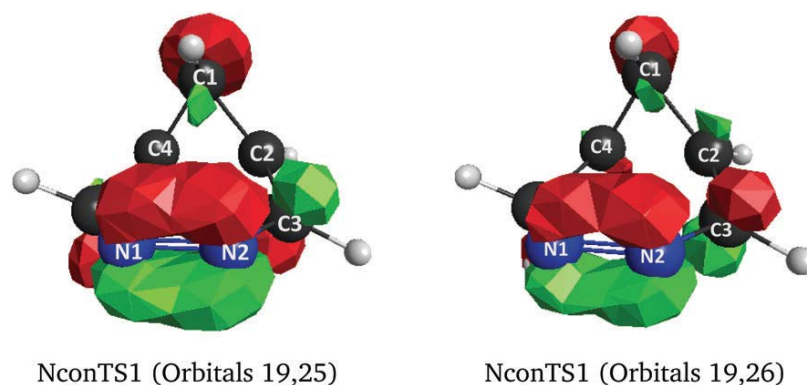
Figure 38. Densities for orbital 19 (p-bonding on N1=N2), orbital 25 (p-type on C1 and C3), and orbital 26 (p-type on C1 and C3) from the MCSCF natural orbitals for NconTS1.

The DATCA reactant does not have N=N π bond, but the N atom lone pairs can participate in delocalization and stabilize the transition states. For the DATCA reactant, transition states, and DHDAP$_1$ and DHDAP$_2$ products, the active space consists of orbitals 22-31. For the MCSCF natural orbitals, 20 and 21 are combinations of the N atom lone pairs. Transition state NdisTS″ has the lowest barrier of the four disrotatory channels and is shown in Figure 39. Orbital 20 consists of the lone pair on N2 while orbitals 26 and 27 are the remnants of the cleaved C1-C3 bonding and antibonding orbitals in the DATCA reactant. Orbital 26 consists of two p-type orbitals on C3 and C2 which are in phase with each other while orbital 27 consists of two p-type orbitals on C3 and C2 which are opposite phases. However, for orbitals 26 and 27, the p-type orbital on C3 are both in phase with the N2 lone pair orbital. The NOON for orbital 26 is 1.231 while that for orbital 27 is 0.770 making orbital 26 lower in energy. Electron density from the lone pair on N2 can delocalize into orbitals 26 and 27 since they are both in phase with the lone pair orbital, but delocalization will be more efficient with the lower energy orbital 26. Resonance between orbitals 20 and 26 would require that delocalization into orbital 26 would

lower its energy and raise its occupation number. This would result in a higher occupation

number for orbital 26 and a lower one for orbital 27. Comparing the NOON's for this transition

state with the two transition states where delocalization is not possible (CdisTS′ and CdisTS″)

shows that orbital 26 on NdisTS″ is 1.231 compared to 1.059 and 1.004 on CdisTS′ and CdisTS″,

respectively. For orbital 27, the NOON value is lower on NdisTS″, 0.770, versus 0.943 for

CdisTS′ and 0.997 for CdisTS″. For the two transition states CdisTS′ and CdisTS″, the cleaved

bond is not adjacent to a nitrogen lone pair, and no delocalization is possible so the NOON's are

much closer to 1.0. The barriers for these two transition states are higher as a result of their

higher electronic energies, and their NOON values reflect almost pure singlet biradical character.

Stabilization is also possible for transition state NdisTS′ since orbital 26 is in phase with the N2

lone pair orbital, and it also has a lower barrier than those for CdisTS′ and CdisTS″. The 5.9 kcal

mol^{-1} difference in the barriers for the CconTS′ and CconTS″ transition states is most likely due

to steric effects and is represented in the IRC's in which the lower barrier is for the earlier

transition state.

NdisTS″ (Orbitals 20,26)   NdisTS″ (Orbitals 20,27)
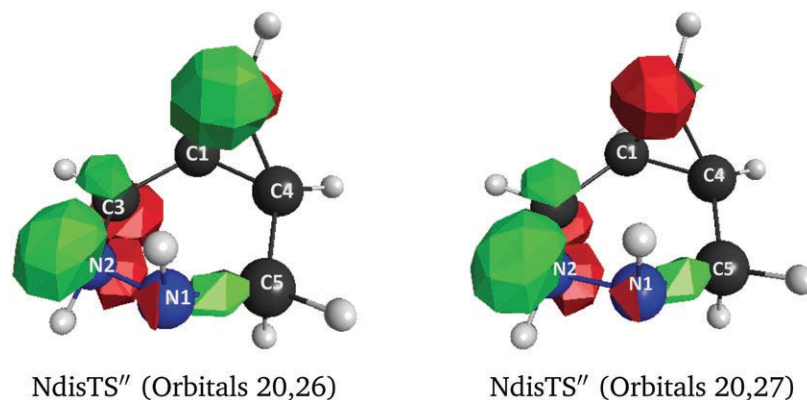
Figure 39. Densities for orbitals 20 (lone pair on N2), 26 (p-type on C2 and C3), and 27 (p-type on C2–C3) from the MCSCF natural orbitals for NdisTS1″ .

3.3.4 3,4,5-Diazatricyclo[4.1.0.0^{2,7}]hept-3-ene

In order to understand the relative stabilizing effects of the N=N π electrons versus the N lone pair electrons, we also looked   at the isomerization of 3,4,5-triazatricyclo[4.1.0.0^{2,7}]hept-3-ene (TATCE) to the 1H-1,2,3-triazepine (TAP$_1$ and TAP$_2$ enantiomers). The TATCE reactant and TAP$_1$ and TAP$_2$ products are shown in Figure 40. The TATCE structure has both the N=N π bond and a sp^3 hybridized N atom lone pair in the same molecule. Since it is the disrotatory transition states that are singlet biradical in character with two orbital NOON's close to 1.0, we present these since they are the most efficient in accepting electron density and reflecting a lower activation barrier.
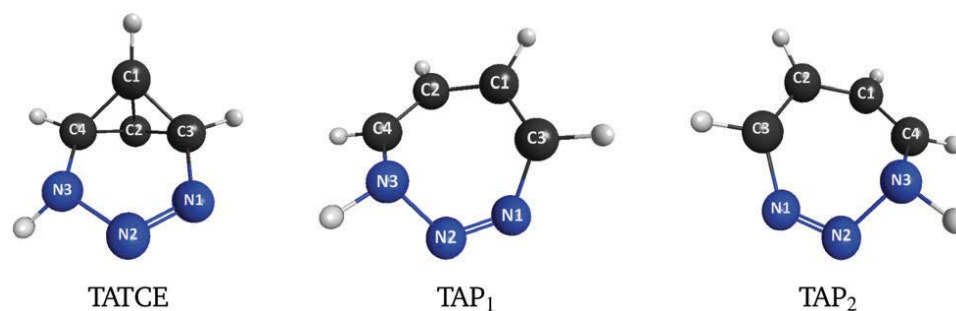
Figure 40. Structures of 3,4,5-triazatricyclo[4.1.0.0^{2,7}]hept-3-ene (TATCE) and isomerization products 1H-1,2,3-triazepine (TAP$_1$ and TAP$_2$).

The first breaking bond can be adjacent to N1 and the N=N π bond or to N3 and the N3 atom lone pair. If the C1-C3 bond breaks first, the transition state is labeled N1disTS1, and if C2-C3 breaks first, it is labeled N1disTS2. If the C1-C4 bond breaks first, the transition state is labeled N3disTS1, and if the C2-C4 bond breaks first, it is labeled N3disTS2. The transition state structures are given in Figure 41, and the activation barriers are given in Table 9. Each barrier is below 50 kcal mol^{-1}, lower than the 57 kcal mol^{-1} for the CdisTS structures for DATCE and DATCA given above. In addition, the two channels for which the π electrons are adjacent to the breaking bond have lower barriers than the two with the N3 lone pair adjacent to the breaking bond. This suggests that the stabilization energy is greater through the π electrons than through the N lone pair consistent with the bonding picture of double bond electrons being more delocalized across two atoms, than a lone pair more confined to a single atom.

91
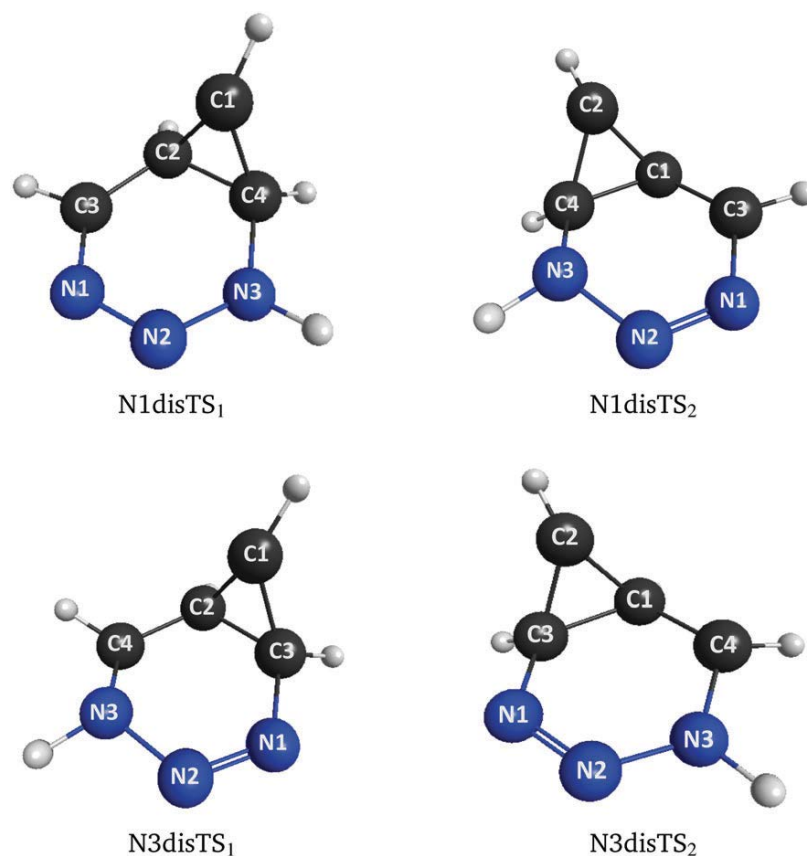
Figure 41. Structures of the disrotatory transition states for the TATCE to TAP$_1$ and TAP$_2$ isomerizations.

Table 9. Activation barriers, E_a, for each pathway (kcal mol^{-1}) including ZPE correction.

Reaction[a]	TS[a]	MCSCF[b]	MRMP2[c]
TATCE $\rightarrow$ TAP$_2$	N1disTS$_1$	50.0.	42.3
TATCE $\rightarrow$ TAP$_1$	N1disTS$_2$	51.2	44.4
TATCE $\rightarrow$ TAP$_1$	N3disTS$_1$	50.7	47.4
TATCE $\rightarrow$ TAP$_2$	N3disTS$_2$	52.2	49.1

[a]All geometries are optimized at the MCSCF(10,10)/cc-pVDZ level. [b]The energies are calculated at the MCSCF/cc-pVDZ level. [c]The energies are calculated at the MRMP2/cc-pVDZ// MCSCF// cc-pVDZ level.

3.5 Conclusion

The thermal isomerizations of 3,4-diazatricyclo[4.1.0.0^{2,7}]hept-3-ene, 3,4 diazatricyclo[4.1.0.0^{2,7}]heptane, and 3,4,5-triazatricyclo[4.1.0.0^{2,7}]hept-3-ene, were modeled using computational chemistry. In order to get a consistent picture of the energies and potential energy surfaces for both the allowed and forbidden pathways, MCSCF calculations were used. CCSD(T) energies were also computed where single reference wavefunctions were adequate for a description of the molecules.

The lowest allowed barrier for the isomerization of DATCE is 36.1 kcal mol^{-1}, lower than the 39.5 kcal mol^{-1} for the all carbon tricyclo[4.1.0.0^{2,7}]heptane. The energy reduction of the barrier is proposed to be due to electron delocalization of the N=N π bond in DATCE in the transition state and steric effects. It is difficult to apportion the individual contribution of each, but compared to structure 2 which had a 6.2 kcal mol^{-1} lower barrier for the first cleaved bond being adjacent to the C=C double bond, the difference for DATCE is only 1.8 kcal mol^{-1}. Likewise, the lowest forbidden barrier for DATCE isomerization is 44.3 kcal mol^{-1}, also with the cleaved bond adjacent to the N=N double bond, stabilized by π electron donation to the half filled orbital left due to the cleaved C-C bond. This barrier is 12.2 kcal mol^{-1} lower than the other forbidden one where the cleaved bond in non-adjacent to the N=N double bond - no π electron donation possible. The transition states for the forbidden pathways have singlet biradical character with NOON's of two orbitals close to 1.2 and 0.8. The stabilization of the forbidden pathways is greater than the allowed pathways due to this singlet biradical character. For the allowed conrotatory pathways, the NOON's for the two resulting orbitals of the cleaved C-C

bond are around 1.75 and 0.25, so they are not as effective in the resonance stabilization with the N=N π bonding orbital.

The DATCA structure does not have a N=N double bond, but does have an N atom lone pair for possible delocalization and stabilization of the transition states. The isomerization of DATCA shows results similar to DATCE mentioned previously: the four allowed barriers range from 37.4 to 43.3 kcal mol^{-1}, but the two lowest values (37.4 and 37.9 kcal mol^{-1}) are for an adjacent and nonadjacent bond cleavage to the N atom lone pair. It appears both steric and delocalization effects are present. The forbidden pathways follow a more consistent pattern with the two lowest barriers belonging to the pathways where the first C-C bond cleaves adjacent to the N atom lone pair. This suggests that delocalization of the N atom lone pair into the half-filled orbital on the adjacent carbon atom lowers the energy of the transition state.

Since delocalization is more easily delineated in the forbidden pathways, we also looked at those for the isomerization of TATCE in which a C-C bond cleaves either adjacent to a N=N double bond or an N atom lone pair. The lowest barriers were for the cleaved bond being adjacent to the N=N double bond consistent with the π electrons being able to delocalize more effectively than a lone pair on a single atom.

One allowed pathway for DATCA formed an intermediate with a structure very close to the transition state. The barrier is only 0.5 kcal mol^{-1} higher than the lowest allowed barrier so would be kinetically competitive. The minimum on the PES was described by bonding between the N atom lone pair orbital and the resulting p-type orbital on the adjacent C atom from the bond cleavage. The minimum has only a 1.7 kcal mol^{-1} barrier leading to the normal *trans* double

bond intermediate of the isomerization pathway. The allowed pathways from DATCE and DATCA form a ring with a *trans* double bond: rotation of this double bond from the trans to *cis* orientation occurs with a barrier between 12.5 and 16.3 kcal mol^{-1}. The release of strain energy caused by the *trans* double bond orientation in the seven-membered ring lowers the barrier of the double bond rotation significantly from that of a non-strained counterpart such as ethylene.

A previous paper compared activation energies of MRMP2 and various DFT functionals for wavefunctions with significant multiconfigurational character[137]. The PBEPBE-D3 functional gave activation barriers close to those of MRMP2 for both the allowed and forbidden pathways. For the DATCE isomerization, the PBEPBE-D3 functional gave energies very close to the MRMP2 results except for the trans double bond rotations which go through transition states with significant singlet biradical character. For the DATCA isomerization, this functional gave good results for allowed pathways and for only two of the four forbidden ones. The activation barriers were close to 14 and 19 kcal mol^{-1} higher than the MRMP2 results for those two forbidden pathways. The trans double bond energies were also about 10 kcal mol^{-1} higher than the MRMP2 results.

CHAPTER IV

THE *AB INITIO* STUDY OF THERMAL ISOMERIZATION OF BENZVALENE TO BENZENE AND BENZVALYNE TO BENZYNE

4.1 Introduction

Benzvalene (tricyclo[3.1.0.0^{2,6}]hex-3-ene) was first reported in 1967 by Wilzbach, etc. as a photoproduct of benzene,[138] and is an energy-rich cyclic compound due to its highly strained structure. The low stability of benzvalene along with extraordinary reactivity exhibits diverse chemistry. The kinetic stability at room temperature[138](half-life of about 10 days in isohexane) also makes benzvalene an interesting structure. The investigation of thermal barriers for conversion of high energy-density benzvalene to the stable benzene isomer could pave the way for exploration of benzene-benzvalene MOST for energy storage and release. The activation energy for isomerization of benzvalene to benzene via a biradical transition state was initially calculated to be 21.5 kcal mol^{-1} by MINDO,[139] showing a barrier 5.2 kcal mol^{-1} lower than the experimental thermolysis in n-heptane.[140] The activation barrier for benzvalene isomerization has also been calculated to be 39.9 kcal mol^{-1} using ab initio methods at the MP3/6-31G*//HF/6-31G* level[141] and 27.7 kcal mol^{-1} using DFT with the B3LYP functional.[142] Other theoretical studies focused on the heat of formation and strain energy of benzvalene at single configuration self-consistent field/6-31G* level[143] and G2(MP2,SVP) level.[144] Previous studies of similar

tricyclco compounds showed multireference calculations were required due to the biradical character of the transition states, especially for disrotatory pathways.[46,126-129,137] However there is no multi-reference self-consistent field (MCSCF) report to revisit the isomerization of benzvalene to benzene, and a multi-reference wave function should be a better description of the biradical nature of transition states.

The pyrolysis of benzene would generate another chemically interesting six-member ring compound benzyne via C-H fission.[145,146] The peculiar chemical structure of benzyne makes it an essential tool in synthetic chemistry.[147] Besides, studies reveal that benzyne plays a vital role in the formation of polycyclic aromatic hydrocarbons(PHAs).[148,149] PHAs produced from combustion of fuels pose considerable damage to human health. Therefore, the benzyne structure has been the subject of extensive theoretical studies. Current calculations focus on the thermochemistry,[150,151] fragmentation pathway[152,153] and isomerization pathway between *o*-benzyne, *p*-benzyne and *m*-benzyne.[152-154] Inspired by the remarkable reactivity of benzvalene, we are curious about the analogous valence isomer of benzyne. To our knowledge, benzvalyne (tricyclo[3.1.0.0^{2,6}]hex-3-yne), the analogous structure of benzvalene, was only mentioned once in the literature and that in the study of triafulvene (bicyclopropenylidene).[155]

Herein, we would like to investigate the isomerization pathways of benzvalene to benzene and benzvalyne to benzyne at the MCSCF calculation level.

4.2 Computational methods

To obtain a highly accurate description of the wave function, geometry optimizations including benzvalyne, benzvalene, benzyne and benzene, were performed at the multi

configuration self-consistent field (MCSCF) level using the cc-pVTZ basis set[132] performed by GAMESS.[130] For benzvalene, four σ and σ* orbitals consisting of the C1-C3, C1-C4, C2-C3, and C2-C4 bonds in the bicyclobutane moiety and one π and π* of the C5=C6 double bond were localized by the Foster-Boys method.[36] The resulting five occupied and five virtual orbitals made the MCSCF (10,10) subset for the complete active space calculation. Two C-C bonds broke in the bicyclobutane moiety, and two C=C double bonds formed during isomerization, so the active space in the product benzene consisted of two C-C σ and σ* orbitals plus three C=C π and π* orbitals. For benzvalyne, four σ and σ* orbitals in the bicyclobutane moiety and the in-plane and out-plane π and π* were localized also by the Foster-Boys method. The resulting six occupied and virtual orbitals made the MCSCF (12,12) subset for complete active space calculation. For benzyne, the full conjugated systems including two σ and σ* orbitals and four π and π* made MCSCF(12,12). Analytical gradients were employed for both geometry optimizations (first derivatives) and harmonic frequency calculations (second derivatives). All transition structures had only one imaginary frequency. Intrinsic reaction coordinates were calculated to verify the connection of the located transition state to the correct reactant and product.[133] Dynamic electron correlation was included by performing single point energy calculations at the single state second order MRMP level at the MCSCF optimized geometries using the cc-pVTZ basis set.[134,135] The resulting energies were used to compare the differences in isomerization barriers and strain energy release.

4.3 Results and discussion

4.3.1 Benzvalene

The thermal isomerization of benzvalene to benzene is discussed in this section. The molecular structures of benzvalene and benzene are shown in Figure 42. The isomerization process involves the rupture of two nonadjacent C-C σ bonds in the bicyclobutane moiety and the formation of a conjugated π cyclo-compound. Benzvalene belongs to point group C_{2v} with the C1-C2 bond bisected by the plane containing the C3, C4, C5 and C6 atoms. The isomerization reaction involved cleavage of a C-C bond pair: this can be C1-C3, C2-C4; C1-C4, C2-C3; C1-C4, C2-C3; C2-C4, C1-C3. Any four of these possibilities will lead to the same transition state due to the C_{2v} symmetry of benzvalene. Therefore, there is only one disrotatory and one conrotatory pathway given the Woodward-Hoffman symmetry rules. The transition states for the disrotatory and conrotatory pathways are labeled as disTS and conTS respectively. The schematic energy diagram for the isomerization pathways are presented in Figure 43.

Benzvalene   Benzene
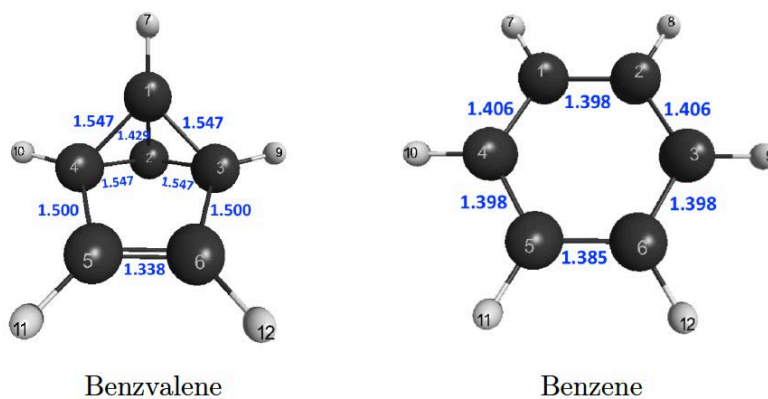
Figure 42. Structures of benzvalene and and isomerization product benzene.
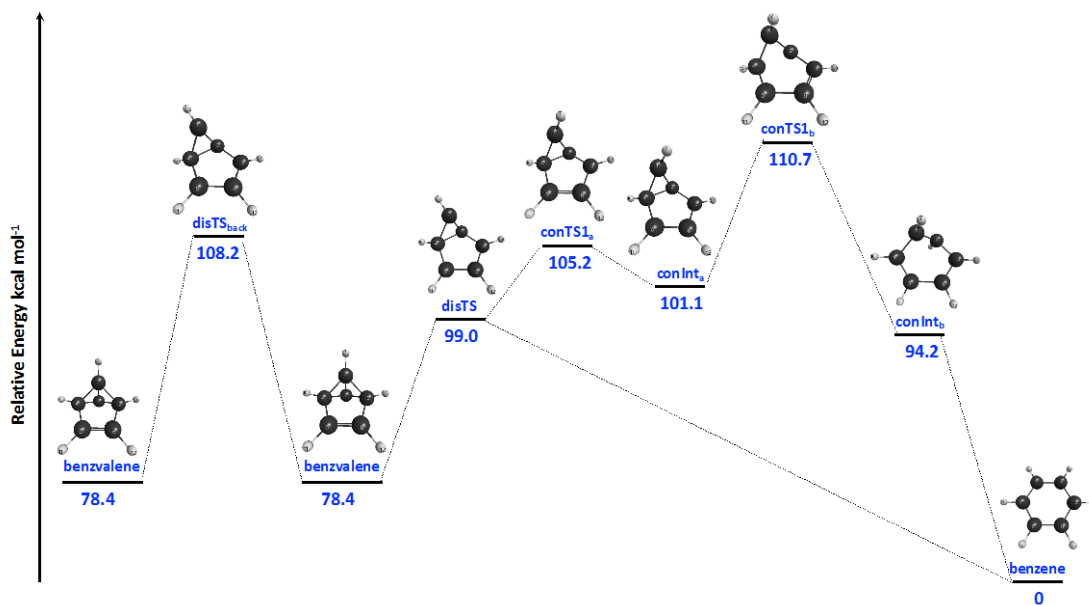
Figure 43. Schematic diagram for the isomerization of benzvalene to benzene and benzvalene.

4.3.1.1 Disrotatory pathways

Features of the disrotatory transition state are presented in Figure 44. The activation barrier of disTS has been determined to 20.6 kcal mol^{-1} at the MRMP2 level, shown in Table 10. For comparison with the experimental value, the activation barrier was corrected to 18.7 kcal mol^{-1} at 298K using unscaled harmonic vibrational frequencies. It is 8.0 kcal mol^{-1} lower than the experimental barrier obtained in n-heptane. In comparison, the barrier height at 298K was previously reported to be 39.9 kcal mol^{-1} at the MP3/6-31G*//HF/6-31G* level[141] and 29.3 kcal mol^{-1} at the B3LYP level;[142] they are instead higher than the experimental barrier. In contrast to similar tricyclo compounds, [46,126-129,137] the transition state for the disrotatory pathway is mostly single configurational in character as witnessed by the natural orbital occupation numbers (NOON's) in the active space. For disTS, orbital 21 (p orbital on C1 and C3) and orbital 22 (p

orbital on C1 and C3) have NOON values of 1.711 and 0.295. This uncustomary non biradical

transition state was also found by Bettinger etc. at the B3LYP, CCSD and CCSD(T) levels.[142]

The initial breaking bond, C1-C3, has a length of 2.353 Å in the transition state, while the second

breaking bond length is 1.668 Å. The 0.685 Å difference in the two bond lengths is an indicator

of a less asynchronous progress. The double bond between C5 and C6 in reactant benzvalene

tends to transfer to adjacent C3 and C6 in disTS. The C3-C6 bond length shortens from 1.500 Å

in benzvalene to 1.366 Å in disTS, while the C5-C6 bond lengthens from 1.338 Å in benzvalene

to 1.409 Å in disTS. This suggests the C5=C6 double bond is not inert as it participates in

breaking the bicyclobutane moiety. The C4-C5 bond length also shrinks to 1.423 Å in disTS.

(The p orbital should on C3, but now on C5).
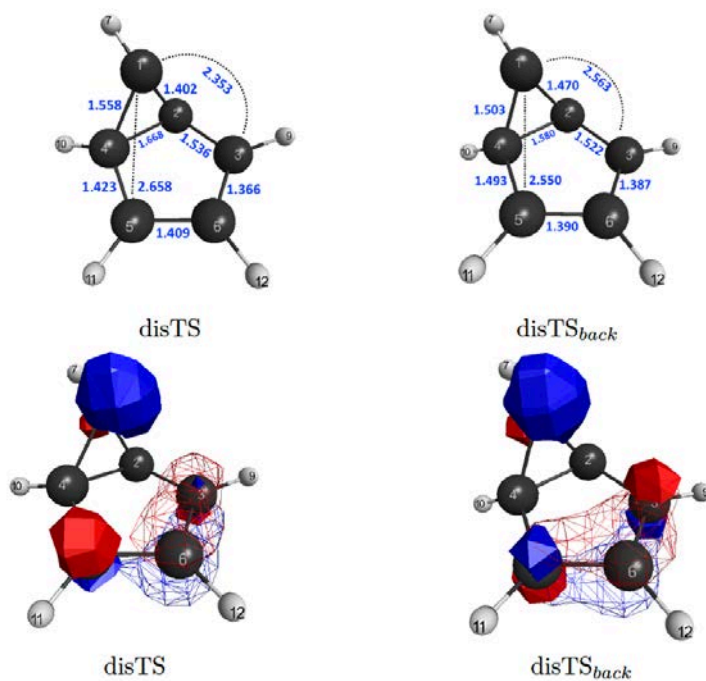
Figure 44. Transition state structures disTS and disTSback for the two disrotatory pathways.

101

Table 10. Activation barriers, E_a, for each pathway (kcal mol^{-1}) Including ZPE correction.

Reaction[a]	TS[a]	MCSCF[b]	MRMP2[c]
benzvalene $\rightarrow$ benzene	disTS	25.8	20.6
benzvalene $\rightarrow$ benzvalene	disTS$_{back}$	30.0	29.8
benzvalene $\rightarrow$ conInt$_a$	conTS1$_a$	29.1	26.8
conInt$_a$ $\rightarrow$ conInt$_b$	conTS1$_a$	9.6	3.6
conInt$_b$ $\rightarrow$ benzene	conTS2	2.7	4.7

[a] All geometries are optimized at the MCSCF(10,10)/cc-pVTZ level. [b] The energies are calculated at the MCSCF/cc-pVTZ level. [c] The energies are calculated at the MRMP2/cc-pVTZ//MCSCF/cc-pVTZ level.

Remarkably, the transition state disTS$_{back}$ with singlet biradical nature was found for a concerted disrotatory pathway. For disTS$_{back}$, orbital 21 (p orbital on C1 and C3) and orbital 22 (p orbital on C1 and C3) have NOON values of 1.039 and 0.962. However, the intrinsic reaction coordinate from disTS$_{back}$ leads to benzvalene in both the forward and reverse directions. The isomerization occurs by breaking C1-C3 bond in reactant benzvalene and forming C1-C5 bond in product benzvalene. This is apparently a biradical transition state in which one C-C bond cleaves and reforms to restore the benzvalene reactant. The two disrotatory pathways of benzvalene are presented in Figure 45. The barrier height of disTS$_{back}$ is 29.8 kcal mol^{-1} at MRMP2 level, shown in Table 10. The activation energy of disTS$_{back}$ is 8.8 kcal mol^{-1} higher than that of disTS consistent with the isomerization of benzvalene to benzene being more kinetically favorable than back to benzvalene. The ruptured bond C1-C3 has length of 2.563 Å in disTS$_{back}$, longer than that of 2.353 Å in disTS. The distance between C1 and C5 is 2.550 Å, close to C1-C3 bond length so that the disTS$_{back}$ transition state would lead to benzvalene by connecting C1 and C5 to close the bicyclobutane moiety. The bond length of C5-C6 and C3-C6 are almost equal to 1.390 Å suggests π electron delocalization through atoms C5, C6 and C3,

also visualized by orbital 21 from the MCSCF natural orbitals for disTS$_{back}$, shown in Figure 44.

disTS

disTS$_{back}$
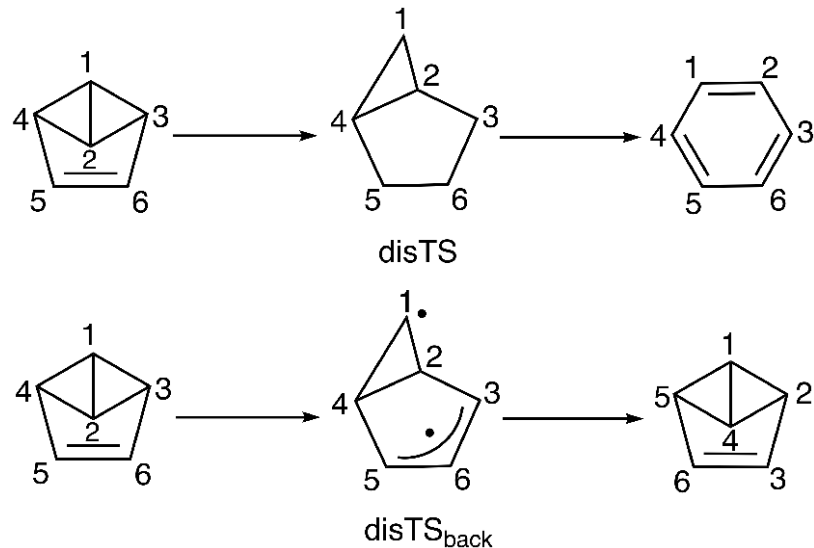
Figure 45. Reactions for the isomerization of benzvalene to benzene and benzvalene.

4.3.1.2 Conrotatory pathways

The structures of the conrotatory transition states and intermediates are presented in Figure 46. The activation barrier of conTS1$_a$ is 26.8 kcal mol^{-1}, 6.2 kcal mol^{-1} higher than that of the disrotatory pathway (Table 10). Remarkably, an additional intermediate conInt$_a$ and transition state conTS1$_a$ were located which leads to the transition state conTS2 which rotates the trans double bond to the cis configuration. The geometry of the intermediate conInt$_a$ has been optimization at the MCSCF/cc-pVTZ level, and confirmed a minimum by having all real harmonic frequencies. This is consistent with one of pathways of isomerization of 3,4-diazatricyclo[4.1.0.0^{2,7}]heptane.[46] conInt$_a$ is just 4.1 kcal mol^{-1} lower than conTS1$_a$ at the MRMP2 level, listed in Table 11. For conTS1$_a$, the first breaking bond C1-C3 has a length of 2.265 Å, while the secondary breaking bond C2-C4 has a length of 1.565 Å, close to 1.547 Å in

the reactant benzvalene. The extra intermediate conInt$_a$ only lengthened the C1-C3 bond to 2.458

Å and maintained the C2-C4 bond as 1.566 Å. Additionally, compared to conTS1$_a$, the C5-C6

bond of conInt$_a$ is lengthened to 1.378 Å and the C3-C6 bond is shortened to 1.414 Å. The nearly

equal bond lengths between C5-C6 and C3-C6 suggests the π bond delocalization runs across

C5-C6-C3, as illustrated in orbital 21 from the MCSCF natural orbitals for conInt$_a$ in Figure 46.

The singlet biradical character of conInt$_a$ is witnessed by NOON values of 1.248 and 0.753 for

the σ and σ^* orbital across C1-C3. Along with the reaction progress, the conTS1$_b$ lengthens the

secondary breaking bond C2-C4 to 1.846 Å. The C5-C6 and C3-C6 bonds of conTS1$_b$ changed

to 1.472 Å and 1.350 Å, respectively. This shortening of C3-C6 implies the double bond transfer

from C5-C6 in conTS1$_a$ to C3-C6 in conTS1$_b$. This is proof that the double bond in C5-C6

participated in the isomerization of benzvalene to benzene, not serving as just a spectator.
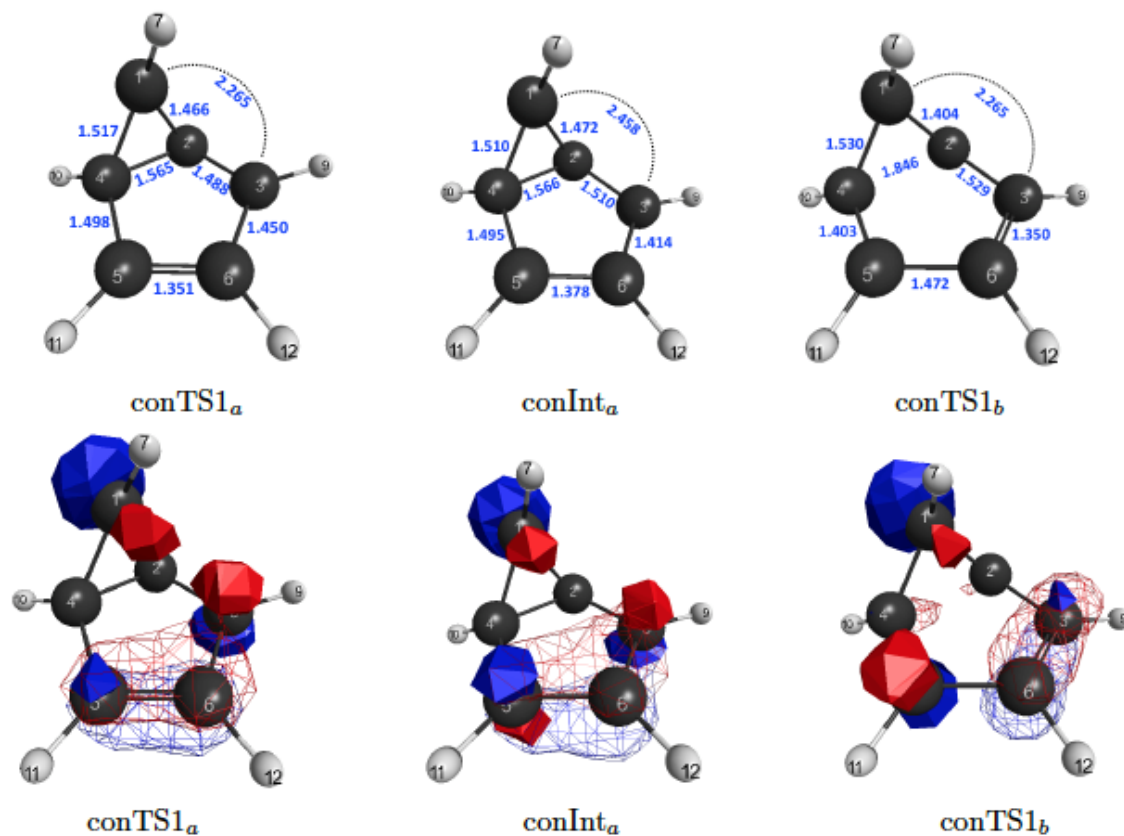
Figure 46. Structures for transition state conTS1a, conTS1b, and intermediate conInta for the conrotatory pathway.

Table 11. Relative energies including ZPE correction.

Structure[a]	MCSCF[b]	MRMP2[c]
benzvalene	86.9	78.4
conTS1a	116.0	105.2
conInta	115.8	101.1
conTS1b	125.4	110.7
conIntb	99.3	94.2
benzene	0	0

[a] All geometries were optimized at the MCSCF(10,10)/cc-pVTZ level. [b] The geometries and energies are calculated at the MCSCF/cc-pVTZ level. [c] The energies are calculated at the MRMP2/cc-pVTZ/MCSCF/cc-pVTZ level.

4.3.2 Benzvalyne

The geometries of benzvalyne and benzyne are shown in Figure 47. For the isomerization of benzvalyne to benzyne, there are also a single disrotatory and single conrotatory pathway given the point group of C_{2v} for both benzvalyne and benzvalene. The saddle points and intermediates associated with the isomerization of benzvalyne to benzyne were denoted with a prime symbol to distinguish them from the structures associated with the isomerization of benzvalene to benzene. A schematic diagram for the reaction pathways is shown in Figure 48.
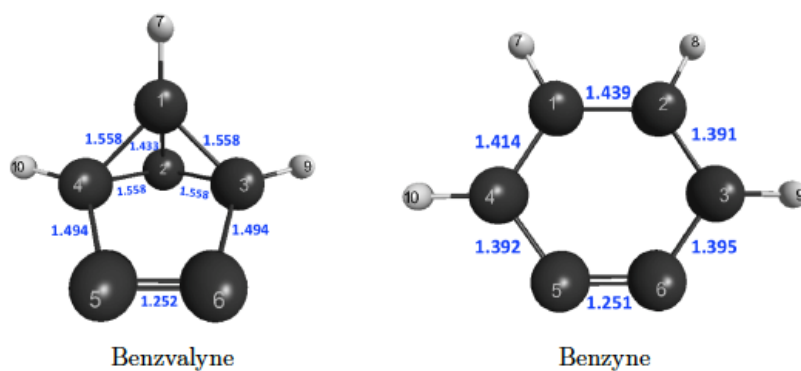
Figure 47. Structures of benzvalyne and isomerization product benzyne.

106
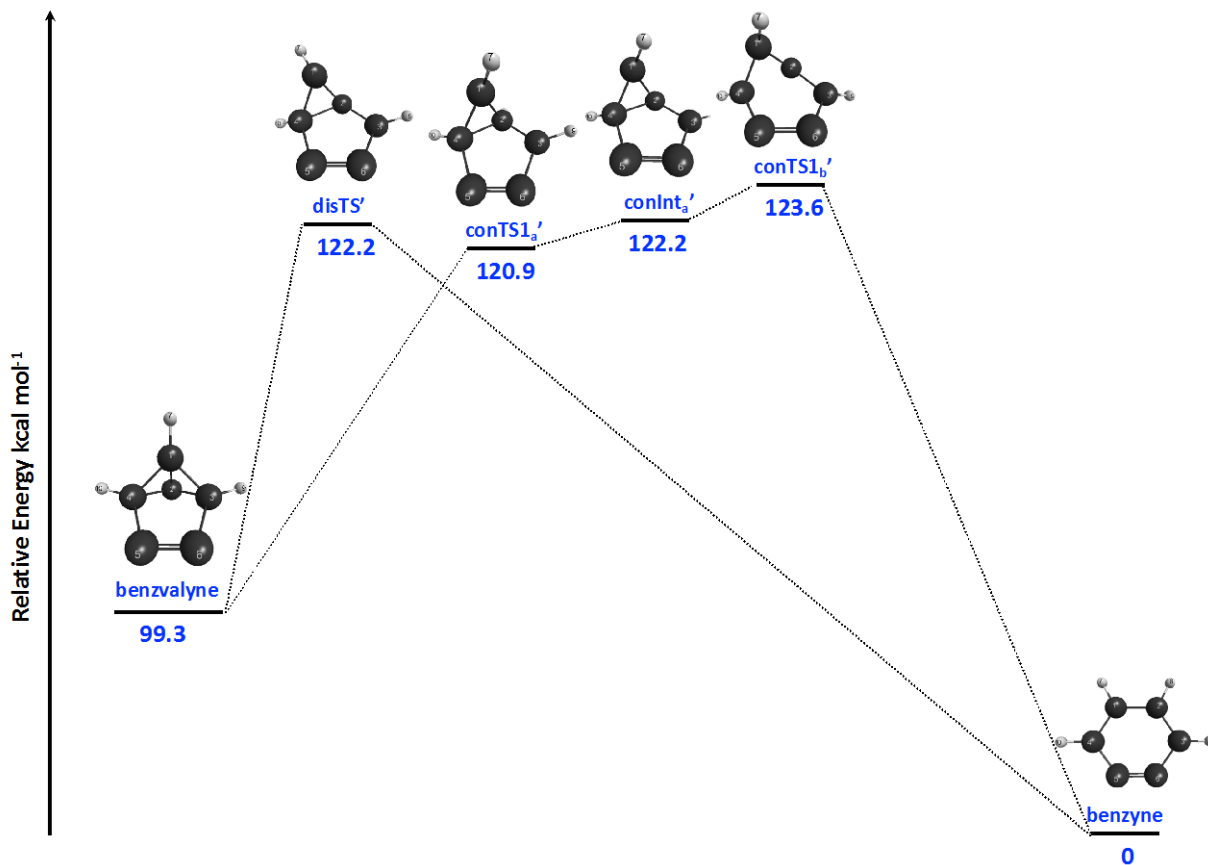
Figure 48. Schematic diagram for the isomerization of benzvalyne to benzyne.

4.3.2.1 Disrotatory pathways

The structure of the transition state with key geometric feature in the disrotatory pathway is presented in Figure 49. The activation barrier of disTS′ has been determined to be 22.9 kcal mol^{-1} at the MRMP2 level, listed in Table 12. The barrier height for benzvalyne is close to the 20.6 kcal mol^{-1} for benzvalene. This is consistent with the second π bond in the triple bond in benzvalyne being orthogonal to the p orbitals on C1 and C3, resulting in the cleavage of the C1-C3 sigma bond, and not in a favorable overlap for delocalization. The transition state disTS′

107

exhibits singlet biradical nature with 1.236 Å and 0.767 Å NOON values in orbitals 20 and 21.

This is obviously different from the transition state disTS with non biradical nature. The bond

lengths of the breaking bond pair C1-C3 and C2-C4 are 2.506Å and 1.628 Å in disTS′ compared

to 2.353 Å and 1.668 Å in disTS, shown in Figure 44. This suggests the isomerization of

benzvalyne via disTS′ is a slightly more asynchronous process. The bond length of C5-C6 is

1.252 Å in reactant benzvalyne and lengthens to 1.274 Å in disTS′, while the C3-C6 bond

shortens from 1.494 Å in benzvalyne to 1.408 Å in disTS′. This is consistent with electron

delocalization from the in-plane π bonding orbital into the half empty orbital on C3. The p-type

orbital on C3 and delocalized in-plane π orbital across C5-C6-C3 are presented in Figure 49.
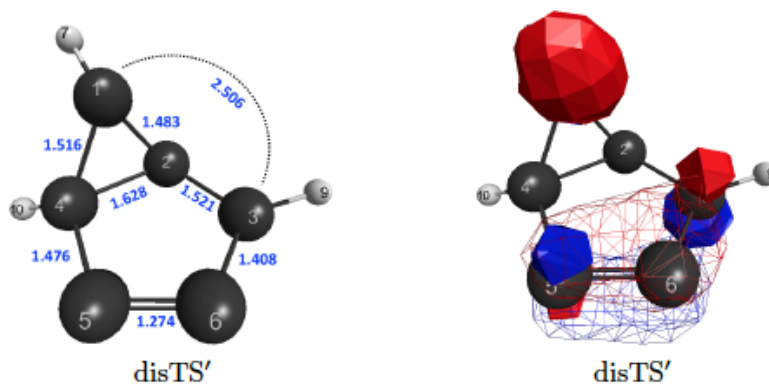
Figure 49. Transition state structure disTS′ for the disrotatory pathway.

Table 12. Activation barriers, E_a, for each pathway (kcal mol^{-1}) Including ZPE correction.

Reaction[a]	TS[a]	MCSCF[b]	MRMP2[c]
benzvalyne → benzyne	disTS′	26.3	22.9
benzvalyne → conInt$_a$′	conTS1$_a$′	25.8	21.7
conInt$_a$′→ benzyne	conTS1$_b$′	9.6	1.4

[a] All geometries are optimized at the MCSCF(12,12)/cc-pVTZ level. [b] The energies are calculated at the MCSCF/cc-pVTZ level. [c] The energies are calculated at the MRMP2/cc-pVTZ//MCSCF/cc-pVTZ level.

4.3.2.2 Conrotatory pathways

The structures of the transition states and intermediates for the conrotatory pathway are presented in Figure 50. The activation barrier of conTS1$_a$′ is calculated to be 21.7 kcal mol^{-1}, only 1.2 kcal mol^{-1} lower than that of disrotatory pathway at MRMP2 level, listed in Table 12. This means the conrotatory and disrotatory pathways have nearly equally kinetic favorability. In the progress of the isomerization, the conrotatory pathway leads to intermediate conInt$_a$′. The minimum nature of conInt$_a$′ has been verified by geometry optimization and all real harmonic frequencies. conInt$_a$′ has a relative energy of 122.2 kcal mol^{-1} compared to the benzyne reactant, 1.3 kcal mol^{-1} higher than that of conTS1$_a$′ at the MRMP2 level, listed in Table 13. The conTS1$_a$′ and conInt$_a$′ exhibit similar structural behavior in the reaction. The first breaking bond C1-C3 lengthens to 2.191 Å in conTS1$_a$′ and 2.431 Å in conInt$_a$′ compared to 1.558Å in reactant benzvalyne. While the second breaking bond C2-C4 is 1.595 Å in conTS1$_a$′ and almost intact in conInt$_a$′ with bond length of 1.602 Å. The slight lengthening of C5-C6 and shortening of C3-C6 in conInt$_a$′ compared to conTS1$_a$′ suggests in-plane π bond delocalization between C5-C6-C3. It is also implied by the singlet biradical nature of intermediate conInt$_a$′ with 1.477 and 0.524 NOON values in orbitals 20 and 21. The activation barrier for conTS1$_b$′ is only 1.4 kcal mol^{-1} at the MRMP2 level, listed in Table 12. The breaking bond pair C1-C3 and C2-C4 lengthen to 2.544 Å and 1.904 Å in conTS1$_b$′, respectively. The neighboring C5-C6 and C3-C6 bonds have lengths of 1.317 Å and 1.370 Å in conTS1$_b$′ respectively. The closer equality of bond lengths between C5-C6 and C3-C6 implies in-plane π bond delocalization across C5-C6-C3. It is consistent with the singlet biradical nature of transition state conTS1$_b$′, witnessed by the NOON

109

values of 1.426 and 0.584 in orbital 20 and 21. Interestingly, the intrinsic reaction coordinates show conTS1b′ directly connects the intermediate conInta′ and product benzyne without an intermediate bearing a trans double bond. It is inconsistent with the conrotatory pathway of benzvalene isomerization and previous studies of similar tricylco-compounds isomerization.[46,126-129,137] This means the 122.2 kcal mol^{-1} relative energy in conInta′ could be directly released by only a 1.4 kcal mol^{-1} barrier height.
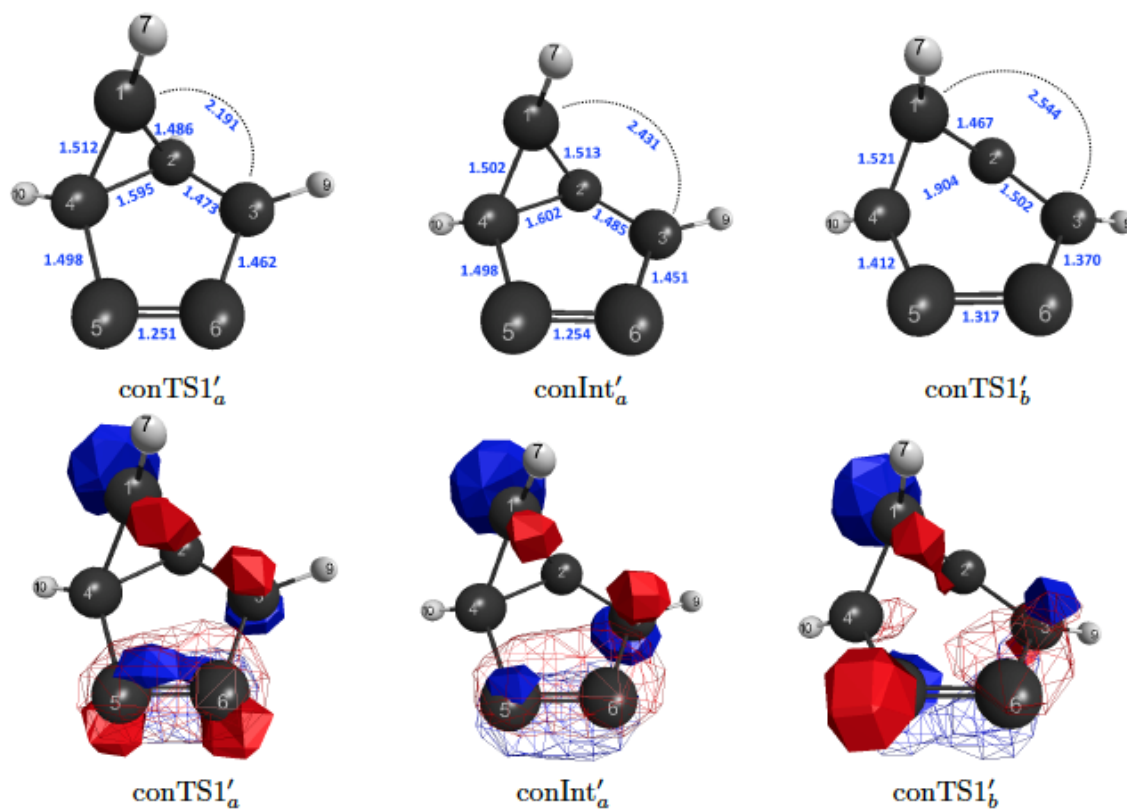
Figure 50. Structures for transition state conTS1a′ , conTS1b′ and intermediate conInta′ for the conrotatory pathway.

Table 13. Relative energies including ZPE correction.

Structure[a]	MCSCF[b]	MRMP2[c]
benzvalyne	106.1	99.3
conTS1$_a'$	131.9	120.9
conInt$_a'$	131.3	122.2
conTS1$_b'$	140.9	123.6
benzyne	0	0

[a] All geometries were optimized at the MCSCF(12,12)/cc-pVTZ level. [b] The geometries and energies are calculated at the MCSCF/cc-pVTZ level. [c] The energies are calculated at the MRMP2/cc-pVTZ/MCSCF/cc-pVTZ level.

4.4 Conclusion

Both conrotatory and disrotatory pathways for the thermal isomerization of benzvalene and benzvalyne were calculated at the MCSCF/cc-pVTZ level. The lowest allowed activation barrier for the benzvalene isomerization was determined to 25.8 kcal mol^{-1} through transition state disTS with uncustomary singlet configuration character. The transition state disTS$_{back}$ with singlet biradical nature isomerizes back to the benzvalene reactant via a disrotatory pathway. The activation barrier height for disTS$_{back}$ is 8.8 kcal mol^{-1} higher than that of disTS. It shows the isomerization of benzvalene to benzene is more kinetically favorable than back to benzvalene. For the conrotatory pathway, the activation barrier of conTS1$_a$ is 26.8 kcal mol^{-1}. The extra intermediate conInt$_a$ and transition state conTS1$_a$ were located on the IRC before the normal transition state conTS2 bearing the *trans* double bond in the progress of isomerization. During both disrotatory and conrotatory pathways, the double bond between C5-C6 participated in the isomerization of benzvalene to benzene, not serving as a spectator, as witnessed by the double bond transferring from C5-C6 to C3-C6.

For the benzvalyne isomerization, the activation barrier of disTS$'$ has been determined to be 22.9 kcal mol^{-1}, 2.3 kcal mol^{-1} lower than that of benzvalene. The second π bond in the triple

111

bond contained in benzvalyne is orthogonal to the p orbitals in atom C1 and C3 and is not in a favorable geometry for delocalization. The activation barrier of conTS1$_a'$ is 21.7 kcal mol^{-1}, 1.2 kcal mol^{-1} lower compared to the disrotatory pathway. The intrinsic reaction coordinates demonstrate that conTS1$_b'$ leads to the product without an intermediate bearing a *trans* double bond. This means the 122.2 kcal mol^{-1} stored energy in conInt$_a'$ can be released by only a 1.4 kcal mol^{-1} barrier.

CONCLUSION

Dinuclear rhenium catalysts, including *cis* and *trans* conformers have been synthesized, isolated and characterized. Both Re_2 complexes were efficient electrocatalyst for CO_2 reduction to CO. Catalytic rates were measured by cyclic voltammetry for *cis*-Re_2Cl_2, *trans*-Re_2Cl_2, $Re(bpy)(CO)_3Cl$, and anthryl-Re with estimated TOFs of 35.3, 22.9, 11.1, and 19.2 s^{-1}, respectively. The mechanistic studies proved the *cis*-Re_2Cl_2 went through bimetallic CO_2 activation and conversion. The outstanding performance than *trans*-Re_2Cl_2 is due to the limitation of intermolecular deactivation by cofacial arrangement of active sites and the prevention of intramolecular Re-Re bond formation by the rigid anthracene backbone.

The photocatalytic results showed the Re_2 catalysts perform significantly better ($\sim$ 4X higher TON) than $Re(bpy)(CO)_3Cl$ when the relative concentration in rhenium is held constant (0.1 mM dinuclear *vs* 0.2 mM mononuclear). The mechanism study suggests a photosensitizer-based pathway is existed in both Re_2 catalysts due to their comparable reactivity despite their structure. The excited-state kinetics and emission spectra reveal that the anthracene backbone plays a more significant role beyond a simple structural unit.

The lowest allowed barrier for the isomerization of DATCE is 36.1 kcal mol^{-1}, the 12.2 kcal mol^{-1} disparity in the disrotatory barriers is due to electron delocalization of the N=N π bond in DATCE in the transition state and steric effects. The isomerization of DATCA shows the

energy disparity in the forbidden pathways is explained by the delocalization of the N atom lone pair into the half-filled orbital on the adjacent carbon atom. The isomerization of TATCE was used to identify π bond electrons showed greater contribution for molecular stabilization than lone pair electrons.

The isomerization of benzvalene to benzene has barriers of 25.8 kcal mol^{-1} in disrotatory channel and 26.8 kcal mol^{-1} in conrotatory channel. The intrinsic reaction coordinate shows double bond in C5-C6 participated in the progress of isomerization, not server as a spectator. The benzvalyne has barrier of 22.9 kcal mol^{-1} in disrotatory channel. The slight 2.3 kcal mol^{-1} lower than that of benzvalene due to the second π bond in triple bond in benzvalyne is orthogonal to p orbitals in atom C1 and C3 and is not in favorable geometry to delocalization. The absence of normally intermediate with *trans* double bond suggests the up to 122.2 kcal mol^{-1} energy storing in conInt$_a$′ would be released only by 1.4 kcal mol^{-1} barrier.

BIBLIOGRAPHY

(1)   Ashford, D. L.; Gish, M. K.; Vannucci, A. K.; Brennaman, M. K.; Templeton, J. L.;
        Papanikolas, J. M.; Meyer, T. J. Molecular Chromophore-Catalyst Assemblies for Solar
        Fuel Applications. *Chem. Rev.* **2015**, *115* (23), 13006–13049.

(2)   Feely, R. a; Sabine, C. L.; Lee, K.; Berelson, W.; Kleypas, J.; Fabry, V. J.; Millero, F. J.
        Impact of Anthropogenic CO_2 on the $CaCO_3$ System in the Oceans. *Science (80-.).* **2004**,
        305 (5682), 362–366.

(3)   Houghton, J. Global Warming. *Reports Prog. Phys.* **2005**, *68* (6), 1343–1403.

(4)   Concepcion, J. J.; House, R. L.; Papanikolas, J. M.; Meyer, T. J. Chemical Approaches to
        Artificial Photosynthesis. *Proc. Natl. Acad. Sci. U. S. A.* **2012**, *109* (39), 16660–15564.

(5)   Benson, E. E.; Kubiak, C. P.; Sathrum, A. J.; Smieja, J. M. Electrocatalytic and
        Homogeneous Approaches to Conversion of CO_2 to Liquid Fuels. *Chem. Soc. Rev.* **2009**,
        38 (1), 89–99.

(6)   Yui, T.; Tamaki, Y.; Sekizawa, K.; Ishitani, O. Photocatalytic Reduction of CO_2: From
        Molecules to Semiconductors. *Top. Curr. Chem.* **2011**; 303, 151–184.

(7)   Finn, C.; Schnittger, S.; Yellowlees, L. J.; Love, J. B. Molecular Approaches to the
        Electrochemical Reduction of Carbon Dioxide. *Chem. Commun.* **2012**, *48* (10), 1392–
        1399.

(8)   Appel, A. M.; Bercaw, J. E.; Bocarsly, A. B.; Dobbek, H.; Dubois, D. L.; Dupuis, M.;
Ferry, J. G.; Fujita, E.; Hille, R.; Kenis, P. J. A.; et al. Frontiers, Opportunities, and Challenges in

Biochemical and Chemical Catalysis of CO_2 Fixation. *Chem. Rev*. **2013**, 6621–6658.

(9)   Kang, P.; Chen, Z.; Brookhart, M.; Meyer, T. J. Electrocatalytic Reduction of Carbon

Dioxide: Let the Molecules Do the Work. *Top. Catal*. **2015**, 30–45.

(10)   Takeda, H.; Cometto, C.; Ishitani, O.; Robert, M. Electrons, Photons, Protons and Earth-

Abundant Metal Complexes for Molecular Catalysis of CO_2 Reduction. *ACS Catal.* **2017**,

7 (1), 70–88.

(11)   Francke, R.; Schille, B.; Roemelt, M. Homogeneously Catalyzed Electroreduction of

Carbon Dioxide - Methods, Mechanisms, and Catalysts. *Chem. Reviw*. **2018**, 4631–4701.

(12)   Finn, C.; Schnittger, S.; Yellowlees, L. J.; Love, J. B. Molecular Approaches to the

Electrochemical Reduction of Carbon Dioxide. *Chem. Commun*. **2012**, 1392–1399.

(13)   Hawecker, J.; Lehn, J.-M.; Ziessel, R. Efficient Photochemical Reduction of CO_2 to CO

by Visible Light Irradiation of Systems Containing $Re(Bipy)(CO)_3X$ or $Ru(Bipy)_3^{2+}$ –

Co^{2+} Combinations as Homogeneous Catalysts. *J. Chem. Soc. Chem. Commun.* **1983**, 9,

536–538.

(14)   Hawecker, J.; Lehn, J.-M.; Ziessel, R. Electrocatalytic Reduction of Carbon Dioxide

Mediated by $Re(Bipy)(CO)_3Cl$ (Bipy = 2,2'-Bipyridine). *J. Chem. Soc. Chem. Commun.*

1984, 328–330.

(15)   Hawecker, J.; Lehn, J.; Ziessel, R. Photochemical and Electrochemical Reduction of

Carbon Dioxide to Carbon Monoxide Mediated by (2, 2′-Bipyridine)

Tricarbonylchlororhenium (I) and Related Complexes as Homogeneous Catalysts'). *Helv.*

Chim. Acta. **1986**, *69*, 1990–2012.

(16)   Johnson, F. P. A.; George, M. W.; Hartl, F.; Turner, J. J. Electrocatalytic Reduction of

CO_2 Using the Complexes [Re(Bpy)$(CO)_3$L]n (n = +1, L = P$(OEt)_3$, CH_3CN; n = 0, L =

Cl^-, Otf^-; Bpy = 2,2'-Bipyridine; Otf^- = CF_3SO_3. *Organometallics* **1996**, *15* (15), 3374–

3387.

(17)   Breikss, A. I.; Abruna, H. D. Electrochemical and Mechanistic Studies of

[Re$(CO)_3$(Dmbpy)Cl] and Their Relation to the Catalytic Reduction of CO_2. *J.*

Electroanal. Chem. interfacial Electrochem. **1986**, *201* (2), 347–358.

(18)   Kurz, P.; Probst, B.; Spingler, B.; Alberto, R. Ligand Variations in [ReX(Diimine)$(CO)_3$]

Complexes: Effects on Photocatalytic CO_2 Reduction. *Eur. J. Inorg. Chem.* **2006**, 15,

2966–2974.

(19)   Smieja, J. M.; Kubiak, C. P. Re(Bipy-TBu)$(CO)_3$Cl-Improved Catalytic Activity for

Reduction of Carbon Dioxide: IR-Spectroelectrochemical and Mechanistic Studies. *Inorg.*

Chem. **2010**, *49* (20), 9283–9289.

(20)   Machan, C. W.; Chabolla, S. A.; Kubiak, C. P. Reductive Disproportionation of Carbon

Dioxide by an Alkyl-Functionalized Pyridine Monoimine Re(I) Fac-Tricarbonyl

Electrocatalyst. *Organometallics* **2015**, *34* (19), 4678–4683.

(21)   Stanton, C. J.; Machan, C. W.; Vandezande, J. E.; Jin, T.; Majetich, G. F.; Schaefer, H. F.;

Kubiak, C. P.; Li, G.; Agarwal, J. Re(I) NHC Complexes for Electrocatalytic Conversion

of CO_2. *Inorg. Chem.* **2016**, *55* (6), 3136–3144.

(22)   Huckaba, A. J.; Sharpe, E. A.; Delcamp, J. H. Photocatalytic Reduction of CO_2 with Re-

Pyridyl-NHCs. *Inorg. Chem.* **2016**, *55* (2), 682–690.

(23)   Liyanage, N. P.; Dulaney, H. A.; Huckaba, A. J.; Jurss, J. W.; Delcamp, J. H. Electrocatalytic Reduction of CO_2 to CO with Re-Pyridyl-NHCs: Proton Source Influence on Rates and Product Selectivities. *Inorg. Chem.* **2016**, *55* (12), 6085–6094.

(24)   Ching, H. Y. V.; Wang, X.; He, M.; Perujo Holland, N.; Guillot, R.; Slim, C.; Griveau, S.; Bertrand, H. C.; Policar, C.; Bedioui, F.; et al. Rhenium Complexes Based on 2-Pyridyl-1,2,3-Triazole Ligands: A New Class of CO_2 Reduction Catalysts. *Inorg. Chem.* **2017**, *56* (5), 2966–2976.

(25)   Sung, S.; Kumar, D.; Gil-Sepulcre, M.; Nippe, M. Electrocatalytic CO_2 Reduction by Imidazolium-Functionalized Molecular Catalysts. *J. Am. Chem. Soc.* **2017**, *139* (40), 13993–13996.

(26)   Nganga, J. K.; Samanamu, C. R.; Tanski, J. M.; Pacheco, C.; Saucedo, C.; Batista, V. S.; Grice, K. A.; Ertem, M. Z.; Angeles-Boza, A. M. Electrochemical Reduction of CO_2 Catalyzed by Re(Pyridine-Oxazoline)(CO)$_3$Cl Complexes. *Inorg. Chem.* **2017**, *56* (6), 3214–3226.

(27)   Nakada, A.; Ishitani, O. Selective Electrocatalysis of a Water-Soluble Rhenium(I) Complex for CO_2 Reduction Using Water As an Electron Donor. *ACS Catal.* **2018**, *8* (1), 354–363.

(28)   Ha, E. G.; Chang, J. A.; Byun, S. M.; Pac, C.; Jang, D. M.; Park, J.; Kang, S. O. High-Turnover Visible-Light Photoreduction of CO_2 by a Re(i) Complex Stabilized on Dye-Sensitized TiO_2. *Chem. Commun.* **2014**, *50* (34), 4462–4464.

(29) Won, D. Il; Lee, J. S.; Ji, J. M.; Jung, W. J.; Son, H. J.; Pac, C.; Kang, S. O. Highly Robust Hybrid Photocatalyst for Carbon Dioxide Reduction: Tuning and Optimization of Catalytic Activities of Dye/TiO$_2$/Re(I) Organic-Inorganic Ternary Systems. *J. Am. Chem. Soc.* **2015**, *137* (42), 13679–13690.

(30) Windle, C. D.; Pastor, E.; Reynal, A.; Witwood, A. C.; Vaynzof, Y.; Durrant, J. R.; Perutz, R. N.; Reisner, E. Improving the Photocatalytic Reduction of CO$_2$ to CO through Immobilisation of a Molecular Re Catalyst on TiO$_2$. *Chem. - A Eur. Journals.* **2015**, *21*, 3746–3754.

(31) Sahara, G.; Abe, R.; Higashi, M.; Morikawa, T.; Maeda, K.; Ueda, Y.; Ishitani, O. Photoelectrochemical CO$_2$ Reduction Using a Ru(Ii)-Re(i) Multinuclear Metal Complex on a p-Type Semiconducting NiO Electrode. *Chem. Commun.* **2015**, *51* (53), 10722–10725.

(32) Sahara, G.; Kumagai, H.; Maeda, K.; Kaeffer, N.; Artero, V.; Higashi, M.; Abe, R.; Ishitani, O. Photoelectrochemical Reduction of CO$_2$ Coupled to Water Oxidation Using a Photocathode with a Ru(II)-Re(I) Complex Photocatalyst and a CoOx/TaON Photoanode. *J. Am. Chem. Soc.* **2016**, *138* (42), 14152–14158.

(33) Schreier, M.; Luo, J.; Gao, P.; Moehl, T.; Mayer, M. T.; Grätzel, M. Covalent Immobilization of a Molecular Catalyst on Cu$_2$O Photocathodes for CO$_2$ Reduction. *J. Am. Chem. Soc.* **2016**, *138* (6), 1938–1946.

(34) Kucharski, T. J.; Tian, Y.; Akbulatov, S.; Boulatov, R. Chemical Solutions for the Closed-Cycle Storage of Solar Energy. *Energy Environ. Sci.* **2011**, *4* (11), 4449.

(35) Kuisma, M. J.; Lundin, A. M.; Moth-Poulsen, K.; Hyldgaard, P.; Erhart, P. Comparative Ab-Initio Study of Substituted Norbornadiene-Quadricyclane Compounds for Solar Thermal Storage. *J. Phys. Chem. C* **2016**, *120* (7), 3635–3645.

(36) Blanchard, E. P.; Cairncross, A. Bicyclo[1.1.0]Butane Chemistry. I. The Synthesis and Reactions of 3-Methylbicyclo[1.1.0]Butanecarbonitriles. *J. Am. Chem. Soc.* **1966**, *88* (3), 487–495.

(37) Cairncross, A.; Blanchard, E. P. Bicyclo[1.1.0]Butane Chemistry. II. Cycloaddition Reactions of 3-Methylbicyclo[1.1.0]Butanecarbonitriles. The Formation of Bicyclo[2.1.1]Hexanes. *J. Am. Chem. Soc.* **1966**, *88* (3), 496–504.

(38) Dewar, M. J. S.; Kirschner, S. MINDO/3 Study of Thermolysis of Bicyclobutane. Allowed and Stereoselective Reaction That Is Not Concerted. *J. Am. Chem. Soc.* **1975**, *97* (10), 2931–2932.

(39) Shevlin, P. B.; McKee, M. L. A Theoretical Investigation of the Thermal Ring Opening of Bicyclobutane to Butadiene. Evidence for a Nonsynchronous Process†. *J. Am. Chem. Soc.* **1988**, *110* (6), 1666–1671.

(40) Nguyen, K. A.; Gordon, M. S. Isomerization Of Bicyclo[1.1.0]Butane to Butadiene. *J. Am. Chem. Soc.* **1995**, *117* (13), 3835–3847.

(41) Wang, H.; Law, C. K. Thermochemistry of Benzvalene, Dihydrobenzvalene, and Cubane: A High-Level Computational Study. *J. Phys. Chem. B* **1997**, *101* (17), 3400–3403.

(42) Davis, S. R.; Veals, J. D.; Scardino, D. J.; Zhao, Z. Isomerization Barriers and Strain Energies of Selected Dihydropyridines and Pyrans with Trans Double Bonds. *J. Phys.*

Chem. A **2009**, *113* (30), 8724–8730.

(43) Cuppoletti, A.; Dinnocenzo, J. P.; Goodman, J. L.; Gould, I. R. Bond-Coupled Electron Transfer Reactions: Photoisomerization of Norbornadiene to Quadricyclane. *J. Phys. Chem. A* **1999**, *103* (51), 11253–11256.

(44) Yang, W.; Roy, S. S.; Pitts, W. C.; Nelson, R. L.; Fronczek, F. R.; Jurss, J. W. Electrocatalytic CO2 Reduction with *Cis* and *Trans* Conformers of a Rigid Dinuclear Rhenium Complex : Comparing the Monometallic and Cooperative Bimetallic Pathways. *Inorg. Chem.* **2018**, *57*, 9564–9575.

(45) Liyanage, N. P.; Yang, W.; Guertin, S. L.; Sinha Roy, S.; Carpenter, C. A.; Adams, R. E.; Schmehl, R.; Delcamp, J.; Jurss, J. W. Photochemical CO2 Reduction with Mononuclear and Dinuclear Rhenium Catalysts Bearing a Pendant Anthracene Chromophore. *Chem. Commun.* **2018**, *2*, 993–996.

(46) Yang, W.; Poland, K. N.; Davis, S. R. Isomerization Barriers and Resonance Stabilization for the Conrotatory and Disrotatory Isomerizations of Nitrogen Containing Tricyclo Moieties. *Phys. Chem. Chem. Phys.* **2018**, *20* (41), 26608–26620.

(47) Sullivan, B. P.; Bolinger, C. M.; Conrad, D.; Vining, W. J.; Meyer, T. J. One-and Two-Electron Pathways in the Electrocatalytic Reduction of CO2 by Fac-Re(Bpy)(CO)3Cl (Bpy = 2,2'-Bipyridine). *J. Chem. Soc. Chem. Commun.* **1985**, 1414–1416.

(48) Roffia, S.; Amatore, C.; Paradisi, C.; Marcaccio, M.; Bignozzi, C. A.; Paolucci, F. Dynamics of the Electrochemical Behavior of Diimine Tricarbonyl Rhenium(I) Complexes in Strictly Aprotic Media. *J. Phys. Chem. B* **1998**, *102* (24), 4759–4769.

(49) Hayashi, Y.; Kita, S.; Brunschwig, B. S.; Fujita, E. Involvement of a Binuclear Species with the Re-C(O)O-Re Moiety in CO_2 Reduction Catalyzed by Tricarbonyl Rhenium(I) Complexes with Diimine Ligands: Strikingly Slow Formation of the Re-Re and Re-C(O)O-Re Species from Re(Dmb)(CO)$_3$S (Dmb=4,4′-Dimethyl-2,2′-B. *J. Am. Chem. Soc.* **2003**, *125* (39), 11976–11987.

(50) Fujita, E.; Muckerman, J. T. Why Is Re-Re Bond Formation/Cleavage in [Re(Bpy)(CO)$_3$]$_2$ Different from That in [Re(CO)$_5$]$_2$? Experimental and Theoretical Studies on the Dimers and Fragments. *Inorg. Chem.* **2004**, *43* (24), 7636–7647.

(51) Agarwal, J.; Fujita, E.; Schaefer, H. F.; Muckerman, J. T. Mechanisms for CO Production from CO2 Using Reduced Rhenium Tricarbonyl Catalysts. *J. Am. Chem. Soc.* **2012**, *134*, 5180–5186.

(52) Benson, E. E.; Kubiak, C. P. Structural Investigations into the Deactivation Pathway of the CO_2 Reduction Electrocatalyst Re(Bpy)(CO)$_3$Cl. *Chem. Commun.* **2012**, *48* (59), 7374–7376.

(53) Church, T. L.; Zhou, C.; Liang, W.; Zheng, S.; D'Alessandro, D. M.; Haynes, B. S. Site Isolation Leads to Stable Photocatalytic Reduction of CO_2 over a Rhenium-Based Catalyst. *Chem. - A Eur. J.* **2015**, *21* (51), 18576–18579.

(54) Machan, C. W.; Sampson, M. D.; Chabolla, S. A.; Dang, T.; Kubiak, C. P. Developing a Mechanistic Understanding of Molecular Electrocatalysts for CO_2 Reduction Using Infrared Spectroelectrochemistry. *Organometallics* **2014**, *33* (18), 4550–4559.

(55) Kou, Y.; Nabetani, Y.; Masui, D.; Shimada, T.; Takagi, S.; Tachibana, H.; Inoue, H.

Direct Detection of Key Reaction Intermediates in Photochemical CO_2 Reduction Sensitized by a Rhenium Bipyridine Complex. *J. Am. Chem. Soc.* **2014**, *136* (16), 6021–6030.

(56) Bruckmeier, C.; Lehenmeier, M. W.; Reithmeier, R.; Rieger, B.; Herranz, J.; Kavakli, C. Binuclear Rhenium(i) Complexes for the Photocatalytic Reduction of CO_2. *Dalt. Trans.* **2012**, *41* (16), 5026–5037.

(57) Tamaki, Y.; Imori, D.; Morimoto, T.; Koike, K.; Ishitani, O. High Catalytic Abilities of Binuclear Rhenium(i) Complexes in the Photochemical Reduction of CO_2 with a Ruthenium(II) Photosensitiser. *Dalt. Trans.* **2016**, *45* (37), 14668–14677.

(58) Machan, C. W.; Chabolla, S. A.; Yin, J.; Gilson, M. K.; Tezcan, F. A.; Kubiak, C. P. Supramolecular Assembly Promotes the Electrocatalytic Reduction of Carbon Dioxide by Re(I) Bipyridine Catalysts at a Lower Overpotential. *J. Am. Chem. Soc.* **2014**, *136* (41), 14598–14607.

(59) Machan, C. W.; Yin, J.; Chabolla, S. A.; Gilson, M. K.; Kubiak, C. P. Improving the Efficiency and Activity of Electrocatalysts for the Reduction of CO_2 through Supramolecular Assembly with Amino Acid-Modified Ligands. *J. Am. Chem. Soc.* **2016**, *138* (26), 8184–8193.

(60) Shakeri, J.; Hadadzadeh, H.; Tavakol, H. Photocatalytic Reduction of CO_2 to CO by a Dinuclear Carbonyl Polypyridyl Rhenium(I) Complex. *Polyhedron* **2014**, *78*, 112–122.

(61) Rezaei, B.; Ensafi, A. A.; Hadadzadeh, H.; Shakeri, J.; Mokhtarianpour, M. Electrocatalytic Reduction of CO_2 Using the Dinuclear Rhenium(I) Complex

[ReCl(CO)$_3$(μ-TptzH)Re(CO)$_3$]. *Polyhedron* **2015**, *101*, 160–164.

(62) Wilting, A.; Stolper, T.; Mata, R. A.; Siewert, I. Dinuclear Rhenium Complex with a Proton Responsive Ligand as a Redox Catalyst for the Electrochemical CO$_2$ Reduction. *Inorg. Chem.* **2017**, *56* (7), 4176–4185.

(63) Wilting, A.; Siewert, I. A Dincuclear Rhenium Complex with a Proton Responsive Ligand in the Electrochemical-Driven CO$_2$-Reduction Catalysis. *ChemistrySelect* **2018**, *3* (17), 4593–4597.

(64) APEX2, v. 2009; Bruker Analytical X-Ray Systems, Inc: Madison, WI, 2009.

(65) Sheldrick, G. M. SADABS, Version 2.03; Bruker Analytical X-Ray Sys-Tems, Inc: Madison, WI, 2000.

(66) Sheldrick, G. M. Phase Annealing in SHELX-90: Direct Methods for Larger Structures. *Acta Crystallogr. Sect. A* **1990**, *46* (6), 467–473.

(67) Sheldrick, G. M. A Short History of SHELX. *Acta Crystallogr. Sect. A Found. Crystallogr.* **2008**, *64* (1), 112–122.

(68) Sheldrick, G. M. SHELXL-2014/7: Program for Crystal Structure Determina-Tion, University of Göttingen: Göttingen, Germany, 2014.

(69) Spek, A. L. PLATON - A Multipurpose Crystallographic Tool, Utrecht Uni-Versity, Utrecht, The Netherlands, 2007.

(70) Spek, A. L. PLATON SQUEEZE: A Tool for the Calculation of the Disordered Solvent Contribution to the Calculated Structure Factors. *Acta Crystallogr. Sect. C Struct. Chem.* **2015**, *71*, 9–18.

(71) Frisch, M. J. et Al. Gaussian 09, Revision D.01; Gaussian, Inc., Wallingford, CT, 2009.

(72) Lin, Y. S.; Li, G. De; Mao, S. P.; Chai, J. Da. Long-Range Corrected Hybrid Density Functionals with Improved Dispersion Corrections. *J. Chem. Theory Comput.* **2013**, *9* (1), 263–272.

(73) Minenkov, Y.; Singstad, Å.; Occhipinti, G.; Jensen, V. R. The Accuracy of DFT-Optimized Geometries of Functional Transition Metal Compounds: A Validation Study of Catalysts for Olefin Metathesis and Other Reactions in the Homogeneous Phase. *Dalt. Trans.* **2012**, *41* (18), 5526–5541.

(74) Caspar, J. V; Meyer, T. J. Application of the Energy Gap Law to Nonradiative, Excited-State Decay. *J. Phys. Chem.* **1983**, *87* (6), 952–957.

(75) Böttger, M.; Wiegmann, B.; Schaumburg, S.; Jones, P. G.; Kowalsky, W.; Johannes, H.-H. Synthesis of New Pyrrole-Pyridine-Based Ligands Using an in Situ Suzuki Coupling Method. *Beilstein J. Org. Chem.* **2012**, *8*, 1037–1047.

(76) Wada, T.; Muckerman, J. T.; Fujita, E.; Tanaka, K. Substituents Dependent Capability of Bis(Ruthenium-Dioxolene-Terpyridine) Complexes toward Water Oxidation. *Dalt. Trans.* **2011**, *40* (10), 2225–2233.

(77) Richard, P.; Collman, J. P.; Guilard, R.; Brandes, S.; Tabard, A.; Lopez, M. A.; Lecomte, C.; Hutchison, J. E. Synthesis and Characterization of Novel Cobalt Aluminum Cofacial Porphyrins. First Crystal and Molecular Structure of a Heterobimetallic Biphenylene Pillared Cofacial Diporphyrin. *J. Am. Chem. Soc.* **1992**, *114* (25), 9877–9889.

(78) Fraser, M. G.; Clark, C. A.; Horvath, R.; Lind, S. J.; Blackman, A. G.; Sun, X. Z.; George,

M. W.; Gordon, K. C. Complete Family of Mono-, Bi-, and Trinuclear $Re^I(CO)_3Cl$ Complexes of the Bridging Polypyridyl Ligand 2,3,8,9,14,15- Hexamethyl-5,6,11,12,17,18-Hexaazatrinapthalene: Syn/Anti Isomer Separation, Characterization, and Photophysics. *Inorg. Chem.* **2011**, *50* (13), 6093–6106.

(79) Kolthoff, L.; Polurogruphy (interscience, N. Y. A Cathode Ray Polarography. Part II.- The Current- Voltage Curves. *Trans. Favaduy SOC* **1948**, 327–328.

(80) Bard, A. J.; Faulkner, L. R. *Electrochemical Methods: Fundamentals and Applications*, 2nd Editio.; John Wiley and Sons: New York, 2001.

(81) Richardson, D. E.; Taube, H. Mixed-Valence Molecules: Electronic Delocalization and Stabilization. *Coord. Chem. Rev.* **1984**, *60*, 107–129.

(82) Manes, T. A.; Rose, M. J. Redox Properties of a Bis-Pyridine Rhenium Carbonyl Derived from an Anthracene Scaffold. *Inorg. Chem. Commun.* **2015**, *61*, 221–224.

(83) Savéant, J. M.; Vianello, E. Potential-Sweep Chronoamperometry Theory of Kinetic Currents in the Case of a First Order Chemical Reaction Preceding the Electron-Transfer Process. *Electrochim. Acta.* **1963**, *8* (12), 905–923.

(84) Nicholson, R. S.; Shain, I. Theory of Stationary Electrode Polarography Single Scan and Cyclic Methods Applied to Reversible, Irreversible, and Kinetic Systems. *Anal. Chem.* **1964**, *36* (4), 706–723.

(85) Rountree, E. S.; McCarthy, B. D.; Eisenhart, T. T.; Dempsey, J. L. Evaluation of Homogeneous Electrocatalysts by Cyclic Voltammetry. *Inorg. Chem.* **2014**, *53* (19), 9983–10002.

(86)   Huang, D.; Makhlynets, O. V; Tan, L. L.; Lee, S. C.; Rybak-Akimova, E. V; Holm, R. H. Kinetics and Mechanistic Analysis of an Extremely Rapid Carbon Dioxide Fixation Reaction. *Proc. Natl. Acad. Sci.* **2011**, *108* (4), 1222–1227.

(87)   Steffey, B. D.; Curtis, C. J.; Dubois, D. L. *Electrochemical Reduction of CO2 Catalyzed by a Dinuclear Palladium Complex Containing a Bridging Hexaphosphine Ligand: Evidence for Cooperativity*; 1995; Vol. 14.

(88)   Raebiger, J. W.; Turner, J. W.; Noll, B. C.; Curtis, C. J.; Miedaner, A.; Cox, B.; DuBois, D. L. Electrochemical Reduction of CO2 to CO Catalyzed by a Bimetallic Palladium Complex. *Organometallics* **2006**, *25* (14), 3345–3351.

(89)   Yang, L.; Abu-Omar, M. M.; Wegenhart, B.; Liu, S.; Ison, E. A.; Senocak, A.; Kenttämaa, H. I.; Smeltz, J. L.; Yi, J. Mechanism of MTO-Catalyzed Deoxydehydration of Diols to Alkenes Using Sacrificial Alcohols. *Organometallics* **2013**, *32* (11), 3210–3219.

(90)   Guisán-Ceinos, M.; Buñuel, E.; Soler-Yanes, R.; Arribas-Álvarez, I.; Cárdenas, D. J. Ni[I] Catalyzes the Regioselective Cross-Coupling of Alkylzinc Halides and Propargyl Bromides to Allenes. *Chem. - A Eur. J.* **2017**, *23* (7), 1584–1590.

(91)   Costentin, C.; Drouet, S.; Robert, M.; Savéant, J. M. Turnover Numbers, Turnover Frequencies, and Overpotential in Molecular Catalysis of Electrochemical Reactions. Cyclic Voltammetry and Preparative-Scale Electrolysis. *J. Am. Chem. Soc.* **2012**, *134* (27), 11235–11242.

(92)   Costentin, C.; Robert, M.; Savéant, J.-M. Catalysis of the Electrochemical Reduction of Carbon Dioxide †. *Chem. Soc. Rev.* **2013**, *42*, 2423.

(93)   Wiedner, E. S.; Bullock, R. M. Electrochemical Detection of Transient Cobalt Hydride Intermediates of Electrocatalytic Hydrogen Production. *J. Am. Chem. Soc.* **2016**, *138* (26), 8309–8318.

(94)   Wong, K. Y.; Chung, W. H.; Lau, C. P. The Effect of Weak Brönsted Acids on the Electrocatalytic Reduction of Carbon Dioxide by a Rhenium Tricarbonyl Bipyridyl Complex. *J. Electroanal. Chem.* **1998**, *453*(1), 161-170.

(95)   Seu, C. S.; Grice, K. A.; Mayer, J. M.; Smieja, J. M.; Kubiak, C. P.; Miller, A. J. M.; Benson, E. E.; Kumar, B. Kinetic and Structural Studies, Origins of Selectivity, and Interfacial Charge Transfer in the Artificial Photosynthesis of CO. *Proc. Natl. Acad. Sci.* **2012**, *109* (39), 15646–15650.

(96)   Maran, F.; Celadon, D.; Severin, M. G.; Vianello, E. Electrochemical Determination of the PKa of Weak Acids in N,N-Dimethylformamide. *J. Am. Chem. Soc.* **1991**, *113*, 9320–9329.

(97)   Olmstead, B.; Steiner, J. H. ; Acidities of Water and Simple Alcohols in Dimethyl Sulfoxide Solution. *J. Org. Chem.* **1980**, *45* (16), 299–329.

(98)   Taft, R. W.; Bordwell, F. G. Structural and Solvent Effects Evaluated from Acidities Measured in Dimethyl Sulfoxide and in the Gas Phase. *Acc. Chem. Res.* **1988**, *21* (14), 463–469.

(99)   Bordwell, F. G.; Mccallum, R. J.; Olmstead, W. N. Acidities and Hydrogen Bonding of Phenols in Dimethyl Sulfoxide. *J. Org. Chem.* **1984**, *49* (38), 1424–1427.

(100)   Pegis, M. L.; Roberts, J. A. S.; Wasylenko, D. J.; Mader, E. A.; Appel, A. M.; Mayer, J.

M. Standard Reduction Potentials for Oxygen and Carbon Dioxide Couples in Acetonitrile and N,N-Dimethylformamide. *Inorg. Chem.* **2015**, *54* (24), 11883–11888.

(101) Appel, A. M.; Helm, M. L. Determining the Overpotential for a Molecular Eelectrocatalyst. *ACS Catal.* **2014**, *4* (2), 630–633.

(102) Lee, G. R.; Maher, J. M.; Cooper, N. J. Reductive Disproportionation of Carbon Dioxide by Dianionic Carbonylmetalates of the Transition Metals. *J. Am. Chem. Soc.* **1987**, *109* (10), 2956–2962.

(103) Ratliff, K. S.; Lentz, R. E.; Kubiak, C. P. Carbon Dioxide Chemistry of the Trinuclear Complex $[Ni_3(\mu_3\text{-}CNMe)(\mu_3\text{-}I)(Dppm)_3][PF_6]$. Electrocatalytic Reduction of Carbon Dioxide. *Organometallics* **1992**, *11* (6), 1986–1988.

(104) Fei, H.; Sampson, M. D.; Lee, Y.; Kubiak, C. P.; Cohen, S. M. Photocatalytic CO_2 Reduction to Formate Using a Mn(I) Molecular Catalyst in a Robust Metal−Organic Framework. *Inorg. Chem.* **2015**, *54*, 6821–6828.

(105) Story, N.; Bolinger, C. M.; Conrad, D.; Gilbert, J. A.; Meyer, T. J.; Sullivan, B. P. Electrocatalytic Reduction of CO_2 Based on Polypyridyl Complexes of Rhodium and Ruthenium. *J. Chem. Soc. Chem. Commun.* **1985**, *12*, 796–797.

(106) Sampson, M. D.; Froehlich, J. D.; Smieja, J. M.; Benson, E. E.; Sharp, I. D.; Kubiak, C. P. Direct Observation of the Reduction of Carbon Dioxide by Rhenium Bipyridine Catalysts. *Energy Environ. Sci.* **2013**, *6* (12), 3748–3755.

(107) Christensen, P. A.; Hamnett, A.; Muir, A. V. G.; Freeman, N. A. CO2 Reduction at Platinum, Gold and Glassy Carbon Electrodes in Acetonitrile An in-Situ FTIR Study. *J.*

Electroanal. Chem. **1990**, *288*, 197–215.

(108) Cheng, S. C.; Blaine, C. A.; Hill, M. G.; Mann, K. R. Electrochemical and IR Spectroelectrochemical Studies of the Electrocatalytic Reduction of Carbon Dioxide by [Ir 2 (Dimen) 4] 2+ (Dimen = 1,8-Diisocyanomenthane). *Inorg. Chem.* **1996**, *35* (26), 7704–7708.

(109) Takeda, H.; Koike, K.; Inoue, H.; Ishitani, O. Development of an Efficient Photocatalytic System for CO_2 Reduction Using Rhenium(I) Complexes Based on Mechanistic Studies. *J. Am. Chem. Soc.* **2008**, *130* (6), 2023–2031.

(110) Bruckmeier, C.; Lehenmeier, M. W.; Reithmeier, R.; Rieger, B.; Herranz, J.; Kavakli, C. Binuclear Rhenium(i) Complexes for the Photocatalytic Reduction of CO_2. *Dalt. Trans.* **2012**, *41* (16), 5026–5037.

(111) Thoi, V. S.; Kornienko, N.; Margarit, C. G.; Yang, P.; Chang, C. J. Visible-Light Photoredox Catalysis: Selective Reduction of Carbon Dioxide to Carbon Monoxide by a Nickel N-Heterocyclic Carbene-Isoquinoline Complex. *J. Am. Chem. Soc.* **2013**, *135* (38), 14413–14424.

(112) Guo, Z.; Yu, F.; Yang, Y.; Leung, C.-F.; Ng, S.-M.; Ko, C.-C.; Cometto, C.; Lau, T.-C.; Robert, M. Photocatalytic Conversion of CO_2 to CO by a Copper(II) Quaterpyridine Complex. *ChemSusChem* **2017**, *10* (20), 4009–4013.

(113) Simon, J. A.; Curry, S. L.; Schmehl, R. H.; Schatz, T. R.; Piotrowiak, P.; Jin, X.; Thummel, R. P. Intramolecular Electronic Energy Transfer in Ruthenium(II) Diimine Donor/Pyrene Acceptor Complexes Linked by a Single C-C Bond. *J. Am. Chem. Soc.*

1997, *119* (45), 11012–11022.

(114) Tyson, D. S.; Henbest, K. B.; Bialecki, J.; Castellano, F. N. Excited State Processes in Ruthenium(II)/Pyrenyl Complexes Displaying Extended Lifetimes. *J. Phys. Chem. A* **2001**, *105* (35), 8154–8161.

(115) Del Guerzo, A.; Leroy, S.; Fages, F.; Schmehl, R. H. Photophysics of Re(I) and Ru(II) Diimine Complexes Covalently Linked to Pyrene: Contributions from Intra-Ligand Charge Transfer States. *Inorg. Chem.* **2002**, *41* (2), 359–366.

(116) Harriman, A.; Hissler, M.; Khatyr, A.; Ziessel, R. A Ruthenium(II) Tris(2,2'-Bipyridine) Derivative Possessing a Triplet Lifetime of 42 Ms. *Chem. Commun.* **1999**, *0* (8), 735–736.

(117) Balazs, G. C.; Schmehl, R. H. Photophysical Behavior and Intramolecular Energy Transfer in Os(II) Diimine Complexes Covalently Linked to Anthracene†. *Photochem. Photobiol. Sci.* **2005**, *4*, 89–94.

(118) Genoni, A.; Chirdon, D. N.; Boniolo, M.; Sartorel, A.; Bernhard, S.; Bonchio, M. Tuning Iridium Photocatalysts and Light Irradiation for Enhanced CO_2 Reduction. *ACS Catal.* **2017**, *7* (1), 154–160.

(119) Naab, B. D.; Guo, S.; Olthof, S.; Evans, E. G. B.; Wei, P.; Millhauser, G. L.; Kahn, A.; Barlow, S.; Marder, S. R.; Bao, Z. Mechanistic Study on the Solution-Phase n-Doping of 1,3-Dimethyl-2-Aryl-2,3-Dihydro-1 H -Benzoimidazole Derivatives. *J. Am. Chem. Soc.* **2013**, *135* (40), 15018–15025.

(120) Cope, J. D.; Liyanage, N. P.; Kelley, P. J.; Denny, J. A.; Valente, E. J.; Webster, C. E.; Delcamp, J. H.; Hollis, T. K.; Li, R. Electrocatalytic Reduction of CO_2 with CCC-NHC

Pincer Nickel Complexes †. *Chem. Commun.* **2017**, *53*, 9442.

(121) Bonin, J.; Robert, M.; Routier, M. Selective and Efficient Photocatalytic CO_2 Reduction to CO Using Visible Light and an Iron-Based Homogeneous Catalyst. *J. Am. Chem. Soc.* **2014**, *136* (48), 16768–16771.

(122) Rodrigues, R. R.; Boudreaux, C. M.; Papish, E. T.; Delcamp, J. H. Photocatalytic Reduction of CO_2 to CO and Formate: Do Reaction Conditions or Ruthenium Catalysts Control Product Selectivity? *ACS Appl. Energy Mater.* **2018**, *2* (1), 37–46.

(123) S. L. Murov, I. Carmichael and G. L. Hug, "Handbook of Photochemistry", Ch. 1, Marcel Dekker, New York, 1993, p. 7.

(124) Walther, M. E.; Wenger, O. S. Energy Transfer from Rhenium(i) Complexes to Covalently Attached Anthracenes and Phenanthrenes. *J. Chem. Soc. Dalt. Trans.* **2008**, *44*, 6311–6318.

(125) Worl, L. A.; Duesing, R.; Chen, P.; Ciana, L. Della; Meyer, T. J. Photophysical Properties of Polypyridyl Carbonyl Complexes of Rhenium(I). *J. Chem. Soc. Dalt. Trans.* **1991**, *0*, 849–858.

(126) Zhao, Z.; Davis, S. R.; Cleland, W. E. Ab Initio Study of the Pathways and Barriers of Tricyclo[4.1.0.0^{2,7}]Heptene Isomerization. *J. Phys. Chem. A* **2010**, *114* (43), 11798–11806.

(127) Veals, J. D.; Davis, S. R. Isomerization Barriers for the Conrotatory and Disrotatory Isomerizations of 3-Aza-Dihydrobenzvalene to 1,2-Dihydropyridine and 3,4-Diaza-Dihydrobenzvalene to 1,2-Dihydropyridazine. *Comput. Theor. Chem.* **2013**, *1020*, 127–

135.

(128) Veals, J. D.; Davis, S. R. Isomerization Barriers for the Disrotatory and Conrotatory

Isomerizations of 3-Aza-Benzvalene and 3,4-Diaza-Benzvalene to Pyridine and

Pyridazine. *Phys. Chem. Chem. Phys.* **2013**, *15* (32), 13593–13600.

(129) Qin, C.; Davis, S. R. Thermal Isomerization of Tricyclo[4.1.0.0^{2,7}]Heptane and

Bicyclo[3.2.0]Hept-6-Ene through the (E,Z)-1,3-Cycloheptadiene Intermediate. *J. Org.*

Chem. **2003**, *68* (23), 9081–9087.

(130) Schmidt, M. W.; Baldridge, K. K.; Boatz, J. A.; Elbert, S. T.; S.Gordon, M.; Jensen, J. H.;

Koseki, S.; Matsunaga, N.; Nguyen, K. A.; Su, S. J.; et al. General Atomic and Molecular

Electronic Structure System. *J. Comput. Chem.* **1993**, *14*, 1347–1363.

(131) Boys, S. F. *Quantum Science of Atoms, Molecules, and Solids*; Ed, A. P., Ed.; NY, 1966.

(132) Woon, D. E.; Thom H. Dunning, J. Gaussian Basis Sets for Use in Correlated Molecular

Calculations. III. The Atoms Aluminum through Argon. *J. Chem. Phys.* **1993**, *98* (2),

1358–1371.

(133) Gonzalez, C.; Bernhard Schlegel, H. An Improved Algorithm for Reaction Path

Following. *J. Chem. Phys.* **1989**, *90* (4), 2154–2161.

(134) Hirao, K. Multireference Møller-Plesset Method. *Chem. Phys. Lett.* **1992**, *190* (3–4), 374–

380.

(135) Hirao, K. Multireference Møller-Plesset Perturbation Theory for High-Spin Open-Shell

Systems. *Chem. Phys. Lett.* **1992**, *196* (5), 397–403.

(136) Frisch, M. J.; Trucks, G. W.; Schlegel, H. B.; Scuseria, G. E.; Robb, M. A.; Cheeseman, J.

R.; Scalmani, G.; Barone, V.; Petersson, G. A.; Nakatsuji, H.; et al. Gaussian16 revision {B}.01. 2016.

(137) Veals, J. D.; Poland, K. N.; Earwood, W. P.; Yeager, S. M.; Copeland, K. L.; Davis, S. R. MRMP2, CCSD(T), and DFT Calculations of the Isomerization Barriers for the Disrotatory and Conrotatory Isomerizations of 3-Aza-3-Ium-Dihydrobenzvalene, 3,4-Diaza-3-Ium-Dihydrobenzvalene, and 3,4-Diaza-Diium-Dihydrobenzvalene. *J. Phys. Chem. A* **2017**, *121* (46), 8899–8911.

(138) Ritscher, J. S.; Kaplan, L.; Wilzbach, K. E. Benzvalene, the Tricyclic Valence Isomer of Benzene. *J. Am. Chem. Soc.* **1967**, *89* (4), 1031–1032.

(139) Dewar, M. J. S.; Kirschner, S. The Conversion of Benzvalene to Benzene. *J. Am. Chem. Soc.* **1975**, *97* (10), 2932–2933.

(140) Renner, C. A.; Katz, J.; Haven, N. Kinetics and Thermochemistry of the Rearrangement of Benzvalene to Benzene. An Energy Sufficient but Non-Chemiluminescent Reaction. *Tetrahedron Lett.* **1976**, *2* (46), 4133–4136.

(141) Merz, K. M.; Lawrence, T. The C6H6 PES: Automerization of Benzene. *J. Chem. Soc.* **1993**, *412*, 412–414.

(142) Bettinger, H. F.; Schreiner, P. R.; Schaefer, H. F.; Schleyer, P. v R. Rearrangements on the C6H6 Potential Energy Surface and the Topomerization of Benzene. *J. Am. Chem. Soc.* **1998**, *120* (23), 5741–5750.

(143) Schulman, J. M.; Disch, R. L. Ab Initio Heats of Formation of Medium-Sized Hydrocarbons. The Heat of Formation of Dodecahedrane. *J. Am. Chem. Soc.* **1985**, *106*

(5), 1202–1204.

(144) Wang, H.; Law, C. K. Thermochemistry of Benzvalene , Dihydrobenzvalene , and Cubane : A High-Level Computational Study. *Society* **1997**, *5647* (96), 3400–3403.

(145) Kislov, V. V.; Nguyen, T. L.; Mebel, A. M.; Lin, S. H.; Smith, S. C. Photodissociation of Benzene under Collision-Free Conditions: An Ab Initio/Rice-Ramsperger-Kassel-Marcus Study. *J. Chem. Phys.* **2004**, *120* (15), 7008–7017.

(146) Wang, H.; Laskin, A.; Moriarty, N. W.; Frenklach, M. On Unimolecular Decomposition of Phenyl Radical. *Proc. Combust. Inst.* **2000**, *28*, 1545–1555.

(147) Dubrovskiy, A. V; Markina, N. A.; Larock, R. C. Use of Benzynes for the Synthesis of Heterocycles. *Org. Biomol. Chem* **2013**, *11*, 191.

(148) Matsugi, A.; Miyoshi, A. Reactions of O-Benzyne with Propargyl and Benzyl Radicals: Potential Sources of Polycyclic Aromatic Hydrocarbons in Combustion. *Phys. Chem. Chem. Phys.* **2012**, *14* (27), 9722–9728.

(149) Comandini, A.; Brezinsky, K. Radical/π-Bond Addition between o -Benzyne and Cyclic C 5 Hydrocarbons. *J. Phys. Chem. A* **2012**, *116* (4), 1183–1190.

(150) Bauschlicher, C. W.; Ricca, A. On the Calculation of the Vibrational Frequencies of C6H4. *Chem. Phys. Lett.* **2013**, *566*, 1–3.

(151) Jiao, H.; Schleyer, P. V. R.; Beno, B. R.; Houk, K. N.; Warmuth, R. Theoretical Studies of the Structure , Aromaticity , and Magnetic Properties of o-Benzyne. *Communications* **1997**, *2*, 2761–2764.

(152) Moskaleva, L. V; Madden, L. K.; Lin, M. C.; Kassel, R. È.; Marcus, È. Unimolecular

Isomerization / Decomposition of Ortho -Benzyne : Ab Initio MO / Statistical Theory Study. **1999**, 3967–3972.

(153) Ghigo, G.; Maranzana, A.; Tonachini, G. *o*-Benzyne Fragmentation and Isomerization Pathways: A CASPT2 Study. *Phys. Chem. Chem. Phys.* **2014**, *16* (43), 23944–23951.

(154) Blake, M. E.; Bartlett, K. L.; Jones, M. A *m*-Benzyne to *o*-Benzyne Conversion through a 1,2-Shift of a Phenyl Group. *Tetrahedron* **2003**, *125* (6), 6485–6490.

(155) Halton, B.; Cooney, M. J.; Jones, C. S.; Boese, R.; Bläser, D. C_6H_4 Valence Bond Isomers: A Reactive Bicyclopropenylidene. *Org. Lett.* **2004**, *6* (22), 4017–4020.

LIST OF APPENDICES

APPENDIX A
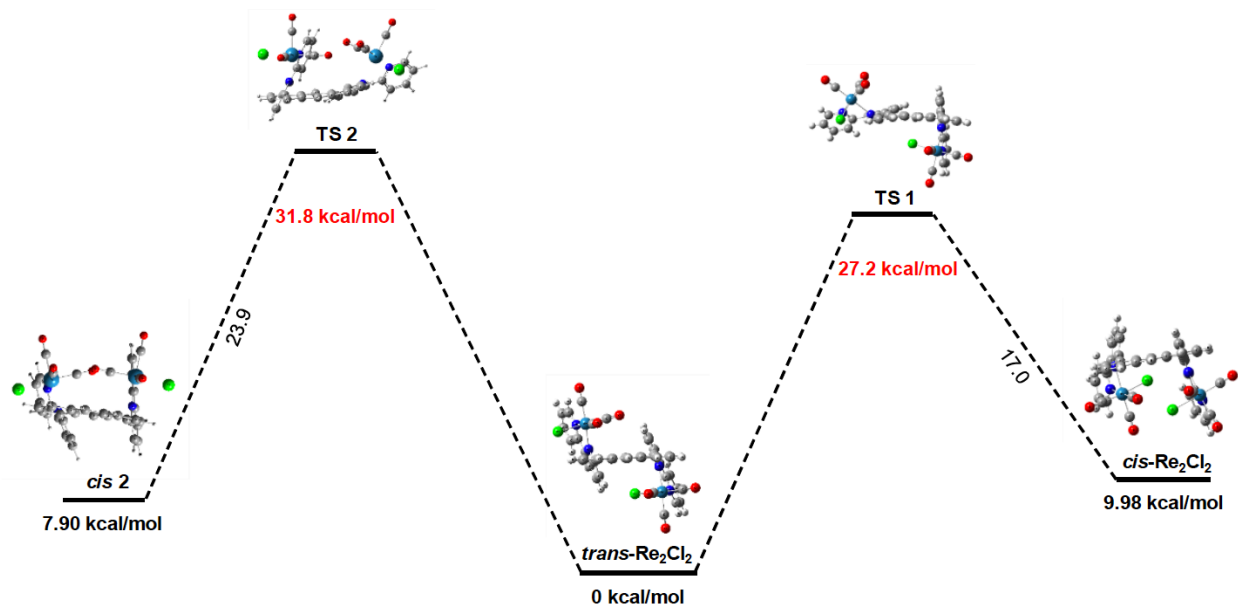
Figure A1. Calculated energy barrier to rotational interconversion between the asymmetric *trans*-Re_2Cl_2 and symmetric *cis* conformers, *cis*-Re_2Cl_2 and *cis* 2 (as identified in Figure A2). Fully optimized with wB97X-D functional and LanL2TZ(f) (Re atoms), 6-311+G* (COs and coordinating Ns), and 6-311G* (all other atoms) basis sets.

1

cis-Re$_2$Cl$_2$
(*C$_S$* symmetric, Cl-in)

2

trans-Re$_2$Cl$_2$
(asymmetric, *C$_1$'*
1Cl-in, 1Cl-out)

same

3

cis 2
(*C$_S$* symmetric, Cl-out)

4

trans 2
(*C$_2$* symmetric, Cl-in)

5

cis 3
(asymmetric, *C$_1$*)

7

cis 4
(asymmetric, *C$_1$*)

enantiomers

6

trans 3
(*C$_2$* symmetric, Cl-out)

141
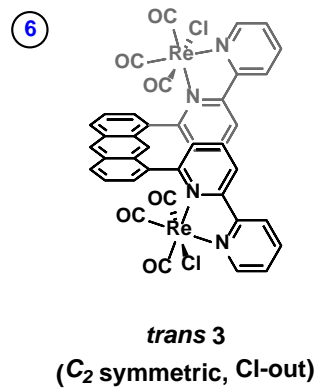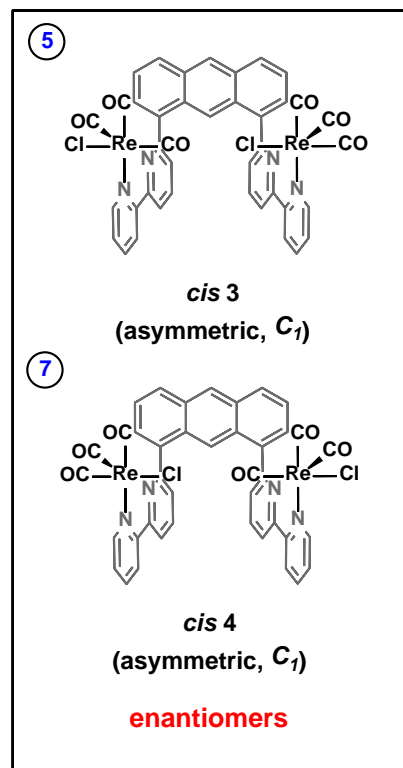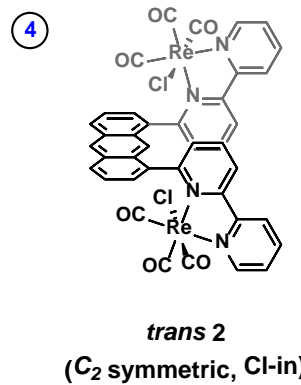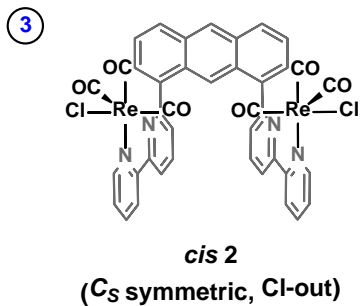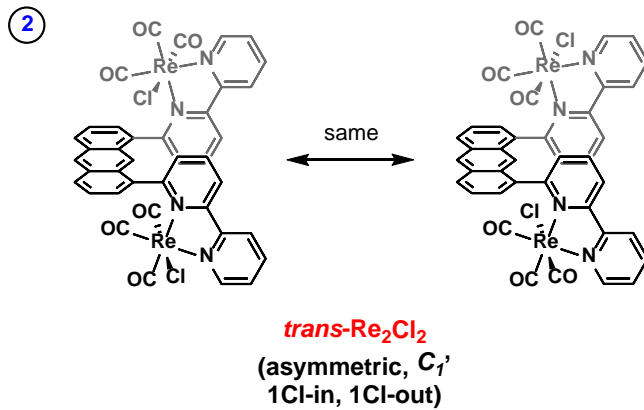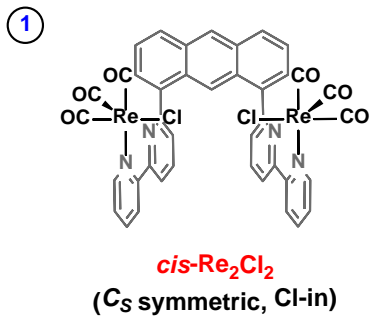
Figure A2. The seven possible isomers, maintaining the *fac*-tricarbonyl arrangement, that could be formed upon metalation
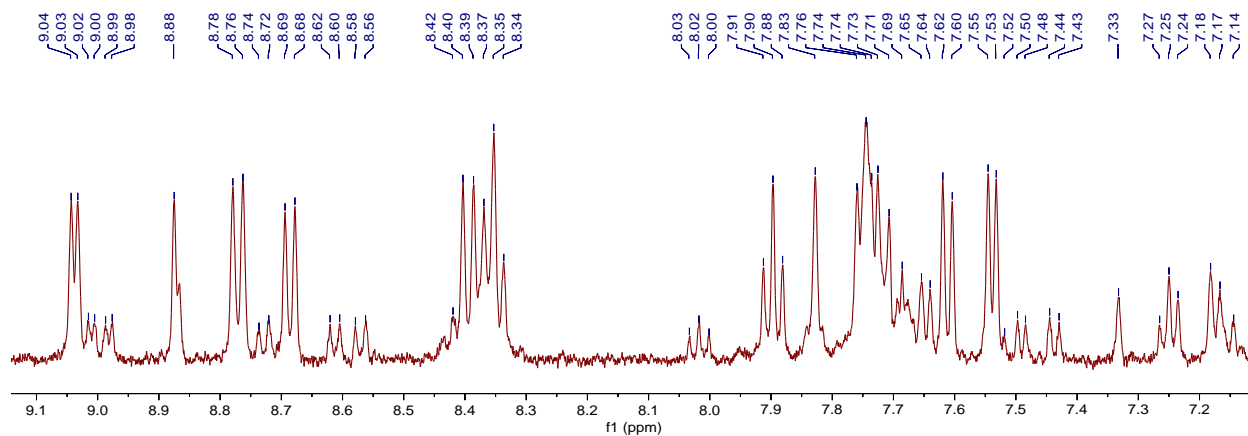
Figure A3. ^{1}H NMR spectrum (500 MHz, DMSO-*d$_6$*) showing the aromatic region of the crude reaction mixture following metalation of ligand **1** with two equivalents of Re(CO)$_5$Cl.
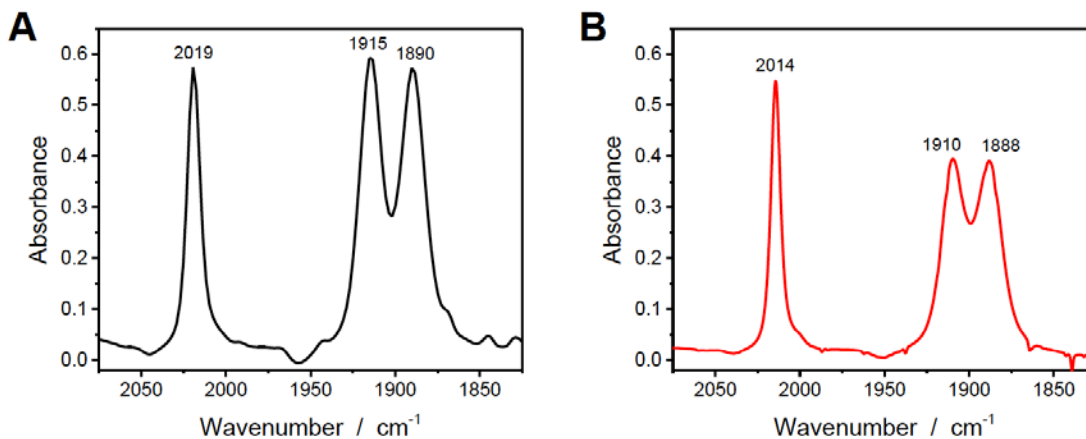
Figure A4. Experimental FTIR spectra of A) *cis*-Re$_2$Cl$_2$ and B) *trans*-Re$_2$Cl$_2$ in DMF solution showing the CO vibrational modes.
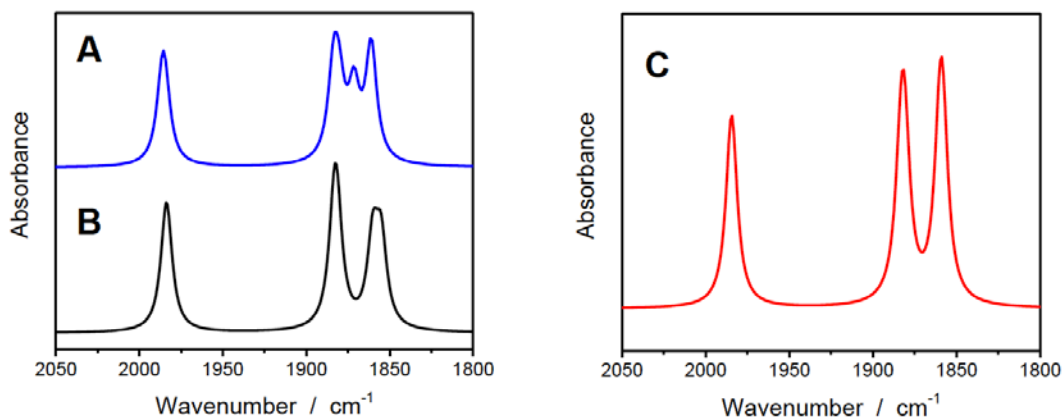
Figure A5. Calculated infrared spectra showing the CO vibrational modes of A) *cis* 2, B) *cis*-Re$_2$Cl$_2$, and C) *trans*-Re$_2$Cl$_2$ as specified in Figure S1 in DMF using the COSMO solvation mode.
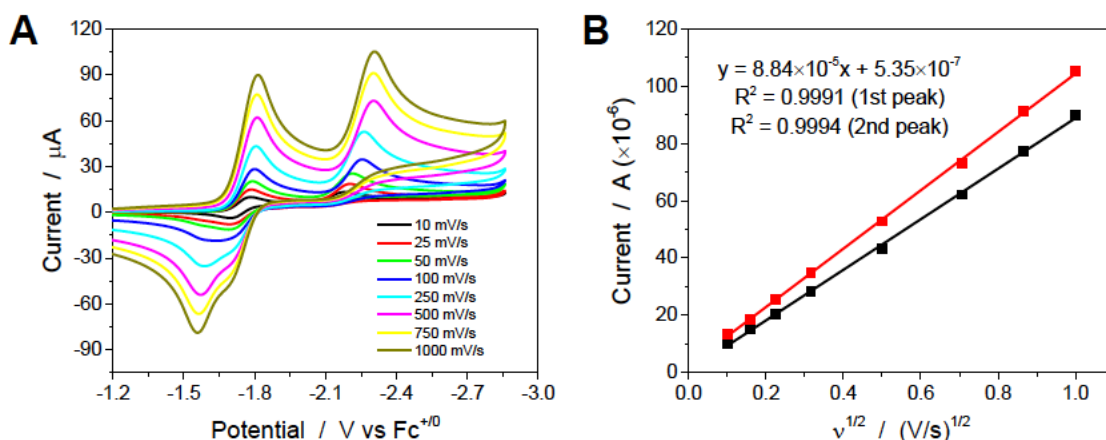
Figure A6. A) Cyclic voltammograms at different scan rates with 2 mM Re(bpy)(CO)$_3$Cl in DMF/0.1 M Bu$_4$NPF$_6$ solutions under Ar, glassy carbon disc. B) Scan rate dependence: reductive peak current vs the square root of scan rate ($v^{1/2}$) for each reduction. The given line equation corresponds to the linear fit shown in black (first reduction), which was used to calculate the diffusion coefficient, $D = 5.40$ x 10^{-6} cm^2 s^{-1}.

Figure A7. A) Cyclic voltammograms at different scan rates with 2 mM anthryl-Re in DMF/0.1 M Bu$_4$NPF$_6$ solutions under Ar, glassy carbon disc. B) Scan rate dependence: reductive peak current vs the square root of scan rate ($v^{1/2}$) for each reduction. The given line equation corresponds to the linear fit shown in black (first reduction), which was used to calculate the diffusion coefficient, $D = 5.40 \times 10^{-6}$ cm^2 s^{-1}.
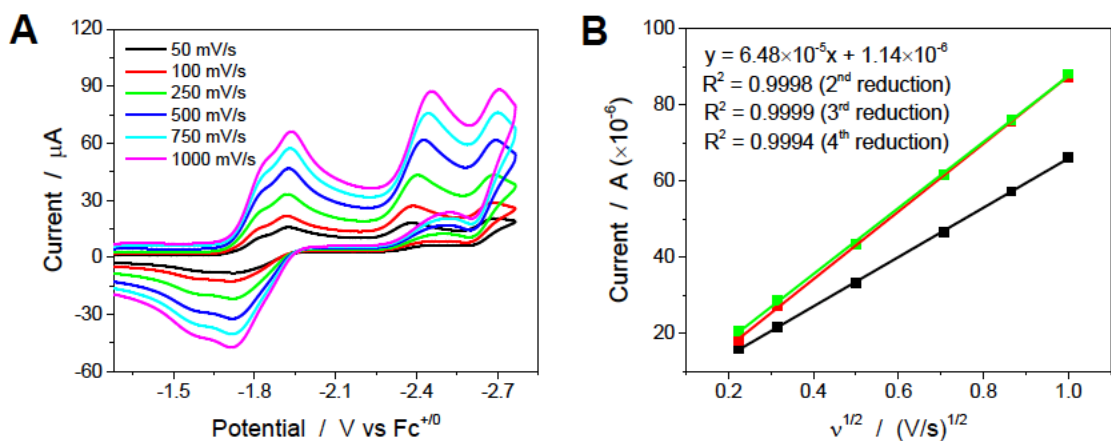
Figure A8. A) Cyclic voltammograms at different scan rates with 1 mM *cis*-Re$_2$Cl$_2$ in DMF/0.1 M Bu$_4$NPF$_6$ solutions under Ar, glassy carbon disc. B) Scan rate dependence: reductive peak current vs the square root of scan rate ($v^{1/2}$) for each reduction. The given line equation corresponds to the linear fit shown in black for the second of the two initial overlapping 1e$^-$ reductions.

144
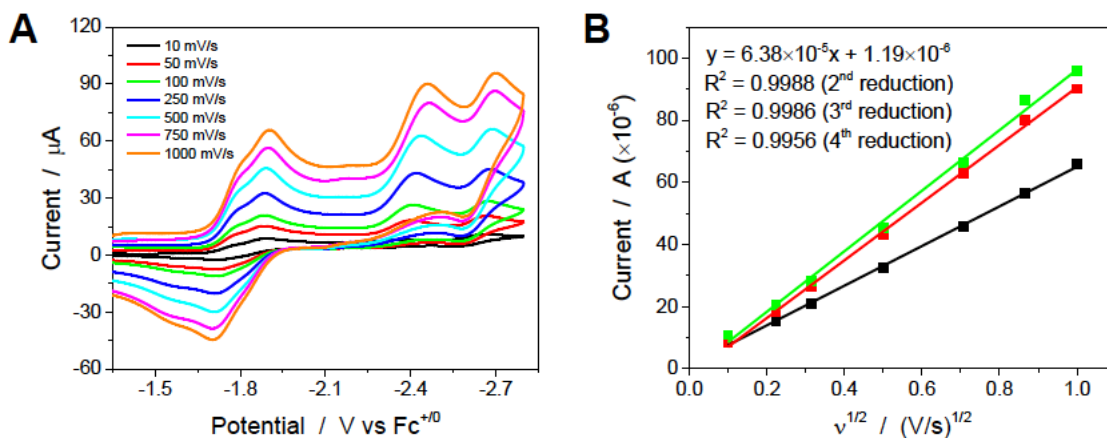
Figure A9. A) Cyclic voltammograms at different scan rates with 1 mM cis-Re$_2$Cl$_2$ in DMF/0.1 M Bu$_4$NPF$_6$ solutions under Ar, glassy carbon disc. B) Scan rate dependence: reductive peak current vs the square root of scan rate ($v^{1/2}$) for each reduction. The given line equation corresponds to the linear fit shown in black for the second of the two initial overlapping 1e⁻ reductions.

Reliable diffusion coefficients could not be calculated from the scan rate dependent CVs of the dinuclear complexes due to the initial overlapping reductions. From the indicated slopes, diffusion coefficients of 1.16 x 10⁻⁵ cm² s⁻¹ (cis-Re$_2$Cl$_2$) and 1.13 x 10⁻⁵ cm² s⁻¹ ($trans$-Re$_2$Cl$_2$) are obtained using the Randles-Sevcik equation (eq 1), where n, the number of electrons transferred in the redox event, was taken to be 1. However, the current response is complicated by the intersecting waves.

$$i_p = 0.4463nFAC\left(\frac{nFvD}{RT}\right)^{1/2} \quad \text{Equation 1}$$

which simplifies to: $i_p = (2.69 \times 10^5)n^{3/2}AD^{1/2}Cv^{1/2}$ (at 298 K)

In eq 1, i_p is the current (in A), F is Faraday's constant (96,485 C/mol), A is the surface area of the working electrode (0.0707 cm² for a 3 mm diameter glassy carbon disc), C is the concentration of the electroactive species (in mol/cm³, i.e. a 1 mM concentration is 1 x 10⁻⁶

mol/cm^3), ν is the scan rate (in V/s), D is the diffusion coefficient (in cm^2/s), R is the ideal gas

constant (8.314 J/(mol•K), and T is the temperature (in K). The following conversion is also

useful, V = J/C, in working out the units.
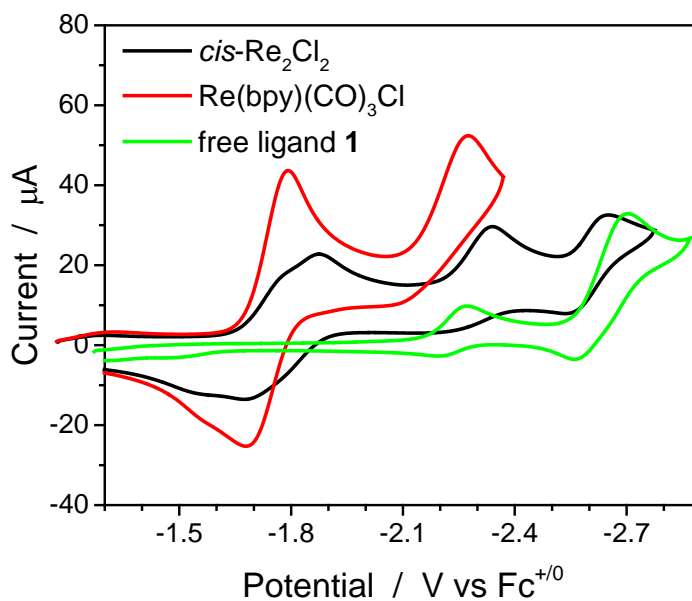
Figure A10. Cyclic voltammetry of *cis*-Re₂Cl₂, free ligand **1** (1,8-di([2,2'-bipyridin]-6-yl) anthracene) and Re(bpy)(CO)₃Cl in DMF/0.1 M Bu₄NPF₆ solutions, glassy carbon disc, ν = 100 mV/s.
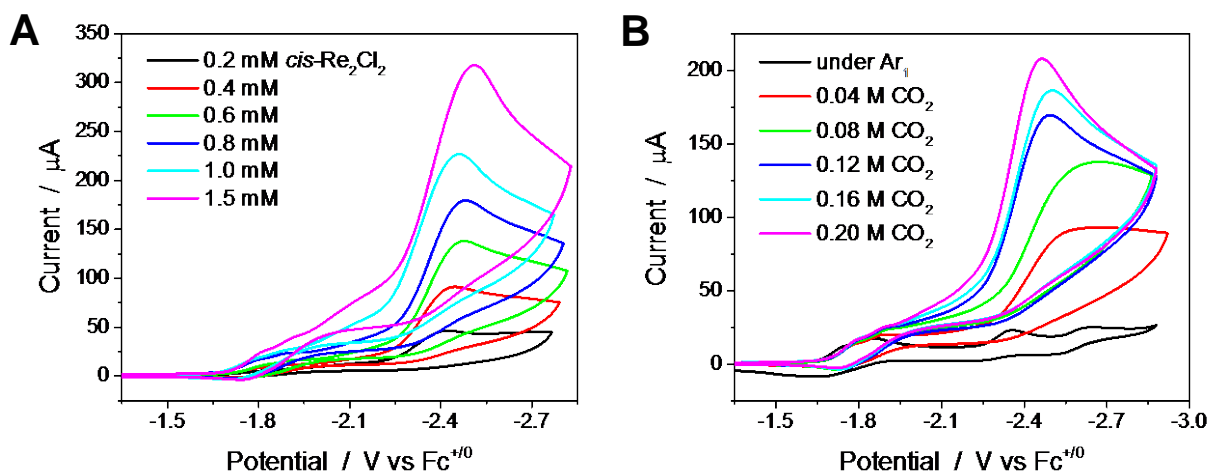
Figure A11. Cyclic voltammograms as a function of A) *cis*-Re$_2$Cl$_2$ catalyst concentration (from 0.2 to 1.5 mM), and of B) CO$_2$ substrate concentration (from 0 to 0.20 M) in DMF/0.1 M Bu$_4$NPF$_6$ solutions, glassy carbon disc, ν = 100 mV/s.
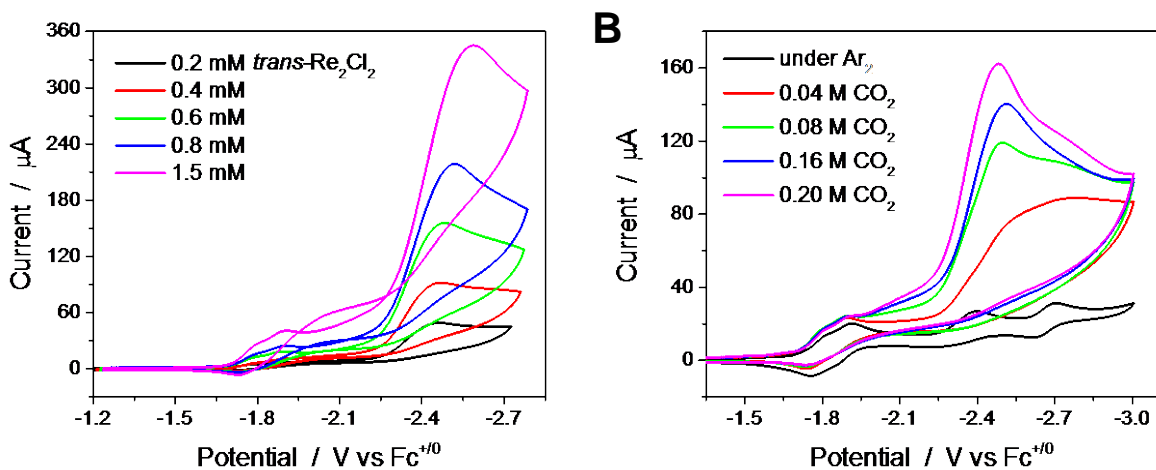
Figure A12. Cyclic voltammograms as a function of A) *trans*-Re$_2$Cl$_2$ catalyst concentration (from 0.2 to 1.5 mM), and of B) CO$_2$ substrate concentration (from 0 to 0.20 M) in DMF/0.1 M Bu$_4$NPF$_6$ solutions, glassy carbon disc, ν = 100 mV/s.

147
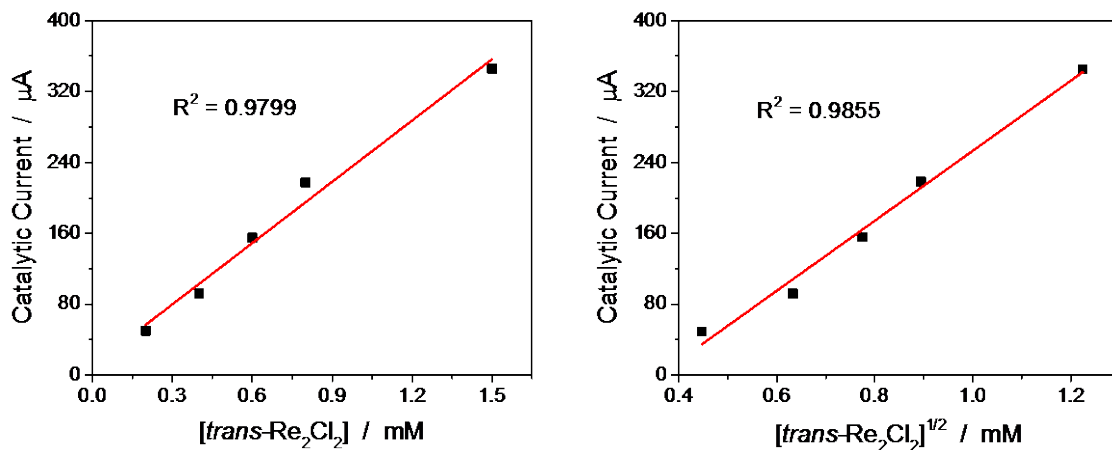
Figure A13. From the cyclic voltammograms in Figure A12, catalytic current is plotted versus [*trans*-Re₂Cl₂] (left graph) and versus [*trans*-Re₂Cl₂]$^{1/2}$ (right graph). Despite the satisfactory linear fits obtained from these plots, a slope of 1 from the log-log plot of the data confirms a first-order dependence on catalyst concentration as shown in Figure 7 of the main text.
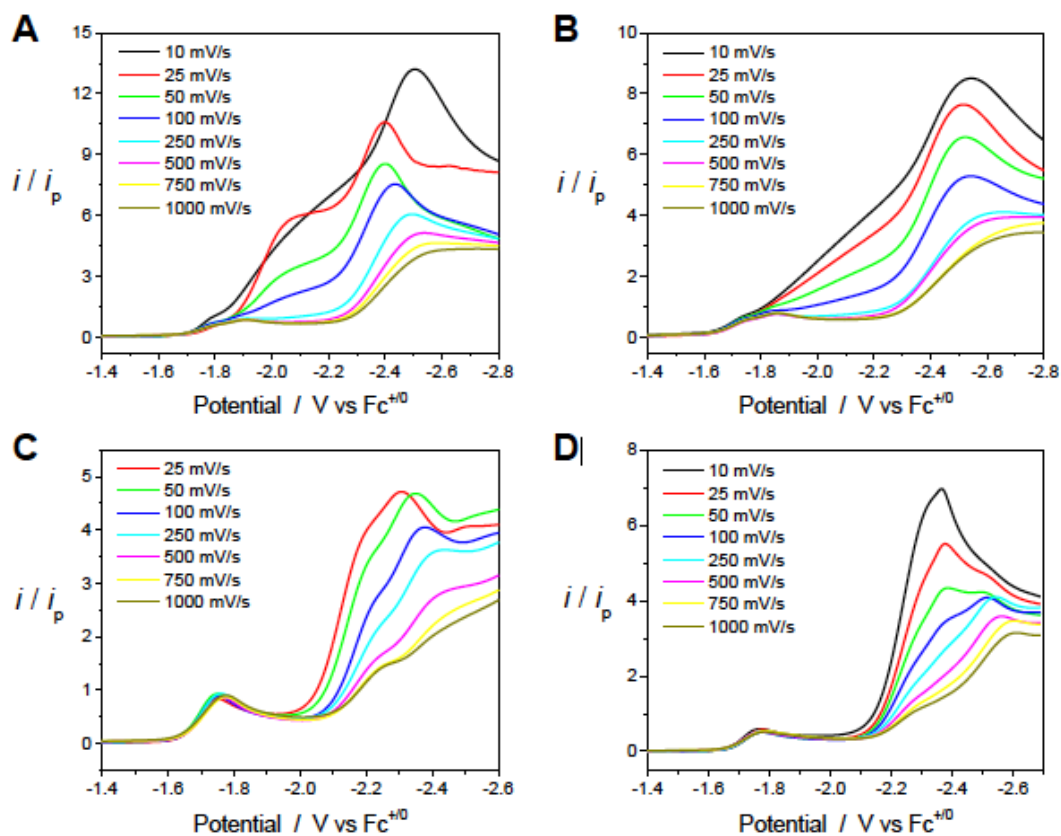
Figure A14. Plots of (i/i_p) from linear sweep voltammograms at different scan rates for A) *cis*-Re₂Cl₂ (1 mM), B) *trans*-Re₂Cl₂ (1 mM), C) Re(bpy)(CO)₃Cl (2 mM), and D) anthryl-Re (2 mM) in DMF/0.1 M Bu₄NPF₆ under CO₂-saturation conditions, glassy carbon disc.
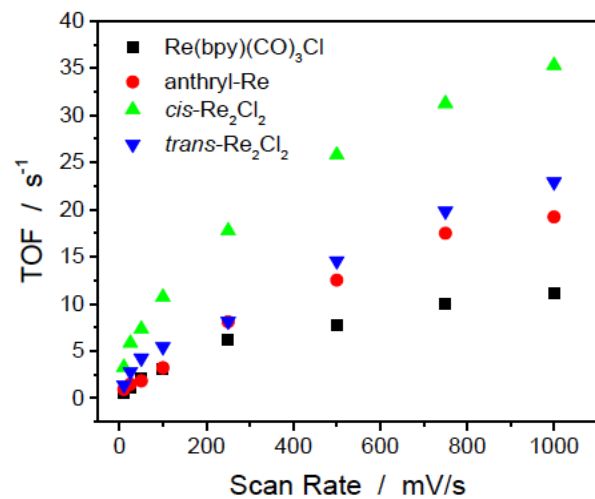
Figure A15. A plot of TOF (s^{-1}) vs scan rate (mV/s) for each catalyst as determined from linear sweep voltammograms at different scan rates using equation 2 in the main text.
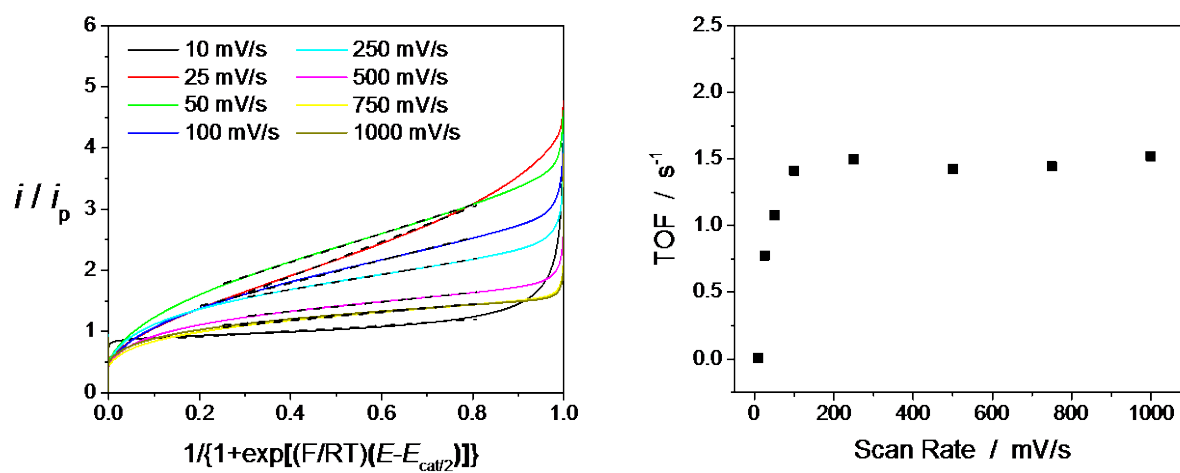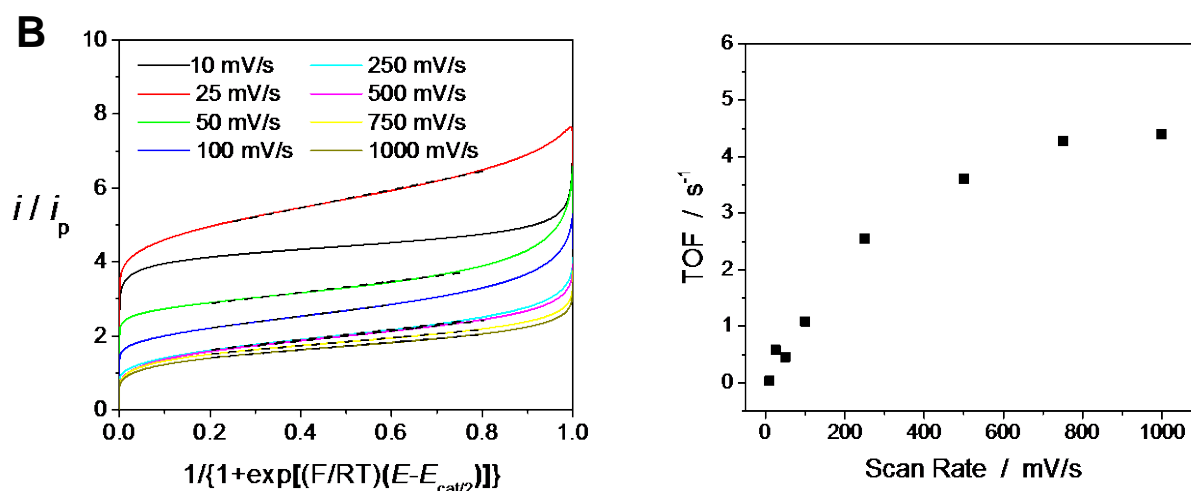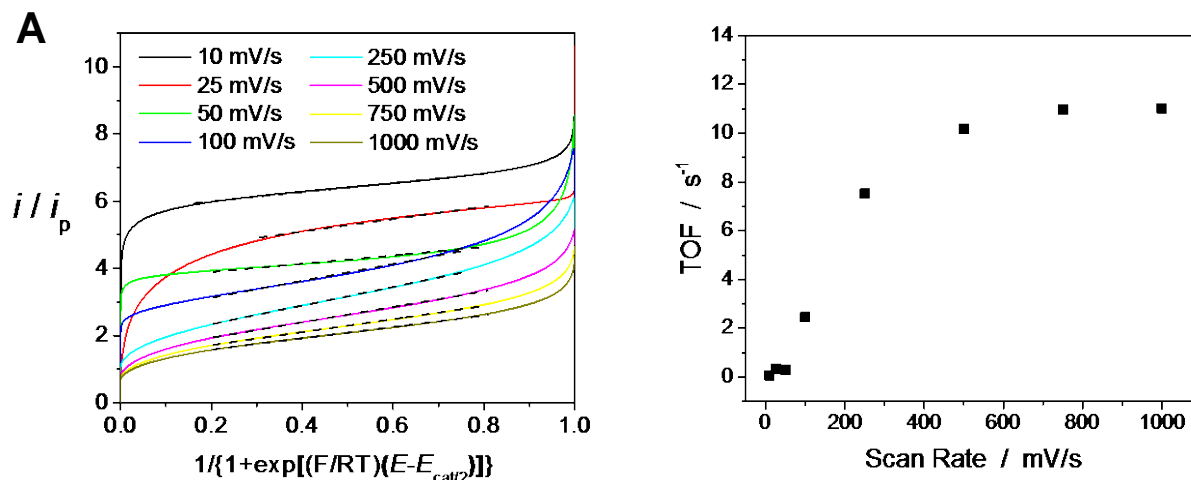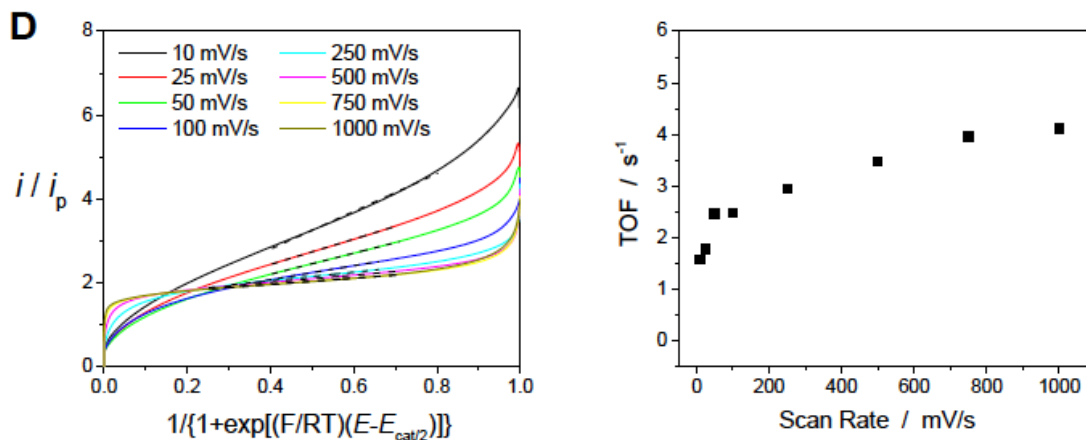
Figure A16. Foot-of-the-wave analysis (FOWA) and associated plot of TOF (s^{-1}) vs scan rate (mV/s) for A) *cis*-Re$_2$Cl$_2$ (1 mM), B) *trans*-Re$_2$Cl$_2$ (1 mM), C) Re(bpy)(CO)$_3$Cl (2 mM), and D) anthryl-Re (2 mM) from linear sweep voltammograms in DMF/0.1 M Bu$_4$NPF$_6$ under CO$_2$-saturation conditions, glassy carbon disc. TOFs were obtained using eq 3 in the main text.

No significant differences were observed in the estimated TOFs from FOWA when using E_{cat}^0 rather than $E_{cat/2}$ in eq 3, except the TOF vs scan rate plots (Figure A16) were more well-behaved before reaching the scan rate independent TOF maximum when using $E_{cat/2}$. Due to slow catalysis following the initial overlapping one-electron reductions of the dinuclear catalysts, the linear portion of FOWA plots was used to estimate TOFs.
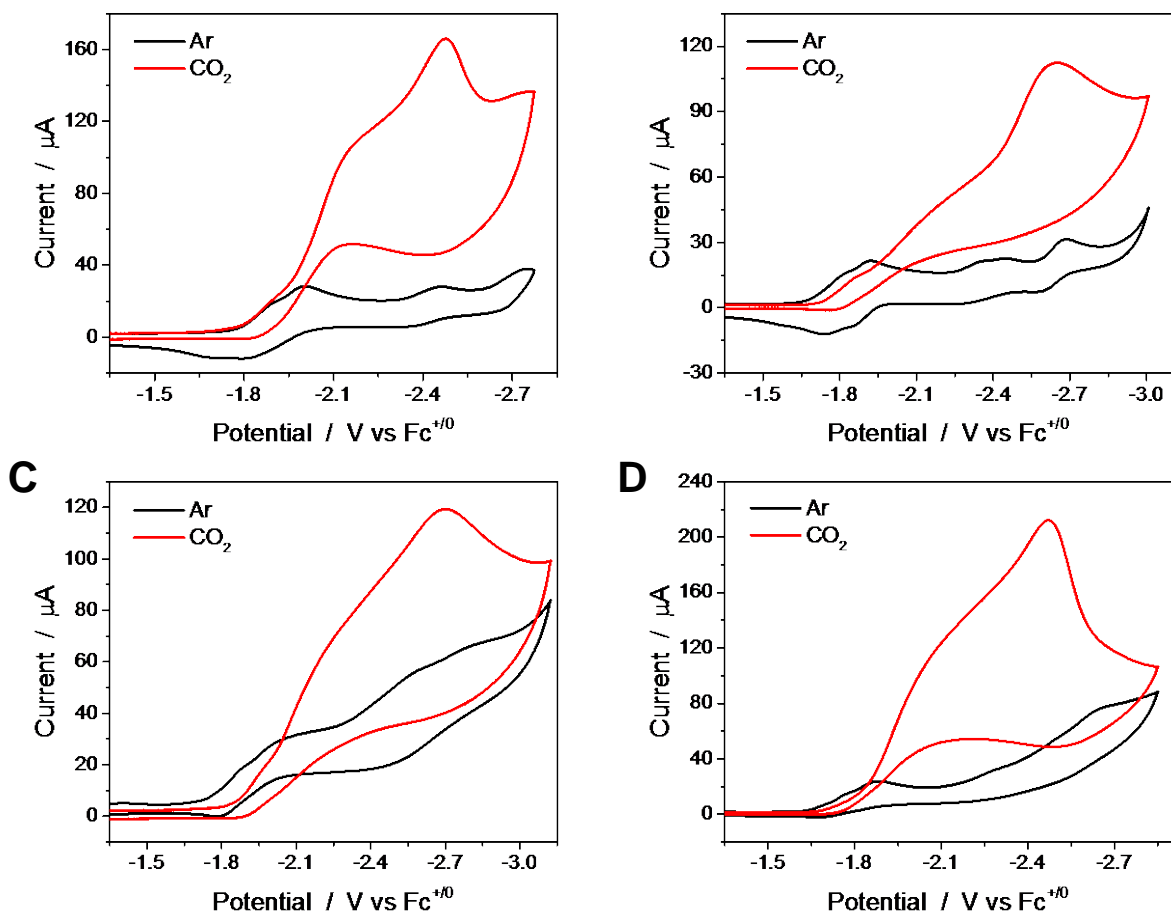
Figure A17. Cyclic voltammograms of catalyst *cis*-Re$_2$Cl$_2$ with different proton sources in DMF/0.1 M Bu$_4$NPF$_6$ under Ar and CO$_2$, glassy carbon disc, $v = 100$ mV/s. A) 2 M H$_2$O, B) 1 M MeOH, C) 1 M TFE, and D) 1 M PhOH.
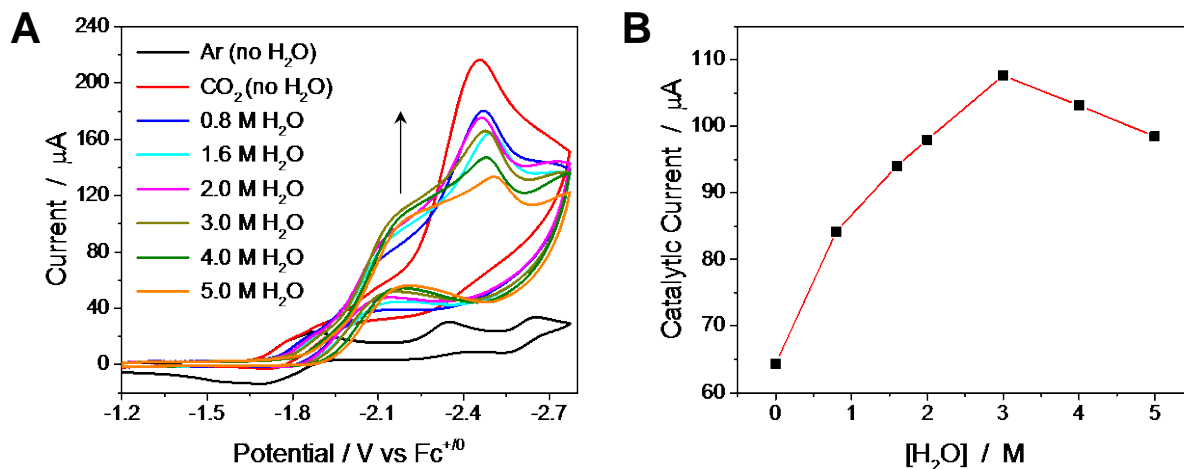
Figure A18. Concentration dependence of added H2O as a proton source. A) Cyclic voltammograms of 1 mM *cis*-Re2Cl2 with increasing amounts of H2O in DMF/0.1 M Bu4NPF6 under CO2, glassy carbon disc, v = 100 mV/s. B) A plot of i_{cat} (at -2.17 V) vs [H2O].
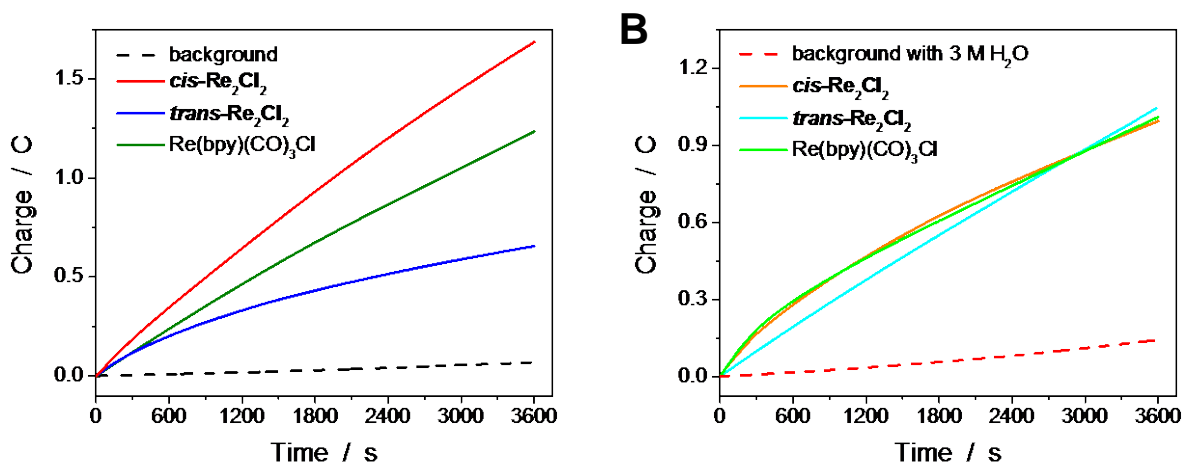
Figure A19. Accumulated charge vs time for representative controlled potential electrolyses in CO2 saturated DMF/0.1 M Bu4NPF6 solutions (A) and with 3 M H2O (B) for 1 mM *cis*-Re2Cl2, 1 mM t*rans*-Re2Cl2, and 2 mM Re(bpy)(CO)3Cl in each condition. Eappl = -2.5 V vs Fc+/0 for electrolyses shown in A; Eappl = -2.4 V vs Fc$^{+/0}$ for electrolyses shown in B.
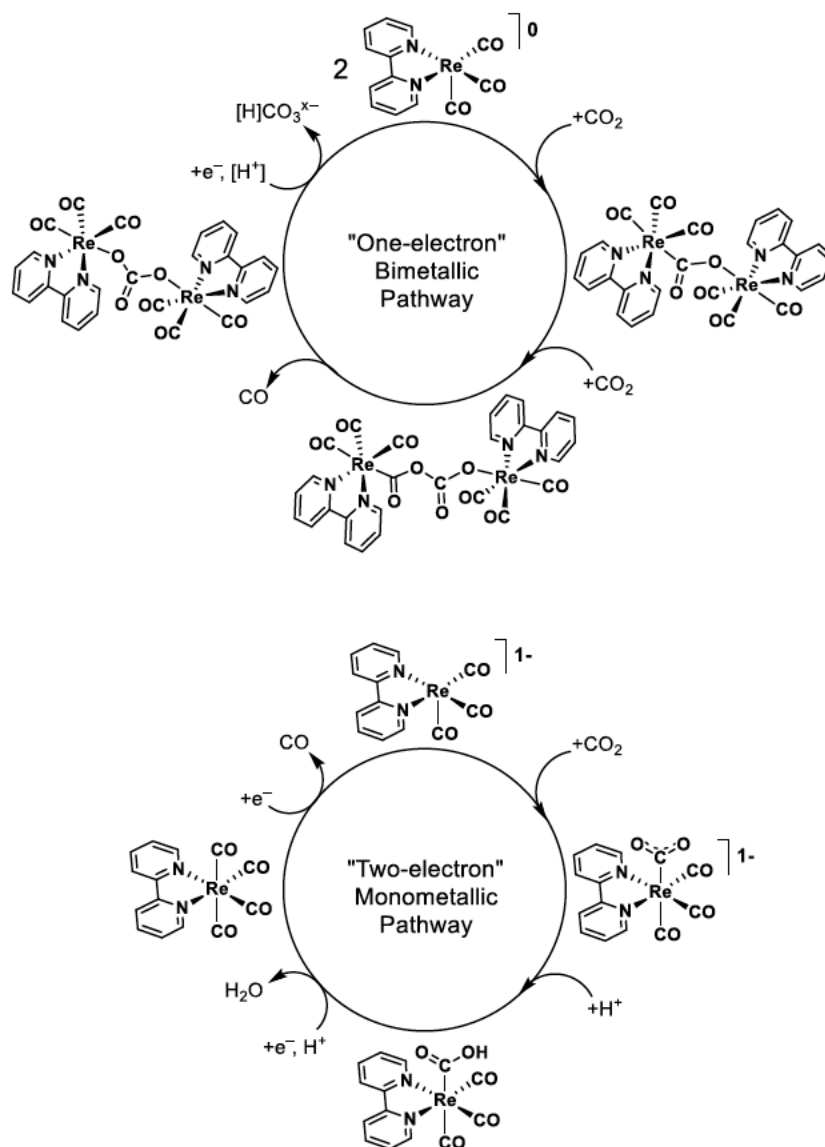
Figure A20. Reported catalytic cycles for the "one-electron" bimetallic (top) and "two-electron" monometallic (bottom) pathways for CO$_2$ reduction by Re(bpy)(CO)$_3$Cl in DMF / 0.1 M Bu$_4$NPF$_6$ (protons originate from Hofmann degradation of the supporting electrolyte).
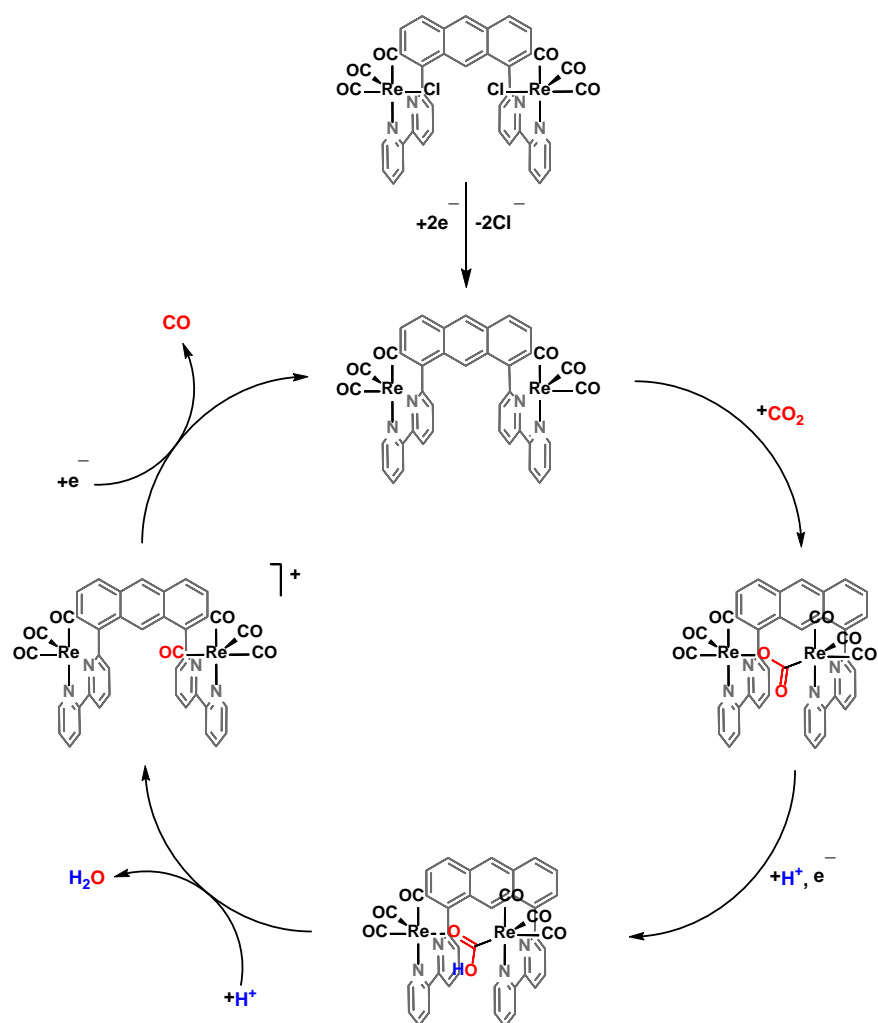
Figure A21. Proposed mechanism for *cis*-Re₂Cl₂ at $E_{appl} = $ -2.5 V vs Fc$^{+/0}$ in DMF/0.1 M Bu₄NPF₆.

Table A1. Cartesian coordinates for optimized *cis*-Re₂Cl₂ conformer.

Element	x	y	z
0 1			
C	-3.91636000	3.82735700	1.19805700
C	-3.02739400	4.54311200	0.46141800
C	-1.68639300	4.08595300	0.28795700
C	-1.27708000	2.86813100	0.91980200
C	-2.27732200	2.08775600	1.59392800
C	-3.54047600	2.57490900	1.75320700

C	-0.77160300	4.77758700	-0.50334900
C	0.06487600	2.48849400	0.86228800
C	0.99581500	3.24561900	0.15429900
C	0.55214500	4.36173400	-0.62064000
C	1.47247400	4.99725900	-1.50858500
H	1.11818800	5.82003100	-2.12174700
C	2.75737200	4.56515500	-1.60800600
C	3.22885500	3.52427100	-0.76246200
C	2.38896700	2.90155900	0.11245300
H	-1.10491500	5.65232700	-1.05476900
H	-4.93263100	4.18034200	1.33184300
H	-3.32483200	5.47225900	-0.01423400
H	-4.28238000	1.98617000	2.28129200
H	0.38676000	1.56342100	1.33033900
H	3.44363100	5.03031600	-2.30656100
H	4.27678000	3.24386200	-0.79653100
C	2.96645400	1.99017600	1.13276200
C	3.06219800	2.46210400	2.44171100
C	3.71050500	1.70417500	3.39523200
H	2.63246400	3.42742800	2.67794700
C	4.12207400	0.06437600	1.70819500
H	3.79426900	2.05276100	4.41850000
C	-1.90412600	0.75823800	2.14395100
C	-1.22878000	0.71429800	3.35861100
C	-0.87644300	-0.50444400	3.90488000
H	-1.00323200	1.64760100	3.85978900
C	-1.82868000	-1.54626500	1.97717400
H	-0.37060000	-0.56192100	4.86186700
C	4.27355800	0.49616300	3.01534400
H	4.79150700	-0.11549700	3.74166700
C	-1.18413800	-1.65186200	3.20160400
H	-0.92731600	-2.62283900	3.60166100
N	3.44347300	0.78610800	0.78825200
N	-2.21412000	-0.36113300	1.46215700
C	4.68263000	-1.21922400	1.23421200
C	5.64240500	-1.93393000	1.94373500
C	4.70822800	-2.79372400	-0.45854400
C	6.12963900	-3.12011800	1.42344800
H	6.02264200	-1.56060800	2.88529300
H	4.30898800	-3.09237100	-1.41903600
H	6.87893800	-3.68721200	1.96401500
C	-2.17262900	-2.75186700	1.19659200
C	-1.54108400	-3.97400500	1.39447600

C	-3.52479800	-3.66653300	-0.43649600
C	-1.94390300	-5.07133200	0.65485900
H	-0.71161600	-4.05304400	2.08368900
H	-4.29497500	-3.49345400	-1.17621400
H	-1.45165400	-6.02844700	0.78443400
N	4.23538900	-1.64599500	0.04135400
N	-3.12778800	-2.59863700	0.26532700
C	-2.97253300	-4.92115800	-0.26287800
H	-3.32475000	-5.74942400	-0.86460900
C	5.65014400	-3.56243300	0.19920600
H	6.00056000	-4.48291800	-0.25034400
Re	2.72036900	-0.41875100	-0.96269800
Re	-3.52531300	-0.54051200	-0.39886800
C	-5.06380800	-0.19694100	0.64740300
O	-6.00497300	0.02959800	1.28414800
C	-4.64672300	-1.00582500	-1.85060600
O	-5.34327600	-1.31415100	-2.71563100
C	-3.54772200	1.22950900	-1.12956800
O	-3.56469900	2.25551200	-1.64206100
C	2.14319700	-1.74227000	-2.20080100
O	1.84500600	-2.57598400	-2.93345300
C	3.95536900	0.25305400	-2.22238800
O	4.71925500	0.66998200	-2.98472000
C	1.41462200	0.74493100	-1.77433500
O	0.71273300	1.44975500	-2.33876800
Cl	-1.45371700	-1.03168500	-1.66580100
Cl	1.29117000	-1.30290900	0.91136100

Zero-point correction =   0.535847 (Hartree/Part.)
Thermal correction to Energy =   0.582462
Thermal correction to Enthalpy =   0.583406
Thermal correction to Gibbs Free Energy =   0.452529
Sum of electronic and zero-point Energies =   -3286.154382
Sum of electronic and thermal Energies =   -3286.107767
Sum of electronic and thermal Enthalpies =   -3286.106823
Sum of electronic and thermal Free Energies =   -3286.237700

Table A2. Cartesian coordinates for optimized transition state (TS1) associated with rotational interconversion between *cis*-Re$_2$Cl$_2$ and *trans*-Re$_2$Cl$_2$ conformers.

Element	x	y	z
0 1			
C	-4.29286500	4.41319400	0.87256100
C	-3.13133400	4.92373300	0.38192600

```
C          -1.95900000       4.11544100       0.29330500
C          -2.01056300       2.76527600       0.74059700
C          -3.23539800       2.27997400       1.30501100
C          -4.34125900       3.07663000       1.35408100
C          -0.78720300       4.55480200      -0.31391900
C          -0.91383800       1.92406400       0.55228400
C           0.28552900       2.36170300      -0.01043400
C           0.31212400       3.71795400      -0.49678200
C           1.41166700       4.17247200      -1.28489400
H           1.41681100       5.20250800      -1.62759200
C           2.38403000       3.30567000      -1.65787000
C           2.38377100       1.98507300      -1.15195800
C           1.45126000       1.52280300      -0.26006200
H          -0.74768200       5.56103900      -0.72172000
H          -5.18884900       5.02219300       0.91388800
H          -3.08598300       5.94808900       0.02528900
H          -5.26384800       2.69529300       1.77986300
H          -1.07625600       0.87239600       0.72127000
H           3.19092200       3.60623900      -2.31605400
H           3.17767600       1.33544100      -1.48729800
C           1.66568900       0.17104500       0.32663000
C           0.83790300      -0.39817200       1.30169000
C           0.90660100      -1.74802800       1.58156200
H           0.14346200       0.21211100       1.85224400
C           2.74872100      -1.87910100       0.11183800
H           0.23401300      -2.18222800       2.31200700
C          -3.25103200       0.95002600       1.96684900
C          -2.68940700       0.85130600       3.23949700
C          -2.71875000      -0.35586600       3.90765100
H          -2.23670200       1.73223800       3.67701400
C          -3.87797600      -1.28297600       2.03281200
H          -2.27605300      -0.45697400       4.89209100
C           1.81802900      -2.53488200       0.90095100
H           1.87675000      -3.60417800       1.05697400
C          -3.34044300      -1.43553500       3.30088300
H          -3.38450400      -2.38892800       3.80918300
N           2.73191800      -0.55339500      -0.10342600
N          -3.79742500      -0.11323600       1.35839200
C           3.88693900      -2.61537600      -0.48501200
C           3.75145600      -3.89646500      -1.00348400
C           6.11445000      -2.54201500      -1.09367900
C           4.85485500      -4.50778900      -1.57629100
H           2.78591800      -4.38667300      -0.98764900
```

159

```
H                    7.02076800    -1.95145800    -1.12917100
H                    4.77042600    -5.50231800    -1.99962700
C                   -4.57999100    -2.38612400     1.33997000
C                   -4.92697200    -3.57742900     1.96918600
C                   -5.55822200    -3.10279300    -0.62897400
C                   -5.60132800    -4.55357200     1.25665600
H                   -4.68862300    -3.74378800     3.01082000
H                   -5.78995000    -2.87057900    -1.65997600
H                   -5.87601500    -5.48676500     1.73482100
N                    5.05360900    -1.95562100    -0.52722900
N                   -4.90452700    -2.15700800     0.05609100
C                   -5.92222900    -4.31333600    -0.07064000
H                   -6.44926300    -5.04404700    -0.67091500
C                    6.05864100    -3.81929000    -1.62081200
H                    6.94321400    -4.25208500    -2.07046400
Re                   5.03639900     0.10915900     0.22063100
Re                  -4.21400100    -0.28138900    -0.84674200
C                   -5.90499800     0.56725500    -0.76134600
O                   -6.93095300     1.09434600    -0.70145200
C                   -4.54494000    -0.79034400    -2.64414600
O                   -4.76642200    -1.13018900    -3.72133900
C                   -3.48286100     1.32570100    -1.59914500
O                   -3.08396700     2.26551900    -2.12036500
C                    6.86960400     0.29089400     0.59967400
O                    7.99483200     0.37477200     0.83118900
C                    4.74271300    -0.37313200     2.02962000
O                    4.57222400    -0.66371500     3.13458500
C                    4.84235800     1.94729300     0.71906000
O                    4.73779800     3.04548500     1.03486000
Cl                  -1.98959000    -1.42819900    -0.73260200
Cl                   5.37290600     0.57551100    -2.19989300


Zero-point correction =                         0.53634 (Hartree/Part.)
Thermal correction to Energy =                  0.582311
Thermal correction to Enthalpy =                0.583255
Thermal correction to Gibbs Free Energy =       0.453217
Sum of electronic and zero-point Energies =    -3286.126771
Sum of electronic and thermal Energies =       -3286.080802
Sum of electronic and thermal Enthalpies =     -3286.079858
Sum of electronic and thermal Free Energies =  -3286.209896
```

Table A3. Cartesian coordinates for optimized *trans*-Re$_2$Cl$_2$ conformer.

Element	x	y	z
0 1			
C	2.93457600	-3.82925000	2.18716800
C	2.00117600	-4.49717300	1.45853300
C	0.99121400	-3.79273900	0.73679100
C	0.97006700	-2.36348200	0.78745900
C	1.95327700	-1.69662000	1.59258900
C	2.90208200	-2.41143000	2.26237000
C	0.04053200	-4.45631100	-0.03532800
C	0.03903100	-1.66704400	0.01930500
C	-0.89307700	-2.33351000	-0.77338100
C	-0.91005000	-3.76399600	-0.78151800
C	-1.90228600	-4.44105200	-1.55311900
H	-1.91531200	-5.52649000	-1.54428200
C	-2.82196100	-3.74435000	-2.27059100
C	-2.80011800	-2.32394400	-2.28194200
C	-1.86579000	-1.63586800	-1.56483100
H	0.04477400	-5.54247000	-0.06177100
H	3.70808400	-4.36896600	2.72158600
H	2.01769800	-5.58117600	1.40283900
H	3.64200200	-1.89342300	2.86330600
H	0.05320400	-0.58308700	0.02275000
H	-3.58581800	-4.26237700	-2.83901500
H	-3.54956000	-1.78150200	-2.84697400
C	-1.80437800	-0.15712500	-1.68081900
C	-0.75555500	0.40430200	-2.40403800
C	-0.70771200	1.77049700	-2.59144500
H	0.02499100	-0.23831100	-2.79035200
C	-2.76026700	1.93272100	-1.37281600
H	0.12459400	2.22123900	-3.11770600
C	1.88974500	-0.22418200	1.76118800
C	0.82842800	0.31514700	2.48382100
C	0.76941600	1.67713400	2.69628200
H	0.05367200	-0.34205900	2.85589400
C	2.83164500	1.88070700	1.50203500
H	-0.06699300	2.10960300	3.23190600
C	-1.74301000	2.54265800	-2.09124000
H	-1.73843200	3.61365800	-2.24254100
C	1.80096300	2.46922300	2.21756700
H	1.78266200	3.53754100	2.38467700
N	-2.76140600	0.60463800	-1.12131700
N	2.85272700	0.55422200	1.23988200
C	-3.91055900	2.69767500	-0.84191200

161

```
C            -4.18376300      4.01060900     -1.21491400
C            -5.80446800      2.64929800      0.48617400
C            -5.30089800      4.64677400     -0.70302000
H            -3.54538400      4.52799800     -1.91797700
H            -6.43106200      2.06284700      1.14457500
H            -5.52624100      5.66782800     -0.98924000
C             3.98114600      2.66032100      0.99104100
C             4.20569100      3.99259800      1.32519000
C             5.92087000      2.62096600     -0.27183700
C             5.32146700      4.64251600      0.82829000
H             3.52315600      4.52167500      1.97602300
H             6.57510200      2.03371400     -0.90260100
H             5.50446900      5.68134900      1.07815100
N            -4.71761900      2.03549000      0.00374600
N             4.83883700      1.99052300      0.20123900
C             6.19973300      3.94326000      0.01391500
H             7.08761700      4.40612900     -0.39760700
C            -6.13006200      3.95304500      0.16509100
H            -7.02266400      4.40176400      0.58206600
Re           -4.24749100     -0.06534900      0.43782700
Re            4.29141600     -0.04830700     -0.38442000
C             5.52391500     -0.89767600      0.77293700
O             6.27215000     -1.42377400      1.47896800
C             5.53011300     -0.20114700     -1.81327300
O             6.29930300     -0.26381400     -2.66788800
C             3.64327800     -1.76514700     -0.94323000
O             3.29941700     -2.78924800     -1.32749100
C            -5.61825500     -0.33497100      1.72191100
O            -6.45156300     -0.46342700      2.50625600
C            -3.05427500      0.35205600      1.83695600
O            -2.33004100      0.61407100      2.70575900
C            -3.84948200     -1.92585300      0.68674700
O            -3.64894900     -3.03371500      0.90553800
Cl            2.59414800      1.16406400     -1.77806100
Cl           -5.76118200     -0.44335400     -1.50172000
```

Zero-point correction =   0.537264 (Hartree/Part.)
Thermal correction to Energy =   0.583698
Thermal correction to Enthalpy =   0.584642
Thermal correction to Gibbs Free Energy =   0.454402
Sum of electronic and zero-point Energies = -3286.170118
Sum of electronic and thermal Energies =   -3286.123685

```
Sum of electronic and thermal Enthalpies =      -3286.122740
Sum of electronic and thermal Free Energies =   -3286.252980
```

Table A4. Cartesian coordinates for optimized transition state (TS2) associated with rotational interconversion between *trans*-Re$_2$Cl$_2$ and *cis* 2 conformers.

Element	x	y	z
0 1			
C	1.64149900	4.24804200	0.20481500
C	0.42174600	4.81821800	0.34732100
C	-0.68267200	4.03155400	0.79298100
C	-0.47703900	2.66220000	1.18859800
C	0.89554800	2.15186300	1.24762200
C	1.84634000	2.90820900	0.61214000
C	-1.97132400	4.55354900	0.69881900
C	-1.62925800	1.89597300	1.34261400
C	-2.92245900	2.39902400	1.21236400
C	-3.10856900	3.77484200	0.90204700
C	-4.43171100	4.28347400	0.74569700
H	-4.56381000	5.33084500	0.49308000
C	-5.50830600	3.46606800	0.89407300
C	-5.33050800	2.09804600	1.23073900
C	-4.08262400	1.56542900	1.37984700
H	-2.09107100	5.58997900	0.39543100
H	2.48062400	4.79465400	-0.20921200
H	0.24693700	5.85129200	0.06336500
H	2.86227700	2.54663700	0.55290400
H	-1.55537200	0.83289100	1.44201800
H	-6.51250100	3.84954900	0.75403900
H	-6.20137700	1.46145500	1.34939400
C	-3.92806300	0.17050600	1.86538300
C	-4.43895100	-0.13983200	3.12343200
C	-4.25142600	-1.40361700	3.64982400
H	-4.96985900	0.62637300	3.67361000
C	-3.02320900	-1.96020500	1.67870700
H	-4.66549000	-1.66766900	4.61629100
C	1.23832800	0.72855200	1.56325000
C	0.40583100	-0.06125500	2.37889000
C	0.84769700	-1.23965100	2.94588400
H	-0.57330500	0.27591600	2.66195900
C	2.97931600	-0.76899900	2.04917500
H	0.16822100	-1.83518700	3.54637200
C	-3.51104100	-2.32111500	2.92633600

163
```

| | | | |
|---|---|---|---|
| H | −3.35072400 | −3.31799000 | 3.31379400 |
| C | 2.17103200 | −1.60645700 | 2.80023700 |
| H | 2.56737200 | −2.51206300 | 3.24128800 |
| N | −3.26176100 | −0.74648500 | 1.13724600 |
| N | 2.53527300 | 0.33867500 | 1.43683300 |
| C | −2.19944500 | −2.88423700 | 0.86894500 |
| C | −1.58883700 | −4.01284400 | 1.40313900 |
| C | −1.25288200 | −3.30492800 | −1.19809600 |
| C | −0.79651200 | −4.80658400 | 0.59021300 |
| H | −1.71595800 | −4.26605700 | 2.44739100 |
| H | −1.13184700 | −2.97432300 | −2.22076300 |
| H | −0.31355000 | −5.68974800 | 0.99269700 |
| C | 4.41337800 | −1.09627600 | 1.86683300 |
| C | 5.17754400 | −1.65378700 | 2.88411400 |
| C | 6.23588300 | −1.04717700 | 0.45051000 |
| C | 6.51742800 | −1.91827100 | 2.65116100 |
| H | 4.73309500 | −1.84284000 | 3.85334700 |
| H | 6.61636900 | −0.76327400 | −0.52191200 |
| H | 7.13640300 | −2.34233900 | 3.43371500 |
| N | −2.02364400 | −2.53955400 | −0.41790800 |
| N | 4.93804900 | −0.80385900 | 0.66907400 |
| C | 7.05596900 | −1.61162600 | 1.41045200 |
| H | 8.10026300 | −1.78795900 | 1.18629900 |
| C | −0.62468900 | −4.44661000 | −0.73624900 |
| H | −0.00277900 | −5.02348400 | −1.40806200 |
| Re | −3.00469300 | −0.70894000 | −1.11467100 |
| Re | 3.65676100 | 0.24509400 | −0.76534100 |
| C | 2.46617600 | −1.18734900 | −1.09247400 |
| O | 1.73895800 | −2.06600500 | −1.28887400 |
| C | 4.59941500 | −0.23034200 | −2.31552700 |
| O | 5.19386400 | −0.54906300 | −3.25040500 |
| C | 2.60695300 | 1.38915300 | −1.90320400 |
| O | 2.04658700 | 2.08792000 | −2.61360100 |
| C | −2.89597900 | −1.07064100 | −2.97497100 |
| O | −2.81611400 | −1.31703600 | −4.09501000 |
| C | −1.33753500 | 0.17726600 | −1.23634300 |
| O | −0.30515500 | 0.68245800 | −1.34592200 |
| C | −3.90604900 | 0.91122300 | −1.59694200 |
| O | −4.42013100 | 1.88190600 | −1.92984400 |
| Cl | 5.18926700 | 2.10349200 | −0.14822200 |
| Cl | −5.11364900 | −2.02227800 | −0.87281900 |

```
Zero-point correction =                              0.536558 (Hartree/Particle)
Thermal correction to Energy =                       0.582441
Thermal correction to Enthalpy =                     0.583385
Thermal correction to Gibbs Free Energy =            0.455008
Sum of electronic and zero-point Energies =    -3286.119454
Sum of electronic and thermal Energies =       -3286.073571
Sum of electronic and thermal Enthalpies =     -3286.072627
Sum of electronic and thermal Free Energies =  -3286.201004
```

Table A5. Cartesian coordinates for optimized *cis* 2 conformer.

Element	x	y	z
0 1			
C	4.89187500	3.48157000	0.87304700
C	3.92244100	4.21857400	0.27202300
C	2.55890500	3.79303000	0.29289700
C	2.22527700	2.56256900	0.93951100
C	3.29200000	1.77748000	1.49850000
C	4.57190200	2.24297100	1.49351700
C	1.53846600	4.55322300	-0.27408300
C	0.88539700	2.19216600	1.04953600
C	-0.14144400	3.00134700	0.56537300
C	0.19820400	4.19097700	-0.15411700
C	-0.84587300	4.99398300	-0.70468500
H	-0.57480700	5.87884900	-1.27211200
C	-2.15037200	4.66292500	-0.52079900
C	-2.49804000	3.51623400	0.23953800
C	-1.53423300	2.70241300	0.76380300
H	1.79185100	5.46864200	-0.80160600
H	5.92442500	3.81041800	0.85304800
H	4.16796400	5.14935500	-0.22942300
H	5.36448400	1.63583700	1.91852800
H	0.63568200	1.25295100	1.52935900
H	-2.94146200	5.26957200	-0.94589500
H	-3.54481200	3.27662700	0.39100600
C	-1.95076000	1.61302800	1.67952200
C	-1.54084100	1.68755900	3.01342900
C	-1.99393800	0.75985600	3.92586900
H	-0.87653300	2.49003700	3.30787800
C	-3.26939400	-0.23468400	2.16526900
H	-1.67899700	0.80052200	4.96248600
C	2.95675700	0.48464000	2.14389600
C	2.91398300	0.41397400	3.53172400
```
165
```

C	2.52481700	-0.76457200	4.14154700
H	3.18440100	1.29031300	4.10734700
C	2.21563800	-1.70591100	1.96461300
H	2.50511300	-0.85103900	5.22225900
C	-2.88731000	-0.20875000	3.49706500
H	-3.26937700	-0.94012400	4.19593500
C	2.15026800	-1.83178400	3.34620000
H	1.84039900	-2.76255800	3.80068600
N	-2.76643800	0.63123700	1.25481700
N	2.64603400	-0.57286700	1.37286800
C	-4.25498400	-1.22028400	1.66572100
C	-5.05735300	-1.97694100	2.51419900
C	-5.26173200	-2.16914500	-0.18601100
C	-5.97660000	-2.86041500	1.97591100
H	-4.98915100	-1.85996100	3.58719100
H	-5.32446900	-2.19813800	-1.26545500
H	-6.61240600	-3.45107200	2.62545800
C	1.80452400	-2.80127200	1.05848500
C	1.13166500	-3.93460600	1.50080900
C	1.71623900	-3.55557800	-1.12185700
C	0.75818500	-4.90438200	0.58671400
H	0.89139700	-4.06301000	2.54748500
H	1.95457200	-3.35822100	-2.15813400
H	0.23621800	-5.79507100	0.91758100
N	-4.36540200	-1.32088100	0.33151800
N	2.08383500	-2.61960800	-0.24185800
C	1.05759400	-4.71263000	-0.75198200
H	0.78225300	-5.43752200	-1.50722300
C	-6.07962200	-2.96163600	0.59726000
H	-6.79036400	-3.62889500	0.12649000
Re	-3.18207500	0.05191600	-0.90245800
Re	3.20460400	-0.82468000	-0.80950400
C	1.71296600	0.10778600	-1.51915400
O	0.83185000	0.69834300	-1.97101400
C	3.64089000	-1.42001400	-2.55335100
O	3.88261500	-1.80867700	-3.61022400
C	4.30407800	0.68224700	-1.23095100
O	4.97806900	1.54914300	-1.56792800
C	-3.68525300	-0.67691800	-2.57561100
O	-4.00043600	-1.15515900	-3.57536100
C	-1.66551200	-1.07227800	-0.89517600
O	-0.76683400	-1.80086500	-0.85779600
C	-2.25130300	1.38894000	-1.92868100

166

```
O                   -1.74774800     2.16733800    -2.59876700
Cl                   5.09744200    -2.02982400     0.28933200
Cl                  -5.24670200     1.43332500    -0.66377800


Zero-point correction =                        0.536745 (Hartree/Particle)
Thermal correction to Energy =                 0.583152
Thermal correction to Enthalpy =               0.584096
Thermal correction to Gibbs Free Energy =      0.453952
Sum of electronic and zero-point Energies =   -3286.157474
Sum of electronic and thermal Energies =      -3286.111067
Sum of electronic and thermal Enthalpies =    -3286.110123
Sum of electronic and thermal Free Energies = -3286.240267
```

Table A6. Cartesian coordinates for symmetric *cis*-Re$_2$Cl$_2$ (Cl in), calculated infrared spectrum in DMF.

Element	x	y	z
0 1			
C	-3.64109700	3.92809100	1.29858000
C	-2.65428200	4.66424000	0.68759200
C	-1.33680200	4.13568100	0.53428300
C	-1.03832200	2.81393800	1.05085800
C	-2.12415800	2.03715900	1.58936400
C	-3.37680000	2.60290500	1.73206100
C	-0.33297300	4.84895800	-0.13918900
C	0.28559800	2.34952300	0.99515000
C	1.30736000	3.12118700	0.42536500
C	0.97623400	4.35666900	-0.24625700
C	1.98573500	5.02017200	-1.00864200
H	1.72619400	5.94299700	-1.53210600
C	3.25701600	4.50018600	-1.09429700
C	3.61174600	3.34178600	-0.35004200
C	2.67451700	2.68431100	0.42214000
H	-0.58275800	5.80709700	-0.60248100
H	-4.64173000	4.34233700	1.42914100
H	-2.86224400	5.66716000	0.30823000
H	-4.17855900	2.01521400	2.17870000
H	0.53425200	1.35090500	1.36070400
H	4.01763700	4.99920600	-1.69657500
H	4.64521900	2.99117800	-0.35495200
C	3.12687800	1.64363100	1.37874000
C	3.11022000	1.94682200	2.74723500

167

C	3.67444700	1.05989000	3.65829200
H	2.67059000	2.89005400	3.06942400
C	4.21754100	−0.38772400	1.81283200
H	3.67172400	1.28094100	4.72587100
C	−1.89448200	0.63800800	2.02859400
C	−1.04545300	0.40156600	3.11782800
C	−0.82078600	−0.89737100	3.55650900
H	−0.57079200	1.25261400	3.60499600
C	−2.34352500	−1.65820700	1.84882000
H	−0.14943400	−1.09805400	4.39139200
C	4.26548300	−0.10687600	3.17938900
H	4.73018000	−0.80841300	3.86926700
C	−1.48696800	−1.93626400	2.91759200
H	−1.34107700	−2.96019100	3.25324400
N	3.61569800	0.46488500	0.92653900
N	−2.52169600	−0.38273400	1.37924800
C	4.78448200	−1.61395100	1.23093700
C	5.64432400	−2.47372100	1.92577800
C	4.96393800	−2.93935800	−0.68675700
C	6.16393900	−3.59435600	1.28432700
H	5.91840400	−2.26000500	2.95726500
H	4.66768900	−3.08132000	−1.72468400
H	6.83516800	−4.26945500	1.81561400
C	−3.13243100	−2.71530100	1.19350300
C	−3.09239200	−4.06086300	1.58483500
C	−4.76396800	−3.21357900	−0.40772600
C	−3.91331900	−4.99106800	0.95593600
H	−2.42564400	−4.38386300	2.38128600
H	−5.41012100	−2.83337400	−1.19654100
H	−3.88444100	−6.03914300	1.25466500
N	4.45019700	−1.85488600	−0.06739700
N	−3.95817400	−2.30747100	0.18921700
C	−4.77483500	−4.55667300	−0.05421600
H	−5.44535500	−5.24306100	−0.56981400
C	5.81898800	−3.83023800	−0.04897600
H	6.20478900	−4.68978400	−0.59567700
Re	3.03281500	−0.47802000	−0.98101000
Re	−3.72302400	−0.26822200	−0.50957800
C	−5.28387000	0.38786700	0.35808000
O	−6.25704800	0.79384200	0.87174800
C	−4.74311700	−0.48735800	−2.10315900
O	−5.38100100	−0.63887200	−3.07217600
C	−3.28664400	1.48573700	−1.17196100

168

```
O                    -3.02447800     2.51570500    -1.65060200
C                     2.54921200    -1.61510000    -2.43676200
O                     2.26774500    -2.33293100    -3.31577400
C                     4.36845700     0.35668500    -2.04852100
O                     5.18337900     0.88138600    -2.70731200
C                     1.75901300     0.77419100    -1.69874300
O                     1.01005500     1.50704800    -2.21095200
Cl                   -1.66998300    -1.18481200    -1.58643500
Cl                    1.39887800    -1.53754300     0.58868200
```

```
Zero-point correction =                         0.514427 (Hartree/Particle)
Thermal correction to Energy =                  0.562481
Thermal correction to Enthalpy =                0.563425
Thermal correction to Gibbs Free Energy =       0.429315
Sum of electronic and zero-point Energies =    -3287.740995
Sum of electronic and thermal Energies =       -3287.692941
Sum of electronic and thermal Enthalpies =     -3287.691997
```

Table A7. Cartesian coordinates for symmetric *cis* 2 (Cl out), calculated infrared spectrum in DMF.

Element	x	y	z
0 1			
C	-3.89621800	3.98237400	1.00661400
C	-2.88429400	4.70904400	0.42505200
C	-1.55308600	4.19498900	0.36969400
C	-1.27374000	2.90724900	0.96972800
C	-2.37220100	2.14814000	1.49778000
C	-3.64403600	2.68450100	1.52678600
C	-0.51191400	4.88481300	-0.27100600
C	0.05013200	2.44376900	1.00863500
C	1.10027000	3.17991300	0.44615400
C	0.80250500	4.39303600	-0.28274400
C	1.85310400	5.03964400	-1.00263900
H	1.62148500	5.94626900	-1.56614500
C	3.12832600	4.52334500	-0.99963300
C	3.44070000	3.37575800	-0.22079500
C	2.46196700	2.73162500	0.50982600
H	-0.73356400	5.82368500	-0.78530900
H	-4.91002800	4.38355300	1.04637500
H	-3.08456500	5.68990400	-0.01188400
H	-4.46458500	2.08660300	1.92492100

169

H	0.27056900	1.47873800	1.46793400
H	3.92135900	5.01075700	-1.56892500
H	4.46532100	3.00452800	-0.18624300
C	2.85809100	1.67385800	1.47461100
C	2.83546100	1.97944000	2.84235900
C	3.33843600	1.06749800	3.76418900
H	2.43742600	2.94402800	3.15564500
C	3.86003600	-0.39949300	1.92584400
H	3.32617500	1.28851200	4.83163800
C	-2.10471900	0.81306600	2.09345000
C	-1.51831500	0.77032500	3.36453400
C	-1.26927900	-0.45352100	3.97445300
H	-1.26993700	1.71078000	3.85530700
C	-2.20629600	-1.52609600	2.02763200
H	-0.81617800	-0.50511300	4.96460100
C	3.88731500	-0.12359800	3.29442900
H	4.31282000	-0.84233700	3.99190000
C	-1.62969000	-1.61286600	3.29775600
H	-1.46654700	-2.58259500	3.76194000
N	3.29834100	0.47090300	1.02976100
N	-2.42153300	-0.32052800	1.41279600
C	4.41649900	-1.63554900	1.35173400
C	5.23847800	-2.51566600	2.06625000
C	4.62637400	-2.95390900	-0.56700100
C	5.75665900	-3.64238000	1.43333900
H	5.48795400	-2.31213800	3.10595200
H	4.35959100	-3.08424300	-1.61421500
H	6.39975400	-4.33220500	1.98023900
C	-2.62907700	-2.72620200	1.28792000
C	-2.42919700	-4.03150700	1.75807900
C	-3.69542500	-3.55804700	-0.61913300
C	-2.88405000	-5.11442900	1.01244900
H	-1.91805800	-4.20529300	2.70234000
H	-4.18826600	-3.32519600	-1.56109400
H	-2.73107700	-6.13202900	1.37249800
N	4.11245400	-1.86570600	0.04431600
N	-3.24776100	-2.50269300	0.09638100
C	-3.53836300	-4.87227800	-0.19720900
H	-3.91996900	-5.68449300	-0.81467200
C	5.44764400	-3.86370800	0.08950600
H	5.83558000	-4.72565900	-0.45185800
Re	2.81921800	-0.41341500	-0.94214000
Re	-3.36262600	-0.44542500	-0.60694100

```
C                    -4.33660700    -0.82298300    -2.19856100
O                    -4.94004900    -1.07127100    -3.16968000
C                    -3.35129800     1.37677800    -1.21774800
O                    -3.31529500     2.43336600    -1.71322400
C                     2.49981600    -1.44089700    -2.51797000
O                     2.30624700    -2.09826900    -3.46593100
C                     1.76194400     0.96089300    -1.77521900
O                     1.12166100     1.75727500    -2.33689900
C                     1.26616300    -1.17416900    -0.15155800
O                     0.34011000    -1.66059300     0.37552900
C                    -1.77372400    -0.66891700    -1.63056100
O                    -0.85155200    -0.81059800    -2.33735800
Cl                    4.97311500     0.54049700    -1.75854900
Cl                   -5.46896400    -0.32397900     0.73947000
```

```
Zero-point correction =                         0.514621 (Hartree/Particle)
Thermal correction to Energy =                  0.562664
Thermal correction to Enthalpy =                0.563608
Thermal correction to Gibbs Free Energy =       0.429354
Sum of electronic and zero-point Energies =    -3287.742226
Sum of electronic and thermal Energies =       -3287.694183
Sum of electronic and thermal Enthalpies =     -3287.693239
Sum of electronic and thermal Free Energies =  -3287.827493
```

Table A8. Cartesian coordinates for asymmetric *trans*-Re_2Cl_2, calculated infrared spectrum in DMF.

Element	x	y	z
0 1			
C	2.80502	-3.74458	2.37334
C	1.89857	-4.43833	1.60579
C	0.93574	-3.74858	0.80773
C	0.91585	-2.30185	0.83035
C	1.87307	-1.61367	1.65031
C	2.79204	-2.32344	2.39605
C	0.02437	-4.42911	-0.01466
C	0.00112	-1.61644	0.01885
C	-0.89778	-2.29818	-0.81240
C	-0.89379	-3.74475	-0.82618
C	-1.82669	-4.42899	-1.66363
H	-1.81848	-5.52121	-1.67294
C	-2.72357	-3.72934	-2.43658

171

C	-2.73467	-2.30790	-2.42386
C	-1.84567	-1.60410	-1.63689
H	0.03537	-5.52290	-0.02918
H	3.54163	-4.27940	2.97472
H	1.90821	-5.53040	1.58689
H	3.51477	-1.78616	3.01165
H	-0.00583	-0.52586	0.02543
H	-3.43766	-4.26034	-3.06794
H	-3.46199	-1.76303	-3.02681
C	-1.79193	-0.12066	-1.71570
C	-0.75510	0.46211	-2.45362
C	-0.69429	1.84380	-2.59293
H	0.00436	-0.18155	-2.89470
C	-2.70967	1.99209	-1.27769
H	0.12100	2.31052	-3.14518
C	1.81399	-0.13250	1.74061
C	0.74933	0.44786	2.43973
C	0.66630	1.83077	2.55407
H	-0.01091	-0.19978	2.87235
C	2.72657	1.98523	1.31097
H	-0.16959	2.29542	3.07702
C	-1.69874	2.61374	-2.01679
H	-1.68611	3.69562	-2.12899
C	1.67822	2.60574	1.99638
H	1.64654	3.68918	2.08805
N	-2.73158	0.63512	-1.09015
N	2.77372	0.62513	1.15068
C	-3.80623	2.75302	-0.65581
C	-3.99648	4.12808	-0.84879
C	-5.70507	2.66148	0.70560
C	-5.07079	4.77035	-0.24052
H	-3.31547	4.69549	-1.47960
H	-6.36003	2.04141	1.31467
H	-5.22557	5.83948	-0.38730
C	3.85248	2.74289	0.74096
C	4.01373	4.12566	0.90204
C	5.87084	2.62451	-0.43569
C	5.13510	4.75757	0.37357
H	3.27134	4.70757	1.44423
H	6.58245	1.98974	-0.96052
H	5.26663	5.83309	0.49383
N	-4.66141	2.03316	0.12191
N	4.77856	2.00650	0.06491

```
C                       6.08662          3.99042        -0.30246
H                       6.98546          4.43657        -0.72628
C                      -5.94366          4.02181         0.55144
H                      -6.80137          4.47649         1.04561
Re                     -4.25318         -0.09497         0.35291
Re                      4.30645         -0.08543        -0.28748
C                       5.46974         -0.74260         1.06687
O                       6.18165         -1.16127         1.89824
C                       5.66807         -0.36898        -1.59347
O                       6.51398         -0.51965        -2.38708
C                       3.73985         -1.88219        -0.67681
O                       3.44821         -2.97063        -0.97620
C                      -5.68593         -0.44284         1.56234
O                      -6.56654         -0.63439         2.30823
C                      -3.11608          0.20845         1.84524
O                      -2.43551          0.39427         2.78185
C                      -3.86445         -1.97334         0.49892
O                      -3.67718         -3.11061         0.67934
Cl                      2.69061          0.84232        -1.95506
Cl                     -5.69935         -0.33825        -1.66663
```

Zero-point correction = 0.514483 (Hartree/Particle)
Thermal correction to Energy = 0.562698
Thermal correction to Enthalpy = 0.563642
Thermal correction to Gibbs Free Energy = 0.427710
Sum of electronic and zero-point Energies = -3287.747424
Sum of electronic and thermal Energies = -3287.699209
Sum of electronic and thermal Enthalpies = -3287.698265
Sum of electronic and thermal Free Energies = -3287.834197

Table A9. Cartesian coordinates for optimized neutral Re-Re dimer.

Element	x	y	z
0 1			
C	-3.55240500	-4.13813000	0.77089800
C	-4.43355600	-3.17443900	0.37084500
C	-4.11299500	-1.78797500	0.51476500
C	-2.87228200	-1.45337600	1.13854300
C	-1.95753200	-2.48342600	1.53110200
C	-2.29355300	-3.79434400	1.35079000
C	-4.91285000	-0.75580200	0.01095500
C	-2.50851500	-0.12365100	1.27369400

C	-3.26889000	0.89487000	0.72061600
C	-4.49904300	0.58070700	0.06544500
C	-5.22519500	1.65422300	-0.54036000
H	-6.15844600	1.43354400	-1.05047900
C	-4.73947400	2.93010900	-0.50989600
C	-3.50872900	3.23688900	0.14565000
C	-2.78787600	2.24619600	0.74669000
H	-5.84764300	-1.00255200	-0.48625200
H	-3.79375000	-5.18668100	0.63003600
H	-5.37456900	-3.44986500	-0.09661100
H	-1.59634900	-4.58094800	1.62335900
H	-1.56557600	0.11334700	1.74498500
H	-5.28690500	3.73089200	-0.99627500
H	-3.14268700	4.25930800	0.15111100
C	-1.56741300	2.48827200	1.56445100
C	-1.76592800	2.95738800	2.85243100
C	-0.69996100	3.02101700	3.74906500
H	-2.77219100	3.22349100	3.15399500
C	0.72007900	2.24897000	1.96852000
H	-0.84891700	3.35417600	4.77044400
C	-0.68381200	-2.05297100	2.17732200
C	-0.66064500	-1.99313200	3.56010100
C	0.47187700	-1.52079900	4.22599600
H	-1.54941700	-2.29234400	4.10335300
C	1.53867000	-1.34297500	2.07905700
H	0.48473500	-1.42563200	5.30632700
C	0.54758500	2.65046900	3.29982200
H	1.39859000	2.70242000	3.96590300
C	1.58105500	-1.20702300	3.47322000
H	2.48923700	-0.86753800	3.95509900
N	-0.33096800	2.12398900	1.10562500
N	0.38858000	-1.66951400	1.41686800
C	2.04215000	2.04382800	1.39517100
C	3.23247000	2.20898300	2.12048100
C	3.26691500	1.77824800	-0.56792800
C	4.44899400	2.17091500	1.47538000
H	3.19768200	2.38281800	3.18852600
H	3.24539200	1.60406400	-1.63560500
H	5.37311700	2.31070900	2.02531900
C	2.73603100	-1.23579400	1.25655300
C	4.03109800	-1.15628200	1.78779500
C	3.61462700	-1.35020300	-0.89600000
C	5.12711800	-1.20123300	0.95200200

H	4.17582000	-1.09272500	2.85861800
H	3.41057100	-1.42641900	-1.95675700
H	6.13228300	-1.16527300	1.35759500
N	2.05513400	1.80498600	0.05420800
N	2.52937900	-1.34839100	-0.08315400
C	4.90781200	-1.29190900	-0.42655800
H	5.72992700	-1.32602400	-1.13207700
C	4.45574000	1.96995800	0.08748200
H	5.38073000	1.94379600	-0.47648100
Re	0.20958500	1.63527400	-0.98291800
Re	0.54553700	-1.71727900	-0.78373000
C	0.63024200	-3.60164700	-0.77236800
O	0.66380600	-4.76591200	-0.76787900
C	1.01402500	-1.72802900	-2.62963500
O	1.34083400	-1.80091700	-3.74209100
C	-1.26991500	-1.84001500	-1.40769000
O	-2.31940300	-1.96780700	-1.87990100
C	1.02596100	1.31429800	-2.67024200
O	1.58700000	1.19960300	-3.68300700
C	-0.05519800	3.44251700	-1.46402300
O	-0.23008700	4.54826200	-1.78487500
C	-1.48130700	1.20882800	-1.80567800
O	-2.47001600	0.99291700	-2.36813200

```
Zero-point correction =                              0.533275 (Hartree/Part.)
Thermal correction to Energy =                       0.575610
Thermal correction to Enthalpy =                     0.576555
Thermal correction to Gibbs Free Energy =            0.458127
Sum of electronic and zero-point Energies =       -2365.184572
Sum of electronic and thermal Energies =          -2365.142236
Sum of electronic and thermal Enthalpies =        -2365.141292
Sum of electronic and thermal Free Energies =     -2365.259720
```

Table A10. Cartesian coordinates for optimized one-electron reduced Re-Re dimer.

Element	x	y	z
-1 2			
C	-5.11334400	-2.21363500	-0.90608100
C	-5.40924600	-0.88854600	-0.76539900
C	-4.54503700	-0.02282700	-0.02276300
C	-3.37300200	-0.58955600	0.56882600
C	-3.10515100	-1.99547400	0.43332400
C	-3.95656600	-2.77953100	-0.29024300

C	−4.78306000	1.34819900	0.12497500
C	−2.47871300	0.23534400	1.23863300
C	−2.66897700	1.60833600	1.30352900
C	−3.86114700	2.18399900	0.76389400
C	−4.01002700	3.60456800	0.83129900
H	−4.91190700	4.05709500	0.42730400
C	−3.01319900	4.38329500	1.34595100
C	−1.80328500	3.80476100	1.83449000
C	−1.62780500	2.45034300	1.81621800
H	−5.67455200	1.78374300	−0.32113200
H	−5.76178100	−2.85522900	−1.49538600
H	−6.29252100	−0.46638100	−1.23753300
H	−3.74861200	−3.83948300	−0.40282700
H	−1.57109600	−0.18456200	1.64986600
H	−3.12163800	5.46371200	1.36310200
H	−1.00598700	4.44872900	2.19305500
C	−0.38787500	1.80381100	2.34238500
C	−0.33725900	1.53444700	3.69210400
C	0.78786400	0.87300400	4.23406200
H	−1.18674600	1.80331900	4.30918700
C	1.79851200	0.99288900	2.04363000
H	0.80928400	0.58089400	5.27919700
C	−1.98261000	−2.54424600	1.24410500
C	−2.33698800	−3.18558800	2.40950400
C	−1.34332300	−3.54105400	3.34987500
H	−3.38890900	−3.34710600	2.61397900
C	0.29596900	−2.63543800	1.82059300
H	−1.60949200	−4.02304700	4.28515800
C	1.84750200	0.61863400	3.41002400
H	2.73132500	0.11849400	3.78858800
C	−0.04437900	−3.24012700	3.05685500
H	0.74155500	−3.49371200	3.75750800
N	0.62158700	1.46762400	1.47821900
N	−0.68142600	−2.27059400	0.90336200
C	2.92952500	0.92962800	1.18772100
C	4.25755500	0.71075400	1.63946300
C	3.74368000	1.19314900	−0.99902100
C	5.30737600	0.75148100	0.76344200
H	4.43855200	0.53742100	2.69354100
H	3.50301800	1.38107500	−2.03900500
H	6.32356000	0.60084300	1.11479100
C	1.64119100	−2.45308000	1.40926600
C	2.77067000	−2.74305500	2.22144700

176

```
C                 3.08379200    -1.98527300    -0.38132100
C                 4.03395400    -2.68632500     1.70263900
H                 2.62547400    -3.01810900     3.25939400
H                 3.17936900    -1.66104100    -1.40950800
H                 4.89714900    -2.90917100     2.32232200
N                 2.68886900     1.20024300    -0.14311900
N                 1.81279900    -2.02232700     0.11122700
C                 4.19311300    -2.31817800     0.34441100
H                 5.17140000    -2.24605700    -0.11484700
C                 5.04148500     0.98267200    -0.60898700
H                 5.83323300     1.00229400    -1.34901500
Re                0.71456600     1.80018900    -0.68184800
Re                0.07988200    -1.63794500    -1.05107900
C                -0.25212800    -3.32847000    -1.79737100
O                -0.46079800    -4.36739600    -2.29186500
C                 1.07400000    -1.15332900    -2.59919200
O                 1.73466400    -0.94726600    -3.53910400
C                -1.49934700    -0.98124500    -1.93354400
O                -2.42490100    -0.61231200    -2.53050300
C                 1.09743200     1.96991000    -2.53952700
O                 1.35577200     2.13644700    -3.66314600
C                 0.91707100     3.65383400    -0.49611400
O                 1.02476200     4.81202300    -0.37696900
C                -1.10368000     2.09307700    -1.22570000
O                -2.15003300     2.33181400    -1.66971500

Zero-point correction =                      0.529699 (Hartree/Particle)
Thermal correction to Energy =                0.572441
Thermal correction to Enthalpy =              0.573385
Thermal correction to Gibbs Free Energy =     0.453371
Sum of electronic and zero-point Energies =   -2365.252805
Sum of electronic and thermal Energies =      -2365.210063
Sum of electronic and thermal Enthalpies =    -2365.209119
Sum of electronic and thermal Free Energies = -2365.329133
```

Table A11. Crystallographic data for *trans*-Re_2Cl_2 (CCDC 1578651).

Moiety Formula	$C_{40}H_{22}Cl_2N_4O_6Re_2, 2(C_3H_7NO)$ [+solvent]
Formula Weight	1288.88 g/mol
T (K)	100(2)
λ (Å)	0.71073
Crystal System / Space Group	Triclinic / P-1

a (Å)	15.797(5)
b (Å)	16.298(5)
c (Å)	20.698(5)
α (º)	68.843(5)
β (º)	74.058(5)
γ (º)	76.127(5)
V (Å^3)	4719(2)
Z	4
ρ_{calc} (g/cm^3)	1.814
μ (mm^{-1})	5.301
F(000)	2506
θ range for data collectn	1.55 to 25.37º
Index ranges	-19 ≤ h ≤ 18, -19 ≤ k ≤ 19, -24 ≤ l ≤ 24
Reflections collected	41094
Independent reflections	16724 [R(int) = 0.0188]
Completeness to θ = 25.00º	96.8%
Max. and min. transmission	0.333 and 0.504
data/restr/params	16724 / 0 / 1161
GOF on F^2	1.036
Final R indices [I > 2σ(I)]	R1 = 0.0237, wR2 = 0.0564
R indices (all data)	R1 = 0.0277, wR2 = 0.0579

Figure A22. NMR Spectra

157.60

154.89
154.52

149.01

137.98
137.85
137.01

131.55

129.14
129.06
127.38
126.91
125.50
124.92
123.84
123.61

119.96
118.61

1

180

f1 (ppm)

cis-Re$_2$Cl$_2$

9.04
9.03
8.87
8.78
8.76
8.69
8.68
8.40
8.38
8.37
8.35
8.34
7.91
7.90
7.88
7.83
7.76
7.74
7.73
7.73
7.62
7.60
7.54
7.53

2.00
0.96
2.00
1.92
1.92
2.20
2.01
1.08
4.16
1.95
1.99

f1 (ppm)

181

cis-Re₂Cl₂

DMF

199.47
195.09
195.07
161.87
158.22
157.57
154.10
141.11
140.77
133.41
131.90
131.57
131.42
131.02
128.77
128.71
128.48
128.32
126.82
126.10
125.93
124.94
124.04

f1 (ppm)

trans-Re₂Cl₂

8.84
8.76
8.75
8.72

8.53
8.51

8.42
8.40

8.24
8.23
8.20
8.18
8.17
8.14
8.12

8.01
7.99
7.95
7.94
7.93
7.93
7.92
7.91
7.86
7.84
7.74
7.72
7.67
7.66
7.66
7.64
7.56
7.55
7.53
7.50
7.49
7.48
7.47

185

158.47

155.82
155.49

149.84

138.87
138.32
137.89

132.16
131.98
131.49
129.73
129.41
129.06
128.26
127.78
127.13
126.43
126.26
125.69
125.50
124.86
124.79
121.07
119.57

2

f1 (ppm)

186

APPENDIX B

Table B1. Photophysical properties of Re complexes in dichloromethane solution.

Complex	λ_{max}^{abs}, nm	λ_{max}^{em}, nm		$h\overline{\omega}, cm^{-1}$	$\tau_0, (N_2)$		TA max, nm (rel. inten.)
	(log ε)	λ_1	λ_2	λ_2	λ_1, ns	λ_2, μs	
anthryl-Re	252 (4.80) 296 (4.15 366 (3.98)	570	688 764	1440	420 23	6	430 (1)
cis-Re$_2$Cl$_2$	258 (4.85) 296 (4.42) 380 (4.12)	592	700 776	1400	210 65	15	440 (1) 520 (1)
trans-Re$_2$Cl$_2$	258 (4.70) 296 (4.27) 376 (3.95)	598	698 772	1370	200 90	15	440 (1) 490 (0.95)
[(dphbpy)Re(CO)$_3$Cl][a]	384	630		---	56	---	---
Anthracene[b]	340 355 375	375	670	---	6	3300	410, 440

Figure B1. Absorption and luminescence spectra of anthracene containing rhenium complexes (*cis*-Re$_2$Cl$_2$, *trans*-Re$_2$Cl$_2$, and anthryl-Re) in deoxygenated CH$_2$Cl$_2$ at room temperature.

Figure B2. Stern-Volmer quenching plots of tau(0)/tau versus the concentration of BIH in DMF solution for (A) anthryl-Re (k_q = 2.2 x 10^7 M^{-1} s^{-1} , average of quenching of both emission lifetime components) and (B) *trans*-Re₂Cl₂ (k_q = 5.1 x 10^7 M^{-1} s^{-1}).

189

```
================================================================
Acq. Operator    : SYSTEM
Sample Operator  : SYSTEM
Acq. Instrument  : Agilent              Location : Vial 1
Injection Date   : 9/7/2016 12:56:45 PM
                                        Inj Volume : Manually
Acq. Method      : C:\CHEM82\2\METHODS\START2.M
Last changed     : 9/2/2016 12:56:40 PM by SYSTEM
Analysis Method  : C:\CHEM82\2\METHODS\CURRENT.M
Last changed     : 11/13/2018 11:29:18 AM by SYSTEM
                   (modified after loading)
```



```
================================================================
               External Standard Report
================================================================
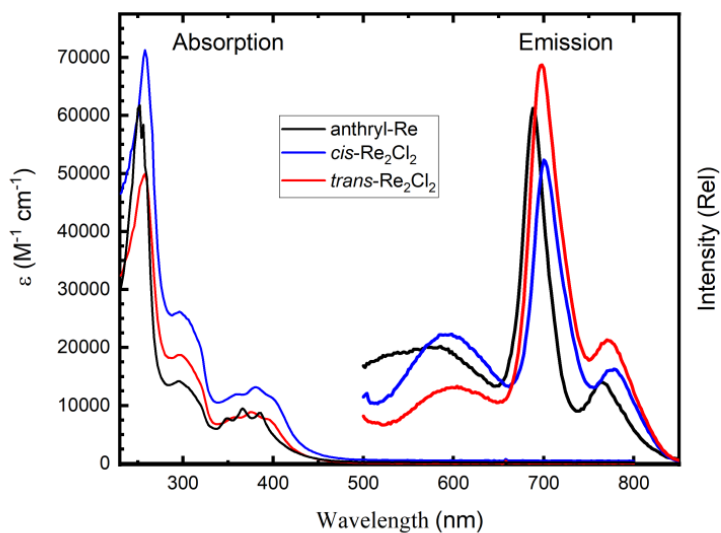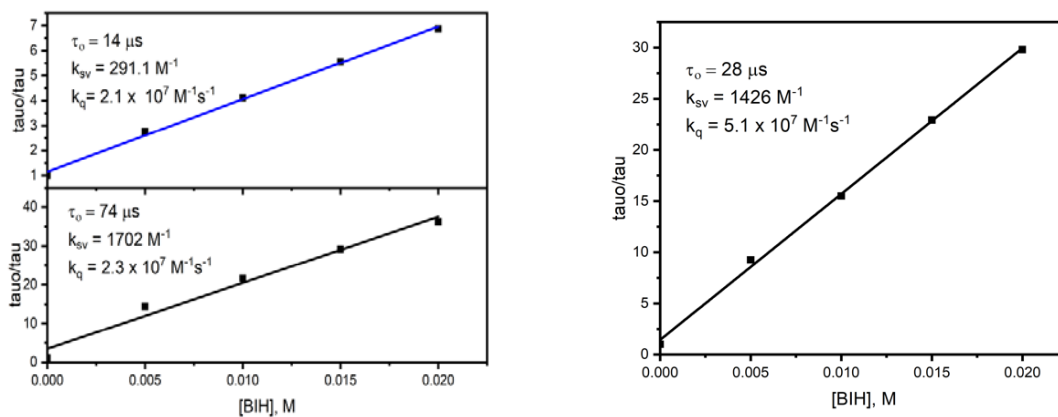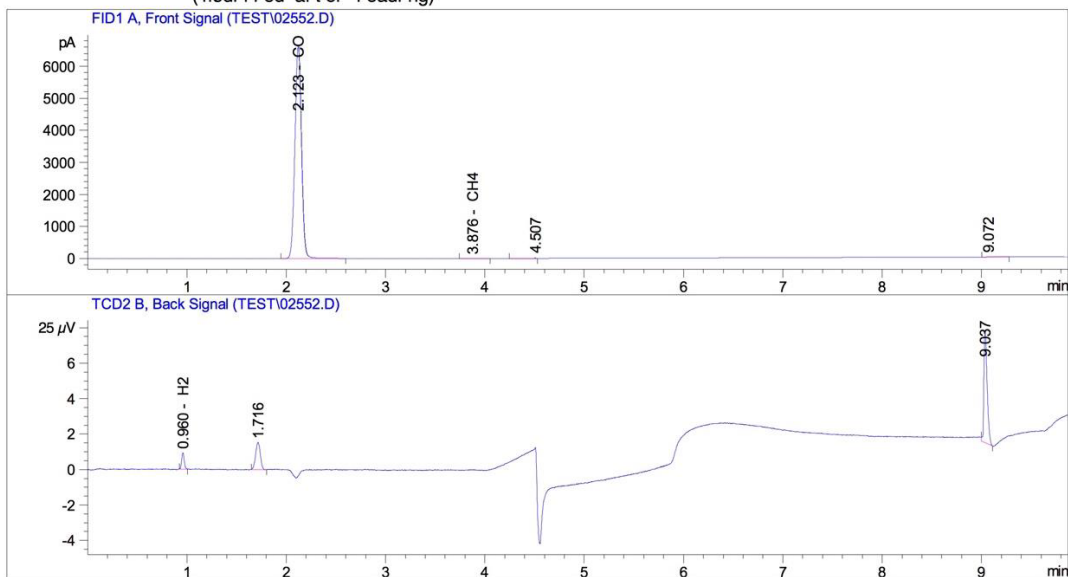

Sorted By           :      Signal
Calib. Data Modified :      11/8/2018 2:55:04 PM
Multiplier          :      1.0000
Dilution            :      1.0000
Do not use Multiplier & Dilution Factor with ISTDs

Signal 1: FID1 A, Front Signal

RetTime Type    Area      Amt/Area     Amount   Grp   Name
 [min]         [pA*s]                  [ng/ul]
-------|------|----------|----------|----------|--|-------------------
 0.000           -          -           -
 2.123 BB     3.05095e4  1.15369e-1  3519.86384       CO
 3.876 BB      15.10497  1.40742e-1     2.12590       CH4
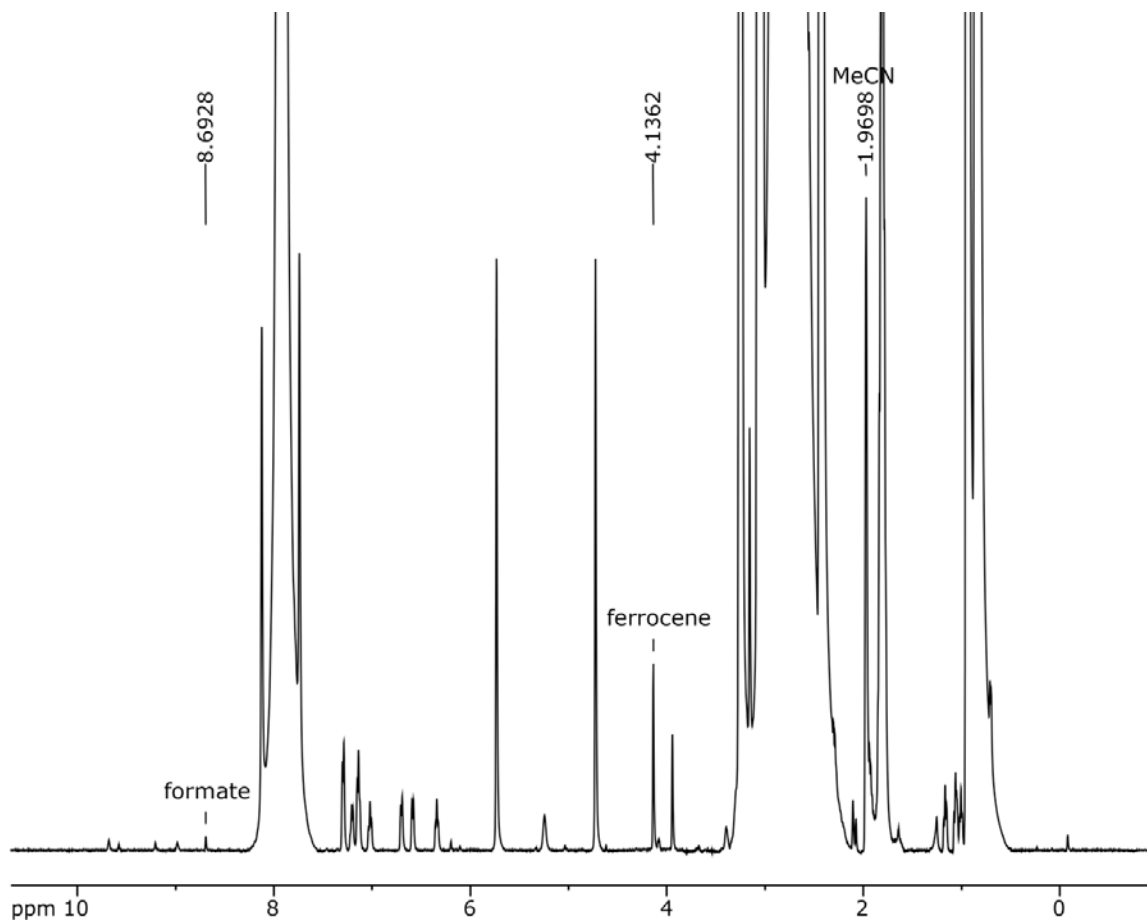
Totals :                            3521.98974
```

Data File C:\CHEM32\2\DATA\TEST\02552.D
Sample Name: Agilent_Standard_valve_syringe

Signal 2: TCD2 B, Back Signal

RetTime [min]	Type	Area [25 µV*s]	Amt/Area	Amount [ng/ul]	Grp	Name
0.000		-	-	-		
0.960	BB	1.66333	2.65015e-4	4.40806e-4		H2
1.610		-	-	-		AIR

Totals :   4.40806e-4

2 Warnings or Errors :

Warning : Calibration warnings (see calibration table listing)
Warning : Calibrated compound(s) not found

===
*** End of Report ***

Figure B3. Example GC trace for a photoreaction with *trans*-Re_2Cl_2 at 0.1 mM concentration. The FID trace (top) shows CO at 2.12 minutes retention time and only trace other products (CH_4 RT = 3.88 min). The TCD trace shows only trace reactivity (H_2 at 0.96 min and O_2 /N_2 at 1.72 min) and is a zoomed in y-axis range with the tallest peak at the top of the spectrum.

Figure B4. Example ^1H NMR formate analysis with ferrocene as an internal standard at 4.18 ppm and formate as an analyte at 8.63 ppm. This example is for a photoreaction with *trans*-Re_2Cl_2 at 0.1 mM concentration. The ratio of the peaks is 20:1, which is 7 TON of formate for this catalytic reaction.

Table B2. Photocatalytic reaction TON, TOF, and quantum yield values.

Complex	concentration (mM)	max. TON (CO)	max. TOF (h^{-1})	max. ϕ (%)
anthryl-Re	0.05	34	43	0.6
anthryl-Re	0.1	38	43	1.1

anthryl-Re	0.2	20	30	1.4
anthryl-Re	0.5	16	18	2.6
anthryl-Re	1.0	12	12	2.9
cis-Re$_2$Cl$_2$	0.05	95	128	1.6
cis-Re$_2$Cl$_2$	0.1	78	105	2.6
cis-Re$_2$Cl$_2$	0.2	52	71	3.4
cis-Re$_2$Cl$_2$	0.5	31	37	4.3
cis-Re$_2$Cl$_2$	1.0	17	20	4.4
trans-Re$_2$Cl$_2$	0.000001	400000	2500	---
trans-Re$_2$Cl$_2$	0.05	105	158	1.6
trans-Re$_2$Cl$_2$	0.1	63	92	2.2
trans-Re$_2$Cl$_2$	0.2	28	38	1.9
trans-Re$_2$Cl$_2$	0.5	27	30	4.0
trans-Re$_2$Cl$_2$	1.0	16	15	4.4
Re(bpy)(CO)$_3$Cl	0.05	16	17	0.2
Re(bpy)(CO)$_3$Cl	0.1	21	23	0.6
Re(bpy)(CO)$_3$Cl	0.2	43	30	2.0
Re(bpy)(CO)$_3$Cl	0.5	24	21	3.1
Re(bpy)(CO)$_3$Cl	1.0	19	16	4.6

Figure B5. Plots of absorbance at 370 nm as a function of concentration in DMF solution for A) Re(bpy)(CO)$_3$ Cl and B)anthryl-Re.

Figure B6. Plot of quantum yield versus catalyst concentration. Conditions: DMF containing 5% triethylamine, 10 mM BIH; irradiated with a solar simulator (AM 1.5 filter, 100 mW/cm^2).

APPENDIX C

Table C1. Cartesian coordinates for each structure (angstroms).

1. Structure DATCE

	x	y	z
N	-1.33864176	0.06926695	-1.14312768
C	0.99088925	0.04023018	-1.31120181
C	-1.16956186	0.03552746	0.30082774
C	1.06715286	0.00649245	0.19109078
C	-0.01169499	0.76534992	0.95553982
C	-0.03304746	-0.75432605	0.92246419
H	1.49665296	0.91842294	-1.71849322
H	1.47209334	-0.83325911	-1.75658917
H	-2.12382007	0.03793455	0.80657989
H	2.06011534	-0.01692376	0.62685603
H	0.02480233	1.45217907	1.78253877
H	-0.01637538	-1.47721994	1.71879339
N	-0.36841473	0.07142519	-1.87093878

2. Structure DAP$_1$

	x	y	z
N	-1.24321604	0.12574799	-1.03812397
C	1.03742003	-0.21093599	-1.30370796
C	-1.25653994	-0.75852501	0.06709400
C	1.54057300	0.32737800	0.00317100
C	0.86407501	0.04521700	1.15865898
C	-0.38955301	-0.73746699	1.13297999
H	1.72502697	0.00448500	-2.11670709
H	0.88891202	-1.29329300	-1.24131298
H	-2.17757297	-1.32030404	0.13091099
H	2.43005109	0.94322199	0.02128800
H	1.24473500	0.38176200	2.11456299
H	-0.66945100	-1.29520500	2.01813602
N	-0.23882701	0.43701500	-1.64848804

3. Structure DAP$_2$

	x	y	z
N	-1.16779101	-0.64002001	-1.08525395
C	0.68300301	0.75432998	-1.25431597
C	-1.47904301	-0.10512900	0.18798700
C	1.48783505	0.28317201	-0.07852600

196

	x	y	z
C	0.86488998	-0.00468100	1.10520506
C	-0.60514897	0.07661000	1.23283005
H	0.06928100	1.61709297	-0.97713298
H	1.32201004	1.03113604	-2.08814597
H	-2.54451108	-0.06943700	0.36536899
H	2.55957389	0.17099699	-0.17685100
H	1.44391096	-0.28888100	1.97464800
H	-1.02901101	0.24935301	2.21440911
N	-0.19210300	-0.32655400	-1.73923600

4. Structure NdisTS

	x	y	z
N	-1.30195343	0.01342211	-1.08620119
C	1.05292690	0.07258783	-1.29336417
C	-1.21845627	-0.64856392	0.12370900
C	1.28874016	-0.29430455	0.15287189
C	0.70504355	0.52046371	1.27374268
C	0.04811408	-0.79807019	0.92320359
H	1.64533305	0.94120276	-1.58244169
H	1.38154840	-0.75137752	-1.93326998
H	-2.17247462	-0.90840471	0.55546230
H	2.23382282	-0.78592616	0.35617012
H	1.14248049	0.83859372	2.20771027
H	0.11646657	-1.64245570	1.59758270
N	-0.31415167	0.37006265	-1.72467542

5. Structure CdisTS

	x	y	z
C	-1.23991597	0.00001755	-1.08678555
N	1.11064184	0.12755996	-1.17369318
C	-1.22954774	-0.88036704	0.12311003
C	1.20902181	-0.22120188	0.22741903
C	0.50301600	0.57922471	1.29399884
C	-0.00173660	-0.81041926	0.99546325
H	-2.17851353	-1.15399027	0.56738806
H	2.19879723	-0.58687681	0.46176511
H	0.89500433	1.00905406	2.20304942
H	0.16966029	-1.61051345	1.70529115
N	0.05061551	0.21945223	-1.75495827
H	-1.89900517	-0.40604001	-1.85402000

	x	y	z
H	-1.62471807	1.00128031	-0.85891795

6. Structure NconTS1

	x	y	z
N	-1.29244304	0.07636036	-1.01047087
C	1.04163992	0.14488558	-1.26618493
C	-1.16634893	-0.75647867	0.13728587
C	1.26299679	-0.10212760	0.20811179
C	0.59815705	0.67613679	1.21299589
C	-0.12937532	-0.67258233	1.08854246
H	1.65934813	0.96744531	-1.62766850
H	1.31439888	-0.73823875	-1.84796941
H	-2.03141189	-1.38707054	0.28535643
H	1.98126447	-0.85941786	0.49409425
H	0.03639345	1.52687764	0.83496058
H	0.02891397	-1.46834338	1.80330479
N	-0.33586344	0.48483324	-1.64720857

7. Structure CconTS1

	x	y	z
C	-1.23598480	0.02076247	-1.07024336
N	1.11656094	0.21811867	-1.17233992
C	-1.21964467	-0.75743264	0.21374667
C	1.20177174	-0.11838255	0.21241990
C	0.55813766	0.68511385	1.23024774
C	-0.10755118	-0.71358263	1.08197474
H	-2.08826065	-1.36226428	0.44462928
H	2.03538108	-0.75830472	0.46382228
H	-0.02436638	1.51902115	0.84208316
H	0.09314413	-1.49601495	1.80005956
N	0.04187234	0.33545503	-1.72625780
H	-1.78527188	-0.54973620	-1.82126570
H	-1.76637816	0.97401685	-0.99474645

8. Structure NconInt

	x	y	z
N	-1.17254436	-0.12935539	-1.03004634
C	1.14911330	0.52507800	-1.32641387
C	-1.20073497	-0.78021890	0.27967709

C	1.34310114	-0.15687630	-0.02968836
C	0.69569921	0.37333986	1.07144785
C	-0.48748320	-0.48004261	1.41496575
H	1.33888507	1.59884501	-1.31786120
H	1.69165754	0.09332362	-2.16674495
H	-2.09250116	-1.39012527	0.32793716
H	1.35121119	-1.23951328	-0.09737577
H	0.64599955	1.44558704	1.23436141
H	-0.81668174	-0.79587555	2.39674282
N	-0.30165136	0.40838382	-1.68327153

9. Structure CconInt

	x	y	z
C	-1.06391704	-0.29168245	-1.09964263
N	1.17967534	0.59556657	-1.25672734
C	-1.27702379	-0.75489688	0.35226682
C	1.28607547	-0.17518854	-0.05344008
C	0.69972783	0.31735843	1.08559728
C	-0.49822330	-0.51729470	1.45452821
H	-2.22556758	-1.27307343	0.47208774
H	1.33984542	-1.24352431	-0.22866115
H	0.64357913	1.39016211	1.23451269
H	-0.80712503	-0.80358273	2.45123553
N	0.04665386	0.53191787	-1.69741893
H	-1.08687139	-1.17469788	-1.74655640
H	-1.95164299	0.27860880	-1.37835872

10. Structure NconTS2

	x	y	z
N	-1.22473168	-0.45778599	-1.13910139
C	0.94505334	0.56573945	-1.36906683
C	-1.31874728	-0.57033855	0.28926978
C	1.41338336	0.01856516	-0.06715097
C	0.73123562	0.49870428	1.17475450
C	-0.57058573	-0.01180191	1.35865033
H	0.81215769	1.65091348	-1.34124863
H	1.63488150	0.34631550	-2.18331766
H	-2.27999783	-1.00280988	0.53255856
H	1.65092111	-1.04281521	-0.07590441
H	1.17330158	1.21783650	1.85320687

	x	y	z
H	-1.07045138	0.05085879	2.31917119
N	-0.35554022	0.02986831	-1.83606148

11. Structure CconTS2

	x	y	z
C	-0.98741549	-0.43501547	-1.14645267
N	0.94523656	0.90839851	-1.08737504
C	-1.30527937	-0.63195413	0.32575455
C	1.41925013	-0.05428514	-0.13735721
C	0.86732721	0.10182675	1.24706852
C	-0.47469309	-0.34508145	1.42275000
H	-2.30822897	-0.98507929	0.53027695
H	1.53624642	-1.06233335	-0.52521968
H	1.40002048	0.63613701	2.02032113
H	-0.90457594	-0.39136788	2.41618919
N	-0.17153913	0.74174345	-1.53880131
H	-0.52493757	-1.32949257	-1.57737041
H	-1.92843127	-0.29718637	-1.67398417

12. Structure DATCA

	x	y	z
N	-1.42293572	0.19845748	-1.14382577
C	0.97666281	0.11770615	-1.38115907
C	-1.21422291	0.12395849	0.27996346
C	1.03657210	-0.02077130	0.13112727
C	0.00653699	0.74467486	0.95053643
C	-0.11138921	-0.77785206	0.80267608
H	1.23057044	1.14303195	-1.66671002
H	1.70794582	-0.53806341	-1.85897791
H	-2.14152622	0.14866386	0.84120041
H	2.02121615	-0.12557875	0.57551348
H	0.11214472	1.31699753	1.85691321
H	-0.11495087	-1.53014958	1.57237792
N	-0.33029807	-0.22865683	-1.92299938
H	-1.65234458	1.13811672	-1.41621232
H	-0.40628135	-1.22710514	-1.98618388

13. Structure DHDAP$_1$

	x	y	z

200

	x	y	z
N	-1.39481902	0.23868400	-1.13966894
C	0.97603899	0.30155301	-1.36241305
C	-1.74704099	-0.15927500	0.15561500
C	1.39266598	0.20351399	0.08435500
C	0.60675901	-0.13192300	1.15226996
C	-0.86680102	-0.37098899	1.17894304
H	0.91113198	1.34645605	-1.66934705
H	1.75735795	-0.15404899	-1.97798204
H	-2.81018090	-0.26625401	0.33284000
H	2.44280696	0.39425400	0.28221199
H	1.09289396	-0.19347601	2.11922097
H	-1.28807199	-0.67126000	2.12922502
N	-0.26623699	-0.35127199	-1.72259498
H	-2.15979195	0.18431900	-1.78064704
H	-0.21916100	-1.32326603	-1.45930195

14. Structure DHDAP$_2$

	x	y	z
N	-1.36570203	-0.32421601	-1.11690795
C	0.93440503	0.44240099	-1.36343503
C	-1.52962899	-0.09297200	0.24612100
C	1.58951902	0.21596000	-0.02402100
C	0.88892901	-0.02088400	1.12418401
C	-0.59541303	-0.03583700	1.24591005
H	0.50688398	1.44633996	-1.42015803
H	1.68743205	0.38124600	-2.15160894
H	-2.57504106	-0.01370400	0.51987100
H	2.67274308	0.22763000	0.01977000
H	1.44114602	-0.16861600	2.04503012
H	-0.99180698	0.03722700	2.25064707
N	-0.12575100	-0.50236100	-1.71296000
H	-1.98272002	0.20465900	-1.69944596
H	0.17379400	-1.44221604	-1.52972806

15. Structure NdisTS′

	x	y	z
N	-1.42339540	-0.14606592	-1.16566598
C	0.93296069	0.25221679	-1.26147401
C	-1.40808904	-0.32721406	0.22840041

201

C	1.19161737	-0.16610871	0.18556029
C	0.84130841	0.81545776	1.26951730
C	-0.12877002	-0.34134027	1.01129293
H	0.80472010	1.33444512	-1.32227707
H	1.79706573	0.00164181	-1.87867403
H	-2.35516500	-0.18690881	0.72857887
H	2.00624251	-0.86340731	0.35096633
H	1.39543521	0.92786473	2.19372249
H	-0.11925846	-1.06822538	1.81810999
N	-0.23407100	-0.35943642	-1.87034750
H	-1.86182213	0.70168203	-1.47589076
H	-0.10957908	-1.35344136	-1.95132947

16. Structure NdisTS″

	x	y	z
N	-1.35345852	0.20459662	-1.05027461
C	1.04206014	0.13321534	-1.34365678
C	-1.22168159	0.42395344	0.33541670
C	1.28673506	-0.14588186	0.12525053
C	0.06758421	0.05781965	1.05366910
C	0.60426700	-1.32363117	0.78441113
H	1.15246558	1.20371866	-1.53755569
H	1.77541852	-0.38642454	-1.96429086
H	-2.15312290	0.39689919	0.89210719
H	2.25471497	0.14308731	0.52221948
H	0.21058591	0.51497751	2.02611446
H	0.94744480	-2.10143733	1.44823039
N	-0.27236584	-0.28958043	-1.79056585
H	-1.77515674	0.97728574	-1.53008449
H	-0.32491049	-1.29297805	-1.74940085

17. Structure CdisTS′

	x	y	z
N	-1.39562595	0.13293861	-1.09109366
C	0.99973285	0.19917566	-1.39172935
C	-1.28806067	0.19103202	0.34260291
C	1.29041827	0.19030157	0.08237755
C	0.11506672	0.24624294	1.03696835
C	-0.77405405	-0.98817056	1.11280930

	x	y	z
H	1.01604879	1.23224723	-1.76587749
H	1.77840137	-0.33207700	-1.94385386
H	-2.09643722	0.75877380	0.78947771
H	2.25147820	0.55132854	0.42733517
H	0.23269734	0.84052205	1.93693876
H	-1.18028319	-1.48607981	1.98114049
N	-0.27926472	-0.37997854	-1.77376115
H	-1.58354163	1.04699314	-1.46162188
H	-0.27862626	-1.37567961	-1.64485288

18. Structure CdisTS″

	x	y	z
N	-1.33637977	0.31465718	-1.09704268
C	1.01107061	-0.03348709	-1.49189413
C	-1.25072801	0.00064490	0.30805078
C	1.25051641	-0.57820606	-0.11412560
C	-0.46861416	0.89247489	1.24482906
C	0.12283386	-0.45685077	0.88532895
H	1.23931909	1.03968787	-1.52898061
H	1.67403328	-0.51324832	-2.21523738
H	-2.13566422	-0.48302138	0.70886517
H	2.26258874	-0.67250121	0.26165459
H	-0.74728137	1.25632071	2.22391558
H	0.10247264	-1.20793450	1.66828823
N	-0.35648748	-0.20929363	-1.95280385
H	-1.39411724	1.30264926	-1.25304103
H	-0.55888206	-1.18373179	-2.08697677

19. Structure NconTS1′

	x	y	z
N	-1.43094933	0.00844477	-1.05635679
C	0.98796737	0.19592127	-1.31666112
C	-1.39533913	-0.48966303	0.27399421
C	1.13849020	-0.02605952	0.17835093
C	0.54325736	0.89400637	1.12329757
C	-0.24462490	-0.43452144	1.10718977
H	1.13207793	1.26165700	-1.51517606
H	1.75230050	-0.34002155	-1.88157892
H	-2.31300664	-0.94758868	0.62348062

	x	y	z
H	1.86804652	-0.73859274	0.54489440
H	0.04017371	1.75133789	0.67512351
H	-0.11543095	-1.15248680	1.90509605
N	-0.30366421	-0.20636971	-1.86336851
H	-1.77593493	0.94211507	-1.17049420
H	-0.29553342	-1.18461883	-2.08670139

20. Structure NconTS1$_a''$

	x	y	z
N	-1.33736515	0.32192284	-1.07347786
C	1.03748357	0.12912646	-1.38524425
C	-1.17192423	0.27935398	0.33617321
C	1.19287157	-0.22303137	0.07880460
C	0.08648123	0.24252611	1.06512630
C	0.36466718	-1.24542284	0.81046021
H	1.27329171	1.18689895	-1.54016256
H	1.73719871	-0.44634843	-1.99471390
H	-2.10495520	0.35779929	0.88236797
H	2.18828321	-0.10601499	0.49635628
H	0.26318210	0.73956609	2.01055074
H	-0.31991121	-2.01209474	0.47015148
N	-0.29615569	-0.13984543	-1.88805306
H	-1.60875452	1.24218035	-1.37538707
H	-0.42383334	-1.13234615	-1.97748208

21. Structure NconTS1$_b''$

	x	y	z
N	-1.37007999	0.21642189	-1.03387082
C	1.01358879	0.09395494	-1.36566508
C	-1.17764771	0.48460183	0.31954116
C	1.24384856	-0.23482305	0.09737201
C	-0.16166560	-0.02143468	1.13447988
C	0.62831956	-1.34321129	0.76988173
H	1.16087043	1.16113365	-1.54630864
H	1.72647870	-0.44072470	-1.99733388
H	-1.94308221	1.12372172	0.74224061
H	1.96049356	0.37644607	0.63625616
H	-0.03499719	0.42012647	2.11345911
H	0.05090978	-1.97989404	0.09782664

204

	x	y	z
N	-0.32054877	-0.28873754	-1.81068313
H	-1.82399678	0.97171456	-1.50863016
H	-0.39848125	-1.28864574	-1.80960560

22. Structure CconTS1′

	x	y	z
N	-1.39204526	0.12252544	-1.07907808
C	1.00119078	0.18888251	-1.36349821
C	-1.23541296	0.07381579	0.34205797
C	1.20927906	0.34241784	0.12560329
C	0.12075529	0.46527982	1.06624746
C	-0.47619471	-0.97196239	1.05428267
H	1.14950013	1.18056560	-1.81362844
H	1.77378404	-0.44973451	-1.79583240
H	-2.08996129	0.46395597	0.88231999
H	2.22906733	0.50248492	0.46082073
H	0.16861869	1.06601584	1.96488047
H	0.02724839	-1.82898188	0.61913151
N	-0.28030020	-0.32539827	-1.80860305
H	-1.62760043	1.04729223	-1.39249980
H	-0.29082894	-1.32732880	-1.78085411

23. Structure CconTS1″

	x	y	z
N	-1.37918520	0.33643577	-1.15644407
C	1.00732672	-0.02059591	-1.45013666
C	-1.21840417	0.20094195	0.26702461
C	1.19852984	-0.57649338	-0.05059063
C	-0.36758199	1.05796087	1.07098007
C	0.20355304	-0.38456950	0.94631630
H	1.27565694	1.03581023	-1.52903795
H	1.67146790	-0.55035418	-2.13445640
H	-1.98380148	-0.37611693	0.77261817
H	2.07487488	-1.17643464	0.16400950
H	0.16595033	1.83800828	0.53014487
H	0.09975848	-1.07083881	1.77547991
N	-0.34726137	-0.19532865	-1.96000302
H	-1.46424091	1.30922759	-1.39181232
H	-0.53978330	-1.17438269	-2.07429242

24. Structure NconInt′

	x	y	z
N	-1.28932583	0.04634845	-0.94741422
C	1.05325341	0.43676457	-1.45664108
C	-1.46003604	-0.52121627	0.36293334
C	1.30981970	-0.01541957	-0.04763298
C	0.55006790	0.56903785	0.94047529
C	-0.60538483	-0.29326814	1.41034186
H	0.90941447	1.51290190	-1.53617311
H	1.79818821	0.12317528	-2.18886948
H	-2.40994430	-1.02145517	0.52036697
H	1.46781588	-1.08894932	0.03664571
H	0.32035694	1.62774205	0.85257143
H	-0.82317519	-0.63420898	2.41286302
N	-0.20619182	-0.24174021	-1.81216311
H	-2.12495565	-0.04916412	-1.48585749
H	-0.03512795	-1.23532736	-1.82547951

25. Structure NconInt$_a$″

	x	y	z
N	-1.37069941	0.21131562	-1.03988624
C	1.00963295	0.11624040	-1.33453441
C	-1.18363142	0.48190045	0.30083588
C	1.21398103	-0.23436050	0.12861913
C	-0.09080713	0.06123838	1.07631958
C	0.59785086	-1.38143158	0.78924429
H	1.15093708	1.18764114	-1.49759293
H	1.73718333	-0.40411642	-1.96020043
H	-1.99088168	1.04974210	0.74667197
H	2.04001880	0.25811371	0.63253444
H	0.03969629	0.49962756	2.05413985
H	-0.01792898	-1.97598946	0.10731504
N	-0.31133908	-0.26844308	-1.81672335
H	-1.88871181	0.91863626	-1.52220869
H	-0.37918606	-1.26993549	-1.82709599

26. Structure NconInt_b″

	x	y	z
N	-1.04582500	0.59907800	-0.92982298
C	1.12143099	-0.27352500	-1.59853399
C	-1.31762600	0.33106801	0.43827900
C	1.33090401	-0.05010000	-0.12573899
C	-0.53163302	-0.34339300	1.34496295
C	0.71292698	-0.93837798	0.73650700
H	1.54193902	0.52914703	-2.20309305
H	1.50284600	-1.22447503	-1.97357702
H	-2.25413203	0.76937902	0.76498801
H	1.25982904	0.99320900	0.16193600
H	-0.89276499	-0.50508499	2.35211492
H	0.71693301	-2.00454593	0.51811498
N	-0.35087201	-0.30252901	-1.77176297
H	-1.85938799	0.91630900	-1.41344297
H	-0.65715700	-1.23778498	-1.55890298

27. Structure CconInt′

	x	y	z
N	-1.54577303	-0.25488600	-1.20525801
C	0.83828998	0.45557699	-1.26606703
C	-1.38421094	0.24584199	0.10359800
C	1.32028306	0.45265099	0.20247300
C	0.65373802	0.00839900	1.31776595
C	-0.70212299	-0.56299299	0.98760098
H	0.60008001	1.48591697	-1.54562104
H	1.70390201	0.18555000	-1.87536299
H	-1.32234395	1.32455599	0.22982199
H	2.33072495	0.83782601	0.31872499
H	1.13432896	-0.02192400	2.28807902
H	-0.78386301	-1.63970304	0.87174499
N	-0.23806199	-0.41413799	-1.76581800
H	-2.05685401	0.36631000	-1.80326200
H	0.01652400	-1.37323594	-1.61801803

28. Structure CconInt″

	x	y	z
N	-1.50680757	0.56806660	-1.30433857

C	0.90254611	-0.13684431	-1.34248567
C	-1.33901668	0.18480022	0.05263753
C	1.22509563	-0.68525136	0.07712884
C	-0.45107952	0.76213592	0.92525667
C	0.66651374	-0.21551019	1.24015796
H	1.28556395	0.88743246	-1.37062228
H	1.51083350	-0.69635767	-2.05396152
H	-1.55124116	-0.86979580	0.18505041
H	2.08378029	-1.34905469	0.12883927
H	-0.18387491	1.81044579	0.81894964
H	1.04705095	-0.47549337	2.22000599
N	-0.43426350	-0.10652254	-1.97062349
H	-1.36226058	1.55375171	-1.43762600
H	-0.75494838	-1.03908885	-2.15765285

29. Structure NconTS2′

	x	y	z
N	-1.29345250	-0.14148657	-1.06223071
C	0.98298764	0.52225679	-1.43695927
C	-1.43154299	-0.46441698	0.30293703
C	1.48590040	0.08770845	-0.08607526
C	0.72291613	0.46808505	1.14760506
C	-0.57767862	-0.12477954	1.35393023
H	0.63843900	1.55562139	-1.4422717
H	1.75030959	0.40812740	-2.2049365
H	-2.42516923	-0.81648183	0.55104113
H	1.81810308	-0.95227081	-0.08509157
H	1.10098279	1.20245564	1.84719050
H	-0.99238783	-0.19823252	2.35249138
N	-0.13304961	-0.33549953	-1.82581079
H	-2.07761145	-0.44912961	-1.59773958
H	0.16546376	-1.29778743	-1.75358987

30. Structure NconTS2″

	x	y	z
N	-0.95442176	0.70564193	-0.90830022
C	1.09275067	-0.32066563	-1.59886014
C	-1.29964244	0.34616992	0.40946886
C	1.53150833	-0.12862645	-0.17070051

C	-0.51763374	-0.47516546	1.24236357
C	0.80180967	-0.90327680	0.89841759
H	1.52177787	0.45718437	-2.23145628
H	1.41152573	-1.28543031	-2.00184107
H	-2.24236107	0.73953104	0.76580024
H	1.77199173	0.89397639	0.10826312
H	-0.98024762	-0.82737643	2.15669823
H	1.25232351	-1.75105810	1.39811301
N	-0.36664572	-0.28272822	-1.71884358
H	-1.72617841	1.10976660	-1.39820719
H	-0.73830664	-1.18157279	-1.45777547

31. Structure CconTS2′

	x	y	z
N	-1.48091173	-0.32316923	-1.22846985
C	0.79944986	0.56121582	-1.26692426
C	-1.60111916	0.18489447	0.07896924
C	1.31259978	0.44162902	0.16073807
C	0.61332721	-0.14667325	1.23267162
C	-0.76902974	-0.47871113	1.14310205
H	0.38076660	1.55287719	-1.45944369
H	1.66327238	0.47200024	-1.92983472
H	-1.80307865	1.24826133	0.20540553
H	2.34386492	0.73415506	0.32333699
H	1.16880322	-0.40741485	2.12682962
H	-1.21259475	-1.19246519	1.82513130
N	-0.16046345	-0.43579715	-1.72102416
H	-2.01503134	0.20841511	-1.88836086
H	0.16917495	-1.35795736	-1.50161695

32. Structure CconTS2″

	x	y	z
N	-1.37026465	0.73302871	-1.28783345
C	0.87258899	-0.26980808	-1.42273438
C	-1.54870033	0.32182592	0.05344129
C	1.16283774	-0.62507212	0.03527457
C	-0.60129660	0.69691128	1.16412342
C	0.62601334	-0.01556111	1.19647968
H	1.41744506	0.66357487	-1.60980988

209

	x	y	z
H	1.35420501	-1.01914442	-2.05298281
H	-1.88953984	-0.70950902	0.10131884
H	2.09415388	-1.16732562	0.16407259
H	-0.87284940	1.39373589	1.94623566
H	1.21124625	-0.05525590	2.10910273
N	-0.46208549	-0.09558035	-1.98351347
H	-1.05760002	1.68298090	-1.36993039
H	-0.91536391	-0.98043090	-2.11986423

33. Structure TATCE

	x	y	z
N	-1.24102449	0.06335469	-1.16420841
N	0.98353422	0.21775147	-1.21458483
C	-1.14219677	0.04522111	0.28056934
C	1.06271446	0.05945647	0.20733991
C	-0.01450774	0.76942956	0.99471682
C	-0.01210226	-0.75345653	0.91220111
H	1.68854368	-0.22541514	-1.76783109
H	-2.11477113	0.01972986	0.74835366
H	2.07657313	0.05117608	0.58292556
H	0.00053438	1.46258247	1.81677806
H	0.00012857	-1.53649640	1.64929664
N	-0.22080594	0.09270635	-1.82924676

34. Structure TAP₁

	x	y	z
N	-1.25923800	-0.01367800	-1.06760204
N	0.93691301	-0.49631900	-1.11592805
C	-1.35856998	-0.51352400	0.25779101
C	1.45615697	0.30840701	-0.06771700
C	0.78232801	0.44971099	1.10806799
C	-0.52416301	-0.21822999	1.29869795
H	1.59358597	-0.54096001	-1.87049699
H	-2.30729604	-1.00040996	0.43006501
H	2.40791202	0.79541701	-0.23728800
H	1.21059501	1.04139698	1.90509200
H	-0.83647400	-0.48687300	2.29989004
N	-0.23817199	0.03142600	-1.70864499

210

35. Structure TAP$_2$

	x	y	z
N	-1.25038016	0.06708711	-1.03472793
N	0.98191047	0.30544290	-1.13496149
C	-1.23415029	0.39496627	0.34649506
C	1.43981278	-0.69842780	-0.24118215
C	-0.40244716	-0.13646780	1.29148936
C	0.79877442	-0.92553216	0.93960589
H	1.61059022	0.38616386	-1.91021681
H	-2.10653996	0.96405649	0.63256407
H	2.31400514	-1.26715899	-0.53131658
H	-0.63691020	0.02892942	2.33540797
H	1.17717683	-1.67305398	1.62283337
N	-0.26755595	-0.00521927	-1.73074698

36. Structure N1disTS$_2$

	x	y	z
N	-1.33099222	-0.33006421	-1.14672804
N	0.86660159	0.12573440	-1.16036201
C	-1.35058701	-0.19655491	0.22691783
C	1.15805352	-0.20634329	0.20225337
C	0.83608705	0.80457932	1.27590036
C	-0.11088291	-0.36102125	1.06437349
H	1.62620080	0.04583286	-1.80154109
H	-2.33074379	-0.20847273	0.67531455
H	1.98558068	-0.89060324	0.34683317
H	1.40113795	1.02322769	2.17011189
H	-0.13698517	-1.13811433	1.81993032
N	-0.28204060	-0.21620022	-1.78218412

37. Structure N1disTS$_1$

	x	y	z
N	-1.30169976	0.19081797	-1.04405200
N	0.94327176	0.05109686	-1.23695779
C	-1.21334004	0.30604666	0.32166755
C	1.23439634	-0.20356037	0.14254661
C	0.04350619	-0.00710853	1.08998549
C	0.64197320	-1.38673258	0.87150085
H	1.56055403	-0.38587660	-1.89167881
H	-2.15111351	0.45885873	0.83115613

	x	y	z
H	2.20896363	0.16127288	0.43982437
H	0.18502170	0.49485105	2.03912592
H	1.08914125	-2.05898929	1.58883250
N	-0.30465758	0.03788886	-1.75479543

38. Structure N3disTS$_2$

	x	y	z
N	-1.26098287	-0.11335032	-1.09756756
N	0.96018976	0.19475992	-1.23826563
C	-1.22259617	0.11114339	0.32740036
C	1.29074740	0.03986797	0.11038735
C	0.13311155	0.19243215	1.06727517
C	-0.78314894	-1.00025153	1.24457669
H	1.67388237	0.02211608	-1.91340268
H	-2.04474854	0.73682499	0.64738613
H	2.26751041	0.41516444	0.37965891
H	0.24753155	0.89269352	1.88646662
H	-1.26557875	-1.35765290	2.14206529
N	-0.25107780	-0.07207775	-1.77588069

39. Structure N3disTS$_1$

	x	y	z
N	-1.33402169	0.07713960	-1.10628259
N	0.89154190	-0.10330334	-1.31662345
C	-1.22622192	-0.08966351	0.32074741
C	1.18516088	-0.70151305	-0.08374879
C	-0.40124962	0.85500580	1.16130280
C	0.10227987	-0.54994255	0.95930445
H	1.54356277	-0.24694774	-2.05811739
H	-2.15559125	-0.44409946	0.74359560
H	2.22735739	-0.62521011	0.20406279
H	-0.66284949	1.39568162	2.05771351
H	0.08753270	-1.26916194	1.76845801
N	-0.35202155	0.05420474	-1.82448196

Table C2. Imaginary frequencies for transition state.

3,4-diazatricyclo[4.1.0.0^{2,7}]hept-3-ene (DATCE)

Transition State	Imaginary Frequencies

Transition State	Imaginary Frequencies
NdisTS	403.3i
CdisTS	441.3i
NconTS1	326.8i
CconTS1	235.6i
NconTS2	708.1i
CconTS2	774.7i

3,4-diazatricyclo[4.1.0.0^{2,7}]heptane (DATCA)

Transition State	Imaginary Frequencies
NdisTS′	439.8i
NdisTS″	329.4i
CdisTS′	462.0i
CdisTS″	364.3i
NconTS1′	422.7i
NconTS1$_a$″	330.1i **488.5i**
NconTS1$_b$″	305.2i **460.6i**
CconTS1′	200.0i
CconTS1″	313.2i
NconTS2′	909.8i
NconTS2″	872.4i
CconTS2′	769.4i
CconTS2″	648.8i

Bold values are obtained at CCSD/ cc-pVDZ//CCSD/cc-pVDZ level.

3,4,5-triazatricyclo[4.1.0.0^{2,7}] hept-3-ene (TATCE)

Transition State	Imaginary Frequencies
N1disTS$_1$	433.4i
N1disTS$_2$	358.4i
N3disTS$_2$	433.1i
N3disTS$_1$	367.5i
N3disTS$_2$	433.1i

Table C3. Calculated energies (Hartree) for each structure.

3,4-diazatricyclo[4.1.0.0^{2,7}]hept-3-ene (DATCE)

Structure	MCSCF	ZPE	MRMP2	PBEPBE-D3
DATCE	-301.7236903001	0.109598	-302.5916366963	-303.154923914
DAP$_1$	-301.7852845205	0.109653	-302.6411678211	-303.200469402
DAP$_2$	-301.7852845205	0.109653	-302.6411678211	-303.200469402

NdisTS	-301.6377758015	0.104762	-302.5165611764	-303.084220255
CdisTS	-301.6297400607	0.104782	-302.4971132792	-303.070595746
NconTS1	-301.6548840380	0.105993	-302.5306600574	-303.096217765
CconTS1	-301.6541621627	0.105710	-302.5275531027	-303.092147066
NconTS2	-301.6716130840	0.104074	-302.5408009928	-303.102330698
CconTS2	-301.6753745419	0.104256	-302.5406569291	-303.071244272
NconInt	-301.7029804905	0.107762	-302.5669236398	-303.129153587
CconInt	-301.7068060498	0.107480	-302.5684475418	-303.120216093

3,4-diazatricyclo[4.1.0.0^{2,7}]heptane(DATCA)

Structure	MCSCF	ZPE	MRMP2	PBEPBE-D3	CCSD(T)
DATCA	-302.9014682620	0.136254	-303.7919340517	-304.358283994	**-304.2159678**
DHDAP$_1$	-302.9699715730	0.136015	-303.8422778172	-304.405386697	**-304.2646917**
DHDAP$_2$	-302.9670840146	0.135608	-303.8400754340	-304.405322061	**-304.264046**
NdisTS′	-302.8103316983	0.130948	-303.7036413285	-304.264818910	
NdisTS″	-302.8142990640	0.131305	-303.7083851669	-304.271767750	
CdisTS′	-302.8084016120	0.131051	-303.6966586044	-304.238467370	
CdisTS″	-302.8088782722	0.131338	-303.6960771353	-304.244315176	
NconTS1′	-302.8258076723	0.131611	-303.7186204701	-304.283595573	
NconTS1$_a$″	-302.8318041029	0.132247	-303.7277955740	-304.293443717	**-304.1477485**
NconTS1$_b$″	-302.8387148631	0.133087	-303.7336127380	-304.307086151	**-304.1565024**
CconTS1′	-302.8342550094	0.132362	-303.7286637027	-304.292573920	
CconTS1″	-302.8266871968	0.132188	-303.7191381912	-304.280327288	
NconTS2′	-302.8579700341	0.130918	-303.7471642280	-304.294975744	
NconTS2″	-302.8679603487	0.131180	-303.7567059467	-304.299523558	
CconTS2′	-302.8647380936	0.130944	-303.7527406669	-304.295483333	
CconTS2″	-302.8535195921	0.130730	-303.7403459915	-304.283278600	
NconInt′	-302.8946024660	0.134561	-303.7760106639	-304.334280565	
NconInt$_a$″	-302.8392140314	0.133210	-303.7365206912	-304.310168129	**-304.1625306**
NconInt$_b$″	-302.8979780559	0.134985	-303.7803967063	-304.339154227	
CconInt′	-302.8978176085	0.134888	-303.779060056	-304.335552596	
CconInt″	-302.8890279445	0.134556	-303.7700277060	-304.326755513	

Bold values are obtained at CCSD(T)/aug- cc-pVTZ//CCSD/cc-pVDZ level.

3,4,5-triazatricyclo[4.1.0.0^{2,7}] hept-3-ene (TATCE)

Structure	MCSCF	ZPE	MRMP2	PBEPBE-D3
TATCE	-317.7018181259	0.097622	-318.5983668777	-319.184536393
TAP$_1$	-317.7612944617	0.097650	-318.6421572698	-319.220672449
TAP$_2$	-317.7612944617	0.097650	-318.6421572698	-319.220672449
N1disTS$_1$	-317.6174718748	0.092727	-318.5263960453	-319.115340267
N1disTS$_2$	-317.6157311962	0.092735	-318.5229665412	-319.112267448
N3disTS$_1$	-317.6175024882	0.093715	-318.5191920020	-319.112849315

| N3disTS$_2$ | -317.6147485780 | 0.093452 | -318.5162733931 | -319.109702140 |

Table C4. Natural orbital occupation numbers for active space orbitals.

3,4-diazatricyclo[4.1.0.0^{2,7}]hept-3-ene (DATCE)

MOs	11	22	23	24	25	26	27	28	29	30
NdisTS	1.984	1.979	1.969	1.968	1.122	0.879	0.037	0.022	0.021	0.018
CdisTS	1.984	1.979	1.969	1.969	1.089	0.912	0.037	0.022	0.021	0.018
NconTS1	1.983	1.980	1.969	1.951	1.815	0.195	0.042	0.027	0.020	0.017
CconTS1	1.983	1.980	1.969	1.957	1.801	0.207	0.038	0.026	0.020	0.017
NconTS2	1.984	1.979	1.977	1.911	1.259	0.741	0.089	0.022	0.021	0.017
CconTS2	1.984	1.979	1.977	1.911	1.184	0.817	0.089	0.023	0.021	0.017
NconInt	1.984	1.980	1.975	1.923	1.880	0.123	0.075	0.021	0.020	0.018
CconInt	1.984	1.981	1.975	1.924	1.879	0.124	0.074	0.021	0.020	0.018
DATCE	1.984	1.976	1.972	1.967	1.961	0.049	0.029	0.022	0.021	0.020
DAP$_1$	1.984	1.981	1.977	1.936	1.914	0.090	0.059	0.022	0.020	0.016
DAP$_2$	1.984	1.981	1.977	1.936	1.914	0.090	0.059	0.022	0.020	0.016

3,4-diazatricyclo[4.1.0.0^{2,7}]heptane(DATCA)

MOs	22	23	24	25	26	27	28	29	30	31
NdisTS'	1.983	1.979	1.968	1.967	1.170	0.833	0.038	0.024	0.021	0.018
NdisTS''	1.984	1.979	1.969	1.969	1.231	0.770	0.037	0.023	0.021	0.019
CdisTS'	1.984	1.979	1.968	1.967	1.059	0.943	0.037	0.024	0.021	0.018
CdisTS''	1.983	1.979	1.968	1.968	1.004	0.997	0.038	0.023	0.021	0.018
NconTS1'	1.983	1.980	1.970	1.954	1.774	0.234	0.041	0.027	0.020	0.017
NconTS1$_a$''	1.984	1.978	1.969	1.967	1.786	0.216	0.037	0.022	0.021	0.019
NconTS1''	1.983	1.981	1.970	1.952	1.886	0.122	0.039	0.029	0.021	0.017
CconTS1'	1.984	1.979	1.969	1.965	1.766	0.237	0.036	0.024	0.020	0.019
CconTS1''	1.983	1.980	1.969	1.956	1.760	0.247	0.040	0.027	0.020	0.018
NconTS2'	1.983	1.978	1.976	1.915	1.241	0.759	0.086	0.024	0.021	0.017
NconTS2''	1.983	1.979	1.976	1.915	1.164	0.835	0.085	0.023	0.021	0.017
CconTS2'	1.983	1.979	1.976	1.910	1.171	0.829	0.090	0.023	0.021	0.017
CconTS2''	1.983	1.979	1.976	1.906	1.215	0.785	0.094	0.022	0.021	0.017
NconInt'	1.984	1.981	1.975	1.923	1.878	0.124	0.076	0.021	0.020	0.018
NconInt$_a$''	1.983	1.981	1.971	1.961	1.874	0.130	0.036	0.026	0.020	0.018
NconInt$_b$''	1.984	1.980	1.975	1.930	1.867	0.135	0.069	0.022	0.020	0.018
CconInt'	1.984	1.981	1.975	1.924	1.877	0.126	0.074	0.021	0.020	0.018
CconInt''	1.984	1.981	1.974	1.920	1.889	0.114	0.079	0.022	0.020	0.018
DATCA	1.984	1.976	1.972	1.966	1.960	0.050	0.028	0.023	0.021	0.021
DHDAP$_1$	1.984	1.981	1.977	1.939	1.908	0.094	0.058	0.023	0.020	0.015
DHDAP$_2$	1.984	1.981	1.978	1.940	1.911	0.091	0.058	0.023	0.020	0.015

Figure C1. Intrinsic reaction coordinates for the four disrotatory channels for DATCA isomerization.

APPENDIX D

Table D1. Cartesian coordinates for each structure (angstroms).

1. Structure benzvalene

	x	y	z
C	-0.09361444	0.47055408	-0.10371051
C	-0.15200381	-0.93900025	-0.33385876
C	0.95184845	-0.41491333	0.61543894
C	-1.21816230	-0.32307038	0.60327506
C	-0.81929094	-0.57226294	2.02780032
C	0.51743531	-0.62880653	2.03529787
H	-0.05338311	1.34433365	-0.71904308
H	-0.17388284	-1.57227170	-1.19538975
H	1.97589266	-0.40561116	0.29796284
H	-2.23413920	-0.22717814	0.27443075
H	-1.49503589	-0.67865151	2.85061836
H	1.17252612	-0.79153156	2.86556792

2. Structure benzene

	x	y	z
C	-0.85505617	0.05631929	-0.53752303
C	0.43540058	-0.47491845	-0.62239611
C	1.09553993	-0.89561617	0.54381967
C	-1.48410404	0.16636011	0.71348870
C	-0.81795794	-0.25544071	1.86849093
C	0.46022141	-0.78167289	1.78441966
H	-1.36642194	0.38006210	-1.42382693
H	0.92312366	-0.56240672	-1.57440042
H	2.08624983	-1.30372095	0.48048058
H	-2.47475815	0.57401460	0.78048342
H	-1.30065346	-0.17032450	2.82354045
H	0.96666014	-1.10388637	2.67439914

3. Structure disTS

	x	y	z
C	-0.49969479	0.58574504	-0.58668292
C	-0.09237672	-0.74989456	-0.45842883
C	1.03684449	-0.75878704	0.58275461
C	-1.29300070	-0.15087587	0.53330708
C	-0.82796496	-0.42341381	1.85065973
C	0.56331784	-0.64315730	1.85904157
H	-1.01842010	0.96551085	-1.44943500
H	-0.21508378	-1.55600154	-1.16254115

	x	y	z
H	2.06526399	-0.74706024	0.28235289
H	-2.33259010	-0.25569454	0.28742656
H	-1.47755671	-0.48780558	2.69919682
H	1.17592144	-0.63192546	2.73840833

4. Structure disTS$_{back}$

	x	y	z
C	-0.83365291	0.76601261	-0.28751311
C	-0.13934161	-0.52607137	-0.38490373
C	0.98791903	-0.80366969	0.59954035
C	-1.40357661	-0.34796393	0.54592538
C	-0.85863698	-0.49698934	1.92777777
C	0.50904024	-0.74149728	1.89933956
H	-1.33881521	1.27744353	-1.08230245
H	-0.17327148	-1.07300365	-1.30959940
H	2.00000572	-0.98970556	0.30545846
H	-2.36579657	-0.75747287	0.29911140
H	-1.45088768	-0.37111005	2.81052780
H	1.12194383	-0.83879250	2.77356815

5. Structure conTS1$_a$

	x	y	z
C	-0.48189056	0.55429846	-0.49755874
C	-0.13888088	-0.86964154	-0.44251925
C	0.99560082	-0.82889163	0.51910233
C	-1.26933527	-0.29995376	0.47757158
C	-0.79340148	-0.38347018	1.89495397
C	0.53385794	-0.63527673	1.88017821
H	0.08552479	1.45014083	-0.34385839
H	-0.23843694	-1.56830096	-1.25148058
H	2.02433872	-0.88419771	0.22420867
H	-2.29417372	-0.48871240	0.21709068
H	-1.40814221	-0.21891335	2.75520730
H	1.18380952	-0.65634114	2.73140359

6. Structure conTS1$_b$

	x	y	z
C	-0.50297093	0.57183838	-0.51857948
C	0.11780674	-0.68796760	-0.50674665
C	1.17886078	-0.91360807	0.57008582
C	-1.38284039	-0.21255155	0.45741639
C	-0.79290003	-0.26335379	1.72978771
C	0.64550996	-0.57442611	1.76313233
H	0.04066788	1.41775155	-0.13330726

	x	y	z
H	-0.24384066	-1.49950397	-1.10985982
H	2.14899445	-1.33708191	0.41018009
H	-2.38862038	-0.51306462	0.23680490
H	-1.37164462	-0.27439317	2.63406634
H	1.17979980	-0.62746698	2.69191432

7. Structure conTS2

	x	y	z
C	-0.60312861	0.33196312	-0.60104370
C	0.40970480	-0.69692659	-0.72337109
C	1.27138186	-0.78242040	0.51838052
C	-1.51094031	0.08356415	0.58478689
C	-0.86735332	-0.36093181	1.68573689
C	0.58521593	-0.64758307	1.67377901
H	-0.28780583	1.35953712	-0.70557755
H	0.10424759	-1.65644002	-1.11363649
H	2.30138612	-1.08459997	0.49898896
H	-2.54118514	0.38453919	0.60916448
H	-1.39321041	-0.47924933	2.61498356
H	1.07564771	-0.78701591	2.61932731

8. Structure conInt$_a$

	x	y	z
C	-0.57760823	0.58788604	-0.51373708
C	-0.09346341	-0.79986894	-0.43302998
C	1.03086138	-0.92376935	0.56775945
C	-1.28645205	-0.32114619	0.46115687
C	-0.78221571	-0.34203702	1.86838901
C	0.55880922	-0.64883810	1.87184274
H	-0.05448128	1.49982798	-0.30086973
H	-0.20677087	-1.49327898	-1.24427605
H	2.04866624	-1.13118958	0.30732131
H	-2.28421497	-0.63807350	0.22281939
H	-1.37552834	-0.10177384	2.72601128
H	1.18277133	-0.65095592	2.74345875

9. Structure conInt$_b$

	x	y	z
C	-0.51464897	0.34783122	-0.48861307
C	0.31462818	-0.74718034	-0.62273878
C	1.29794645	-0.76641470	0.54574531
C	-1.54038537	0.05896322	0.60560381
C	-0.87581515	-0.37048936	1.70687735
C	0.59228200	-0.64087760	1.69694412

	x	y	z
H	-0.02741032	1.30146420	-0.33919087
H	-0.17220303	-1.70378208	-0.75352222
H	2.33453703	-1.04218507	0.52124327
H	-2.57708979	0.33494130	0.61710888
H	-1.39146316	-0.49250481	2.64236450
H	1.07345223	-0.77493781	2.64900017

10. Structure benzvalyne

	x	y	z
C	-0.09655527	0.46972793	-0.08906191
C	-0.15227714	-0.94399583	-0.31827629
C	0.96095592	-0.41598082	0.63547862
C	-1.23455715	-0.32644540	0.61718422
C	-0.78297228	-0.57163441	2.01951647
C	0.46763608	-0.62262678	2.02995729
H	-0.05597737	1.33870459	-0.71054584
H	-0.17067322	-1.57307601	-1.18251884
H	1.98582458	-0.40685388	0.32961217
H	-2.25004411	-0.23404928	0.29431415

11. Structure benzyne

	x	y	z
C	-0.85433865	0.07954445	-0.50540119
C	0.45567364	-0.51211542	-0.56695950
C	1.11552680	-0.95593274	0.57378685
C	-1.53788245	0.23954958	0.72220904
C	-0.77983809	-0.23981614	1.78692305
C	0.35904256	-0.75357455	1.72803020
H	-1.31895959	0.40563443	-1.41686261
H	0.92737263	-0.60839272	-1.52674186
H	2.09028578	-1.39730299	0.53802228
H	-2.51223373	0.67773306	0.78508759

12. Structure disTS′

	x	y	z
C	-0.57148534	0.64626724	-0.53885663
C	-0.07987246	-0.74889797	-0.42853338
C	1.03785706	-0.90788382	0.59108502
C	-1.31887484	-0.19899753	0.47291785
C	-0.75266618	-0.29607776	1.83234119
C	0.48937288	-0.57841164	1.84531891
H	-1.00361979	1.09947145	-1.40774906
H	-0.18274766	-1.44842732	-1.23862195
H	2.07025957	-1.00489724	0.33048084

| | H | -2.33933306 | -0.44720116 | 0.26152629 |

13. Structure conTS1$_a$′

	x	y	z
C	-0.48499542	0.57807237	-0.44684583
C	-0.18107219	-0.87599397	-0.42789406
C	0.95849288	-0.77209949	0.49913400
C	-1.31527638	-0.25317946	0.50453913
C	-0.77220047	-0.35460770	1.89710152
C	0.45264027	-0.60662371	1.86098838
H	0.06353579	1.49203587	-0.37687969
H	-0.26955703	-1.55766630	-1.25254023
H	1.98156440	-0.73115003	0.19051071
H	-2.34816957	-0.39383724	0.25838998

14. Structure conTS1$_b$′

	x	y	z
C	-0.56745547	0.58684391	-0.48268569
C	0.15725785	-0.68826091	-0.49418423
C	1.15661573	-0.93949485	0.59854102
C	-1.41760385	-0.23299107	0.47563148
C	-0.70996094	-0.20483841	1.69769883
C	0.57978088	-0.46565640	1.74749911
H	-0.10151576	1.50768197	-0.18310136
H	-0.05886872	-1.42647159	-1.24150288
H	2.02429724	-1.55759370	0.50416756
H	-2.42468691	-0.54710895	0.29699609

15. Structure conInt$_a$′

	x	y	z
C	-0.59775037	0.62431282	-0.46530423
C	-0.12702130	-0.81251937	-0.42224678
C	0.99712479	-0.90821701	0.54368252
C	-1.32997572	-0.27527353	0.48931655
C	-0.75663209	-0.31396541	1.87261868
C	0.46679676	-0.59068650	1.85656762
H	-0.05315014	1.51507330	-0.22183387
H	-0.22591665	-1.46724463	-1.26617146
H	2.02726650	-1.01349378	0.27691770
H	-2.33505273	-0.56371480	0.25802734

Table D2. Imaginary frequencies for transition state.

benzvalene

Transition State	Imaginary Frequencies
disTS	294.92i
disTS$_{back}$	336.76i
conTS1$_a$	159.27i
conTS1$_b$	728.43i
conTS2	849.86i

benzvalyne

Transition State	Imaginary Frequencies
disTS'	226.38i
conTS1$_a$'	316.99i
conTS1$_b$'	1071.86i

Table D3. Calculated energies (Hartree) for each structure.

benzvalene

Structure	MCSCF	ZPE	MRMP2
benzvalene	-230.7610277333	0.101768	-231.6034371904
benzene	-230.9012367588	0.104108	-231.7302258617
disTS	-230.7166847405	0.098434	-231.5674694378
disTS$_{back}$	-230.7094137023	0.097831	-231.5521850547
conTS1$_a$	-230.7110932530	0.098057	-231.5571473528
conInt$_a$	-230.7113331421	0.098003	-231.5540633982
conTS1$_b$	-230.6955856068	0.097540	-231.5479338186
conInt$_b$	-230.7399238638	0.100427	-231.5769472948
conTS2	-230.7328819966	0.097628	-231.5666894649

benzvalyne

Structure	MCSCF	ZPE	MRMP2
benzvalyne	-229.4824455493	0.077037	-230.2567437929
benzyne	-229.6520074000	0.078155	-230.4154135000
disTS'	-229.4355307572	0.071925	-230.2152332228
conTS1$_a$'	-229.4373847249	0.072905	-230.2182070091
conInt$_a$'	-229.4384786149	0.073032	-230.2163170536
conTS1$_b$'	-229.4206545733	0.070416	-230.2114283808

Table D4. Natural orbital occupation numbers for active space orbitals.

benzvalene

MOs	17	18	19	20	21	22	23	24	25	26
disTS	1.978	1.973	1.962	1.926	1.711	0.295	0.073	0.036	0.024	0.022
disTS$_{back}$	1.980	1.979	1.967	1.913	1.039	0.962	0.087	0.033	0.021	0.020
conTS1$_a$	1.982	1.977	1.967	1.914	1.618	0.384	0.084	0.033	0.022	0.019
conTS1$_b$	1.978	1.975	1.936	1.915	1.679	0.330	0.078	0.066	0.022	0.022
conTS2	1.978	1.978	1.932	1.885	1.309	0.697	0.115	0.065	0.023	0.019
conInt$_a$	1.981	1.979	1.968	1.908	1.248	0.753	0.091	0.032	0.021	0.019
conInt$_b$	1.977	1.975	1.931	1.889	1.756	0.252	0.112	0.065	0.023	0.020
Benzvalene	1.979	1.975	1.971	1.964	1.912	0.088	0.038	0.029	0.023	0.021
Benzene	1.982	1.981	1.961	1.911	1.908	0.093	0.090	0.036	0.019	0.017

benzyne

MOs	15	16	17	18	19	20	21	21	23	24	25	26
disTS′	1.981	1.969	1.962	1.908	1.697	1.236	0.767	0.303	0.091	0.041	0.024	0.020
conTS1$_a$′	1.981	1.970	1.965	1.911	1.763	1.710	0.290	0.241	0.086	0.039	0.023	0.021
conTS1$_b$′	1.981	1.970	1.925	1.891	1.689	1.426	0.584	0.319	0.089	0.081	0.025	0.020
conInt$_a$′	1.981	1.970	1.965	1.911	1.751	1.477	0.524	0.252	0.087	0.039	0.023	0.020
Benzvalyne	1.978	1.974	1.970	1.962	1.901	1.735	0.268	0.095	0.040	0.030	0.024	0.021
Benzyne	1.982	1.977	1.958	1.912	1.905	1.835	0.166	0.098	0.087	0.039	0.022	0.017

RightsLink®

ACS Publications
Most Trusted. Most Cited. Most Read.

LOGIN

If you're a copyright.com user, you can login to RightsLink using your copyright.com credentials.

Already **a RightsLink user** or want to learn more?

PERMISSION/LICENSE IS GRANTED FOR YOUR ORDER AT NO CHARGE

This type of permission/license, instead of the standard Terms & Conditions, is sent to you because no fee is being charged for your order. Please note the following:

- Permission is granted for your request in both print and electronic formats, and translations.
- If figures and/or tables were requested, they may be adapted or used in part.
- Please print this page for your records and send a copy of it to your publisher/graduate school.
- Appropriate credit for the requested material should be given as follows: "Reprinted (adapted) with permission from (COMPLETE REFERENCE CITATION). Copyright (YEAR) American Chemical Society." Insert appropriate information in place of the capitalized words.
- One-time permission is granted only for the use specified in your request. No additional uses are granted (such as derivative works or other editions). For any other uses, please submit a new request.

BACK   CLOSE WINDOW

VITA

WEIWEI YANG

Education

Ph.D., The University of Mississippi, USA	08/2015-08/2019
M.S. in Chemical Engineering, Ocean University of China, China	09/2012-07/2015
B.S. in Pharmaceutical Engineering, Northwest University, China	09/2008-07/2012

Publication and Patent

- **Yang, W**., Davis, S. R. The *ab initio* Study of Thermal Isomerization of Benzvalene to Benzene and Benzvalyne to Benzyne. *Manuscript preparation.*
- Poland, K. N., **Yang, W**., Mitchell E. C., Dam A. A., Davis, S. R. Heterocyclic Isomers of Forbidden and Allowed Pathways Forged from a Pericyclic Reactant. *Manuscript preparation.*
- **Yang, W**., Poland, K. N., Davis, S. R. Isomerization barriers and resonance stabilization for the conrotatory and disrotatory isomerizations of nitrogen containing tricyclo moieties. *Physical Chemistry Chemical Physics.***2018**, 20, 26608.
- Liyanage, N. P., **Yang, W**., Guertin, S., Sinha Roy, S., Carpenter, C. A., Schmehl, R. H., Delcamp, J. H., Jurss, J. W. Photochemical CO_2 reduction with mononuclear and dinuclear rhenium catalysts bearing a pendant anthracene Chromophore. *Chemical Communication.* **2019**, *55*, 993-996.
- **Yang, W**., Sinha Roy, S., Pitts, W. C., Nelson, R., Fronczek, F. R., Jurss, J. W. Electrocatalytic CO_2 Reduction with *cis* and *trans* Conformers of a Rigid Dinuclear Rhenium Complex: Comparing the Mon-ometallic and Cooperative Bimetallic Pathways. *Inorganic Chemistry.*, **2018**, *57* (15),9564–9575
- Zhang, J**., Yang, W.**, Vo, AQ., Feng, X., Ye, X., Kim. DW., et al. Hydroxypropyl methylcellulose-based controlled release dosage by melt extrusion and 3D printing: Structure and drug release correlation. *Carbohydrate Polymers*. **2017**, 177, 49–57.
- **Yang, W.**, Li, C., Wang, L., Sun, S., Yan, X., Solvothermal fabrication of activated semi-coke supported TiO_2-rGO nanocomposite photocatalysts and application for NO removal under visible light. *Applied Surface Science.* **2015**, 353, 307-316.
- Li, C., **Yang, W.**, Wang, L., A Preparation Method of Carbon-based Photocatalyst for NO Removal*.* Pub NO. *CN104307542B*

Honors and Awards

- Outstanding Chemistry Graduate Student for the American Chemist Society, The University of Mississippi. 04/2016
- Third Prize of the 2014 ShanDong Province College Students Entrepreneurship Competition (Leader). 06/2014
- First Prize of the 9th OUC Challenge Cup Entrepreneurship Competition (Leader). 05/2014
- Outstanding Student (i.e. First-class Scholarship), OUC. 11/2013
- Third Prize of the 9th National Post-graduate Mathematical Contest in Modeling, China. 12/2012
- First Prize of the 3rd Sinology Knowledge Competition, OUC. 11/2012
- Second Prize of the "Mitsui cup" Chemical Engineering Design Competition, NWU. 05/2011
- Outstanding Student (i.e. First-class Scholarship), NWU. 12/2010
- National Encouragement Scholarship, NWU. 05/2010
- Second-class Scholarship, NWU. 12/2009